IN-34

NASA Technical Memorandum 106532

Calculation of Propulsive Nozzle Flowfields in Multidiffusing Chemically Reacting Environments

Kenneth John Kacynski
Lewis Research Center
Cleveland, Ohio

April 1994

(NASA-TM-106532) CALCULATION OF PROPULSIVE NOZZLE FLOWFIELDS IN MULTIDIFFUSING CHEMICALLY REACTING ENVIRONMENTS Ph.D. Thesis - Purdue Univ. (NASA. Lewis Research Center) 295 p

N94-28835

Unclas

G3/34 0003007

National Aeronautics and
Space Administration

CALCULATION OF PROPULSIVE NOZZLE FLOWFIELDS IN MULTIDIFFUSING CHEMICALLY REACTING ENVIRONMENTS

A Thesis

Submitted to the Faculty

of

Purdue University

by

Kenneth John Kacynski

In Partial Fulfillment of the

Requirements for the Degree

of

Doctor of Philosophy

May 1994

TABLE OF CONTENTS

	Page
LIST OF TABLES	vi
LIST OF FIGURES	ix
LIST OF SYMBOLS	xvi
ABSTRACT	xx
SECTION 1 - INTRODUCTION	1
1.1 Previous Efforts	2
1.2 Present Analysis	2
SECTION 2 - GOVERNING EQUATIONS	4
2.1 Navier-Stokes Equations	4
2.2 Constitutive Equations	5
2.3 Species Source Function	7
2.4 Thermal and Caloric Equations of State	9
2.5 Time-Averaged Turbulent Flow Equations	10
2.6 Nondimensionalization of Fluid Flow Equations	13
SECTION 3 - GENERALIZED COORDINATE TRANSFORMATION	19
3.1 Generalized Transformation of the Advective and Pressure Flowfield Expressions	19
3.2 Flow Conservation of the Advective and Pressure Terms	21
3.3 Generalized Transformation of Diffusive Terms in the Navier-Stokes Equations	24
3.4 Conservation of Diffusion Terms	27
SECTION 4 - BOUNDARY CONDITIONS	33
4.1 Constant-η Reference Plane Method of Characteristics	34
4.2 Subsonic Nozzle Inlet Boundary Conditions	38

Page

4.3 Nozzle Exit Boundary Conditions 38
4.4 Nozzle Centerline and Free Slip Wall Boundary Conditions 39
4.5 No Slip Wall Boundary Conditions 39
4.6 Transpired Wall Boundary Conditions 40

SECTION 5 - OVERALL NUMERICAL ALGORITHM 43

SECTION 6 - VALIDATION STUDIES 46

6.1 Conservation of One-Dimensional Inviscid Flow 47
6.2 Inviscid Pipe Flow - One-Dimensional Grid Transformation 48
6.3 Inviscid Pipe Flow - Two-Dimensional Grid Transformation 50
6.4 Couette Flow 53
6.5 Supersonic Radial Source Flow 57
6.6 Inlet, Exit, and Wall Reference Plane Characteristics Verification 63

SECTION 7 - DEMONSTRATION STUDIES 70

7.1 1030:1 High Area Ratio Nozzle 71
7.1.1 Analytical Assumptions 73
7.1.2 Boundary Conditions 74
7.1.3 Computational Grid Used for Analytical Study 75
7.1.4 Analytical Study and Results 79
7.1.4.1 Mach Number Contour Predictions 80
7.1.4.2 Comparison of Experimental and Predicted Wall Pressures and Heat Fluxes 90
7.1.4.3 Prediction of Hydrogen Mass Fraction Along the Wall 92
7.1.4.4 Performance Predictions 94
7.1.4.5 Comparison of Experimental and Predicted Performance 95
7.2 25 lbf Film Cooled Rocket Engine 97
7.2.1 Analytical Assumptions for the 25 lbf Film Cooled Nozzle 100
7.2.2 Boundary Conditions for the 25 lbf Film Cooled Nozzle 101
7.2.3 Computational Grid Used for the 25 lbf Film Cooled Nozzle Study 103
7.2.4 Analytical Study of the 25 lbf Film Cooled Nozzle 106
7.2.5 Analytical Results and Comparison with Experimental Measurements 109
7.2.5.1 Mach Number Contour Predictions 109
7.2.5.2 Fluid Velocity Vectors 112
7.2.5.3 Predicted Steam Mass Fraction Contours 115

Page

7.2.5.4 Predicted and Measured Pressure Profiles 120
7.2.5.5 Predicted and Experimental Heat Transfer Rates 121
7.2.5.6 Predicted and Measured Performance Parameters 125
7.3 Transpiration Cooled Rocket Nozzle 129
7.3.1 Analytical Modeling of the Transpiration Cooled Rocket Nozzle 132
7.3.2 Boundary Conditions Employed for the Transpiration Cooled Rocket Nozzle 132
7.3.3 Computational Grid Used for Analysis of the Transpiration Cooled Rocket Nozzle 135
7.3.4 Analytic Results and Comparison with Experimental Measurements 138
7.3.4.1 Mach Number Contour Predictions 138
7.3.4.2 Hydrogen Wall Mass Fraction Prediction 141
7.3.4.3 Transpiration Coolant Mass Flux Predictions 143
7.6.4.4 Heat Flux Predictions 146

SECTION 8 - CONCLUSIONS 149

SECTION 9 - RECOMMENDATIONS 151

LIST OF REFERENCES 155

APPENDICES

Appendix A - Interior Point Numerical Algorithm of the Proteus Code 160
Appendix B - Interior Point Numerical Algorithm 177
Appendix C - Multicomponent Species Diffusion 191
Appendix D - Species Source Function 197
Appendix E - Time-Averaged, Density-Weighted, Turbulent Flow Equations 205
Appendix F - Turbulence Modelling 212
Appendix G - Transformation of the Governing Equations 218
Appendix H - Reference Plane Characteristic Method 224
Appendix I - Chemical Reaction Mechanism and Reaction Rate Constants 237
Appendix J - Chemical Kinetics Validation 239
Appendix K - Fluid Properties Validation 249
Appendix L - Flow Modelling Validation of Species Ordinary Diffusion Equations 255
Appendix M - Evaluation of Flowfield Parameters Using the JANNAF Procedure 258
Appendix N - Artificial Diffusion Model 264
Appendix O - Fluid Thermodynamic and Transport Property Equations 270

VITA 275

LIST OF TABLES

Table		Page
1.	Nondimensional parameters used in the Tethys model	13
2.	Nondimensional reference numbers	14
3.	Species Source number for selected H_2/O_2 rocket engines	16
4.	Constant-η referance plane method of characteristics	36
5.	Inlet boundary conditions used for frozen source flow examination	58
6.	JPL nozzle boundary conditions	67
7.	Boundary conditions applied to the LeRC 1030:1 nozzle	74
8.	Various analysis methodologies employed for the 1030:1 LeRC nozzle	80
9.	Tethys performance predictions	94
10.	Experimental performance comparison of the LeRC 1030:1 nozzle	96
11.	Nominal operating conditions for the 25 lbf film cooled nozzle	100
12.	Boundary conditions applied to the 25 lbf film cooled nozzle	102
13.	Analysis methods used for the 25 lbf film cooled nozzle.	107
14.	Comaprison of measured and predicted global heat transfer rates	125
15.	Comparison of measured and predicted performance parameters	128
16.	Nominal operating conditions of the transpiration cooled rocket nozzle	131
17.	Boundary conditions applied to the transpiration cooled rocket nozzle	133

Table | Page

18. Various analysis methods used for the transpiration cooled rocket nozzle 134

19. Total coolant flow rate requirements 144

Appendix
Table

20. Comparison of the formulation of the radial pressure gradient 178

21. Comparison of the formulation of the radius terms 178

22. Finite difference approximation of a ξ-only derivative component of axial shear stress term in the axial momentum equation in the Proteus code 181

23. Finite difference approximation of a ξ-only derivative component of the axial shear stress term in the axial momentum equation in the Tethys code 182

24. Finite difference approximation of cross-derivative components of the axial shear stress term in the axial momentum equation in the Proteus code 183

25. Finite difference approximation of cross-derivative components of the axial shear stress term in the axial momentum equation in the Tethys code 184

26. Characteristic and compatibility equations for a constant-η reference plane 232

27. Artificial diffusion applied to constant-η reference plane characteristic equations 234

28. Characteristic and compatibility equations for species equations 236

29. Artificial diffusion applied to species equations 236

30. Chemical reaction rate constants 237

31. Catalytic efficiencies 238

32. Inlet boundary conditions for reacting source flow study 240

Appendix
Table

Page

33. Specy generation rates at the inlet, low density analysis 244

34. Specy generation rates at the inlet, moderate density analysis 244

35. Specy generation rates at the inlet, high density analysis 245

36. Fluid conditions for validation of specific heat, thermal conductivity, and viscosity models 251

37. Comparison of CET89 and Tethys fluid property predictions 251

38. Comparison of theoretical and predicted multispecies diffusion coefficients for a ternary system 252

39. Boundary conditions for species ordinary diffusion validation study 256

40. Low temperature thermodynamic property coefficients 271

41. High temperature thermodynamic property coefficients 271

42. Low temperature thermal conductivity coefficients 272

43. High temperature thermal conductivity coefficients 273

44. Low temperature viscosity coefficients 273

45. High temperature viscosity coefficients 273

46. Binary diffusion coefficients 274

LIST OF FIGURES

Figure		Page
1.	Discretization of flowfield about point 0 for an arbitrary grid	22
2.	Flow between concentric tubes	27
3.	Discretization about point 0 for an arbitrary grid	28
4.	Characteristic surfaces and lines for unsteady two-dimensional flow	35
5.	Constant-η reference plane	35
6.	Characteristics at a subsonic flow inlet	38
7.	Transpiration cooled wall	41
8.	One-dimensional transformed grid for inviscid pipe flow calculation	49
9.	Convergence rate of standard, exact radius, and conservative techniques for inviscid pipe flow with a one-dimensional grid transformation	50
10.	Two-dimensional grid used in the inviscid flow conversation study	51
11.	Convergence rate of conservative technique for inviscid flow with a two-dimensional grid transformation	52
12.	Divergence rate of standard and exact radius techniques for inviscid pipe flow with a two-dimensional grid transformation	52
13.	6X11 Computational grid employed for the analysis of Couette flow	53

Figure Page

14. Predicted velocity profiles for a Couette flow simulation..... 54

15. Axial velocity error at the computational midline of a Couette flow simulation..... 55

16. Predicted velocity distribution for axisymmetric Couette flow simulation..... 56

17. Axial velocity error at the computational midline of an axisymmetric Couette flow simulation..... 56

18. One-dimensional radial source flow..... 57

19. Computational grid used for supersonic planar source flow simulation..... 59

20. Mach number predictions for a chemically frozen 100:1 area ratio planar source flow calculation..... 60

21. Mass flow rate conservation study for a 100:1 planar source flow simulation..... 61

22. Stagnation enthalpy conservation study for a 100:1 planar source flow simulation..... 62

23. Stagnation pressure conservation study for a 100:1 planar source flow simulation..... 62

24. Numerical implementation of the constant-η reference plane method of characteristics..... 64

25. Schematic of small radius of curvature nozzle tested at JPL..... 65

26. 45X11 grid used for JPL transonic nozzle flow study..... 66

27. Comparison of Mach number contour predictions and experimental measurements for the JPL nozzle..... 69

28. High area ratio nozzle test program conducted at NASA LeRC..... 71

29. Rocket engine test facility used for evaluation of 1030:1 area ratio nozzle..... 72

Figure Page

30. Wall temperature distribution applied to high area ratio rocket nozzle analysis 75

31. Computational grid employed for high area ratio nozzle analysis 76

32. Throat region view of computational grid employed for high area ratio nozzle analysis 77

33. Mach number contour predictions for the LeRC high area ratio nozzle using an inviscid, chemically frozen analysis (Test case 1) 82

34. Throat region Mach number contour predictions for the LeRC high area ratio nozzle using an inviscid, chemically frozen analysis (Test case 1) 83

35. Mach number contour predictions for the LeRC high area ratio nozzle using a viscous, chemically frozen analysis (Test case 2) 84

36. Throat region Mach number contour predictions for the LeRC high area ratio nozzle using a viscous, chemically frozen analysis (Test case 2) 85

37. Mach number contour predictions for the LeRC high area ratio nozzle using a viscous, chemically reacting analysis (Test case 3) 86

38. Throat region Mach number contour predictions for the LeRC high area ratio nozzle using a viscous, chemically reacting analysis (Test case 3) 87

39. Mach number contour predictions for the LeRC high area ratio nozzle using a viscous, multiple diffusing, chemically reacting analysis (Test case 4) 88

40. Throat region Mach number contour predictions for the LeRC high area ratio nozzle using a viscious, multiple diffusing, chemically reacting analysis (Test case 4) 89

41. Comparison of experimental wall static pressure measurements and predictions from Tethys model (Test case 4) 90

Figure Page

42. Comparison of experimental heat flux measurements and predictions from Tethys model (Test case 4) 91

43. Comparison of the difference in heat transfer predictions between the three different viscous flow assumptions 92

44. Hydrogen mass fraction predictions along the wall of the LeRC high area ratio nozzle 93

45. 25 lbf film cooled rocket hardware and instrumentation schematic 97

46. Injector and film cooled sleeve assembly 98

47. Film cooled sleeve geometry 98

48. Detail drawing of the 25 lbf film cooled nozzle 99

49. Experimental facility used for the 25 lbf film cooled nozzle tests 99

50. Temperature distribution used for wall boundary condition of the Tethys fluid flow simulation of the 25 lbf film cooled nozzle 103

51. Computational grid employed for the 25 lbf film cooled nozzle analysis 104

52. Oxygen to fuel mixture ratio profile assumed for the stratified core analysis 106

53. Mixing layer origination point 108

54. Mach number contour predictions for the 25 lbf film cooled nozzle using the fully mixed core assumption 110

55. Mach number contour predictions for the 25 lbf cooled nozzle using the stratified core assumption 111

56. Velocity vector predictions for the 25 lbf film cooled nozzle using the stratified core assumption 113

57. Throat region velocity vector predictions for the 25 lbf film cooled nozzle using the stratified core assumption 114

Figure Page

58. Steam mass fraction contours for the 25 lbf film cooled nozzle using the fully mixed core assumption 116

59. Steam mass fraction contours in the throat region of the 25 lbf film cooled nozzle using the fully mixed core assumption 117

60. Steam mass fraction contours in the 25 lbf film cooled nozzle using the stratified core assumption 118

61. Steam mass fraction contours in the throat region of the 25 lbf film cooled nozzle using the stratified core assumption 119

62. Comparison of experimental and predicted wall pressure distributions in the 25 lbf film cooled nozzle using a fully mixed core assumption 120

63. Comparison of experimental and predicted wall pressure distributions in the 25 lbf film cooled nozzle using a stratified core assumption 121

64. Wall heat flux predictions of the 25 lbf film cooled nozzle using the fully mixed core assumption 122

65. Wall heat flux predictions of the 25 lbf film cooled nozzle using the stratified core assumption 123

66. Streaking effects on the wall temperature distribution of the 25 lbf film cooled nozzle 124

67. Comparison of experimental and predicted specific impulse for the 25 lbf film cooled nozzle study 126

68. Comparison of experimental and predicted thrust coefficient for the 25 lbf film cooled nozzle study 126

69. Plug and spool rocket engine tested at NASA LeRC 130

70. Schematic of the transpiration cooled spoolpiece section 131

71. Schematic of surface roughening caused by excessive electro-polishing of the transpiration cooled rocket nozzle 134

Figure Page

72. Temperature distribution used for analysis of the transpiration cooled rocket nozzle..... 135

73. Computational grid employed for the analysis of the transpiration cooled rocket nozzle..... 136

74. Predicted Mach number contours for the transpiration cooled plug and spool rocket nozzle using smooth wall analysis..... 139

75. Predicted Mach number contours for the transpiration cooled plug and spool rocket nozzle using a rough wall analysis..... 140

76. Hydrogen wall mass fraction predictions using a smoothed walled analysis..... 142

77. Hydrogen wall mass fraction predictions using a rough walled analysis..... 142

78. Transpiration coolant flow rate predictions and experimental comparison..... 144

79. Predicted hydrogen mass fluxes along the wall of the transpiration cooled plug and spool rocket engine using a smooth wall analysis..... 145

80. Predicted hydrogen mass fluxes along the wall of the transpiration cooled plug and spool rocket nozzle using a rough wall analysis..... 146

81. Predicted heat flux into the mainstream of the plug and spool rocket nozzle using a smooth wall analysis..... 147

82. Predicted heat flux into the mainstream of the plug and spool rocket nozzle using a rough wall analysis..... 148

Appendix
Figure

83. Computational grid for comparison of viscous term finite difference approximations used in Proteus and Tethys codes..... 180

84. Schematic of source flow geometry used for chemical kinetics validation..... 239

Appendix Figure | Page

85. Computational grid used for chemical kinetics source flow validation 241

86. Mach number distribution from LSENS code for chemical kinetics study.. 242

87. Mach number error associated with Tethys flow model 243

88. Variation of the OH radical in a chemically reacting source flow study 245

89. Variation of the monatomic hydrogen radical in a chemically reacting source flow study 246

90. Variation of the monatomic oxygen radical in a chemically reacting source flow study 246

91. Error in OH mass fraction in a chemically reacting source flow study 247

92. Error in monatomic hydrogen species mass fraction in a chemically reacting source flow study 248

93. Error in monatomic oxygen species mass fraction in a chemically reacting source flow study 248

94. Comparison of experimental and predicted values of the thermal diffusion factor in a hydrogen/oxygen system 253

95. Temperature sensitivity of the thermal diffusion coefficient in a chemically reacted hydrogen/oxygen system 254

96. Computational grid and geometry of species diffusion validation study 255

97. Comparison of theoretical and predicted species concentration for ordinary species diffisuion validation studies 257

98. Control surface employed for evaluation of nozzle performance parameters 258

99. Control surface across the nozzle throat 259

100. Nozzle surface examination of shear stress calculation procedure 261

LIST OF SYMBOLS

a	Fluid speed of sound
A_{ij}	Multicomponent ordinary species mass diffusion coefficient in relation to n-1 mass fraction gradients
B_j	Chemical reaction rate coefficient for binary exchange reaction j
B_{ij}	Chemical reaction rate coefficient for species i in catalytic reaction j
C_p	Constant pressure specific heat of the fluid
C_v	Constant volume specific heat
$\overline{C}_{vi}$	Temperature averaged specific heat of species i
D_i^T	Thermal diffusion coefficient
d	Total derivative operator
e	Specific total energy of the fluid
E	Axial direction advective flux vector in the Navier-Stokes equations
E_v	Axial direction viscous flux vector in the Navier-Stokes equations
E_j	Exponential coefficent for chemical reaction j
F	Radial direction flux vector in the Navier-Stokes equations
F_v	Radial direction viscous flux vector in the Navier-Stokes equations
h_i	Specific enthalpy of species i
h_o	Specific total enthalpy of the fluid
H	Source vector in the Navier-Stokes equations
H_v	Viscous source vector in the Navier-Stokes equations
j_i	Species mass flux with respect to average velocity for the ith species
J	Jacobian of the coordinate transformation
k	Fluid thermal conductivity or wall surface roughness
k^t	Turbulent fluid viscosity

K_{bj}	Backward chemical reaction rate of reaction j
K_{fj}	Forward chemical reaction rate of reaction j
K_{Pj}	Equillibium constant for reaction j
Le^t	Turbulent Lewis number
M	Molecular weight of the mixture
M_i	Molecular weight of species i
n	Unit normal direction or total number of species present
P	Fluid static pressure
P_o	Fluid stagnation pressure
Pr^t	Turbulent Prandtl number
q	Heat flux
Q	Dependent variable vector of the Navier-Stokes equations
r	Radius
R	Specific gas constant
$\overline{R}$	Universal gas constant
Re	Reynolds number
s	Fluid entropy
t	Time
T	Fluid static temperature
T_o	Fluid stagnation temperature
u	Axial velocity
u	Internal energy of the fluid
u_i	Internal energy of species i
U	Contravarient velocity in the ξ-direction
v	Radial velocity
V	Contravarient velocity in the η-direction
x	Axial location
x_i	Mole fraction of species i

y	Distance from a wall
α_j	Temperature power coefficient of chemical reaction j
α_T	Thermal diffusion factor
$\wp_{ij}$	Binary diffusion coefficient between species i and j
$\wp^t_{iM}$	Turbulent diffusion coefficient between species i and the rest of the mixture
δ	Partial differential operator
Δ	Difference operator
∇	Divergence operator
ξ,η	Computational space coordinates
λ	Second coefficient of viscosity
λ^t	Second coefficient of turbulent viscosity
μ	Fluid viscosity
μ^t	Turbulent viscosity
ν'_{ij}	Stoichiometric coefficient of species i in the reactants of the jth chemical reaction
ν''_{ij}	Stoichiometric coefficient of species i in the products of the jth chemical reaction
Π	Product operator
ρ	Fluid static density
ρ_i	Fluid static density of species i
σ_i	Mass generation rate of species i (i.e., species source function)
Σ	Summation operator
τ	Computational time derivative or shear stress tensor
ω_i	Mass fraction of species i

General superscripts

T	Transposed matrix

General overscripts

–	Time-averaged quantity
~	Density-weighted, time-averaged, quantity
^	Vectors in computational space and time

ABSTRACT

Kacynski, Kenneth John. Ph.D., Purdue University, May 1994. Calculation of Propulsive Nozzle Flowfields in Multidiffusing Chemically Reacting Environments. Major Professor: Joe D. Hoffman, School of Mechanical Engineering.

An advanced engineering model has been developed to aid in the analysis and design of hydrogen/oxygen chemical rocket engines. The complete multispecies, chemically reacting and multidiffusing Navier-Stokes equations are modelled, including the Soret thermal diffusion and the Dufour energy transfer terms. In addition to the spectrum of multispecies aspects developed, the model developed in this study is also conservative in axisymmetric flow for both inviscid and viscous flow environments and the boundary conditions employ a viscous, chemically reacting, reference plane characteristics method. Demonstration cases are presented for a 1030:1 area ratio nozzle, a 25 lbf film cooled nozzle, and a transpiration cooled plug and spool rocket engine. The results indicate that the thrust coefficient predictions of the 1030:1 and the 25 lbf film cooled nozzle are within 0.2 to 0.5 %, respectively, of experimental measurements when all of the chemical reaction and diffusion terms are considered. Further, the model's predictions agree very well with the heat transfer measurements made in all of the nozzle test cases.

The Soret thermal diffusion term is demonstrated to have a significant effect on the predicted mass fraction of hydrogen along the wall of the nozzle in both the laminar flow 1030:1 nozzle and the turbulent flow plug and spool nozzle analysis cases performed. Further, the Soret term was shown to represent an important fraction of the diffusion fluxes occurring in a transpiration cooled rocket engine.

SECTION 1

INTRODUCTION

The computation of rocket nozzle performance is of critical importance to the rocket engine industry. Often, the rocket engine manufacturer needs to compare various engine operating systems before deciding on a specific configuration. Two items that are of critical importance are nozzle performance and nozzle heat transfer characteristics. Often these two parameters are interrelated. This is most apparent in cases involving transpiration cooling or film cooling. Under these circumstances, the actively cooled boundary layer serves to thermally (and perhaps chemically) protect the nozzle wall from the exhaust gasses of the rocket engine core flowfield. In such conditions, the coolant allows the rocket engine to operate at conditions otherwise not attainable, such as high chamber pressures or low thrust levels. The engine designer must then ascertain whether the increased operating pressure or lower thrust level is worth the decreased performance of the engine due to active cooling. Consequently, a need exists for a comprehensive rocket nozzle performance prediction capability that can accurately determine nozzle performance and heat transfer characteristics for design and trade-off studies.

A different need exists for individuals interested in improving rocket nozzle performance predictions and modelling. In these cases, it is important for the individual to ascertain the primary limitations of the nozzle performance prediction technique. A model which would include as many of the potential performance and heat transfer effects as possible and also allow the examination of individual effects, such as species diffusion or chemical kinetics, would be most desirable, with the additional constraint that the solution should be reasonably insensitive to the computational grid employed for the analysis.

1.1. Previous Efforts

Rocket nozzle performance and heat transfer predictions have previously been accomplished primarily by the use of an inviscid core/boundary layer analysis technique, such as the JANNAF (Joint Army, Navy, NASA, Air Force) standard code, TDK/BLM (Reference 1), although others have used the full Navier-Stokes equations (References 2 to 4). In either case, significant simplifying assumptions regarding the species diffusion and heat transfer mechanism are made. In general, all rocket engine performance prediction procedures known by the author have employed at least some of the following assumptions:

- No chemical reactions
- No thermal diffusion
- No interdiffusional heat transfer
- No diffusion thermo heat transfer
- Laminar and turbulent Lewis numbers equal to unity
- Simplified fluid transport coefficient models
- Nonconservative evaluation of the finite difference equations
- Extrapolated boundary conditions

For many rocket engine applications, some or all of the above simplifications may be justifiable. In other cases, some, but not all, of the effects will be important. It is conceivable that there may exist conditions where all of the above processes should be included.

1.2. Present Analysis

In the present study, inclusion of the multispecies advection, production (i.e., chemical kinetics), and diffusion terms, with full coupling in the total energy equation, was developed. Further, species and heat transfer by diffusion processes were modelled with consideration of the interrelation between species and heat transfer mechanisms (i.e., the Soret and Dufour effects).

Modelling the multispecies rocket nozzle flowfield calculations was accomplished by

modifying the compressible, two-dimensional Navier-Stokes code, Proteus (Reference 5). In general, prior to these modifications, the Proteus code capabilities included the ability to numerically model the time-averaged Navier-Stokes equations for a single species perfect gas (constant γ). The Proteus code also included the ability to model a temperature dependent specific heat, thermal conductivity, and viscosity, fluid with the properties of air. Either an algebraic turbulence model or a two-equation (Chien k-ε) turbulence model can be used for the closure of the Reynolds averaged turbulent transport terms. However the Proteus code can not adequately approximate turbulence conditions for a transpired wall and thus required modification.

Axisymmetric flow can be modelled in the Proteus code although the analysis was nonconservative and could prove to be unstable (as described later). Modification of the code, based on a 'conservation of one-dimensional flow' concept was applied to both the inviscid and viscous terms to allow robust and accurate handling of the flow equations.

Rocket nozzle performance prediction capabilities and accuracy were further enhanced by the inclusion of the following boundary conditions:

- Characteristic equations at the boundaries
- Mixed subsonic-supersonic exit conditions
- Coupled temperature/species gradient wall conditions
- Coupled heat transfer/transpired fluid wall conditions

A very desirable attribute of the Proteus code is the available documentation (References 5 to 7) and the modular program structure. As stated in the documentation "The Proteus two-dimensional Navier-Stokes computer program is a user-orientated and easily-modifiable flow analysis program for aerospace propulsion applications. Readability, modularity, and documentation were primary objectives during its development." In maintaining the fundamental objective of the Proteus code, a new model, Tethys, was developed for modelling chemically reacting and diffusing rocket nozzle flowfields.

SECTION 2

GOVERNING EQUATIONS

The governing equations for unsteady, viscous, compressible, multispecies laminar or turbulent flow in a two-dimensional axisymmetric coordinate system are quite complicated. They contain terms and correlations that are substantially less well characterized than the flow of a single species gas. While the general equations of multispecies fluid flow are reasonably well characterized for flows of engineering interest, the uncertainties of multispecies fluid flow lie in the determination of the chemical kinetic reaction rates and the transfer of heat, mass, and momentum by diffusion.

2.1. Navier-Stokes Equations

The general form of the axisymmetric equations governing the flow of a multiple species chemically reacting and diffusing gas can be written as follows (References 8 and 9):

$$\frac{\partial (rQ)}{\partial t} + \frac{\partial (rE)}{\partial x} + \frac{\partial (rF)}{\partial r} + H = \frac{\partial (rE_v)}{\partial x} + \frac{\partial (rF_v)}{\partial r} + H_v \tag{2.1.1}$$

$$Q = [\rho, \rho u, \rho v, \rho e, \rho_i]^T \tag{2.1.2}$$

$$E = [\rho u, \rho u^2 + P, \rho uv, (\rho e + P)u, \rho_i u]^T \tag{2.1.3}$$

$$F = [\rho v, \rho uv, \rho v^2, (\rho e + P)v, \rho_i v]^T \tag{2.1.4}$$

$$H = \left[0, 0, r\frac{\partial P}{\partial r}, 0, -r\sigma_i\right]^T \tag{2.1.5}$$

(2.1.6) $$E_v = [0, \tau_{xx}, \tau_{xr}, u\tau_{xx} + v\tau_{xr} - q_x, -j_{i,x}]^T$$

(2.1.7) $$F_v = [0, \tau_{xr}, \tau_{rr}, u\tau_{xr} + v\tau_{rr} - q_r, -j_{i,r}]^T$$

(2.1.8) $$H_v = [0, 0, -\tau_{\theta\theta}, 0, 0]^T$$

For a chemical system comprised of n different species, the species continuity equations (denoted by the i subscript) are solved for the density ρ_i of species 1 to n-1, while ρ_n is determined from the total density:

(2.1.9) $$\rho_n = \rho - \sum_{i=1}^{n-1} \rho_i$$

2.2. Constitutive Equations

The constitutive equations governing the diffusive transfer of momentum, energy, and mass, are somewhat complicated by the presence of multiple species fluid flow due to the coupled nature of the mass transfer and heat transfer terms. Mass transfer will be a function of the concentration gradients, temperature gradient, and the pressure gradient, and the species gradient, although for the particular applications of interest only the temperature and concentration gradients are of significance. Likewise, the heat transfer will also be coupled to the mass transfer, being comprised of conduction, interdiffusion, and Dufour heat transfer mechanisms, the latter two mechanisms being a function of the extent of mass transfer occurring. The general form of the constitutive equations is presented in Equations (2.2.1) through (2.2.8).

Momentum transfer

(2.2.1) $$\tau_{xx} = 2\mu\frac{\partial u}{\partial x} + \lambda\left[\frac{\partial u}{\partial x} + \frac{1}{r}\frac{\partial (rv)}{\partial r}\right]$$

(2.2.2) $$\tau_{rr} = 2\mu\frac{\partial v}{\partial r} + \lambda\left[\frac{\partial u}{\partial x} + \frac{1}{r}\frac{\partial (rv)}{\partial r}\right]$$

(2.2.3) $$\tau_{xr} = \mu\left[\frac{\partial u}{\partial r} + \frac{\partial v}{\partial x}\right]$$

(2.2.4) $$\tau_{\theta\theta} = 2\mu\frac{v}{r} + \lambda\left[\frac{\partial u}{\partial x} + \frac{1}{r}\frac{\partial (rv)}{\partial r}\right]$$

Heat transfer

(2.2.5) $$q_x = \underbrace{-k\frac{\partial T}{\partial x}}_{\text{Conduction heat transfer}} + \underbrace{\sum_{i=1}^{n} h_i\, j_{i,x}}_{\text{Interdiffusion heat transfer}} + \underbrace{\bar{R}\frac{T}{\rho}\sum_{i=1}^{n}\sum_{j=1}^{n}\frac{MD_i^T}{M_j M_i \wp_{ij}}\omega_j\left[\frac{j_{i,x}}{\omega_i} - \frac{j_{j,x}}{\omega_j}\right]}_{\text{Diffusion thermo heat transfer (Dufour effect)}}$$

(2.2.6) $$q_r = \underbrace{-k\frac{\partial T}{\partial r}}_{\text{Conduction heat transfer}} + \underbrace{\sum_{i=1}^{n} h_i\, j_{i,r}}_{\text{Interdiffusion heat transfer}} + \underbrace{\bar{R}\frac{T}{\rho}\sum_{i=1}^{n}\sum_{j=1}^{n}\frac{MD_i^T}{M_j M_i \wp_{ij}}\omega_j\left[\frac{j_{i,r}}{\omega_i} - \frac{j_{j,r}}{\omega_j}\right]}_{\text{Diffusion thermo heat transfer (Dufour effect)}}$$

Mass transfer

(2.2.7) $$j_{i,x} = \underbrace{\sum_{j=1}^{n-1} A_{ij}\frac{\partial \omega_j}{\partial x}}_{\text{Ordinary diffusion}} - \underbrace{\frac{D_i^T}{T}\frac{\partial T}{\partial x}}_{\text{Thermal diffusion (Soret effect)}}$$

(2.2.8) $$j_{i,r} = \underbrace{\sum_{j=1}^{n-1} A_{ij}\frac{\partial \omega_j}{\partial r}}_{\text{Ordinary diffusion}} - \underbrace{\frac{D_i^T}{T}\frac{\partial T}{\partial r}}_{\text{Thermal diffusion (Soret effect)}}$$

The actual determination of the transport coefficients involved in momentum, heat, and mass transfer is very complicated, highly empirical, and rather inaccurate. This is especially true for the multicomponent species ordinary and thermal diffusion coefficients. The multicomponent solution for the coefficients of ordinary diffusion (A_{ij}) and thermal diffusion (D_i^T) are discussed in Appendix C.

2.3. Species Source Function

The species source function, σ_i, is the term that represents the creation or destruction of a species by chemical reaction. Depending on the application, the term may be a relatively significant factor for both rocket engine performance (i.e., specific impulse) and heat transfer.

For a mixture of n different gasses in which a total of m different chemical reactions can occur simultaneously, the general chemical reaction equation is discussed in Reference 10 and is given below in Equation (2.3.1):

$$\sum_{i=1}^{n} \nu'_{ij} A_i \underset{K_{bj}}{\overset{K_{fj}}{\rightleftharpoons}} \sum_{i=1}^{n} \nu''_{ij} A_i \qquad (j = 1, \ldots, m) \tag{2.3.1}$$

where K_{fj} and K_{bj} refer to the forward and backward chemical reaction rates, respectively, ν' and ν'' refer to the stoichiometric coefficients of the reactants and products, respectively, and A_i denotes the specific chemical species. The equation governing the production or destruction of a chemical species is given by the following expression:

$$\sigma_i = M_i \sum_{j=1}^{m} \Delta\nu_{ij} \left[K_{fj} \prod_{i=1}^{n} \left(\frac{\rho_i}{M_i} \right)^{\nu'_{ij}} - K_{bj} \prod_{i=1}^{n} \left(\frac{\rho_i}{M_i} \right)^{\nu''_{ij}} \right] \tag{2.3.2}$$

For the jth reaction, K_{fj} is related to the backward reaction rate, K_{bj}, and the equilibrium constant, K_{pj}, by the following relation:

$$\frac{K_{fj}}{K_{bj}} = K_{pj}(\bar{R}T)^{-\Delta\nu_j} \tag{2.3.3}$$

where $\Delta\nu_j = \nu_j'' - \nu_j'$.

For binary exchange chemical reactions, the backward reaction rate, K_{bj}, is a function of temperature only, and the functional relation is assumed to behave according to a modified form of the Arrhenius equation (Reference 11):

$$K_{bj} = B_j T^{\alpha_j} \exp\left(-\frac{E_j}{\bar{R}T}\right) \tag{2.3.4}$$

For catalytic reactions (reactions involving a third body), a mean third body catalytic efficiency is used to determine a density weighted reaction rate:

$$K_{bj} = \bar{K}_{bj} \sum_{i=1}^{n} \left(\frac{\rho_i}{M_i}\right)\left(\frac{B_{ij}}{\bar{B}_j}\right) \tag{2.3.5}$$

where $\bar{K}_{bj}$ is a baseline backward chemical reaction rate for reaction j and the ratio $B_{ij}/\bar{B}_j$ is the catalytic efficiency of species i. Equations (2.3.4) and (2.3.5) readily show that the mechanisms for chemical reaction may be a strong function of species density. While the backward reaction rate of binary exchange reactions is a function only of temperature, catalytic reactions are an explicit function of the species density. Consequently, at low pressures, hence low species densities, chemical reactions tend to favor binary exchange mechanisms, whereas at high pressures (i.e., combustor chamber pressure) catalytic reactions dominate. This is an important consideration in the design of many chemical rocket engines. Since many of the chemical reaction mechanisms of interest involve catalytic reactions, rocket engine reaction efficiencies improve dramatically with increasing chamber pressures. A complete description of the species source term and its relation to the dependent variables (ρ, ρu, ρv, ρe, ρ_i) is given in Appendix D.

2.4. Thermal and Caloric Equations of State

In general, the combustion gasses of a hydrogen-oxygen rocket engine are appreciably in excess of the critical temperature of all of the individual species. Further, since the rocket engine gasses expand through the nozzle in a nearly isentropic fashion, the decay of fluid pressure maintains thermodynamic conditions that are significantly distant from the critical pressures and temperatures of all the chemical species. Consequently, the exhaust gasses of the rocket engine are assumed to obey the ideal gas law:

$$P = \rho R T \tag{2.4.1}$$

The gas constant, R, is a weighted summation of the molecular weights of the individual species:

$$R = \bar{R} \sum_{i=1}^{n} \frac{\omega_i}{M_i} \tag{2.4.2}$$

The assumption of ideal gas behavior also implies that the specific enthalpies and internal energies for individual species are solely functions of temperature and the average fluid enthalpy and internal energy are comprised of a mass fraction weighting of the individual species properties:

$$u_i = u_{iR} + \int_{T_R}^{T} C_{vi} dT \tag{2.4.3}$$

$$u = \sum_{i=1}^{n} \omega_i u_i \tag{2.4.4}$$

The fluid temperature can be determined by integration and rearrangement, and substitution of the definition of the total fluid energy (i.e., $\rho e = \rho (u + (u^2 + v^2)/2)$), which results in the following correlation:

$$T = \frac{\rho e - \frac{\rho}{2}(u^2+v^2) - \rho \sum_{i=1}^{n} \omega_i (u_{iR} - \bar{C}_{vi} T_R)}{\rho \sum_{i=1}^{n} \omega_i \bar{C}_{vi}} \tag{2.4.5}$$

2.5. Time-Averaged Turbulent Flow Equations

The presence of turbulence creates flow conditions that cannot be fully simulated with modern computational hardware. Consequently, the conventional technique of handling turbulent fluid flow is to time-average the fluid flow equations and model those terms that arise due to turbulent fluctuations. As the flow of concern may have appreciable Mach number variations throughout the turbulent region of the flow, a density-weighted, time-averaging technique has come into favor (Reference 12) as the preferred starting point for turbulence modelling. The complete derivation of the time-averaged fluid equations and the assumptions associated with the averaging technique are presented in Appendix E. The resulting flow equations are presented below:

$$\frac{\partial (r\tilde{Q})}{\partial t} + \frac{\partial (r\tilde{E})}{\partial x} + \frac{\partial (r\tilde{F})}{\partial r} + \bar{H} = \frac{\partial (r\tilde{E}_v)}{\partial x} + \frac{\partial (r\tilde{F}_v)}{\partial r} + \tilde{H}_v \tag{2.5.1}$$

$$\tilde{Q} = [\bar{\rho}, \bar{\rho}\tilde{u}, \bar{\rho}\tilde{v}, \bar{\rho}\tilde{e}, \tilde{\rho}_i]^T \tag{2.5.2}$$

$$\tilde{E} = \left[\bar{\rho}\tilde{u}, \bar{\rho}\tilde{u}^2 + \bar{P}, \bar{\rho}\tilde{u}\tilde{v}, (\bar{\rho}\,\tilde{e} + \bar{P})\,\tilde{u}, \tilde{\rho}_i\tilde{u}\right]^T \tag{2.5.3}$$

$$\tilde{F} = \left[\bar{\rho}\tilde{v}, \bar{\rho}\tilde{u}\tilde{v}, \bar{\rho}\tilde{v}^2, (\bar{\rho}\,\tilde{e} + \bar{P})\,\tilde{v}, \tilde{\rho}_i\tilde{v}\right]^T \tag{2.5.4}$$

$$\bar{H} = \left[0, 0, r\frac{\partial \bar{P}}{\partial r}, 0, -r\bar{\sigma}_i\right]^T \tag{2.5.5}$$

$$\tilde{E}_v = \left[\begin{array}{c} 0, \bar{\tau}_{xx} + \tau^t_{xx}\ , \bar{\tau}_{xr} + \tau^t_{xr}\ , \\ \\ \tilde{u}\bar{\tau}_{xx} + \tilde{v}\bar{\tau}_{xr} - \bar{q}_x + \tilde{u}\tau^t_{xx} + \tilde{v}\tau^t_{xr} - q^t_x\ , -\bar{j}_{i,x} - j^t_{i,x} \end{array} \right]^T \tag{2.5.6}$$

$$\tilde{F}_v = \left[\begin{array}{c} 0, \bar{\tau}_{xr} + \tau^t_{xr}\ , \bar{\tau}_{rr} + \tau^t_{rr}\ , \\ \\ \tilde{u}\bar{\tau}_{xr} + \tilde{v}\bar{\tau}_{rr} - \bar{q}_r + \tilde{u}\tau^t_{xr} + \tilde{v}\tau^t_{rr} - q^t_r\ , -\bar{j}_{i,r} - j^t_{i,r} \end{array} \right]^T \tag{2.5.7}$$

$$\tilde{H}_v = [0, 0, -\bar{\tau}_{\theta\theta} - \tau^t_{\theta\theta}, 0, 0]^T \tag{2.5.8}$$

where the turbulent stress terms (denoted by the t superscript and defined in Appendix F) are assumed to have diffusive-like characteristics (i.e., the Boussinesq approximation) and can be defined as follows:

$$\tau^t_{xx} = 2\mu^t \frac{\partial \tilde{u}}{\partial x} + \lambda^t \left[\frac{\partial \tilde{u}}{\partial x} + \frac{1}{r}\frac{\partial (r\tilde{v})}{\partial r} \right] \tag{2.5.9}$$

$$\tau^t_{xr} = \mu^t \left[\frac{\partial \tilde{u}}{\partial r} + \frac{\partial \tilde{v}}{\partial x} \right] \tag{2.5.10}$$

$$\tau^t_{rr} = 2\mu^t \frac{\partial \tilde{v}}{\partial r} + \lambda^t \left[\frac{\partial \tilde{u}}{\partial x} + \frac{1}{r}\frac{\partial (r\tilde{v})}{\partial r} \right] \tag{2.5.11}$$

$$\tau^t_{\theta\theta} = 2\frac{\mu^t}{r}\tilde{v} + \lambda^t \left[\frac{\partial \tilde{u}}{\partial x} + \frac{1}{r}\frac{\partial (r\tilde{v})}{\partial r} \right] \tag{2.5.12}$$

$$q^t_x = -\, k^t \frac{\partial \bar{T}}{\partial x} + \sum_{i=1}^{n} \bar{h}_i\, j^t_{i,x} \tag{2.5.13}$$

$$q^t_r = -\, k^t \frac{\partial \bar{T}}{\partial r} + \sum_{i=1}^{n} \bar{h}_i\, j^t_{i,r} \tag{2.5.14}$$

$$j^t_{i,x} = - \wp^t_{iM} \frac{\partial \tilde{\omega}_i}{\partial x} \tag{2.5.15}$$

$$j^t_{i,r} = - \wp^t_{iM} \frac{\partial \tilde{\omega}_i}{\partial r} \tag{2.5.16}$$

It is seen that the assumptions made concerning the transfer of momentum and conduction heat transfer result in correlations that are entirely analogous to their laminar counterparts. As a result, the description of the turbulent fluid flow equations can be described in the same manner as laminar flow, with the exception that the constitutive equations for conduction heat transfer and for momentum transfer be represented by an effective thermal conductivity and viscosity terms, respectively. However, for multicomponent species transfer, no complete analogy exists between the laminar and turbulent energy and species transport terms, except in cases of binary species mass transfer with negligible thermal diffusion and negligible Dufour energy transfer.

The introduction of turbulent viscosities, thermal conductivities, and diffusion coefficients has been found to yield acceptable results for many engineering applications provided the appropriate dependence of the turbulent properties on the fluid flow conditions and the geometry are adequately modelled. Typically, the modelling of the turbulent viscosity is performed by the use of either an algebraic or a differential equation turbulence model. In the Tethys model, only an algebraic (enhanced Baldwin-Lomax) turbulence model has been used. On the other hand, the modelling of the turbulent thermal conductivity and mass diffusivities is performed by the introduction of turbulent Prandtl and Lewis numbers that are assumed to be either constant or an algebraic function of the turbulent viscosity and laminar Prandtl or Lewis numbers. A complete description of the models used in the Tethys fluid flow model and the enhancements required to model a multispecies rocket engine flow are described in Appendix F.

Hereafter, the superscripts denoting time-averaged quantities will be discontinued (except in Appendices E and F) and it will be implied that the solution of the governing flow equations represent a time-averaged solution.

2.6. Nondimensionalization of Fluid Flow Equations

In maintaining similarity with the original Proteus code, the multispecies Navier-Stokes equations are cast in a nondimensional form. The nondimensionalizing factors used for the flow variables are listed in Table 1.

Table 1. Nondimensional parameters used in the Tethys model.

Nondimensional term	Definition
x°, r°	$\frac{x}{L_{ref}}, \frac{r}{L_{ref}}$
u°, v°	$\frac{u}{u_{ref}}, \frac{v}{u_{ref}}$
$T^\circ, \rho^\circ, \rho_i^\circ$	$\frac{T}{T_{ref}}, \frac{\rho}{\rho_{ref}}, \frac{\rho_i}{\rho_{ref}}$
$P^\circ, e^\circ, R^\circ, C_{p\ ref}$	$\frac{P}{\rho_{ref}\, u_{ref}^2}, \frac{e}{\rho_{ref}\, u_{ref}^2}, R\,\frac{T_{ref}}{u_{ref}^2}, C_p\,\frac{T_{ref}}{u_{ref}^2}$
t°	$t\,\frac{u_{ref}}{L_{ref}}$
σ_i°	$\frac{\sigma_i}{\sigma_{ref}}$
$D_{ij}^\circ, A_{ij}^\circ, D_i^{T\circ}$	$\frac{D_{ij}}{D_{ab\ ref}}, \frac{A_{ij}}{\rho_{ref}\, D_{ab\ ref}}, \frac{D_i^T}{\rho_{ref}\, D_{ab\ ref}}$
k°, μ°	$\frac{k_{eff}}{k_{ref}}, \frac{\mu_{eff}}{\mu_{ref}}$

The application of the above nondimensionalizing terms results in equations that are identical in form to the dimensional counterparts with the exception that various nondimensional groupings of reference terms are created. These groupings are listed in Table 2.

Table 2. Nondimensional reference numbers.

Nondimensional parameter	Definition
Reynolds Number, Re_{ref}	$\frac{\rho_{ref}\, u_{ref}\, L_{ref}}{\mu_{ref}}$
Prandtl Number, Pr_{ref}	$\frac{\mu_{ref}\, C_{p\ ref}}{k_{ref}}$
Lewis Number, Le_{ref}	$\frac{\rho_{ref} C_{p\ ref}\, D_{ab\ ref}}{k_{ref}}$
Source Number, S_{ref}	$\frac{\rho_{ref}\, u_{ref}}{\sigma_{ref}\, L_{ref}}$

The Reynolds number (Re_{ref}) and Prandtl number (Pr_{ref}) are nondimensional groupings that are familiar to most engineers. The terms that arise due to multispecies fluid flow, namely the Lewis number (Le_{ref}) and the species Source number (S_{ref}) are less familiar terms. In fact, the Lewis number is occasionally defined as the inverse of the current definition (References 13 and 14) and, to the author's knowledge, the species source number (or any term of a similar form) has never been used for chemical rocket engine studies. However, the source number is a very illuminating parameter. From this number, it can be seen that the species source term tends toward infinity when either the characteristic length (L_{ref}) or the characteristic species production/destruction term

(σ_{ref}) tends toward zero. These two conditions are approached at the extreme ends of rocket engine propulsion systems. A small characteristic length usually represents a physically small, low-thrust rocket engine. On the other hand, a small species production term may be a characteristic of a high pressure rocket engine which has essentially no dissociated species present after combustion. For catalytic reactions, which are the reactions of greatest significance in a hydrogen-oxygen rocket engine, the species production rate increases with increased fluid density much faster than linearly, thus off-setting the reference density term in the numerator of the species source term. Therefore, the species source term has a maximum significance somewhere between the two extreme engine sizes, the source number being large both at small engine sizes (frozen flow) and at large engine chamber pressures (undissociated flow).

Table 3 illustrates the significance of the species source term for a spectrum of hydrogen-oxygen rocket engines that are currently in production or development, including an evaluation of the Space Shuttle Main Engines operating at ten times the present operational chamber pressure. In this table it is seen that the minimum source number occurs for engines in the size and pressure regime of the current Space Shuttle Main Engine, with satellite maneuvering systems being over an order of magnitude less sensitive to the effects of recombination chemistry. However, it is also worthy of note that in all cases examined, the source number does not exhibit the characteristic of being orders of magnitude greater than unity, which would tend to lead one to conclude that chemical reactions should be considered in any chemical rocket engine analysis. However, the source number calculation is a reflection of the importance of chemical reactions to the species equations and is not a direct reflection of the importance of chemical reactions to engine performance.

Table 3. Species Source number for selected H_2/O_2 rocket engines.

Engine	Thrust, lbf	Chamber pressure, $lbf/in.^2$	S_{ref}
10 × Space Shuttle Main Engine	4.7×10^6	3.3×10^4	6.5
Space Shuttle Main Engine[15]	4.7×10^5	3.3×10^3	3.5
RL 10IIB[16]	2.0×10^4	3.6×10^2	7.3
Space Station Maneuvering[17]	7.5×10^1	7.5×10^1	8.9
Satellite Maneuvering[18]	5.0×10^0	2.5×10^1	59.0

The source numbers are based on approximate flow conditions at the throat using one-dimensional kinetics equations (Reference 19), using absolute value of all species production terms.

Insertion of the nondimensional variables and reference terms into the multispecies Navier-Stokes equations and dropping the nondimensional superscripts and subscripts, the nondimensionalization of the Navier-Stokes equations yields the following equations:

$$\frac{\partial (rQ)}{\partial t} + \frac{\partial (rE)}{\partial x} + \frac{\partial (rF)}{\partial r} + H = \frac{\partial (rE_v)}{\partial x} + \frac{\partial (rF_v)}{\partial r} + H_v \tag{2.6.1}$$

$$Q = [\rho, \rho u, \rho v, \rho e, \rho_i]^T \tag{2.6.2}$$

$$E = [\rho u, \rho u^2 + P, \rho uv, (\rho e + P) u, \rho_i u]^T \tag{2.6.3}$$

$$F = [\rho v, \rho uv, \rho v^2, (\rho e + P) v, \rho_i v]^T \tag{2.6.4}$$

$$H = \left[0, 0, r \frac{\partial P}{\partial r}, 0, -r \frac{\sigma_i}{S}\right]^T \tag{2.6.5}$$

$$E_v = \frac{1}{Re}\left[0, \tau_{xx}, \tau_{xr}, u\tau_{xx} + v\tau_{xr} - \frac{q_x}{Pr}, -\frac{Le}{Pr}\left(j_{i,x} + j^t_{i,x} \right)\right]^T \tag{2.6.6}$$

$$F_v = \frac{1}{Re}\left[0, \tau_{xr}, \tau_{rr}, u\tau_{xr} + v\tau_{rr} - \frac{q_r}{Pr}, -\frac{Le}{Pr}\left(j_{i,r} + j^t_{i,r} \right)\right]^T \tag{2.6.7}$$

$$H_v = \frac{1}{Re} \times [0, 0, -\tau_{\theta\theta}, 0, 0]^T \tag{2.6.8}$$

The nondimensionalized constitutive equations have the form given by Equations (2.6.9) to (2.6.18) where it is recognized that the viscosity and thermal conductivity represent contributions from both turbulent and laminar transport coefficients:

$$\tau_{xx} = 2\mu\frac{\partial u}{\partial x} + \lambda\left[\frac{\partial u}{\partial x} + \frac{1}{r}\frac{\partial (rv)}{\partial r}\right] \tag{2.6.9}$$

$$\tau_{rr} = 2\mu\frac{\partial v}{\partial r} + \lambda\left[\frac{\partial u}{\partial x} + \frac{1}{r}\frac{\partial (rv)}{\partial r}\right] \tag{2.6.10}$$

$$\tau_{xr} = \mu\left[\frac{\partial u}{\partial r} + \frac{\partial v}{\partial x}\right] \tag{2.6.11}$$

$$\tau_{\theta\theta} = 2\mu\frac{v}{r} + \lambda\left[\frac{\partial u}{\partial x} + \frac{1}{r}\frac{\partial (rv)}{\partial r}\right] \tag{2.6.12}$$

$$q_x = -k\frac{\partial T}{\partial x} + Le\sum_{i=1}^{n} h_i\left[j_{i,x} + j^t_{i,x} \right] \tag{2.6.13}$$

$$+ \; Le\bar{R}\frac{T}{\rho}\sum_{i=1}^{n}\sum_{j=1}^{n}\frac{MD_i^T}{M_j M_i \wp_{ij}}\omega_j\left[\frac{j_{i,x}}{\omega_i} - \frac{j_{j,x}}{\omega_j}\right]$$

(2.6.14)
$$q_r = -k\frac{\partial T}{\partial r} + Le\sum_{i=1}^{n} h_i\left[\ j_{i,r} + j^t_{i,r}\ \right]$$

$$+\ Le\bar{R}\frac{T}{\rho}\sum_{i=1}^{n}\sum_{j=1}^{n}\frac{MD_i^T}{M_jM_i\wp_{ij}}\omega_j\left[\frac{j_{i,r}}{\omega_i} - \frac{j_{j,r}}{\omega_j}\right]$$

(2.6.15)
$$j_{i,x} = \sum_{j=1}^{n-1} A_{ij}\frac{\partial \omega_j}{\partial x} - \frac{D_i^T}{T}\frac{\partial T}{\partial x}$$

(2.6.16)
$$j_{i,r} = \sum_{j=1}^{n-1} A_{ij}\frac{\partial \omega_j}{\partial r} - \frac{D_i^T}{T}\frac{\partial T}{\partial r}$$

(2.6.17)
$$j^t_{i,x} = -\wp^t_{iM}\frac{\partial \omega_i}{\partial x}$$

(2.6.18)
$$j^t_{i,r} = -\wp^t_{iM}\frac{\partial \omega_i}{\partial r}$$

The thermal and caloric equations of state have the same form as their dimensional counterparts.

SECTION 3

GENERALIZED COORDINATE TRANSFORMATION

The governing equations for axisymmetric two-dimensional flow presented in the previous section are not well suited for nozzle flowfield analysis due to the need for accurate boundary description and varying degrees of flowfield resolution desired throughout the flowfield. Consequently, coordinate transformations are often utilized in numerical computations to improve solution accuracy. This requires two major procedures; the transformation of the grid covering the physical domain of interest to a uniform orthogonal computational grid, and the transformation of the governing equations from the physical domain to the computational domain. The specific details of the coordinate transformation are contained in Appendix G, while the more significant details of the flowfield conservation rules applied to the Tethys flow model are presented in this section.

3.1. Generalized Transformation of the Advective and Pressure Flowfield Expressions

Transformation of the inviscid portion of the governing equations results in the following expression:

$$\frac{\partial (r\hat{Q})}{\partial \tau} + \frac{\partial (r\hat{E})}{\partial \xi} + \frac{\partial (r\hat{F})}{\partial \eta} + \hat{H} = \begin{pmatrix} \text{Viscous} \\ \text{terms} \end{pmatrix} \tag{3.1.1}$$

$$\hat{Q} = \frac{[\rho, \rho u, \rho v, \rho e, \rho_i]^T}{J} \tag{3.1.2}$$

$$\hat{E} = \frac{\xi_x \left[\rho u,\ \rho u^2 + P,\ \rho uv,\ (\rho e + P)u,\ \rho_i u\right]^T}{J} + \frac{\xi_r \left[\rho v,\ \rho uv,\ \rho v^2,\ (\rho e + P)v,\ \rho_i v\right]^T}{J} \tag{3.1.3}$$

$$\hat{F} = \frac{\eta_x \left[\rho u,\ \rho u^2 + P,\ \rho uv,\ (\rho e + P)u,\ \rho_i u\right]^T}{J} + \frac{\eta_r \left[\rho v,\ \rho uv,\ \rho v^2,\ (\rho e + P)v,\ \rho_i v\right]^T}{J} \tag{3.1.4}$$

$$\hat{H} = \left[0, 0,\ r\,\frac{\partial(\xi_r P/J)}{\partial \xi} + r\,\frac{\partial(\eta_r P/J)}{\partial \eta}, 0,\ \frac{-r\,\sigma_i}{J}\right]^T \tag{3.1.5}$$

The metric derivatives and the inverse Jacobian ($J = 1/J^{-1}$) can be evaluated from known geometric quantities:

$$J^{-1} = x_\xi r_\eta - x_\eta r_\xi \tag{3.1.6}$$

$$\xi_x = J r_\eta \tag{3.1.7}$$

$$\xi_r = -J x_\eta \tag{3.1.8}$$

$$\eta_x = -J r_\xi \tag{3.1.9}$$

$$\eta_r = J x_\xi \tag{3.1.10}$$

3.2. Flow Conservation of the Advective and Pressure Terms

A fundamental requirement for any numerical algorithm/grid transformation is to conserve flow properties. In a rectangular coordinate system, the flow conservation requirement dictates that the metric differencing applied to the flow variables be conservative. An additional complication with axisymmetric flow, however, is that it is not entirely clear what flow properties are to be conserved. The reasoning and flow conservation requirements applied to the Tethys model is as follows:

- One-dimensional flow properties in the axial direction (x) must be conservative
- One-dimensional flow properties in the radial direction (r) must be conservative

In general, the advective terms in the Navier-Stokes equations that contain derivatives in the axial direction have a form similar to the following:

$$\frac{\partial (r\phi)}{\partial x} \tag{3.2.1}$$

where, for example, ϕ would be equal to ρu in the continuity equation and $\rho u^2 + P$ in the axial momentum equation. Further, for one-dimensional flow, Equation (3.2.1) is equal to 0. Consequently, integration of Equation (3.2.1) for the case of a one-dimensional fluid flow results in the following relationship:

$$r\phi = C_1 + f(r) \tag{3.2.2}$$

from which it follows that C_1 must be equal to 0 and f(r) must be equal to $r\phi$ for the case where ϕ is equal to a constant, which is the condition which exists in an axial, uniform flow environment.

In a transformed coordinate system, Equation (3.2.1) can be divided by the Jacobian

and can then be written in the following strong conservation form:

$$\frac{1}{J}\frac{\partial(r\phi)}{\partial x} = \frac{\partial}{\partial\eta}\left(\frac{r\eta_x\phi}{J}\right) + \frac{\partial}{\partial\xi}\left(\frac{r\xi_x\phi}{J}\right) \tag{3.2.3}$$

In order to satisfy the conservation of axial flow properties to a first-order requirement (i.e., uniform flow), it is necessary that the following condition hold:

$$\frac{\partial}{\partial\eta}\left(\frac{r\eta_x\phi}{J}\right) + \frac{\partial}{\partial\xi}\left(\frac{r\xi_x\phi}{J}\right) = 0 \quad \text{when } \phi \text{ is constant} \tag{3.2.4}$$

General axial flow conservation requirement

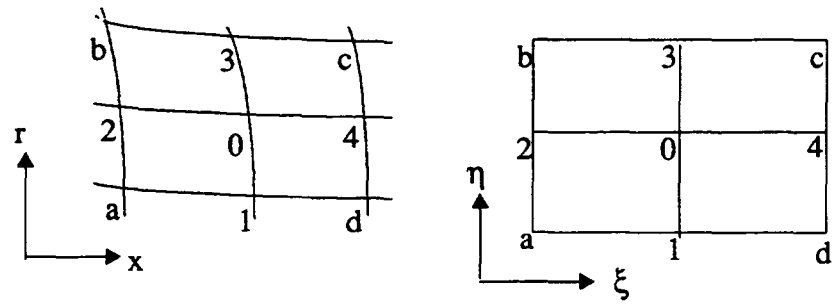

Physical space Computational space

Figure 1. Discretization of flowfield about point 0 for an arbitrary grid.

Consider now the arbitrary grid illustrated in Figure 1. Since central differencing of the flow variables is used in the Tethys code for both the flow variables and the grid metrics, the following relation is required to maintain flow conservation in the axial direction:

$$\frac{\left.\frac{r\eta_x\phi}{J}\right|_3 - \left.\frac{r\eta_x\phi}{J}\right|_1}{2\Delta\eta} + \frac{\left.\frac{r\xi_x\phi}{J}\right|_4 - \left.\frac{r\xi_x\phi}{J}\right|_2}{2\Delta\xi} = 0 \tag{3.2.5}$$

If central differencing of the grid metrics is applied and the radius terms are evaluated in an exact manner, the following discretized expression is obtained:

$$(3.2.6)\qquad \frac{\left[r_3\phi\frac{(r_c-r_b)}{2\Delta\xi}-r_1\phi\frac{(r_d-r_a)}{2\Delta\xi}\right]}{2\Delta\eta}-\frac{\left[r_4\phi\frac{(r_c-r_d)}{2\Delta\eta}-r_2\phi\frac{(r_b-r_a)}{2\Delta\eta}\right]}{2\Delta\xi}$$

Axial flowfield formulation using exact radius technique

To be conservative in the uniform, axial flow case, Equation (3.2.6) must be equal to zero when ϕ is equal to a constant. Apparently, the above discretization does not satisfy the requirement of flowfield conservation (by being equal to 0) for an arbitrary grid in the case where the dependent flow variable, ϕ, is constant. In the Tethys code, flow conservation is satisfied by using a second-order accurate approximation for the radius terms at Nodes 1 to 4:

$$(3.2.7)\qquad r_1=\frac{r_d+r_a}{2},\quad r_2=\frac{r_b+r_a}{2},\quad r_3=\frac{r_b+r_c}{2},\quad r_4=\frac{r_c+r_d}{2}$$

Substitution of the above relation into Equation (3.2.5) yields the following expression:

$$(3.2.8)\qquad \frac{\left[\frac{(r_c^2-r_b^2)}{4\Delta\xi}\phi-\frac{(r_d^2-r_a^2)}{4\Delta\xi}\phi\right]}{2\Delta\eta}-\frac{\left[\frac{(r_c^2-r_d^2)}{4\Delta\eta}\phi-\frac{(r_b^2-r_a^2)}{4\Delta\eta}\phi\right]}{2\Delta\xi}$$

Axial flowfield formulation using average radius technique

It is seen that the use of radius averaging results in axial flow conservation when the dependent variable is constant for all arbitrary grids.

In the radial conservation scheme, the variation of the independent variable r must be considered. Unlike the axial derivative terms where the original presence of the radius inside the derivative was misleading to the one-dimensional flow case, the metric term is

crucial in the radial flow terms. Therefore, the first order conservation of radial flow stipulates that the following condition must be true:

(3.2.9)
$$\frac{\partial}{\partial\eta}\left(\frac{r\eta_r\phi}{J}\right) + \frac{\partial}{\partial\xi}\left(\frac{r\xi_r\phi}{J}\right) = 0 \quad \text{when } r\phi \text{ is constant}$$

General radial flow conservation requirement

For example, the parameter ϕ is equal to ρv in the continuity equation. Additionally, the maintenance of a constant pressure flowfield is crucial and requires that

(3.2.10)
$$\frac{\partial}{\partial\eta}\left(\frac{\eta_r P}{J}\right) + \frac{\partial}{\partial\xi}\left(\frac{\xi_r P}{J}\right) = 0 \quad \text{when} \quad \frac{\partial P}{\partial r} = 0$$

For both the radial flow and the pressure terms, no unconventional handling of the metric terms is required to maintain flowfield conservation. The exact radial formulation outlined in Equation (3.2.6) is adequate for Equation (3.2.9) and Equation (3.2.10). However, it must be noted that the above procedure of flowfield conservation is unable to exactly satisfy conditions existing in the radial momentum equation due to the weak conservation form of the radial pressure gradient.

3.3. Generalized Transformation of Diffusive Terms in the Navier-Stokes Equations

The transformation of the diffusive terms in the Navier-Stokes equations follows the same trend as the advective terms with the additional requirement that the diffusive fluxes of momentum, heat, and mass transfer must also be transformed. A complete description of the transformation is contained in Appendix G. The resultant expressions are presented below.

(3.3.1)
$$\text{Advective and pressure terms} = \frac{\partial(r\hat{E}_v)}{\partial\xi} + \frac{\partial(r\hat{F}_v)}{\partial\eta} + H_v$$

where the transformed viscous terms for the continuity, x-momentum, r-momentum,

energy, and species equations are

$$(3.3.2)\quad \hat{E}_v = \frac{\xi_x}{Re\ J}\left[0, \tau_{xx}, \tau_{xr}, \; u\tau_{xx} + v\tau_{xr} - q_x/Pr, \; -Le\ (j_{i,x} + j^t_{i,x})/Pr\right]^T + \frac{\xi_r}{Re\ J}\left[0, \tau_{xr}, \tau_{rr}, \; u\tau_{xr} + v\tau_{rr} - q_r/Pr, \; -Le\ (j_{i,r} + j^t_{i,r})/Pr\right]^T$$

$$(3.3.3)\quad \hat{F}_v = \frac{\eta_x}{Re\ J}\left[0, \tau_{xx}, \tau_{xr}, \; u\tau_{xx} + v\tau_{xr} - q_x/Pr, \; -Le\ (j_{i,x} + j^t_{i,x})/Pr\right]^T + \frac{\eta_r}{Re\ J}\left[0, \tau_{xr}, \tau_{rr}, \; u\tau_{xr} + v\tau_{rr} - q_r/Pr, \; -Le\ (j_{i,r} + j^t_{i,r})/Pr\right]^T$$

$$(3.3.4)\quad H_v = \frac{1}{Re\ J}\left[0, 0, -\tau_{\theta\theta}, 0, 0\right]^T$$

The fluxes can be expressed in terms of a transformed coordinate system as illustrated below, where the viscosities and thermal conductivity represent both laminar and turbulent contributions.

$$(3.3.5)\quad \tau_{xx} = 2\mu\left[\xi_x\frac{\partial u}{\partial \xi} + \eta_x\frac{\partial u}{\partial \eta}\right] + \lambda\left[\xi_x\frac{\partial u}{\partial \xi} + \eta_x\frac{\partial u}{\partial \eta} + \frac{1}{r}\left(\xi_r\frac{\partial (rv)}{\partial \xi} + \eta_r\frac{\partial (rv)}{\partial \eta}\right)\right]$$

$$(3.3.6)\quad \tau_{rr} = 2\mu\left[\xi_r\frac{\partial v}{\partial \xi} + \eta_r\frac{\partial v}{\partial \eta}\right] + \lambda\left[\xi_x\frac{\partial u}{\partial \xi} + \eta_x\frac{\partial u}{\partial \eta} + \frac{1}{r}\left(\xi_r\frac{\partial (rv)}{\partial \xi} + \eta_r\frac{\partial (rv)}{\partial \eta}\right)\right]$$

$$(3.3.7)\quad \tau_{xr} = \mu\left[\xi_r\frac{\partial u}{\partial \xi} + \eta_r\frac{\partial u}{\partial \eta} + \xi_x\frac{\partial v}{\partial \xi} + \eta_x\frac{\partial v}{\partial \eta}\right]$$

$$(3.3.8)\quad q_r = -k\left[\xi_r\frac{\partial T}{\partial\xi} + \eta_r\frac{\partial T}{\partial\eta}\right] + Le\sum_{i=1}^{n} h_i\left[j_{i,r} + j^t_{i,r}\right] + Le\bar{R}\frac{T}{\rho}\sum_{i=1}^{n}\sum_{j=1}^{n}\frac{MD_i^T}{M_jM_i\wp_{ij}}\omega_j\left[\frac{j_{i,r}}{\omega_i} - \frac{j_{j,r}}{\omega_j}\right]$$

$$(3.3.9)\quad q_x = -k\left[\xi_x\frac{\partial T}{\partial\xi} + \eta_x\frac{\partial T}{\partial\eta}\right] + Le\sum_{i=1}^{n} h_i\left[j_{i,x} + j^t_{i,x}\right] + Le\bar{R}\frac{T}{\rho}\sum_{i=1}^{n}\sum_{j=1}^{n}\frac{MD_i^T}{M_jM_i\wp_{ij}}\omega_j\left[\frac{j_{i,x}}{\omega_i} - \frac{j_{j,x}}{\omega_j}\right]$$

$$(3.3.10)\quad j_{i,r} = \sum_{j=1}^{n-1} A_{ij}\left[\xi_r\frac{\partial\omega_j}{\partial\xi} + \eta_r\frac{\partial\omega_j}{\partial\eta}\right] - \frac{D_i^T}{T}\left[\xi_r\frac{\partial T}{\partial\xi} + \eta_r\frac{\partial T}{\partial\eta}\right]$$

$$(3.3.11)\quad j_{i,x} = \sum_{j=1}^{n-1} A_{ij}\left[\xi_x\frac{\partial\omega_j}{\partial\xi} + \eta_x\frac{\partial\omega_j}{\partial\eta}\right] - \frac{D_i^T}{T}\left[\xi_x\frac{\partial T}{\partial\xi} + \eta_x\frac{\partial T}{\partial\eta}\right]$$

$$(3.3.12)\quad j^t_{i,r} = -\wp^t_{iM}\left[\xi_r\frac{\partial\omega_i}{\partial\xi} + \eta_r\frac{\partial\omega_i}{\partial\eta}\right]$$

$$(3.3.13)\quad j^t_{i,x} = -\wp^t_{iM}\left[\xi_x\frac{\partial\omega_i}{\partial\xi} + \eta_x\frac{\partial\omega_i}{\partial\eta}\right]$$

In transformed coordinates, the nonconservative shear stress term, $\tau_{\theta\theta}$, can be written as

$$(3.3.14)\quad \tau_{\theta\theta} = 2\mu\frac{v}{r} + \lambda\left[\xi_x\frac{\partial u}{\partial\xi} + \eta_x\frac{\partial u}{\partial\eta} + \frac{1}{r}\left(\xi_r\frac{\partial(rv)}{\partial\xi} + \eta_r\frac{\partial(rv)}{\partial\eta}\right)\right]$$

The relationships between the metric derivatives ξ_x, η_x, ξ_r, η_r, the Jacobian, J, and physical space derivatives are presented in Section 3.1.

3.4. Conservation of Diffusion Terms

Similar to the conservation requirements for one-dimensional inviscid flow, it is highly desirable to develop schemes that can retain one-dimensional diffusion solutions independent of the grid transformation. The methodology in which this was accomplished follows. To the author's knowledge this formulation represents the first conservation concept applied to viscous terms.

To exemplify the procedure applied to one-dimensional viscous flow conservation, consider the flow of a fluid contained between a rod moving at some constant velocity within a stationary pipe, as illustrated in Figure 2. Due to its analogy to planar flow, the flow condition will be termed axisymmetric Couette flow.

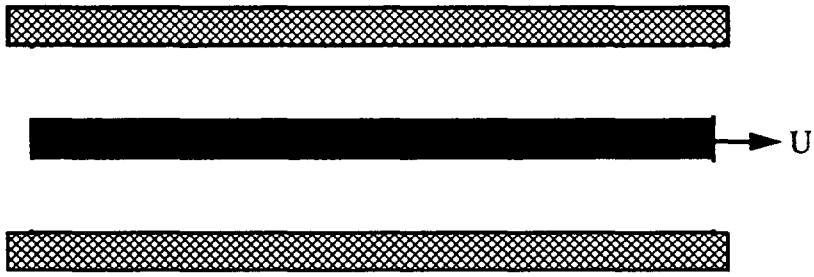

Figure 2. Flow between concentric tubes.

In this flow situation, the shear stress and velocity distribution are governed by the following expression:

$$\frac{\partial (r\tau_{xr})}{\partial r} = 0 \tag{3.4.1}$$

where the shear stress, τ_{xr}, simplifies to the following:

$$\tau_{xr} = \mu \frac{\partial u}{\partial r} \tag{3.4.2}$$

The solution of this flow situation is easily obtained by integration and substitution. The

shear stress has the following radial distribution:

$$\tau_{xr} = \frac{C}{r} \tag{3.4.3}$$

The velocity distribution is obtained in a similar manner.

$$u = C_1 \ln(r) + C_2 \tag{3.4.4}$$

where the viscosity has been assumed to be constant.

Consider now the possibility of obtaining the exact flow solution numerically and with an arbitrary grid. This requires that the following expression (obtained by transformation of Equations (3.4.1) and (3.4.2) and dividing by the Jacobian) be satisfied when the velocity profile given by Equation (3.4.4) is used:

$$\frac{\partial}{\partial \xi}\left[\frac{r\xi_r}{J} \left[\xi_r \frac{\partial u}{\partial \xi} + \eta_r \frac{\partial u}{\partial \eta} \right] \right] + \frac{\partial}{\partial \eta}\left[\frac{r\eta_r}{J} \left[\xi_r \frac{\partial u}{\partial \xi} + \eta_r \frac{\partial u}{\partial \eta} \right] \right] = 0 \tag{3.4.5}$$

Viscous flow conservation requirement

The evaluation of the transformed, viscous term outlined in Equation (3.4.5) can be performed about a point in an arbitrary grid, as illustrated in Figure 3.

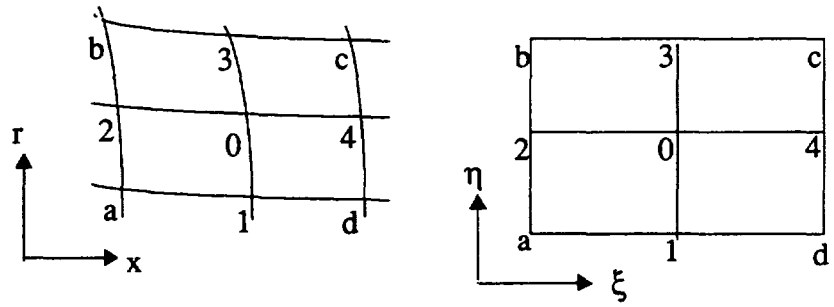

Physical space Computational space

Figure 3. Discretization about point 0 for an arbitrary grid.

A central difference discretization of Equation (3.4.5) can be obtained by averaging about

midpoints, as shown in Equation (3.4.6):

$$(3.4.6)\quad \frac{\partial}{\partial\xi}\left[\frac{r\xi_r}{J}\tau_{xr}\right]+\frac{\partial}{\partial\eta}\left[\frac{r\eta_r}{J}\tau_{xr}\right] \approx \frac{\left.\frac{r\xi_r}{J}\tau_{xr}\right|_4+\left.\frac{r\xi_r}{J}\tau_{xr}\right|_0}{2\Delta\xi} - \frac{\left.\frac{r\xi_r}{J}\tau_{xr}\right|_0+\left.\frac{r\xi_r}{J}\tau_{xr}\right|_2}{2\Delta\xi}$$

$$+ \frac{\left.\frac{r\eta_r}{J}\tau_{xr}\right|_3+\left.\frac{r\eta_r}{J}\tau_{xr}\right|_0}{2\Delta\eta} - \frac{\left.\frac{r\eta_r}{J}\tau_{xr}\right|_0+\left.\frac{r\eta_r}{J}\tau_{xr}\right|_1}{2\Delta\eta}$$

Consider now the substitution of the exact value of the viscous shear stress term, τ_{xr}, for the case of axisymmetric Couette flow, that is, Equation (3.4.3) and apply central differencing to the metric derivative terms. The resulting expression that needs to be satisfied for numerical conservation of the shear stress term is:

$$(3.4.7)\quad -\frac{x_c-x_d}{4\Delta\xi\Delta\eta}C - \frac{x_3-x_1}{4\Delta\xi\Delta\eta}C + \frac{x_3-x_1}{4\Delta\xi\Delta\eta}C + \frac{x_b-x_a}{4\Delta\xi\Delta\eta}C$$

$$+\frac{x_c-x_b}{4\Delta\eta\Delta\xi}C + \frac{x_4-x_2}{4\Delta\eta\Delta\xi}C - \frac{x_4-x_2}{4\Delta\eta\Delta\xi}C - \frac{x_d-x_a}{4\Delta\eta\Delta\xi}C = 0$$

By careful inspection, it is readily observed that the above formulation is satisfied.

The remaining requirement is that the exact solution of the discretized shear stress terms can be realized for an arbitrary grid. This requires that the following condition be true:

$$(3.4.8)\quad \tau_{xr}=\frac{C}{r}=\mu\frac{\partial u}{\partial r}=\mu\xi_r\frac{\partial}{\partial\xi}[C_1\ln(r)+C_2] + \mu\eta_r\frac{\partial}{\partial\eta}[C_1\ln(r)+C_2]$$

As an example, consider the evaluation of the shear stress term at node 4 in Figure 3. Using first-order differencing of the velocity gradient in the ξ direction and central differencing in the η direction, the following requirement for flow conservation are obtained:

$$(3.4.9) \qquad \frac{C}{r_4} = \xi_r \frac{C \ln(r_4/r_0)}{\Delta\xi} + \eta_r \frac{C \ln(r_c/r_d)}{2\Delta\eta}$$

Inspection of the above expression reveals that it is necessary that the evaluation of the metric terms contain terms containing logarithms. Substitution of the metric derivatives in terms of physical space derivatives and rearrangement yields the following requirement for shear stress conservation:

$$(3.4.10) \qquad \left.\frac{J^{-1}}{r}\right|_4 = - x_\eta \frac{\ln(r_4/r_0)}{\Delta\xi} + x_\xi \frac{\ln(r_c/r_d)}{2\Delta\eta}$$

A solution which satisfies the above conservation requirement involves the evaluation of the metric terms and inverse Jacobian in the following manner:

$$(3.4.11) \qquad x_\eta = \left[\frac{(x_c - x_d)(r_4 - r_0)}{2\Delta\eta r_4 \ln(r_4/r_0)} \right]$$

$$(3.4.12) \qquad x_\xi = \left[\frac{(x_4 - x_0)(r_c - r_d)}{2\Delta\xi r_4 \ln(r_c/r_d)} \right]$$

$$(3.4.13) \quad J^{-1} = x_\xi r_\eta - x_\eta r_\xi = \frac{(x_4 - x_0)(r_c - r_d)}{2\Delta\xi\Delta\eta} - \frac{(x_c - x_d)(r_4 - r_0)}{2\Delta\xi\Delta\eta}$$

The metric derivatives are comprised of a standard backward or central difference operator and then 'tuned' by a correction factor. The correction factor is approximately equal to $1 + \Delta r/(2r)$, therefore retaining the accuracy of the differencing technique and being significant only in regions near the centerline or in regions of extremely coarse grid resolution.

Substitution of the expressions for the inverse Jacobian and spatial difference metrics into the flux conservation requirements of Equation (3.4.10) result in the following

expression for the case when the shear stress is inversely proportional to the radius:

$$(3.4.14) \qquad \frac{(x_4 - x_0)\,(r_c - r_d)}{r_4\; 2\Delta\xi\Delta\eta} - \frac{(x_c - x_d)\,(r_4 - r_0)}{r_4\; 2\Delta\xi\Delta\eta}$$

$$= - \frac{(x_c - x_d)\,(r_4 - r_0)}{r_4\; 2\Delta\xi\Delta\eta} + \frac{(x_4 - x_0)\,(r_c - r_d)}{r_4\; 2\Delta\xi\Delta\eta}$$

It is readily observed that the above equation is satisfied and the flux term is therefore fully conservative in the one-dimensional flow situation.

It is also necessary to insure that the flux terms that should be zero in a Couette Flow situation are indeed equal to zero. For instance, the shear stress τ_{xx} should be zero. However, only careful handling of the metric terms and the introduction of correction factors as performed on the τ_{xr} terms insures that this is indeed the case.

The technique applied to the metrics that act on scalar quantities, like temperature, is somewhat less obvious, as it would be desirable to have the following conditions of flux transport satisfied:

$$(3.4.15) \qquad \left[\begin{array}{l} \dfrac{\partial T}{\partial r} = C_1/r \\ \dfrac{\partial T}{\partial x} = C_2 \end{array} \right] \quad \text{when } T = C_1 \ln(r) + C_2 x + C_3$$

Unfortunately, the exact satisfaction of the above equation is not entirely clear. However, applying the same methodology to the scalar quantities as applied to the velocities, the following conservation criteria are readily obtained:

$$(3.4.16) \qquad \left[\begin{array}{l} \dfrac{\partial T}{\partial r} = C_1/r \\ \dfrac{\partial T}{\partial x} = C_2 \end{array} \right] \quad \text{when } T = C_1 \ln(r) + C_2 x + C_3 \text{ and } \frac{\Delta r}{r} \to 0$$

For regions near the centerline, the condition of axial flux conservation is relaxed and the conservation of radial fluxes is enforced:

$$\frac{\partial T}{\partial r} = C_1/r \quad \text{when } T = C_1 \ln(r) + C_3 \tag{3.4.17}$$

In general, the rules that are applied in the Tethys code for viscous flow conservation satisfy the following criteria:

- The Differencing of the metrics is never outside of the computational box. The box outlined in Figure 3 contains all of the necessary locations for evaluation of the dependent and independent variables.

- The thin shear layer assumption cannot conserve diffusive fluxes. Except in cases where the grid transformation is one-dimensional in nature, the application of the thin shear layer assumption removes any possibility of diffusive flow conservation. This is because the balancing of the shear stress and velocity profiles requires the use of all grid metrics and difference equations in order to obtain an expression that is independent of the grid transformation applied. Therefore the thin shear layer approximation is not recommended.

- Radial correction factors are applied to all terms except the radial velocity. Since the primary diffusive transfer of radial momentum will be in the axial direction, conservation of axial momentum transfer dictates that no correction factor be applied.

SECTION 4

BOUNDARY CONDITIONS

In the original Proteus code, boundary conditions were ill-adapted for most nozzle flow situations. At the nozzle inlet, second-order extrapolation of velocities was the recommended technique for solving the velocity profile. Even worse, at the nozzle exit, complete extrapolation of all the fluid properties was recommended for supersonic flow whereas the recommended technique for subsonic flow was to specify the pressure and extrapolate the velocities and temperature. More discouraging was the fact that the Proteus code did not have the means of distinguishing between the two conditions and required that the user specify that the flow at any exit grid point is either subsonic or supersonic. Quite obviously, in the case of a mixed subsonic/supersonic exhaust as experienced in real rocket engines and in transient simulations, the exhaust boundary condition was totally unacceptable.

In the present study, the Tethys code used a reference plane characteristics method. This technique was found to provide a good representation of the actual flow physics and, for inflow and outflow boundaries, it was well adapted for implementation into the structure of the original Proteus code.

Wall boundary conditions in the original Proteus code required modification for the added complexity of multispecies fluid flow, with the additional need for including a coupled fluid injection/heat transfer boundary condition.

In the sections that follow, a discussion of the enhanced boundary condition capabilities developed in the present study for the evaluation of hydrogen/oxygen rocket nozzles are presented.

4.1. Constant-η Reference Plane Method of Characteristics

Appropriate specification of inflow and outflow boundary conditions has been shown to have a significant effect on the overall accuracy and convergence rate of the flowfield equations (Reference 20). The method of characteristics has long been used as the preferred procedure for determining the appropriate equations that need to be solved at fluid flow boundaries (References 21 to 23) due to its ability to decompose the propagation of information into information carried by wave surfaces (the envelope of which is a Mach conoid) and information carried along a pathline, as illustrated in Figure 4. In the constant reference plane characteristic technique applied in this study, the assumption is made a priori that the characteristic lines of interest will lie solely in one direction and the applicable compatibility equations in the specified direction are developed. In the case of a computational scheme employing transformed coordinates as used in this study, the most obvious approach for obtaining characteristic and compatibility relations is to derive expressions valid along a constant-eta (η) or constant-xi (ξ) plane, as illustrated in Figure 5.

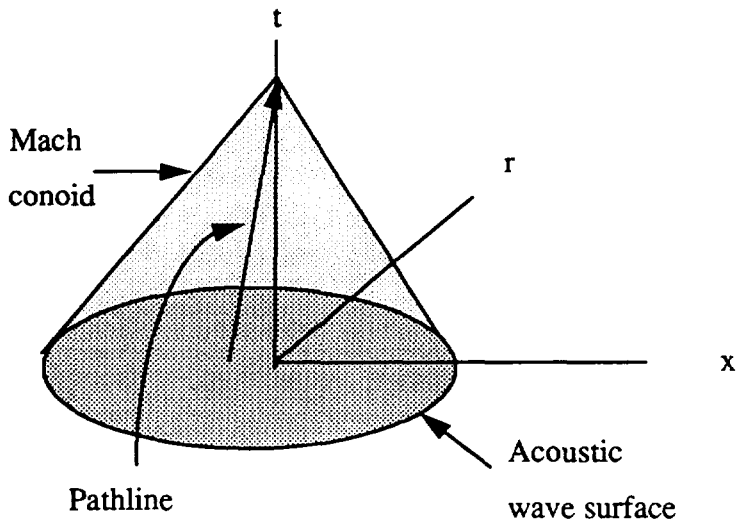

Figure 4. Characteristic surfaces and lines for unsteady two-dimensional flow.

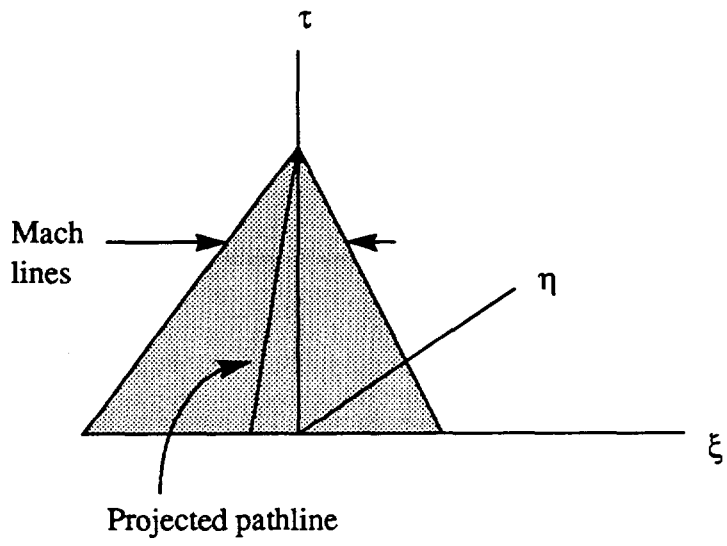

Figure 5. Constant–η reference plane.

The resulting relations for the reference plane characteristic and compatibility equations for an inviscid, nonreacting fluid are given below. A detailed derivation which includes the viscous and chemical reaction terms applied in the Tethys model is presented in Appendix H. The results for the constant-η reference plane are presented in this section. The resulting expressions for a constant-ξ reference plane are analogous (requiring only the switching of the ξ and η coordinates) and are also applied in the Tethys code.

Table 4. Constant-η reference plane method of characteristics.

Characteristic Equation	Compatibility Equation
$\frac{d\xi}{d\tau} = U$	$dP - a^2 d\rho = \psi_4 d\tau$
$\frac{d\xi}{d\tau} = U$	$\xi_r du - \xi_x dv = (\xi_r \psi_2 - \xi_x \psi_3)\, d\tau$
$\frac{d\xi}{d\tau} = U$	$d\omega_i = \psi_{4+i} d\tau$
$\frac{d\xi}{d\tau} = U + a\sqrt{\xi_x^2 + \xi_r^2}$	$\sqrt{\xi_x^2 + \xi_r^2}\, dP + \rho a \xi_x du + \rho a \xi_r dv$ $= \left[(a^2 \psi_1 + \psi_4) \sqrt{\xi_x^2 + \xi_r^2} + \rho a (\xi_x \psi_2 + \xi_r \psi_3) \right] d\tau$
$\frac{d\xi}{d\tau} = U - a\sqrt{\xi_x^2 + \xi_r^2}$	$\sqrt{\xi_x^2 + \xi_r^2}\, dP - \rho a \xi_x du - \rho a \xi_r dv$ $= \left[(a^2 \psi_1 + \psi_4) \sqrt{\xi_x^2 + \xi_r^2} - \rho a (\xi_x \psi_2 + \xi_r \psi_3) \right] d\tau$

In Table 4, the contravarient velocity in the ξ-direction, U, is defined as $U \equiv u\xi_x + v\xi_r$.

In these results, the inviscid source and cross-flow terms, ψ_1 to ψ_{4+i}, for chemically frozen, inviscid fluid flow are given below:

$$\psi_1 \equiv -\frac{\rho v}{r} - \rho\eta_x \frac{\partial u}{\partial \eta} - \rho\eta_r \frac{\partial v}{\partial \eta} - V \frac{\partial \rho}{\partial \eta}$$

$$\psi_2 \equiv - V \frac{\partial u}{\partial \eta} - \frac{\eta_x}{\rho} \frac{\partial P}{\partial \eta}$$

$$\psi_3 \equiv - V \frac{\partial v}{\partial \eta} - \frac{\eta_r}{\rho} \frac{\partial P}{\partial \eta}$$

$$\psi_4 \equiv - V \frac{\partial P}{\partial \eta} + a^2 V \frac{\partial \rho}{\partial \eta}$$

$$\psi_{4+i} \equiv - V \frac{\partial \omega_i}{\partial \eta}$$

where the contravarient velocity in the η-direction, V, is defined as $V \equiv u\eta_x + v\eta_r$.

The characteristic and compatibility equations are of the same form in either dimensional or nondimensional terms.

The characteristic equations are extremely powerful in that they determine the appropriate flow equations that need to be solved at computational boundaries. In regions where the characteristics lie outside of the computational domain, the corresponding compatibility equations must be replaced with appropriate boundary conditions. For instance, at a subsonic nozzle inlet with inflow, as illustrated in Figure 6, the only characteristic that lies within the computational domain is the $d\xi/d\tau = U - a\sqrt{\xi_x^2 + \xi_r^2}$ characteristic. The compatibility equations applicable on the characteristic curves which are outside the computational domain (shown in the figure as the shaded region) must be replaced by appropriate boundary conditions. Similar requirements exist at the fluid outflow boundaries and along the walls.

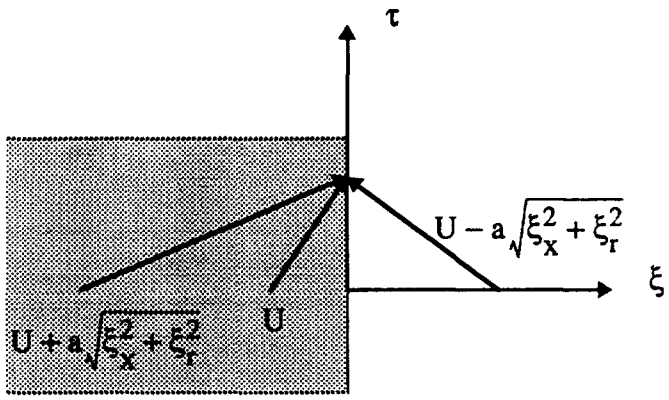

Figure 6. Characteristics at a subsonic flow inlet.

4.2. Subsonic Nozzle Inlet Boundary Conditions

As discussed in the previous section, only one characteristic curve lies within the computational domain of a subsonic inflow nozzle. Consequently, boundary conditions must be specified to form a complete set of inlet conditions. In a chemical rocket engine analysis, one normally has knowledge of the total specific enthalpy of the gasses, the mass concentration of each species (usually determined from an equilibrium chemistry analysis), the flow angle, and the stagnation pressure. An alternative formulation that is equally valid for both chemically reacting and nonreacting flow is to specify the fluid entropy instead of the stagnation pressure.

4.3. Nozzle Exit Boundary Conditions

The exhaust from a propulsive nozzle is primarily supersonic at steady-state conditions. In these circumstances, all of the fluid characteristics lie within the computation domain and no additional boundary conditions need to be specified. However, during transients and at regions very near the wall, the flow may be subsonic. Further, many verification experiments and analyses are performed at subsonic conditions, thus requiring the use of a subsonic nozzle exit boundary condition. For subsonic nozzle exhausts, one characteristic lies outside of the computational domain, and the standard boundary condition to

impose at the exit is the specification of the fluid static pressure. During transients, of course, the ability to discern between subsonic and supersonic flow is essential and is a feature of the present analysis.

4.4. Nozzle Centerline and Free Slip Wall Boundary Conditions

At a nozzle centerline and on an inviscid free slip wall, it is highly desirable to model those conditions where a gradient between the nozzle boundary and the adjacent fluid flow point in the interior of the computational flow exists. This can be achieved by applying one waveline characteristic equation and the following boundary conditions:

- The normal velocity, V_n, equals zero.
- The entropy gradient, $\partial s/\partial n$, equals zero.
- The stagnation enthalpy gradient, $\partial h_0/\partial n$, equals zero.
- All species gradients, $\partial \omega_i/\partial n$, equal zero.

In light of the fact that the above boundary conditions (i.e., the last three listed) would be better modelled with additional characteristic relations that apply along the fluid path-line (which unfortunately were ill-suited for the structure of the numerical procedure employed, as discussed in Appendix A and Section 5), the additional approximation is made on the stagnation enthalpy, entropy, and species concentrations, that the gradient in the physical normal direction is equivalent to the gradient in the computational normal coordinate system.

4.5. No Slip Wall Boundary Conditions

At a no slip wall, the boundary condition dictates that both the radial and axial components of velocity be zero.

$$u = 0$$

$$v = 0$$

Further, there can be no flux of any species normal to the wall. Therefore, the following species flux condition, assuming that no pressure driven species fluxes are of concern, must be satisfied:

$$(4.5.1) \quad j_{i,n} = \sum_{j=1}^{n-1} A_{ij} \frac{\partial \omega_j}{\partial n} - \frac{D_i^T}{T} \frac{\partial T}{\partial n} - \frac{\mu^t \, Le^t}{Pr^t} \frac{\partial \omega_i}{\partial n} = 0$$

Note that only in cases of negligible thermal diffusion will the gradient of the mass fractions be equal to zero.

Another boundary condition that needs to be specified at a no slip solid wall is the thermal boundary condition. A general linear case is specified by the mixed boundary condition:

$$(4.5.2) \quad T_w = a q_w + b$$

For an isothermal wall boundary condition, a = 0, while for a specified heat flux boundary condition, b = 0. For a solid wall boundary, since there can be no species flux, the heat flux equation reduces to the conduction equation:

$$(4.5.3) \quad q_w = - k \frac{\partial T}{\partial n}$$

The remaining boundary condition that needs to be specified at a no slip solid wall is usually obtained by assuming that the normal pressure gradient is equal to zero. This is usually an excellent steady state approximation, even in cases of transpired flow. However, instead of specifying a boundary condition that is essentially valid only at steady state, a more robust boundary condition can be obtained by employing one waveline characteristic equation.

4.6. Transpired Wall Boundary Conditions

Transpiration cooling adds considerable complexity to the appropriate boundary conditions that are necessary for accurate description of the conditions existing at the wall. However, a few boundary conditions are similar to a solid wall. First, in order to be considered a solid boundary, the tangential velocity along a transpired wall must be zero.

(4.6.1) $$V_t = 0$$

Similar to the no slip solid wall case, and somewhat more applicable, one characteristic waveline equation is applied at the wall.

The remaining boundary conditions that need to be applied to the transpired wall are less apparent and somewhat dependent on the application of interest. Figure 7 represents a conventional transpiration cooled nozzle wall.

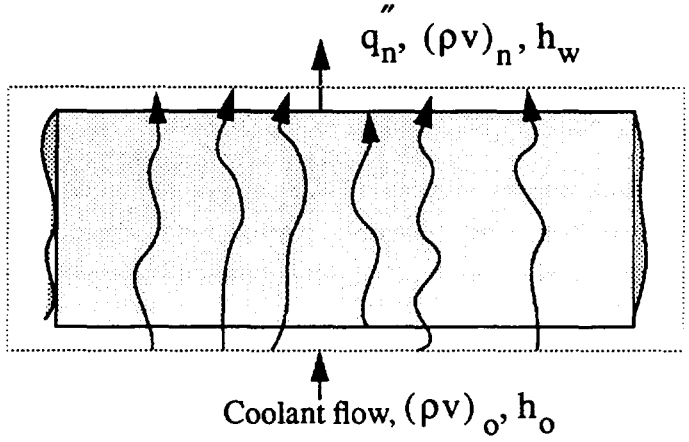

Figure 7. Transpiration cooled wall.

A control volume analysis of the transpired wall yields the following relation:

(4.6.2) $$(\rho v)_o h_o = \left[(\rho v)_n h + q''_n \right]_w$$

where the subscript w indicates conditions existing at the boundary between the transpired wall and the fluid flowfield and the subscript o indicates conditions existing upstream of the transpired wall. Since mass diffusion may occur at the boundary of a transpired wall, the heat flux will be composed of conduction, diffusion, and Dufour energy transfer components:

(4.6.3) $$q_n = -k\frac{\partial T}{\partial n} + \sum_{i=1}^{n} h_i \left[j_{i,n} + j^t_{i,n} \right]$$

$$+ \bar{R}\frac{T}{\rho} \sum_{i=1}^{n} \sum_{j=1}^{n} \frac{M D_i^T}{M_j M_i \wp_{ij}} \omega_j \left[\frac{j_{i,n}}{\omega_i} - \frac{j_{j,n}}{\omega_j} \right]$$

The species density boundary conditions are also complicated somewhat by the transpired wall boundary condition since some species diffusion can occur and the appropriate boundary condition is to relate the known species flux at the wall to the diffusion and advective transport terms:

$$\left[\omega_i (\rho v)_n + j_{i,n} + j^t_{i,n} \right]_w = \left[\rho v \omega_i \right]_o \tag{4.6.4}$$

Two flow conditions of interest may exist. In the 'analysis mode', knowledge of the normal flow rate from the transpired region is known. In these cases, Equations (4.6.2) and (4.6.4) provide the necessary boundary conditions for determining the wall species fluxes, the heat fluxes, and the wall temperature. On the other hand, a 'design mode' condition is often more desirable. In this case, the wall temperature is specified and Equations (4.6.2) and (4.6.4) are used to determine the total mass flow rate necessary to maintain the wall at the required temperature.

The boundary conditions presented for the transpiration cooled wall are in dimensional form. Nondimensional forms will contain reference Reynolds number, Prandtl number, and Lewis number expressions.

SECTION 5

OVERALL NUMERICAL ALGORITHM

The numerical algorithm used to solve the governing fluid flow equations in the Tethys model employs a scheme developed by Beam and Warming (Reference 24). In this scheme, the implicit finite difference operators (see Appendix A) are divided into operators that act in the ξ direction, those that act in the η direction, and those that act on the transient term. In the procedure used by the Tethys model, the implicit operators represent central-difference operators analogous to the operators that act on the explicit side of the equation. This is in contrast to other numerical methods that employ linearized flux-splitting methods on the implicit side of the equation and central difference techniques on the explicit side of the equation (References 25 and 26).

The interior flowfield model is capable of marching forward in time by means of either Euler implicit or explicit methods, or by marching forward in time using a trapezoidal implicit or a three-point backward implicit method. The Euler methods are first-order accurate in time while the other procedures are second-order accurate in time. The Euler implicit procedure was selected as the most appropriate methodology to use throughout the course of the demonstration and verification studies because only the steady state solution was of interest.

The solution methodology used by the Beam and Warming scheme involves the process of first solving the flowfield equations that lie on a constant–η line by using an implicit operator that acts on the transient and the fully coupled ξ direction terms. This procedure is then repeated along all of the interior constant–η lines using a highly vectorized solution methodology. The procedure is then repeated along the interior constant–ξ lines with the explicit side represented by the changes in the flow properties that were observed in the η direction sweep. In the Proteus model, the constant–ξ boundary points

were then updated (after an η and a ξ line sweep) to maintain a more rigorously correct transient solution. However, as the cases of interest in these studies all involved steady state solutions, the boundary points were all updated at the same time after the entire interior solution had been marched forward one time step.

Since only the interior computational lines are swept through in an implicit manner, boundary conditions cannot be applied implicitly except for those terms that lie on the same interior computational line corresponding to the sweep direction. Likewise, since the boundary points at the corners of the flowfield are not located on any interior computational line, they need to be updated in a purely explicit manner.

The CFL (i.e., Courant, Friedrichs, and Lewy, Reference 27) number was used as the basis for the maximum time step that could be taken as the solution proceeded from an initial profile towards a steady state condition. In the Tethys model, the CFL number is based purely on the time that it takes a Mach line to travel from one grid point to an adjoining point. This is in contrast to other computational models that require a viscous correction to the CFL number to account for the propagation speeds of the viscous terms (Reference 25). Because the Tethys code used an implicit formulation of the diffusion terms, a viscous correction was not deemed to be necessary.

In the majority of the verification and demonstration cases studied, the flowfield solution was obtained by marching every grid point at a local CFL number that was in the range of 0.7. However, in some cases, somewhat faster convergence was obtained by using a mixed CFL number criteria, developed by Knight (Reference 28), where the maximum local CFL number in the η direction was set equal to a time step value of around 4.0 and the maximum local CFL number in the ξ direction was not allowed to exceed a value in the region of 0.4. In yet other cases, a global CFL number criteria was used to examine the accuracy of the implicit formulation. In these cases the CFL number varied from maximum values of 10 to as high as 10000, depending on the application.

In general, the initial flowfield used to initiate fluid flow problem should employ a property distribution that is as close to the steady state solution as could be obtained. In many cases this can be accomplished by using one-dimensional flow solutions as a starting point. However, this was not always practical and some cases were started by using a

semisteady truncated nozzle solution. The initial profile for these truncated geometries varied from a one-dimensional chemical equilibrium solution to a near zero velocity condition. Once a reasonably close solution for this geometry was obtained, the remainder of the nozzle was added on to complete the analysis.

In general, a nozzle flowfield problem that started from an initially low velocity distribution would prove to be unstable as the boundary conditions applied at the exit of the nozzle would impose a static pressure that was too great a change from the initially stagnant properties. Significant alleviation of this difficulty was obtained by scaling the maximum change in pressure at the exit as being equal to 15 % of the product of the static pressure multiplied by the local CFL number.

In nearly all of the demonstration cases examined, the heat transfer rate was the last parameter of engineering interest to reach an acceptable level of steady state convergence. Consequently, convergence of the nozzle flowfield was determined to occur when the transient variation in heat flux to the nozzle wall was deemed to be negligible. The flowfield predictions from the Tethys model were inspected at periodic intervals to ascertain when a converged solution had been obtained. In general, the computational resources required of the problem and the accuracy to which a heat transfer prediction was desired was used as the guide as to when an acceptable convergence of the heat transfer rate was established. In all cases, the minimum convergence criteria occurred when the absolute value of the local heat fluxes at selected points had less than a 2 % change after 1000 iterations. In many other cases, the convergence criteria was significantly more stringent.

In general, a flowfield problem required on the order of 10,000 iterations to achieve the desired level of convergence. The computational resources required for this level of convergence varied from 2 to 50 hours of computational time on a Cray Y-MP computer. The chemically frozen, binary species flowfield simulations required the minimum computational effort in the viscous analysis cases performed, while the maximum computational resources were required when the Tethys model was operating at its maximum flowfield simulation capacity of six species and eight chemical reactions.

SECTION 6

VALIDATION STUDIES

Extensive validation studies were performed to verify the prediction accuracy of the Tethys code since there were significant changes made to the Proteus code to obtain the Tethys code. Validation of the following effects was deemed critical:

- Conservation of one-dimensional flow
- Reference plane characteristics boundary conditions
- Chemical kinetics
- Transpired fluid boundary conditions
- Multicomponent diffusion (ordinary and thermal)
- Multicomponent heat transfer (conduction, interdiffusion, and Dufour)
- Turbulence model validation
- Fluid thermodynamic and transport properties validation

With the exception of the first two validation requirements presented above, the validations are either contained in the Appendix or verified within a reasonable level of certainty in the demonstration studies or in other unreported validation tests. Further, the solution procedure of the Tethys fluid flow model is fully implicit in nature with complete coupling between the species and fluid flow equations, including a complete description of the dependency of the fluid pressure, temperature, and total energy on species concentration. A discussion of the solution methodology used throughout the validation studies is given in Appendices A and B.

The two validation studies that follow (conservation of one-dimensional flow and reference plane characteristics boundary conditions) are given more extensive coverage since

the application of these concepts is both a unique and an interesting aspect of the Tethys code.

6.1. Conservation of One-Dimensional Inviscid Flow

Reformulation of the manner in which the original Proteus code analyzed the radius in the axisymmetric flow equations was required. As discussed in Section 3, the original Proteus code evaluated the radius exactly, but one-dimensional axial flow conservation shows that the radius in the axial flow terms are conservative when the radius is evaluated in terms of averaged quantities. About the ξ, η point:

$$r_{\xi+1,\eta} = \frac{r_{\xi+1,\eta+1} + r_{\xi+1,\eta-1}}{2} \tag{6.1.1}$$

$$r_{\xi,\eta+1} = \frac{r_{\xi+1,\eta+1} + r_{\xi-1,\eta+1}}{2} \tag{6.1.2}$$

and likewise for other points.

The 'nonconservative nature' of using the exact formulation for the radius can be reasoned to be a second-order effect since the difference between the exact and the averaged radius procedure is also a second-order difference. Therefore, for cases where the second-order derivative of the radius with respect to the grid metrics is zero, no error in using the exact evaluation of the radius occurs, and the flow is fully conservative. Consequently, verification of the accuracy of a finite difference procedure using metrics that have second-order derivatives that are zero is misleading in the more general case.

The nonconservative error associated with formulating the pressure using the exact radius and a source term formulation is of the following nature:

$$\frac{1}{J}\frac{\partial(rP)}{\partial r} - \frac{P}{J} = \frac{\partial(r\xi_r P/J)}{\partial \xi} + \frac{\partial(r\eta_r P/J)}{\partial \eta} - PJ^{-1} \tag{6.1.3}$$

Substitution of the expressions for the metrics and inverse Jacobian yields the following

condition for pressure conservation:

$$(6.1.4) \qquad -\frac{\partial (r x_\eta P)}{\partial \xi} + \frac{\partial (r x_\xi P)}{\partial \eta} - P(x_\xi r_\eta - r_\xi x_\eta) = 0$$

when the pressure, P, is equal to a constant.

If central differencing of the grid metrics and fluid pressure is used, the conservation requirement given in Equation (6.1.4) is satisfied only for cases in which any one of the axial metric derivatives, such as x_η, is equal to zero. This condition is common for many rocket nozzle types of analysis, although requiring that this metric be equal to zero for pressure conservation is ill-advised since some nozzles flow cases are much more efficiently executed in an environment in which all of the grid metrics are nonzero in nature. Likewise, for cases in which the radial derivative is a function of only one variable, which is typical for many pipe flow simulations, no solution error exists in the above formulation of the pressure.

Verification of the nonconservative nature of the original metric terms and the conservative nature of the reformulated terms will be shown for inviscid flow in a pipe with two different grid generation cases. In one case the metrics are a function of only one independent variable, in which case both the exact and the radial-averaging technique should yield stable solutions. In the other case, the metrics are a modest function of both x and r and consequently the exact radial formulation would be expected to yield nonconservative solutions that may not converge.

6.2. Inviscid Pipe Flow - One-Dimensional Grid Transformation

The 11X11 grid used to demonstrate the nature of the flow in a simply packed grid is shown in Figure 8 where the grid packing involved simple one-dimensional power relationships:

$$(6.2.1) \qquad \frac{r}{r_{max}} = \left[\frac{\eta - 1}{\eta_{max} - 1}\right]^{0.5}$$

(6.2.2)
$$\frac{x}{x_{max}} = \left[\frac{\xi - 1}{\xi_{max} - 1} \right]^{0.5}$$

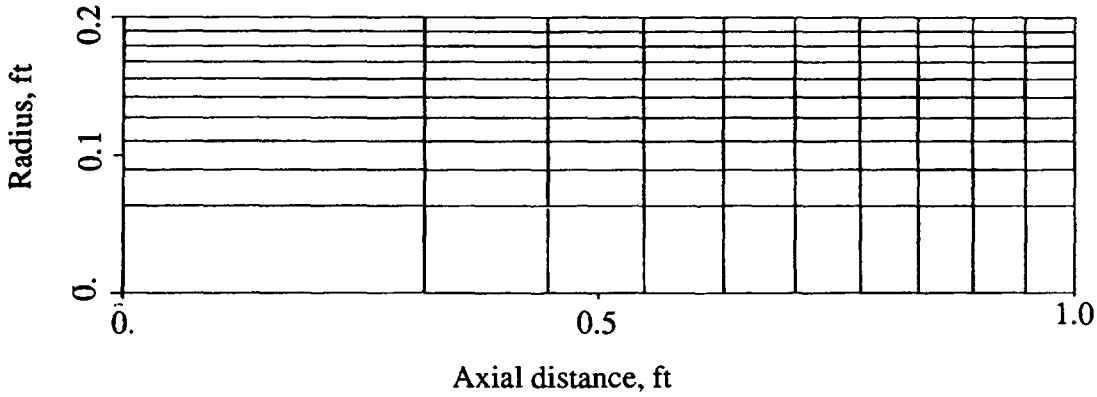

Figure 8. One-dimensional transformed grid for inviscid pipe flow calculation.

Characteristic boundary conditions, as described in Section 4, were used at all boundaries. The back pressure was set to 14.69 lbf/in.^{2}, while the stagnation pressure at the inlet was set to yield a Mach number of 0.4. The fluid was air (75.83 % N_2, 23.13 % O_2, and 1.03 % Ar by weight) and the stagnation enthalpy of the mixture was zero. The exact solution (to 5 significant digits) was used as the starting point for all of the test cases examined. No artificial diffusion was applied. The local CFL number was set to 0.7.

Three discretized flowfield approximations were considered. One formulation, identified in Figures 9 and 12 as the standard technique, employed an exact radius evaluation and formulated the pressure terms in the radial momentum equation as a combination of a strong conservation term and a source term, as shown in Equation (6.1.3). The second flowfield approximation method, identified in Figures 9 and 12 as the exact radius technique, formulated the pressure in a weak conservation form, while evaluating the radius in an exact manner. The third finite difference approximation method used the complete conservation concepts outlined in Section 3, and is identified in Figures 9 and 11 as the conservative technique.

The results for the inviscid pipe flow simulation for all three flowfield formulations is presented in Figure 9. It is evident from Figure 9 that all of the evaluation techniques converge. The standard formulation converged the slowest, while the exact radius and conservative techniques have almost identical convergence rates.

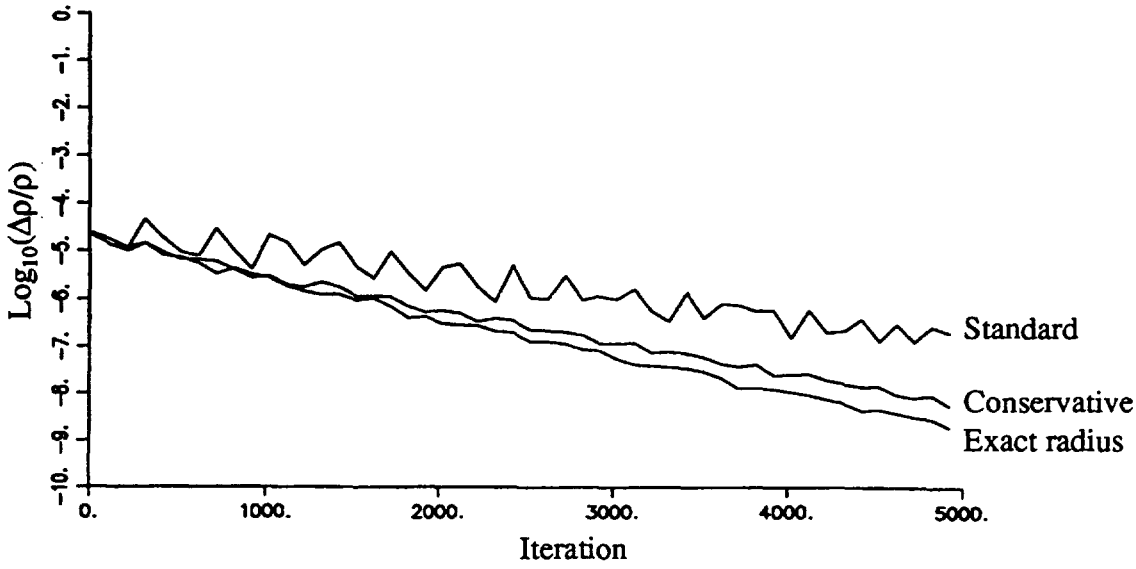

Figure 9. Convergence rate of standard, exact radius, and conservative techniques for inviscid pipe flow with a one-dimensional grid transformation.

6.3. Inviscid Pipe Flow - Two-Dimensional Grid Transformation

A pertubation of the previous grid description was made for the case of the generalized grid transformation. In this case, the grid metrics were determined using the following relations:

$$\frac{r}{r_{max}} = \left[\frac{\eta - 1}{\eta_{max} - 1}\right]^{0.5\,(\xi/\xi_{max})^{0.075}} \tag{6.3.1}$$

$$\frac{x}{x_{max}} = \left[\frac{\xi - 1}{\xi_{max} - 1}\right]^{0.5\,(\eta/\eta_{max})^{0.075}} \tag{6.3.2}$$

Figure 10 presents the resulting grid generated when the above relations are applied.

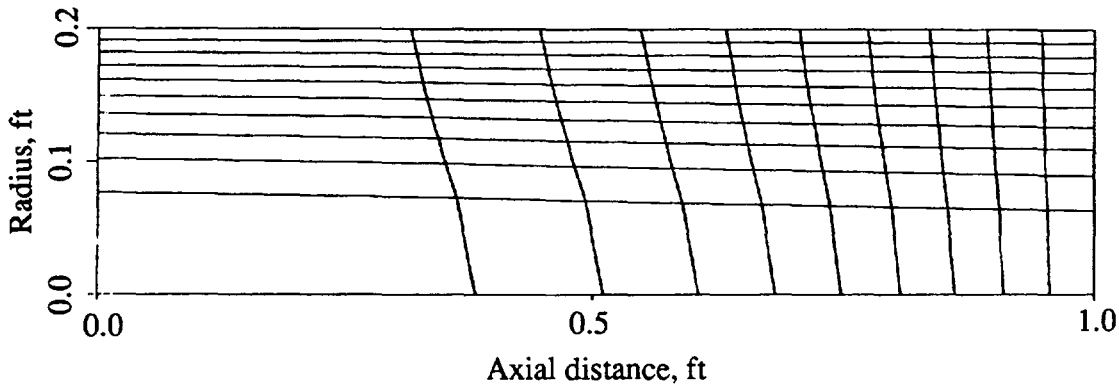

Figure 10. Two-dimensional grid used in the inviscid flow conservation study.

The exact same boundary conditions, initial conditions, and time stepping procedure was applied to the evaluation of inviscid flow in a pipe with a two-dimensional grid transformation as was applied to the test cases performed with inviscid pipe with a one-dimensional grid transformation. These boundary conditions include a back pressure of 14.69 lbf/in.^{2}, a stagnation pressure at the inlet set to yield a Mach number of 0.4, and an inlet stagnation enthalpy of zero. The fluid was air and the local CFL number was set to 0.7. No artificial diffusion was applied.

Three test cases were examined. The cases examined are described in Section 6.2 and represent various finite difference approximations to the radius and the radial pressure gradient. The three different test cases are identified as the standard technique, the exact radius technique, and the conservative technique.

In Figure 11, the stable nature of the conservative technique is apparent as the convergence of the solution continues at about the same rate as that observed for the one-dimensional transformed grid case, with the maximum change in density continuously decreasing as the number of iterations increases.

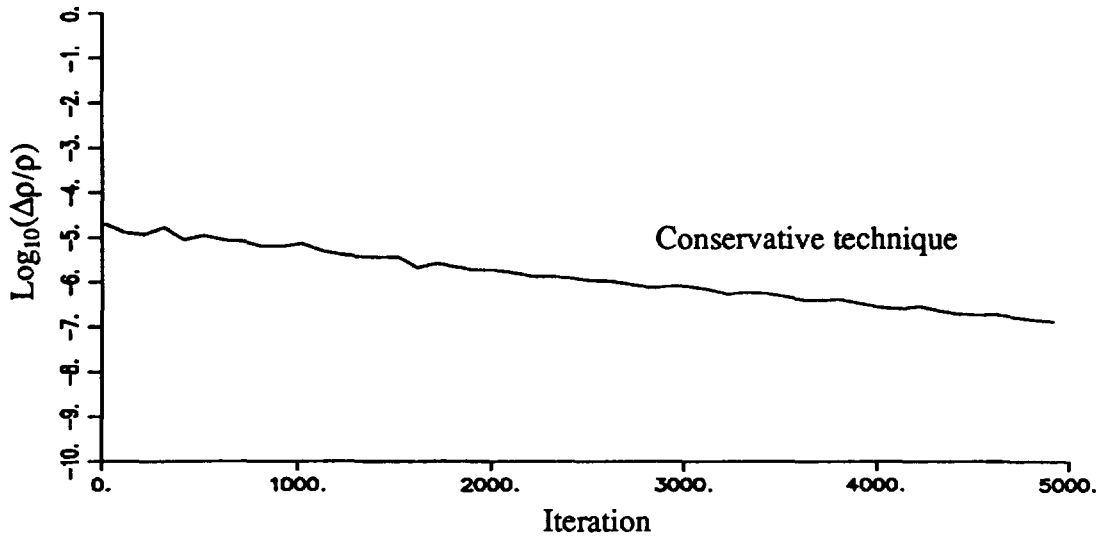

Figure 11. Convergence rate of conservative technique for inviscid pipe flow with a two-dimensional grid transformation.

The standard and the exact radius techniques proved to be unstable when the grid was changed to a more general two-dimensional case, as illustrated in Figure 12. The nonconservative nature of the formulations are apparent as the standard formulation becomes unstable in less than 250 iterations, while the exact radius formulation begins to diverge after about 1000 iterations and becomes unstable in less than 1500 iterations.

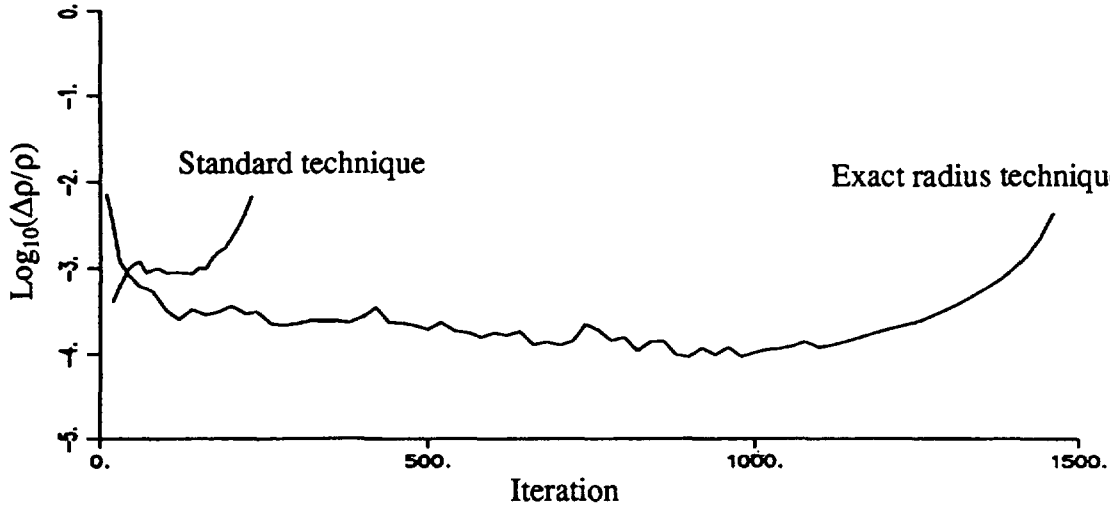

Figure 12. Divergence rate of standard and exact radius techniques for inviscid pipe flow with a two-dimensional grid transformation.

6.4. Couette Flow

The potential benefits of applying a flow conservative formulation to the diffusive terms was examined for the cases of flow between two parallel plates and flow between two concentric cylinders. The 6X11 computational grid used for both studies is two-dimensional and nonorthogonal to the wall as presented in Figure 13. The bottom surface was set to a velocity of 1000 ft/sec and the upper surface was stationary. The exact velocity profile was imposed at the inlet. The fluid examined was air and the Reynolds number based on the bottom surface velocity and gap between the fluid surfaces was equal to 0.1.

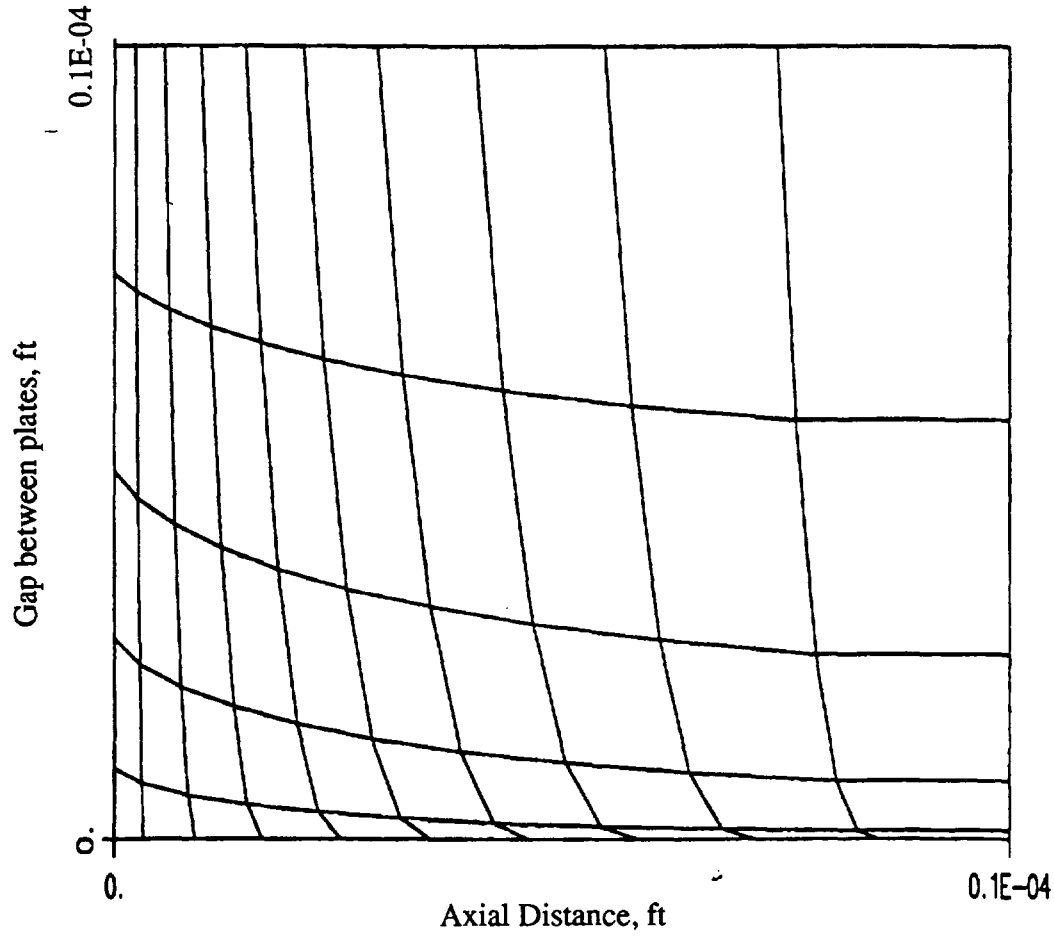

Figure 13. 6X11 Computational grid employed for the analysis of Couette flow.

The results for the planar Couette flow study are given in Figures 14 and 15. On the overall scale shown in Figure 14, it appears as if both the conventional diffusion equation technique and the conservative formulation used in the Tethys model are very accurate. However, closer examination of the actual velocity error as presented in Figure 15 indicates the superiority of the conservative technique. It is observed that the velocity error exceeds 5 percent in the conventional analysis while the flow conservative analysis yields an order of magnitude less error in the velocity.

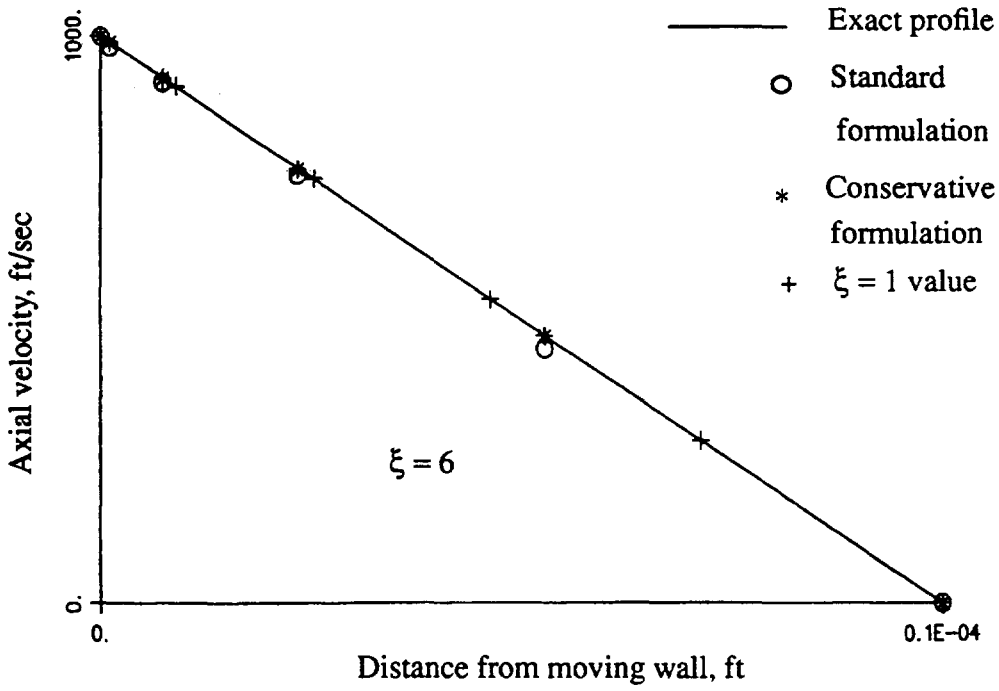

Figure 14. Predicted velocity profiles for a Couette flow simulation.

While it might be expected that the Tethys formulation would yield exact results for this flow situation, this is not the case as the modelling of the inviscid term ρu^2 was designed to be conservative for the case where the axial momentum was independent of the y-location. In the case of Couette flow, the term is not constant throughout the flowfield. Consequently, the introduction of a nonzero gradient of axial momentum in the

radial direction resulted in a nonzero contribution to this advective term in the axial momentum equation.

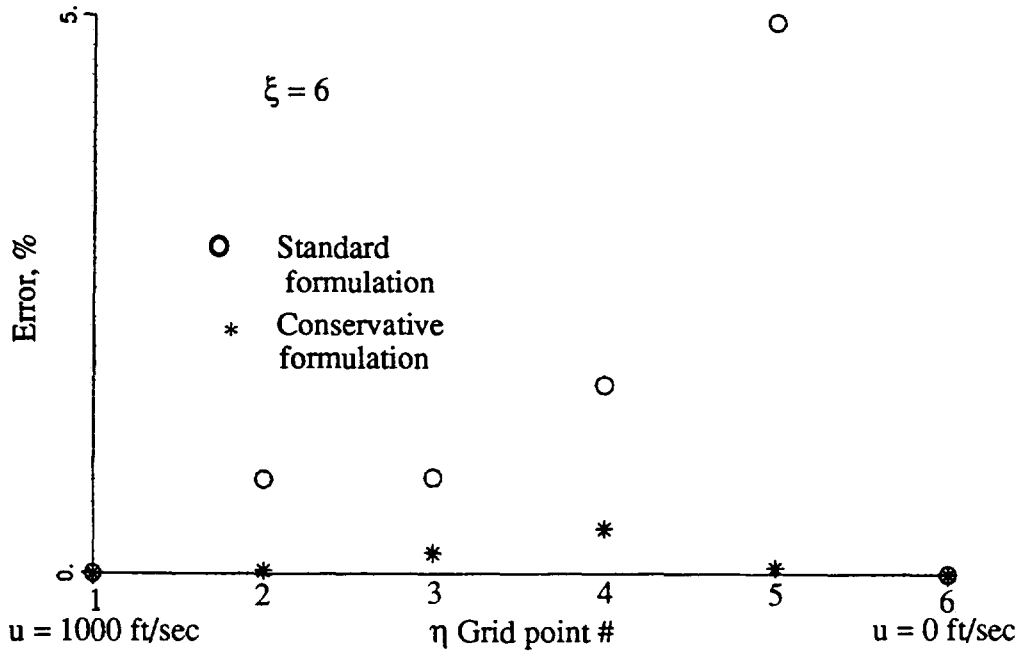

Figure 15. Axial velocity error at the computational midline of a Couette flow simulation.

The results for the annular axisymmetric Couette flow simulation (which used the same grid as used in the planar flow case but was displaced such that the ratio of the inner radius to outer radius was equal to ten) are given in Figures 16 and 17. The trends in the results are similar to the planar flow condition with both the standard finite difference formulation and the conservative Tethys formulation having significantly more error than their planar flow counterparts. The maximum error observed with the conventional, or standard, formulation exceeds 10 percent, which is nearly an order of magnitude greater than the maximum error observed with the Tethys viscous conservative scheme. Again, the failure of the Tethys modelling scheme to exactly yield the correct solution is attributed to the nonconservative nature of the discretized advection term in the axial momentum equation.

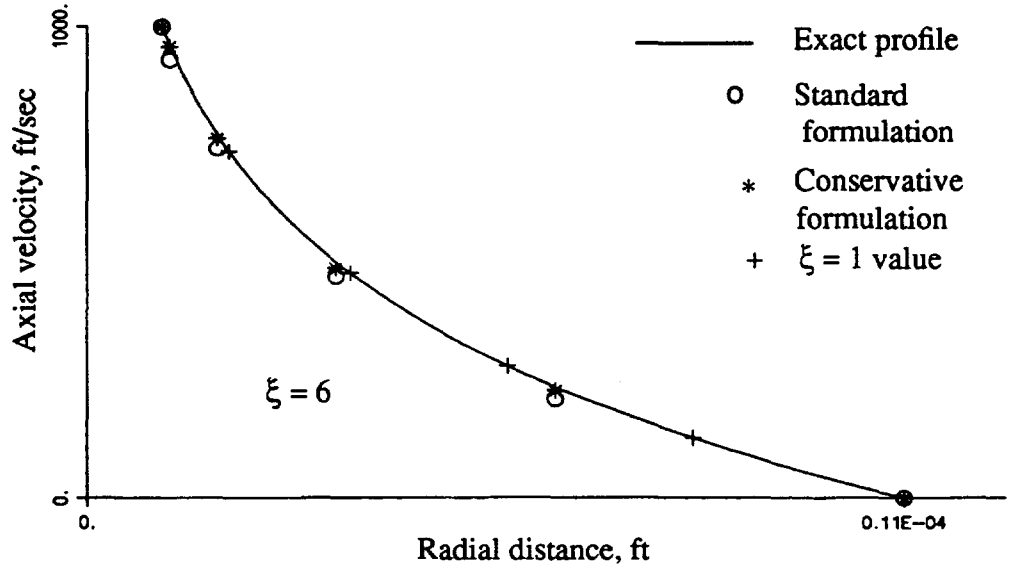

Figure 16. Predicted velocity distribution for axisymmetric Couette flow simulation.

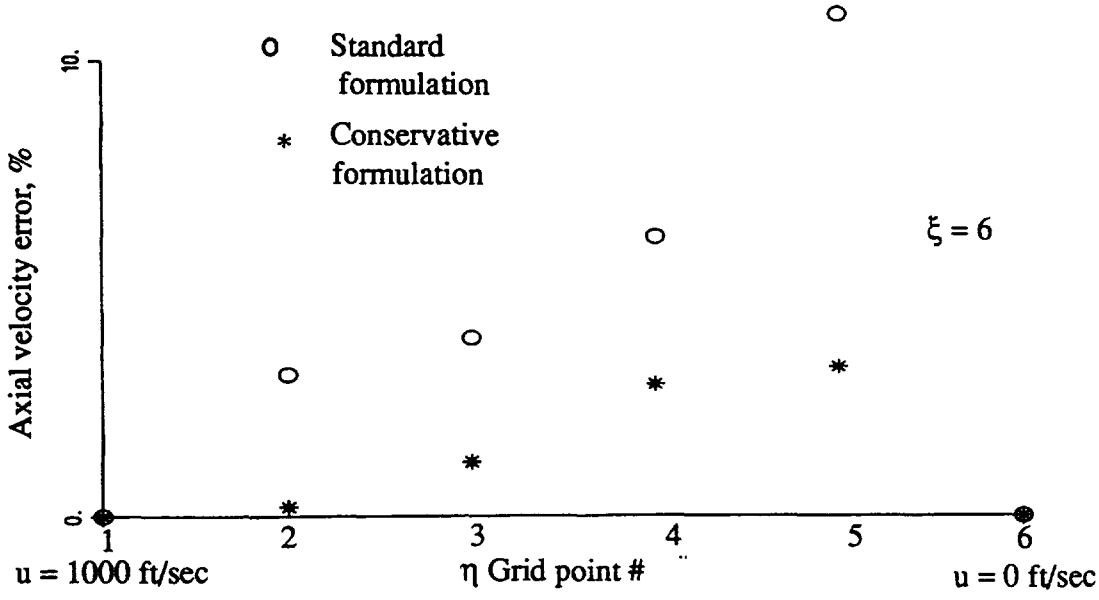

Figure 17. Axial velocity error at the computational midline of an axisymmetric Couette flow simulation.

It is worthy of mention that in all of the Tethys flow cases examined above, the conservation of species mass fraction for all of the constituents of air (nitrogen, oxygen, and argon) was completely satisfied.

6.5. Supersonic Radial Source Flow

Radial source flow represents a one-dimensional flow condition that needs to be considered prior to making judgement of the two-dimensional accuracy of a numerical flow simulation. For the purposes of this study, it represents a flow situation that allows the examination of how well the Tethys model conserves species concentrations, stagnation pressure, stagnation enthalpy, and mass. Further, it provides a baseline case from which one can compare chemically reacting solutions, as is shown in Appendix J.

Figure 18 pictorially presents a general case of radial source flow. Solutions for this type of flow are usually not determined at the centerline but instead the results are scaled from some arbitrary starting radius as represented by the dashes in Figure 18 with the understanding that some type of source flow could produce those conditions at the starting line.

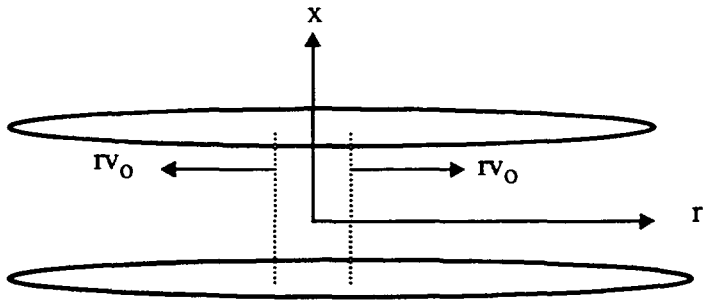

Figure 18. One-dimensional radial source flow.

The inlet boundary conditions applied to the source flow simulation are presented in Table 5, which corresponds to an inlet Mach number of 1.5 and species mass fraction corresponding to a stoichiometric mixture ratio of hydrogen and oxygen. Characteristic boundary conditions were employed at the exit while reflective boundary conditions were used along the upper and lower walls.

Table 5. Inlet boundary conditions used for frozen source flow examination.

Property	Inlet Value
Temperature	6060.6 R
Density	0.005 lbm/ft^3
Velocity	7171.9 ft/sec
ω_{H_2}	0.0156
ω_{O_2}	0.0829
ω_{H_2O}	0.7500
ω_{OH}	0.1050
ω_{H}	0.0025
ω_{O}	0.0190

The 4X21 grid used to demonstrate the accuracy of the radial flow terms in the present metric and flow methodology is shown in Figure 19. The grid represents a radially packed grid that should provide a good check of the ability of the code to model one-dimensional radial flow.

As can be seen in Figure 19, the radial grid packing was one-dimensional and of the form outlined in the following expression:

$$r = r_{Inlet} + \left[r_{Exit} - r_{Inlet} \right] \left[\frac{\xi - 1}{\xi_{Max} - 1} \right]^{2.5} \tag{6.5.1}$$

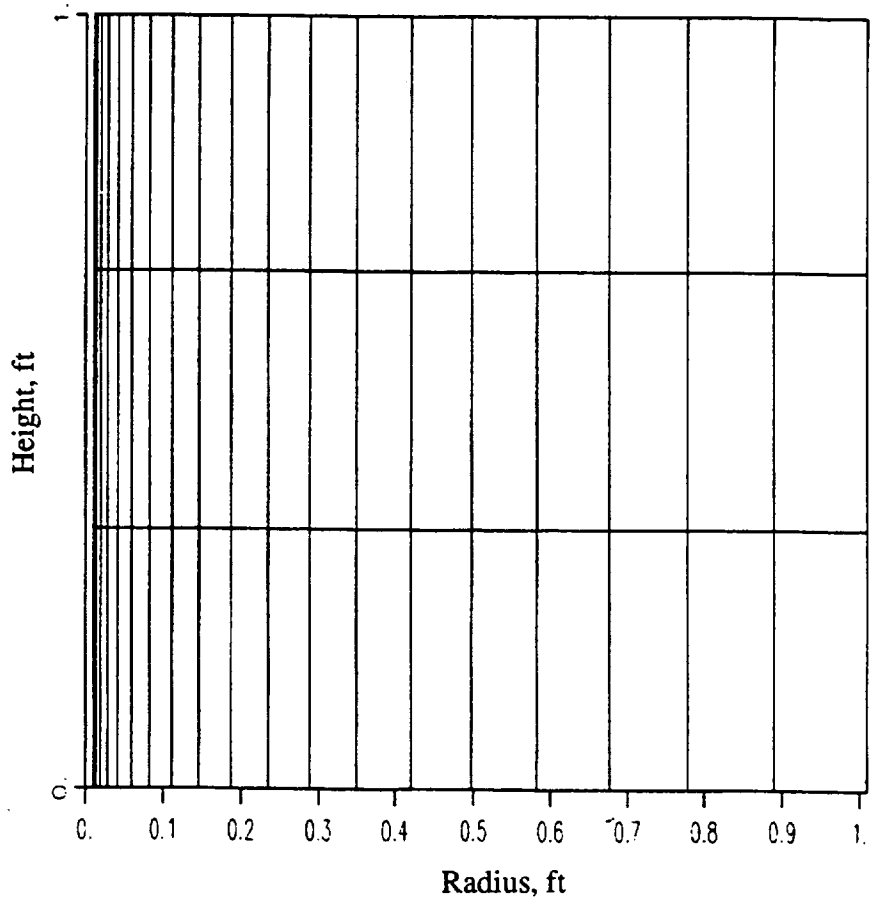

Figure 19. Computational grid used for supersonic planar source flow simulation.

The nonlinear second-order artificial diffusion model (see Appendix N) was applied. The magnitude of the diffusion coefficient was examined at values of 0.5 and 0.125, which is twice as large and one-half as small, respectively, as the recommended value of 0.25 (Reference 29). Since no attempt was made to alter the artificial diffusion model to force one-dimensional flow conservation, its effect on the conservative nature of the flow variables required examination.

In Figure 20, the predicted and exact Mach number distribution for the flow situation described above are shown. The discrepancy between the exact results and those predicted

by the Tethys flow model are hardly distinguishable, which in a rather global sense demonstrates the modelling accuracy of the radial derivative terms contained in the Tethys flow model. However, it can be observed that the artificial diffusion has a distinct effect on the numerical predictions, over predicting the Mach number at low diffusion values and under predicting the exit Mach number at higher levels of diffusion.

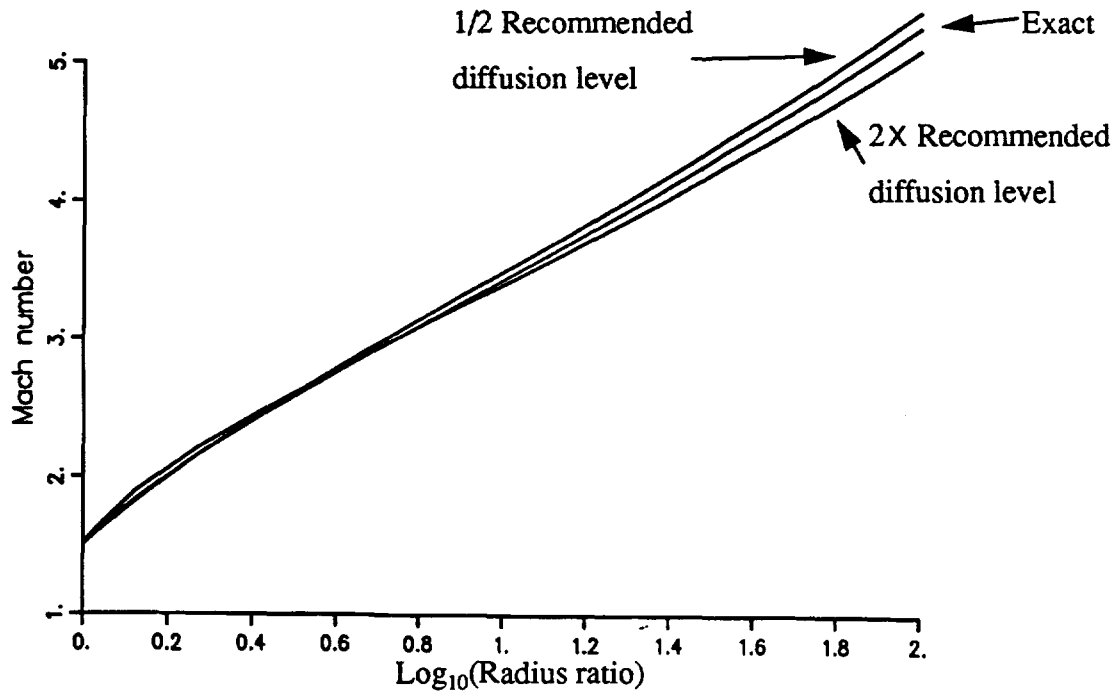

Figure 20. Mach number predictions for a chemically frozen 100:1 area ratio planar source flow calculation.

The extent to which the mass flow rate, stagnation enthalpy, and stagnation pressure are conserved is presented in Figures 21 to 23, respectively, for the two different levels of diffusion examined. It is readily observable from the mass flow rate and stagnation enthalpy conservation cases that artificial diffusion has a deleterious effect on the conservation of mass and stagnation enthalpy. On the other hand, the artificial diffusion has no clear effect on the stagnation pressure and in fact the higher diffusion level actually gave better conservation of stagnation pressure than the lower diffusion level. All of these trends might be expected since the evaluation of the transformation metrics were designed such that one-dimensional radial flow would be exactly conservative in mass and energy

with the exclusion of the consideration of any possible nonconservative effects of the artificial diffusion terms. Quite obviously, complete conservation of mass flow and stagnation enthalpy is not realized and the lack of conservation of these variables is clearly a direct function of the level of artificial diffusion applied. On the other hand, conservation of stagnation pressure requires that all of the flow equations be completely satisfied. However, the modelling of the radial pressure gradient term was performed such that it was equal to zero for the case where the pressure was constant throughout the flowfield. For one-dimensional radial flow, the pressure can vary significantly throughout the flowfield and can consequently result in a lack of conservation of stagnation pressure, in addition to the nonconservative contributions of the artificial diffusion.

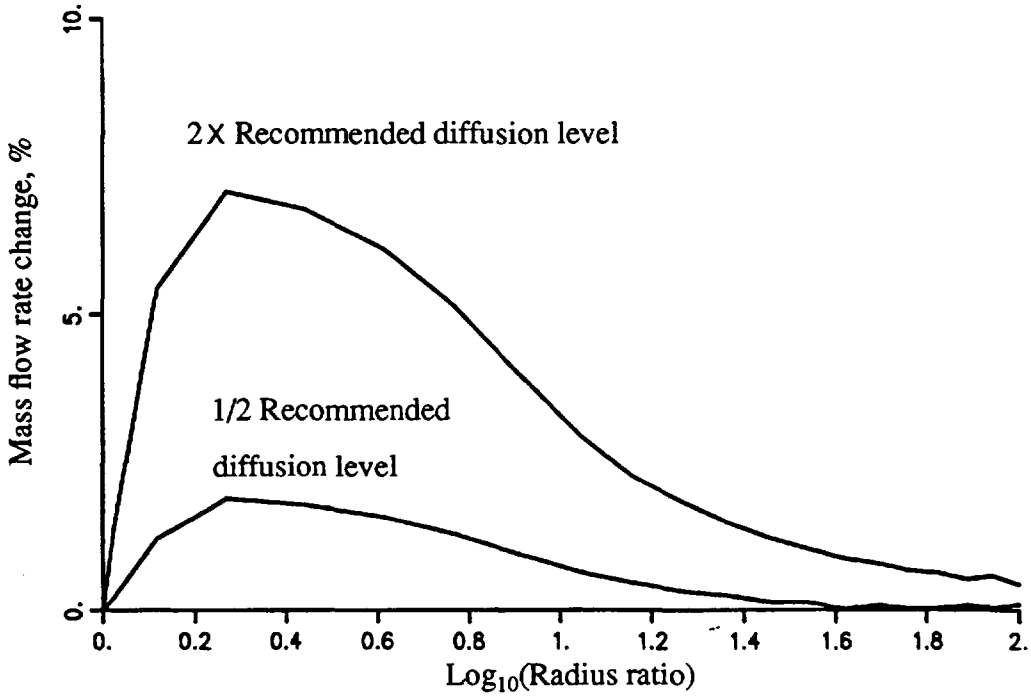

Figure 21. Mass flow rate conservation study for a 100:1 planar source flow simulation.

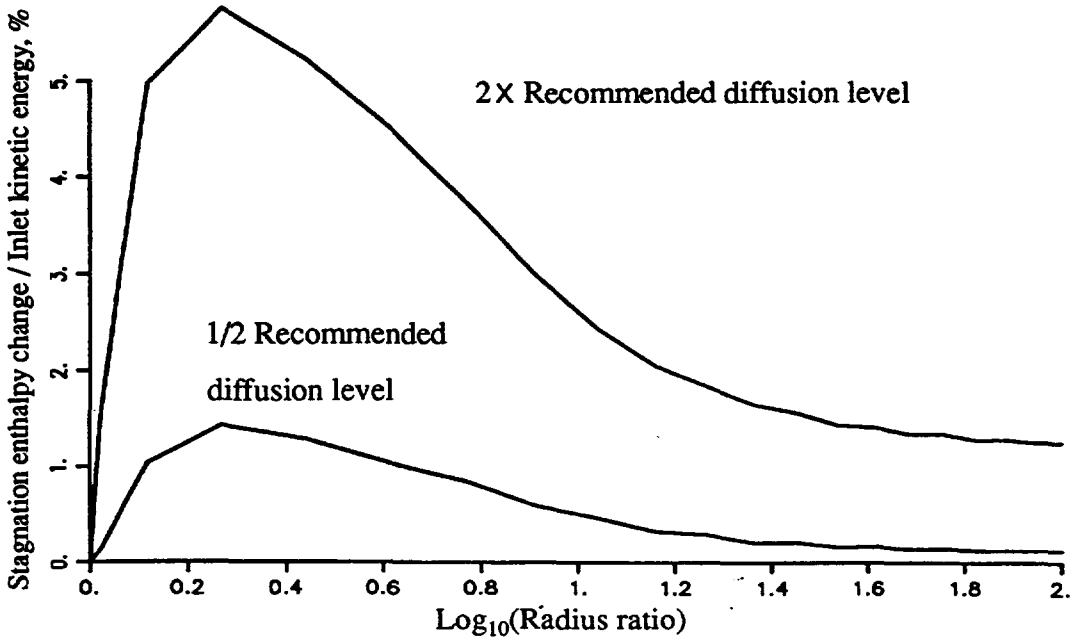

Figure 22. Stagnation enthalpy conservation study for a 100:1 planar source flow simulation.

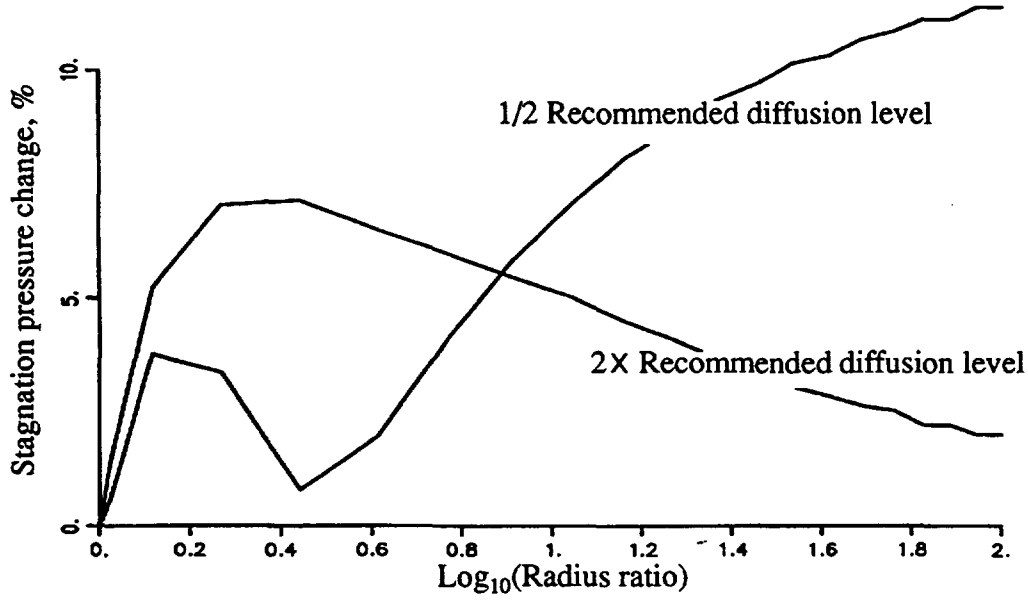

Figure 23. Stagnation pressure conservation study for a 100:1 planar source flow simulation.

6.6. Inlet, Exit, and Wall Reference Plane Characteristics Verification

Verification of the constant-η reference plane characteristics technique for nozzle inlets and exhausts is demonstrated throughout most of the verification and demonstration tests performed. In this particular example, special emphasis is placed on the fundamentals of the subsonic inlet, the supersonic exit, the inviscid wall, and the centerline techniques, leaving more advanced verification tests that involve chemical kinetics, diffusive transport, and artificial diffusion, to the more difficult demonstration tests.

The implementation of the constant-η reference plane characteristic solution at any time level is performed as shown in the Figure 24. The flow variables and appropriate equations are determined by linear scaling with conditions that would exist at the maximum explicit time step, $d\tau_{MOC}$. For example, the solution of the compatibility equation, $dP - a^2 d\rho = \psi_4 d\tau$, along the characteristic curve $d\xi/d\tau = U$, is performed in the following manner (using the nomenclature shown in Figure 24):

$$(6.6.1)\quad dP - a^2 d\rho = \psi_4 d\tau \approx P_{i+1}^{n+1} - P_i^n - a^2\left[\rho_{i+1}^{n+1} - \rho_i^n\right] = \psi_4 \Delta\tau_{MOC}$$

where the terms without subscript and superscript nomenclature are evaluated at time level n and the average of the values existing at spacial levels i and i+1. Values at time level n+1 can be decomposed into quantities at time levels n and a delta form, as shown in Equation (6.6.2):

$$(6.6.2)\qquad P_{i+1}^{n+1} = P_{i+1}^n + \frac{\partial P_{i+1}^n}{\partial \tau} d\tau \approx P_{i+1}^n + \Delta P_{i+1}^n$$

The expression for the density has a similar form.

Substitution and rearrangement of Equation (6.6.1), using the concepts shown in Equation (6.6.2), result in an discretized expression valid along the constant-η plane characteristic pathline.

$$(6.6.3)\quad \Delta P^n_{i+1} - a^2 \Delta \rho^n_{i+1} = \psi_4 \frac{\Delta \xi}{U} - \left[P^n_{i+1} - P^n_i \right] + a^2 \left[\rho^n_{i+1} - \rho^n_i \right]$$

For time steps less than the time step corresponding to the characteristic curve, the solution is scaled by employing a similar triangle methodology, as illustrated in Figure 24. The resulting general compatibility equation (for time steps less than or equal to the time step along the characteristic curve) is given in Equation (6.6.4):

$$(6.6.4)\quad \Delta P^n_{i+1} - a^2 \Delta \rho^n_{i+1} = \left[\psi_4 \frac{\Delta \xi}{U} - (P^n_{i+1} - P^n_i) + a^2 (\rho^n_{i+1} - \rho^n_i) \right] \frac{U \Delta \tau}{\Delta \xi}$$

While this technique is only first-order accurate in time, a desirable attribute to this method is that the steady state solution of the compatibility equations are independent of the size of the time step used in obtaining a solution since the interior flow point algorithm also contains only a global $\Delta\tau$ operator on the explicit side of the equation (see Appendix A), similar to Equation (6.6.4).

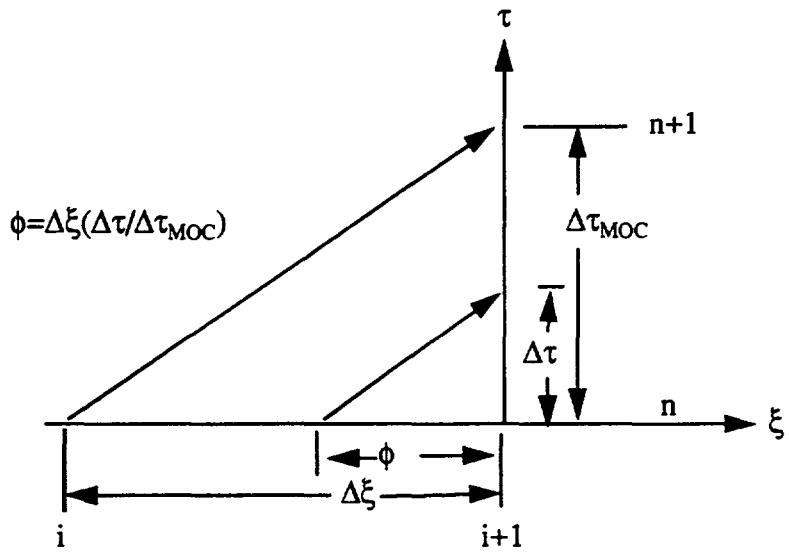

Figure 24. Numerical implementation of the constant-η reference plane method of characteristics.

Verification of the characteristic technique for rocket nozzle flowfield analysis will be performed using the JPL nozzle tested by Cuffel et al. (Reference 30). The nozzle geometry is shown in Figure 25, while the 45X11 grid used for the flowfield analysis is presented in Figure 26. This grid scheme is reasonably close to the grid applied by Driscoll (Reference 20) whose results will be used for comparison between the reference plane characteristic method and the bicharacteristic technique. The boundary conditions applied for this nozzle analysis case are presented in Table 6.

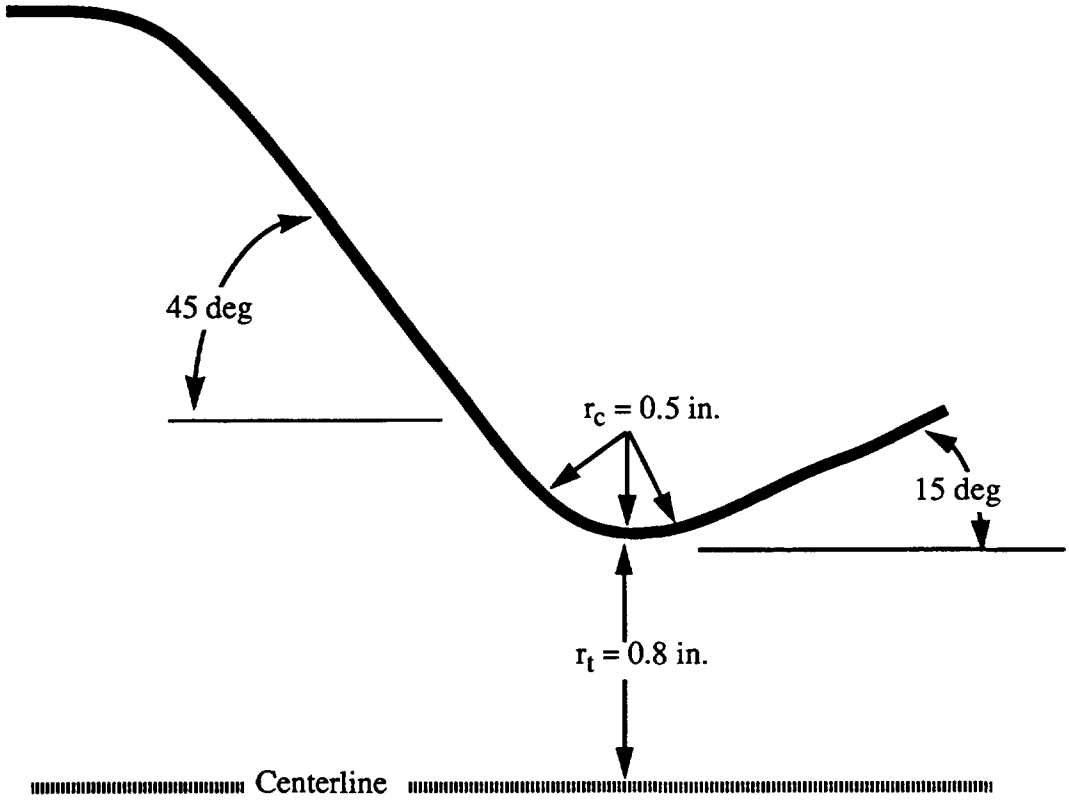

Figure 25. Schematic of small radius of curvature nozzle tested at JPL.

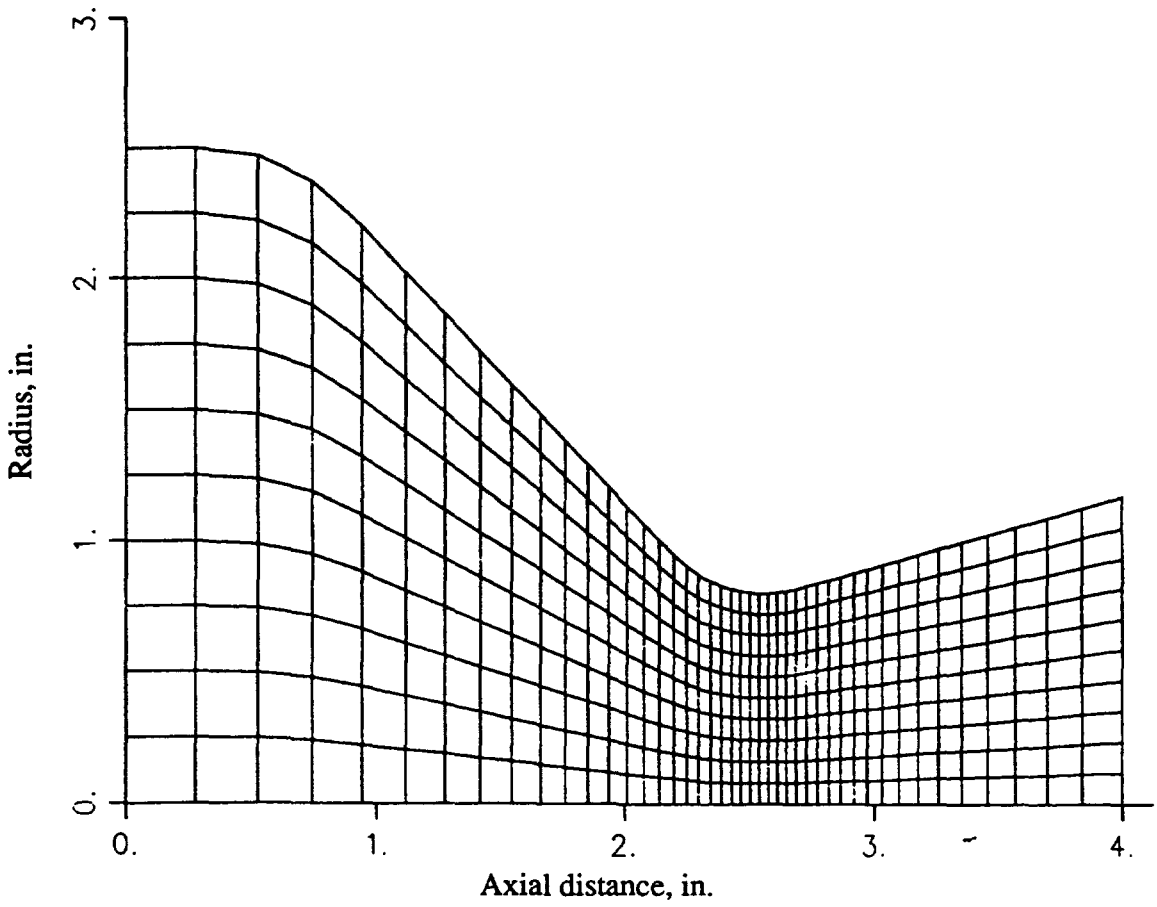

Figure 26. 45X11 grid used for JPL transonic nozzle flow study.

Table 6. JPL nozzle boundary conditions.

Boundary	Boundary conditions
Inlet	Constant-η reference plane $P_o = 70$ lbf/in.^{2} $T_o = 540$ R $v = 0$ Dry air
Exit	Constant-η reference plane $\frac{\partial \omega_i}{\partial \xi} = 0$
Wall	Constant-ξ reference plane $V_n = 0$ $\frac{\partial T_o}{\partial \eta} = 0$ $\frac{\partial P_o}{\partial \eta} = 0$ $\frac{\partial \omega_i}{\partial \eta} = 0$
Centerline	Constant-ξ reference plane $v = 0$ $\frac{\partial T_o}{\partial \eta} = 0$ $\frac{\partial P_o}{\partial \eta} = 0$ $\frac{\partial \omega_i}{\partial \eta} = 0$

In Figure 27, a comparison of predicted Mach number contours, using the reference plane characteristic method, the bicharacteristic method, and experimental measurements is shown. The numerical predictions of the reference plane characteristic method are represented by dashed lines, while the solid lines represent predictions using the bicharacteristic method. When followed along contours originating at the centerline, the shaded contours, solid lines, and experimental measurements, are all near the same origination point from which one can track subsequent disparities in the interior flowfield.

Excellent agreement between experimental measurements and numerical predictions using the present reference plane characteristic method is observed, especially in the transonic region. In the supersonic region, the prediction of the compression wave that originates at the tangency point between the downstream circular arc and the conical nozzle is modelled reasonably well along the wall, although the flow is extensively diffused in the interior of this region. Further, it is observed that the slight streamline curvature between the nozzle centerline and the adjacent interior grid points is predicted in the supersonic region. In general, the results of the reference plane characteristic method appear to predict results at least as well as the bicharacteristic method.

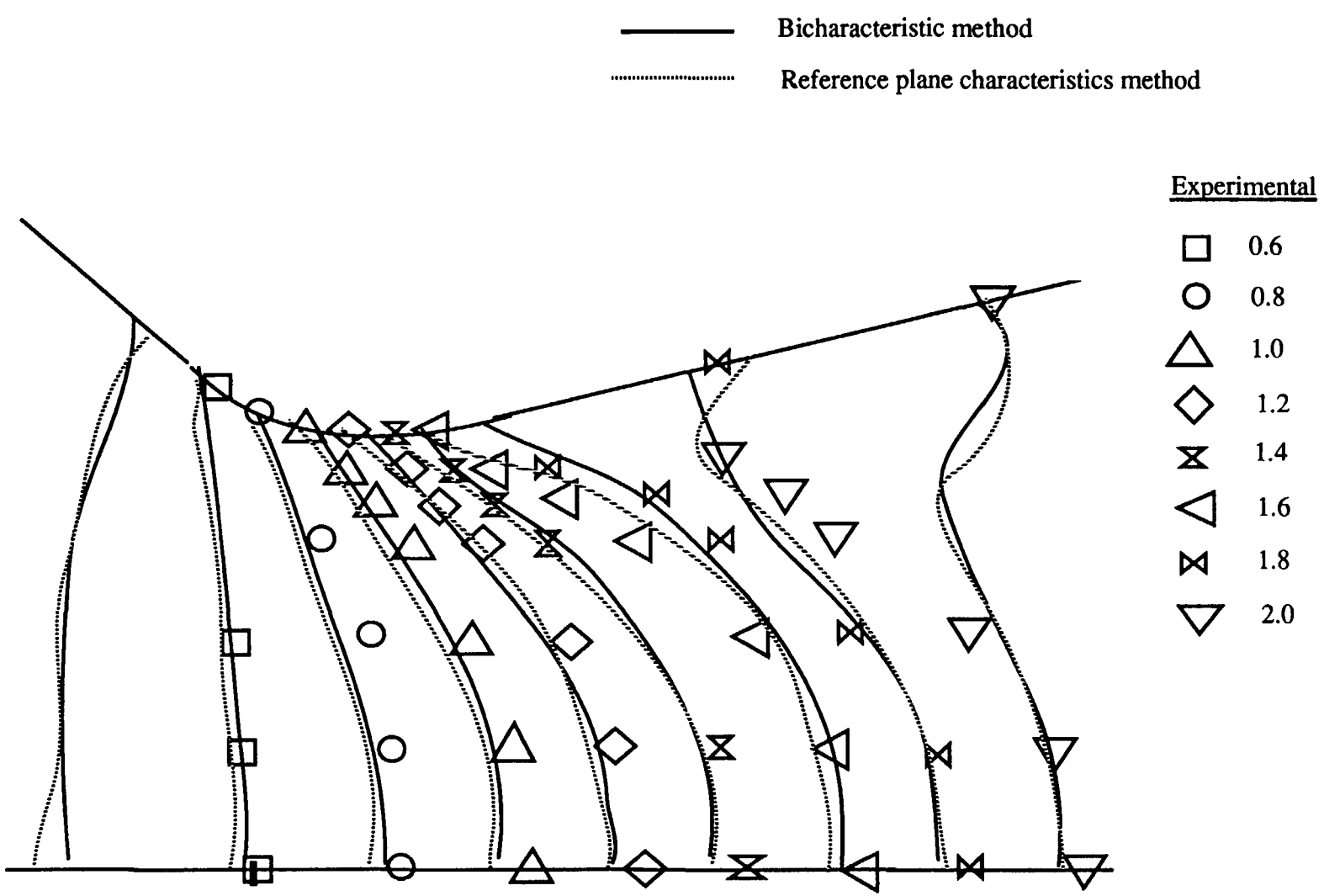

Figure 27. Comparison of Mach number contour predictions and experimental measurements for the JPL nozzle.

SECTION 7

DEMONSTRATION STUDIES

The cumulation of a diverse set of concepts and models intended to ultimately improve the predictive capabilities for a chemical rocket engine is demonstrated in this section. For illustrative and demonstrative purposes, three unique hydrogen-oxygen chemical rocket systems are examined. First, a high area ratio (1030:1) rocket nozzle will be analyzed and discussed in detail. The future application of such a nozzle is envisioned to include orbital transfer, lunar, and planetary missions. The uniqueness of the high area ratio nozzle is that it represents a very high performance rocket nozzle, and it has an extensive experimental database that includes performance, heat flux, and static wall pressure measurements. Further, the nozzle is one with which the author is very familiar, having been involved in the reporting of the experimental data. A second hydrogen-oxygen rocket engine of current interest is a low thrust (25 lbf) engine that is being envisioned for satellite thruster applications and for the orbital maintenance of a man-tended space station. The uniqueness of this nozzle concept is that it is extensively film cooled with hydrogen, and it operates at an overall stoichiometric mixture ratio while having an oxygen/hydrogen mixture ratio of 20 in the core of the engine. This nozzle concept has also been extensively tested. Engine performance, global heat transfer, and static wall pressure measurements are available for comparison. The final configuration studied is a transpiration cooled plug and spool rocket engine. The uniqueness of this configuration is that a discrete section of the rocket engine has hydrogen coolant transpired along the wall. Hydrogen coolant mass flow rate and wall temperatures were measured in this experiment.

A complete discussion of the nozzle geometries, operating conditions, modelling techniques and assumptions employed, and a comparison of experimental results and numerical predictions follows.

7.1. 1030:1 High Area Ratio Nozzle

The high area ratio hydrogen/oxygen rocket nozzle illustrated in Figure 28 (References 31 to 33) was tested at the NASA Lewis Research Center. Gaseous hydrogen and oxygen were injected into a combustion chamber that had a subsonic area ratio of 4.22. In the chamber, the propellants were burned to near completion, with the combustion efficiencies in each test ranging from 93 to 99 percent. The flow then expanded through the converging-diverging nozzle and was exhausted into a diffuser where the pressure was partially recovered. Following the cooling of the exhaust gasses by a water spray, the non-condensable gasses were entrained by nitrogen driven ejectors and exhausted into the atmosphere. The diffuser inlet and the complete rocket nozzle assembly were contained within a vacuum test capsule, as illustrated in Figure 29.

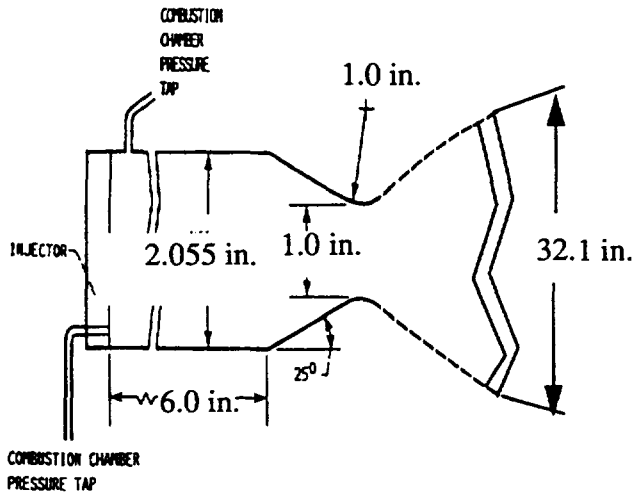

Figure 28. High area ratio nozzle test program conducted at NASA LeRC.

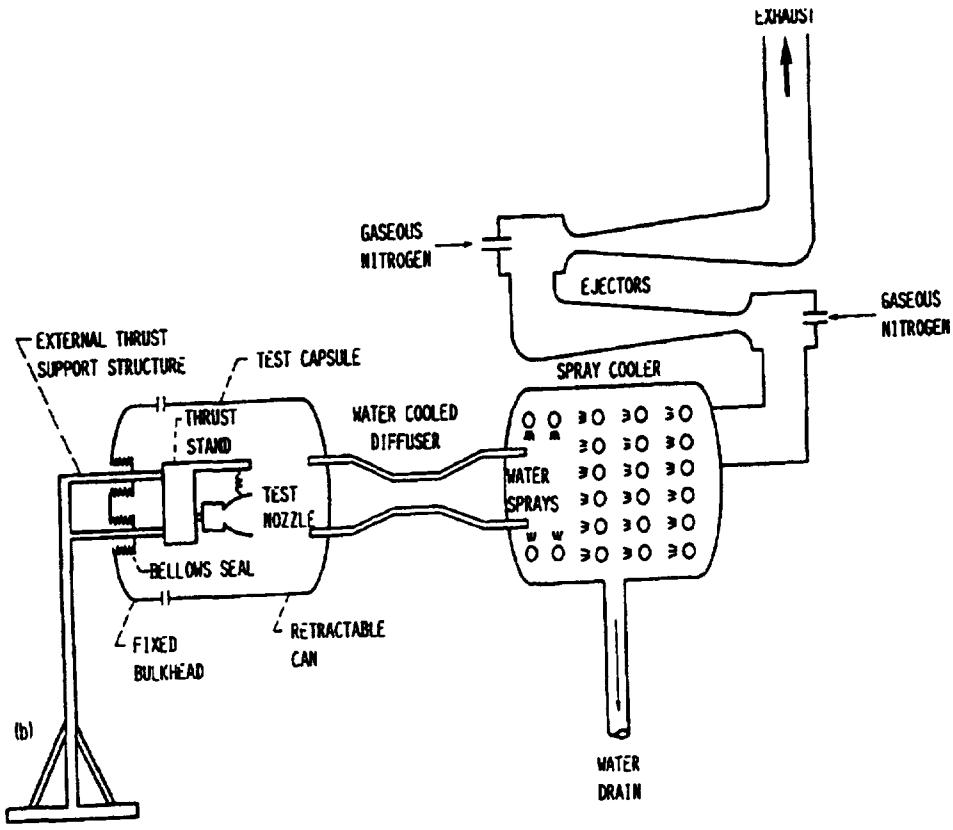

Figure 29. Rocket engine test facility used for evaluation of 1030:1 area ratio nozzle.

Experimental measurements of the nozzle thrust and mass flow rate were made. Further, wall static pressure and temperature measurements were made in the supersonic region of the nozzle. Heat fluxes were computed by employing the transient response of the nozzle thermocouples.

A detailed uncertainty analysis of the experimental program (Reference 34) indicated that the instrumentation uncertainties involved in the nozzle performance measurements were less than 1.3 %. However , the potential biasing effect of throat contraction or expansion during the testing of the nozzle was not accounted for.

The validity of assuming that axial conduction and radiation heat transfer were negligible in the measured heat transfer rates was examined during the experimental program (Reference 32) and estimated to amount to less than a 2 % error. An additional

investigation of the experimental data (performed for this study) indicates that the nonlinear variation in the temperature response of the thermocouples and the use of locally constant material properties in the data reduction may result in an additional data uncertainty/ bias of 3 %.

7.1.1. Analytical Assumptions

For analytical comparison, several important assumptions were made concerning the environment under which the rocket nozzle performed. The major assumptions regarding the flowfield included complete mixing at the nozzle inlet, the magnitude of the exhaust pressure at the nozzle exit, and laminar flow throughout the nozzle.

The chemical composition at the inlet of the nozzle section was assumed to be fully mixed and in chemical equilibrium, leaving the lack of complete mixing as a 'correction factor' that will be applied when engine performance is compared to experimental measurements. Furthermore, the existence of the trace species of monatomic and diatomic oxygen were neglected since the flow was very fuel rich and predictive results from a one-dimensional equilibrium flow analysis indicated that the effect of these trace species was negligible, resulting in less than a 15 degree R change in the stagnation temperature of the nozzle and less than a 0.1 % difference in specific impulse.

The exhaust pressure at the nozzle exit is an important parameter as the nozzle could experience some level of 'boundary layer feedback' where the subsonic flow region of the boundary layer is affected by the ambient pressure at which the nozzle operates. In turn, this can affect the pressure on the nozzle wall for some distance upstream of the nozzle exit plane. Since the nearest static pressure tap on the nozzle was located 2.7 inches from the exit, a small extrapolation (4.4 %), using the interior nozzle static pressures was required to establish the back pressure at which the nozzle was operating. It should be noted that this back pressure was 30 % lower than the capsule pressure, thus indicating that the nozzle was somewhat overexpanded.

The nozzle flowfield was also assumed to be laminar throughout. Extensive studies and correlation with experimental and analytical predictions indicate that the rapid acceleration of the exhaust gasses in the throat region of the nozzle 'laminarizes' the flowfield

(see Reference 32). Additional studies have indicated that the laminarized profile is stable throughout the supersonic region of the nozzle (Reference 35). Since the transonic and supersonic regions of the nozzle are the area of greatest concern, the assumption of laminar flow throughout the nozzle is reasonably justified.

7.1.2. Boundary Conditions

The boundary conditions applied in the Tethys code are presented in Table 7. The reference plane characteristics method (MOC) was employed along all of the boundaries, including the no-slip wall boundary. The wall temperature distribution employed for this analysis, illustrated in Figure 30, was based on experimental measurements and interpolation when possible, and was based on engineering judgement in regions outside of the experimentally measured area. The discontinuous temperature slopes observed near the throat region exist due to the application of a ceramic coating in this region only.

Table 7. Boundary conditions applied to the LeRC 1030:1 nozzle.

Inlet	Exit	Centerline	Wall*
P_0 = 360.0 lbf/in.^{2}	MOC*	MOC	MOC
h_0 = −15 Btu/lbm	MOC	$\partial h_0/\partial \eta = 0$	u = 0
v = 0	MOC	v = 0	v = 0
MOC	MOC	$\partial s/\partial \eta = 0$	T = T(x)
Chemical equilibrium*	MOC	$\partial \omega_i/\partial \eta = 0$	$j_i = 0$
* The inlet mass fractions are: ω_{H_2} = 0.093302 ω_H = 0.003052 ω_{OH} = 0.020253 ω_{H_2O} = 0.883393	*At subsonic contravarient velocities, static pressure is specified: P_{Exit} = 0.0264 lbf/in.^{2}		* For a free slip wall, the boundary conditions used are discussed in Section 4.4.

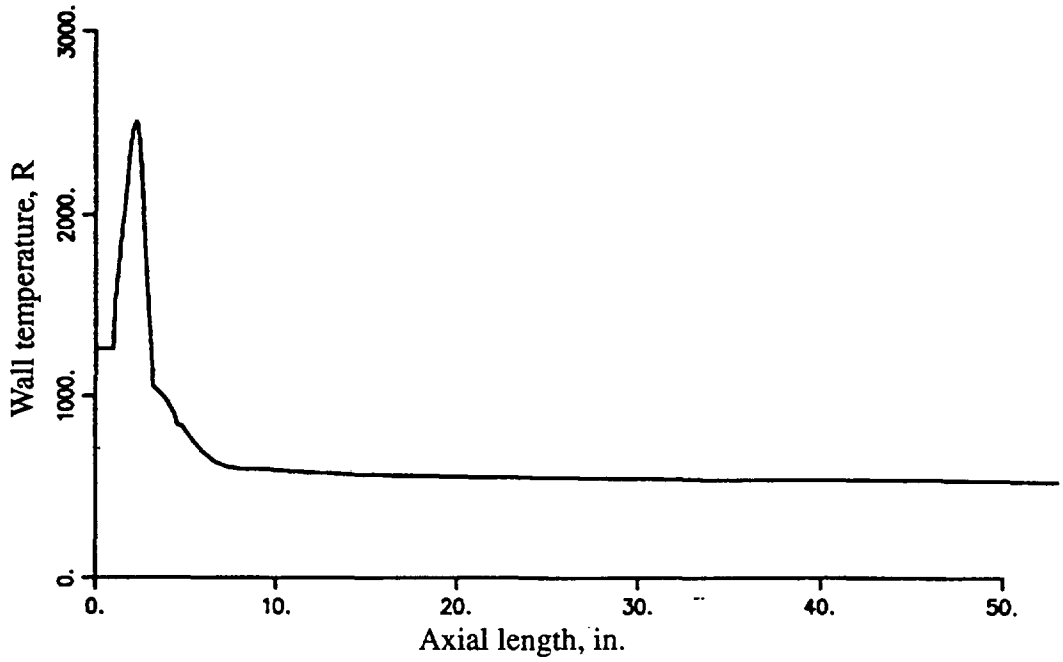

Figure 30. Wall temperature distribution for the high area ratio rocket nozzle analysis.

7.1.3. Computational Grid Used for Analytical Study

In Figures 31 and 32, the 91 X 51 computational grid used for the analysis of all three viscous test cases is presented. The inviscid flow analysis used a slightly more coarse computational grid, as discussed in the following paragraphs, but was nearly indiscernible to visual inspection.

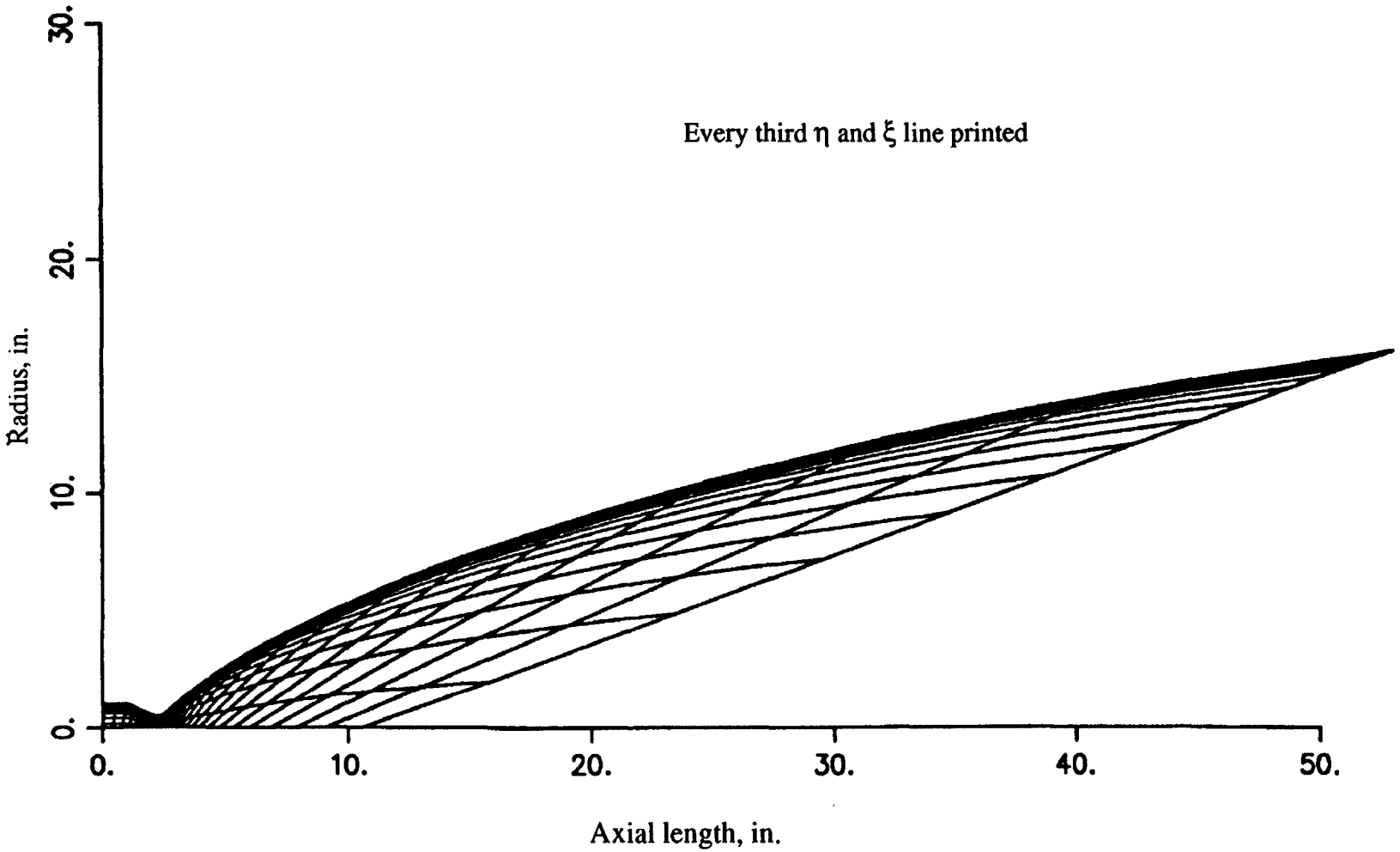

Figure 31. Computational grid employed for high area ratio nozzle analysis.

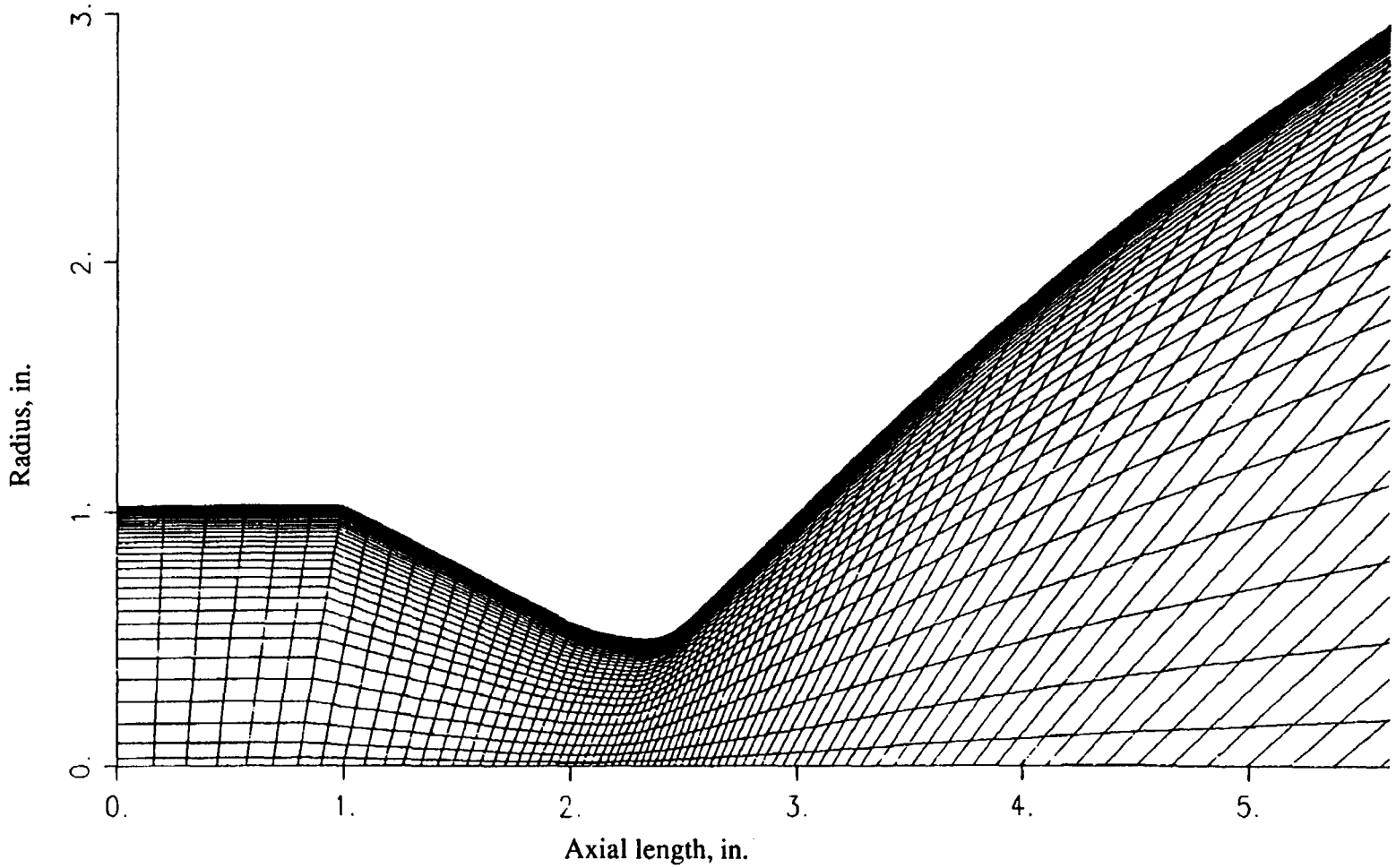

Figure 32. Throat region view of computational grid employed for high area ratio nozzle analysis.

The most noteworthy aspect of the computational grid is that the centerline length is significantly shorter than the nozzle length. This 'centerline coring' of the nozzle takes advantage of the fact that the supersonic flow can only propagate information within a discrete region (the domain of influence) and test runs with coarse grids indicated that the selected grid includes the complete domain of influence. The net result of this 'coring' in the centerline region was that it allowed significantly more grid points to be placed in physical locations where they would be of use to resolve the flowfield and the conditions that exist along the wall.

As illustrated in Figure 32, significant packing was applied along the nozzle wall and in the throat region. The grid is also slightly tighter packed along the nozzle centerline, and the grid packing along the wall is much tighter in the subsonic/transonic regions than near the nozzle exit.

The grid was generated by first determining the location of the ξ end points that would lie along the nozzle and along the centerline. This was done by the application of the transformation discussed in Anderson, Tannehill, and Pletcher (Reference 36), Equations (5.221) and (5-223), which are repeated below:

$$x = x_{Throat}\left[1 + \frac{\sinh\left[\tau\left(\xi - B\right)\right]}{\sinh\left(\tau B\right)}\right] \tag{7.1.1}$$

where B is defined as follows:

$$B = \frac{1}{2\tau}\ln\left[\frac{1 + \left(e^{\tau} - 1\right)\left(\frac{x_{Throat}}{x_{Total}}\right)}{1 + \left(e^{-\tau} - 1\right)\left(\frac{x_{Throat}}{x_{Total}}\right)}\right] \tag{7.1.2}$$

The packing factor, τ, was set equal to 8.0 along the nozzle wall and was equal to 6.0 along the nozzle centerline. For the centerline transformation, the total centerline length was equal to twenty percent of the actual nozzle length.

The transformation of the η grid lines was performed according to Equation (5-216) in Anderson, Tannehill and Pletcher (Reference 36).

$$\phi \equiv \frac{l}{l_{Total}} = \frac{a - b\left[\frac{a}{b}\right]^{1-\eta}}{\left[\frac{a}{b}\right]^{1-\eta} + 1} \tag{7.1.3}$$

where l is the distance along a computational line to the centerline, and the coefficients a and b are related to the packing factor, β, by the following relations:

$$a = \beta + 1, \quad b = \beta - 1 \tag{7.1.4}$$

For the viscous analyses cases (i.e., Test cases 2 to 4), the packing factor, β, was defined as a function of ξ through the following relation:

$$\beta = 1.001 + (1.01 - 1.001)\,\xi^3 \tag{7.1.5}$$

For the inviscid analysis, the packing factor, β, was set equal to 1.01.

The grid points established using the above grid transformation procedure were over-written in the region near the centerline (the nearest seven points) to allow somewhat greater packing near the centerline. The algebraic transformation applied to every grid point number, N, in this region is given below:

$$\phi = \left[\frac{N-1}{8-1} \right]^{1.5 - 0.5\left(\frac{N-1}{8-1}\right)} \tag{7.1.6}$$

Here ϕ is equal to the fractional distance from the centerline to the eighth point located away from the wall and along a constant ξ line.

7.1.4. Analytical Study and Results

Four different Tethys model simulations were performed to examine the significance of the modelling assumptions that were employed. These different analysis methodologies

are presented in Table 8. Here it is seen that the analysis comprised a spectrum from chemically frozen, inviscid flow to chemically reacting diffusing flow with thermal mass transfer and Dufour effects included.

Table 8. Various analysis methodologies employed for 1030:1 LeRC nozzle.

Tethys analysis	Test case 1	Test case 2	Test case 3	Test case 4
Chemical kinetics	No	No	Yes	Yes
Viscous flow	No	Yes	Yes	Yes
Ordinary diffusion	No	No	Yes	Yes
Thermal diffusion	No	No	No	Yes
Interdiffusion heat transfer	No	No	Yes	Yes
Dufour heat transfer	No	No	No	Yes

7.1.4.1. Mach Number Contour Predictions

In Figure 33 to Figure 40, the predicted Mach number contours for all four test cases are shown. The comparison between the inviscid and viscous cases (Test cases 1 and 2, respectively) in Figures 33 to 36 indicates that the Mach number at the exit for the inviscid simulation is slightly higher than the Mach number in the viscous analysis, which is an indication of the fact that the boundary layer, because of its displacement thickness, will tend to reduce the effective area ratio of the expansion, with a resultant decrease in the exit Mach number. Comparison between the frozen and kinetics throat region cases (Test cases

2 and 3, respectively) in Figures 35 to 38 reveals that the Mach number in the chemically frozen analysis is somewhat higher throughout the supersonic portion of the nozzle than in the chemically reacting analysis. Physically, this is as expected since the chemical reactions release sensible energy and tend to slow down the rate of expansion, a 'Rayleigh line' effect. Finally, the last two test cases which are shown in Figures 37 to 40, which are distinguished only by thermal diffusion and Dufour heat transfer effects, have extremely similar Mach number profiles.

Close inspection of the inviscid analysis case shown in Figures 33 and 34 indicates that the flow near the wall of the nozzle in the supersonic region of the flow undergoes a large amount of compression. The result of this compression in the supersonic region of the nozzle is that the Mach number contours are nearly parallel to the wall.

The Mach number contours along the centerline in the supersonic region of the flow are retarded. This is possibly because of the computational grid employed for the analysis, as the constant ξ lines go from left -to- right as the physical location goes from the centerline to the wall. On the other hand, the actual wavelines striking the center of the nozzle emanate from the leftward direction. As a result, the reference plane characteristic method uses an adjacent point that is well outside of its domain of dependence, and the predictive accuracy of the centerline boundary point would be expected to suffer. Fortunately, the analysis of the centerline region appears excellent in the transonic and slightly supersonic region, and the error that occurs near the end of the centerline region has little effect on the wall solution.

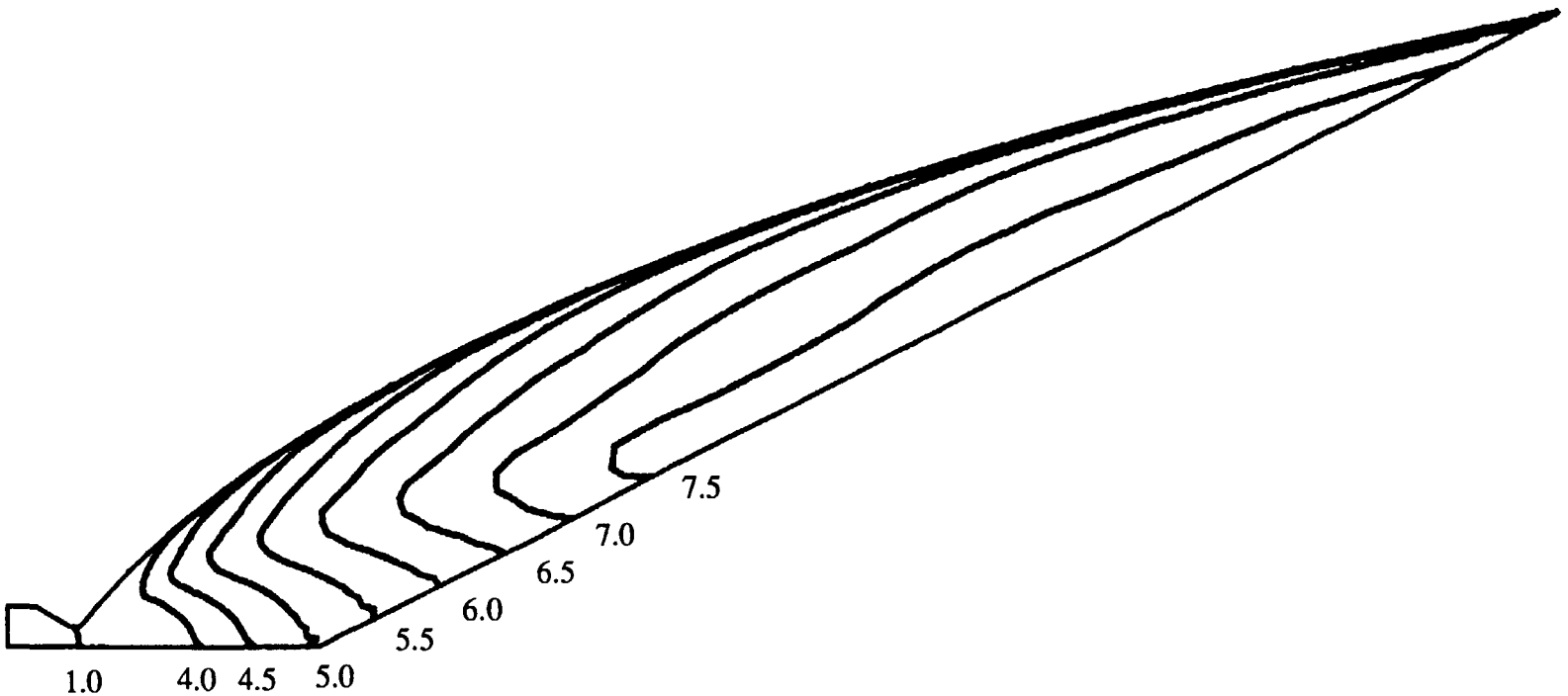

Figure 33. Mach number contour predictions for the LeRC high area ratio nozzle using an inviscid, chemically frozen analysis (Test case 1).

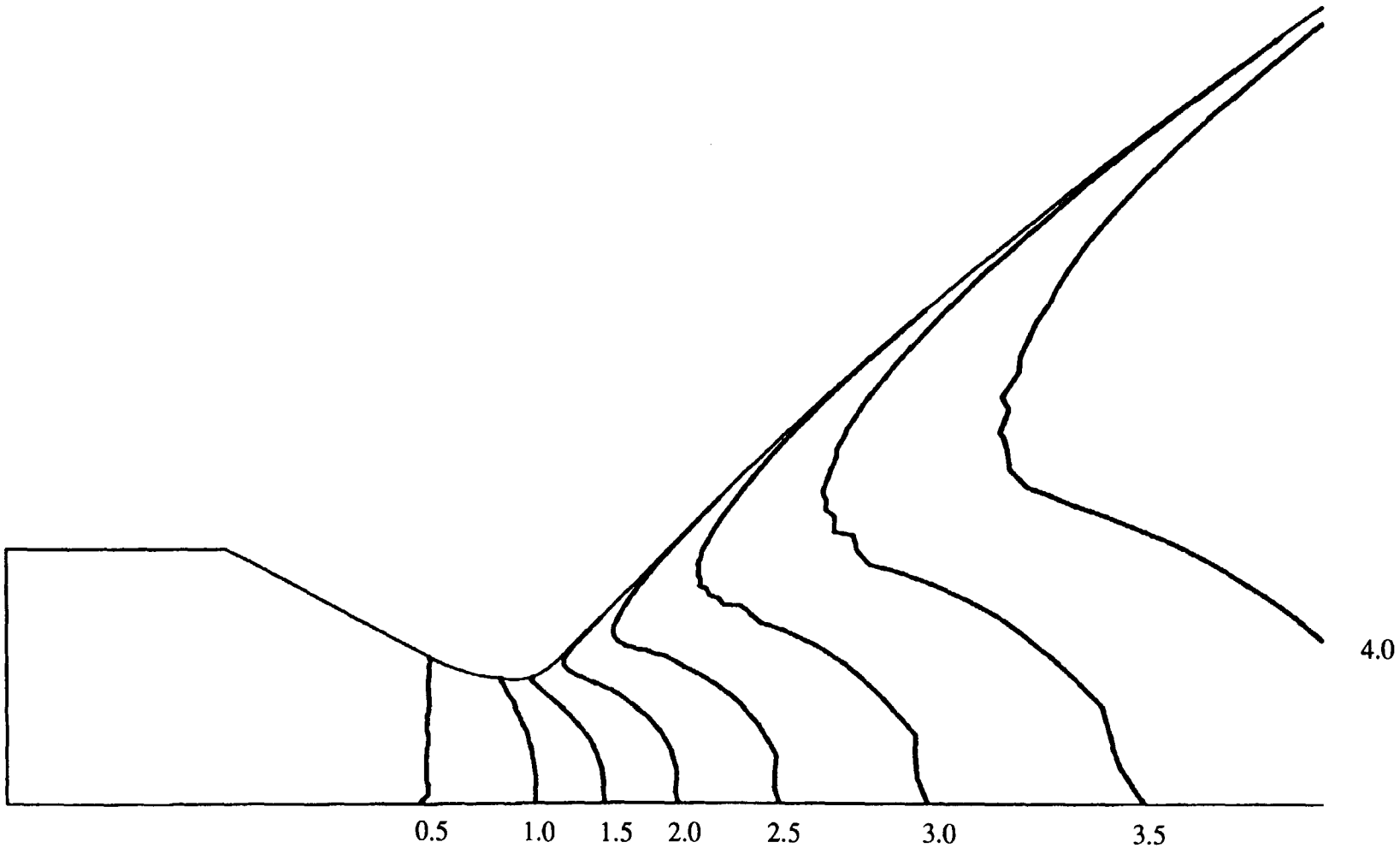

Figure 34. Throat region Mach number contour predictions for the LeRC high area ratio nozzle using an inviscid, chemically frozen analysis (Test case 1).

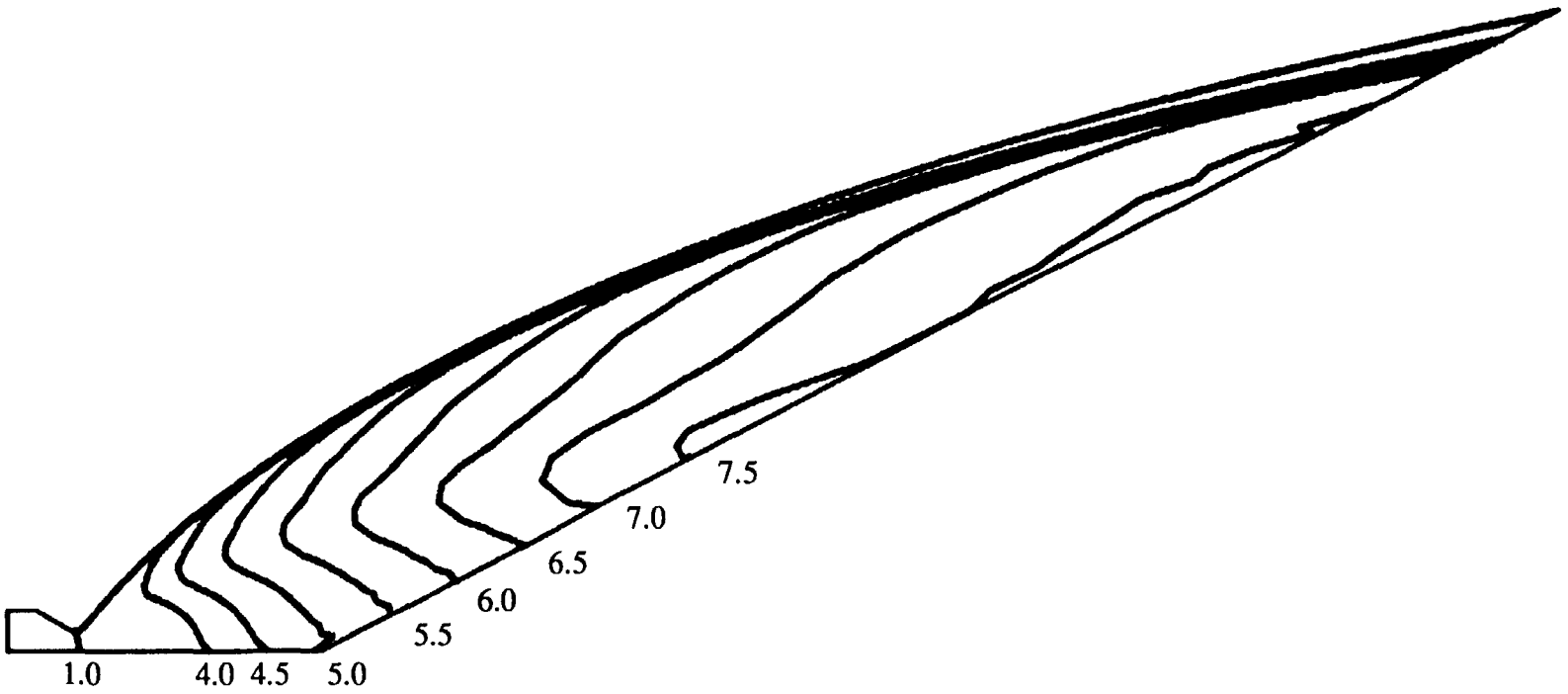

Figure 35. Mach number contour predictions for the LeRC high area ratio nozzle using a viscous, chemically frozen analysis (Test case 2).

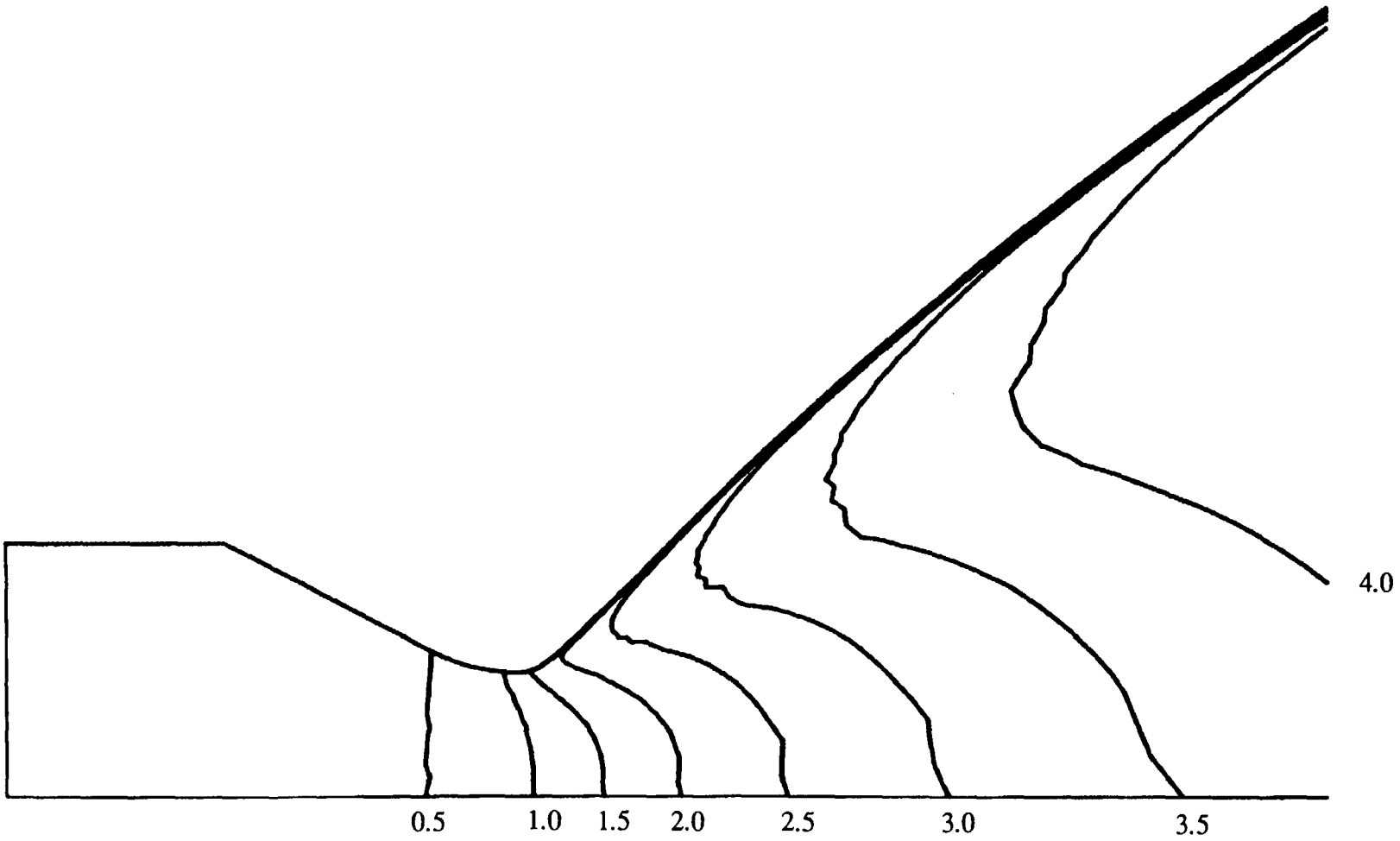

Figure 36. Throat region Mach number contour predictions for the LeRC high area ratio nozzle using a viscous, chemically frozen analysis (Test case 2).

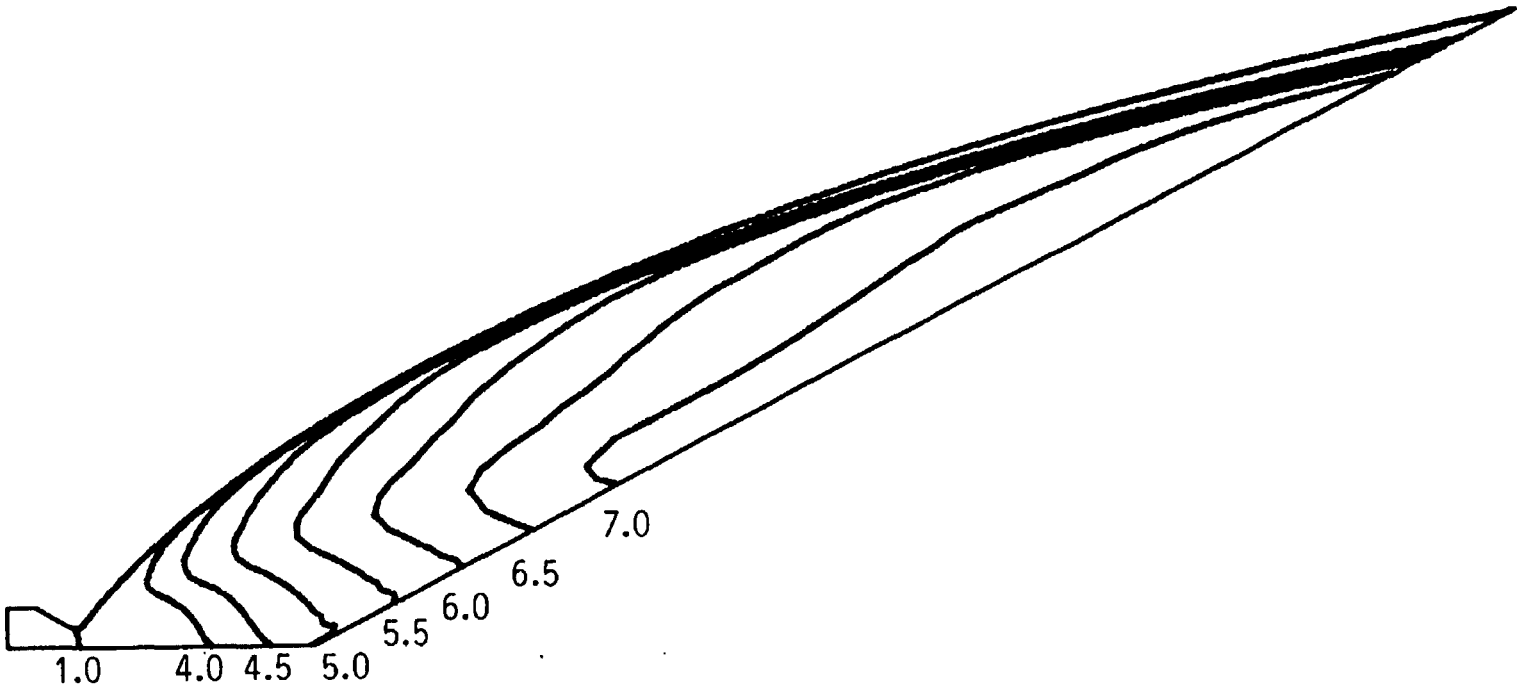

Figure 37. Mach number contour predictions for the LeRC high area ratio nozzle using a viscous, chemically reacting analysis (Test case 3).

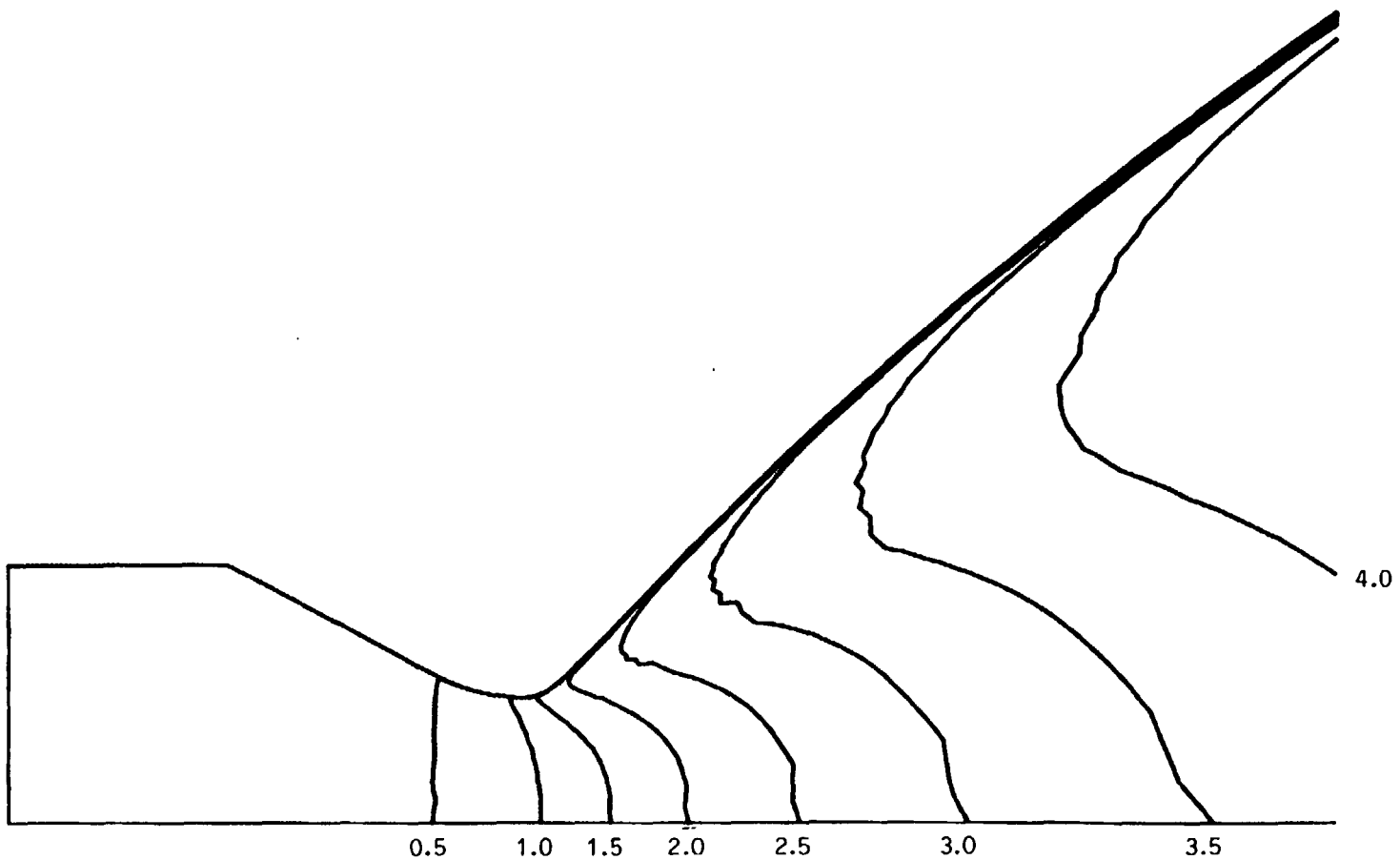

Figure 38. Throat region Mach number contour predictions for the LeRC high area ratio nozzle using a viscous, chemically reacting analysis (Test case 3).

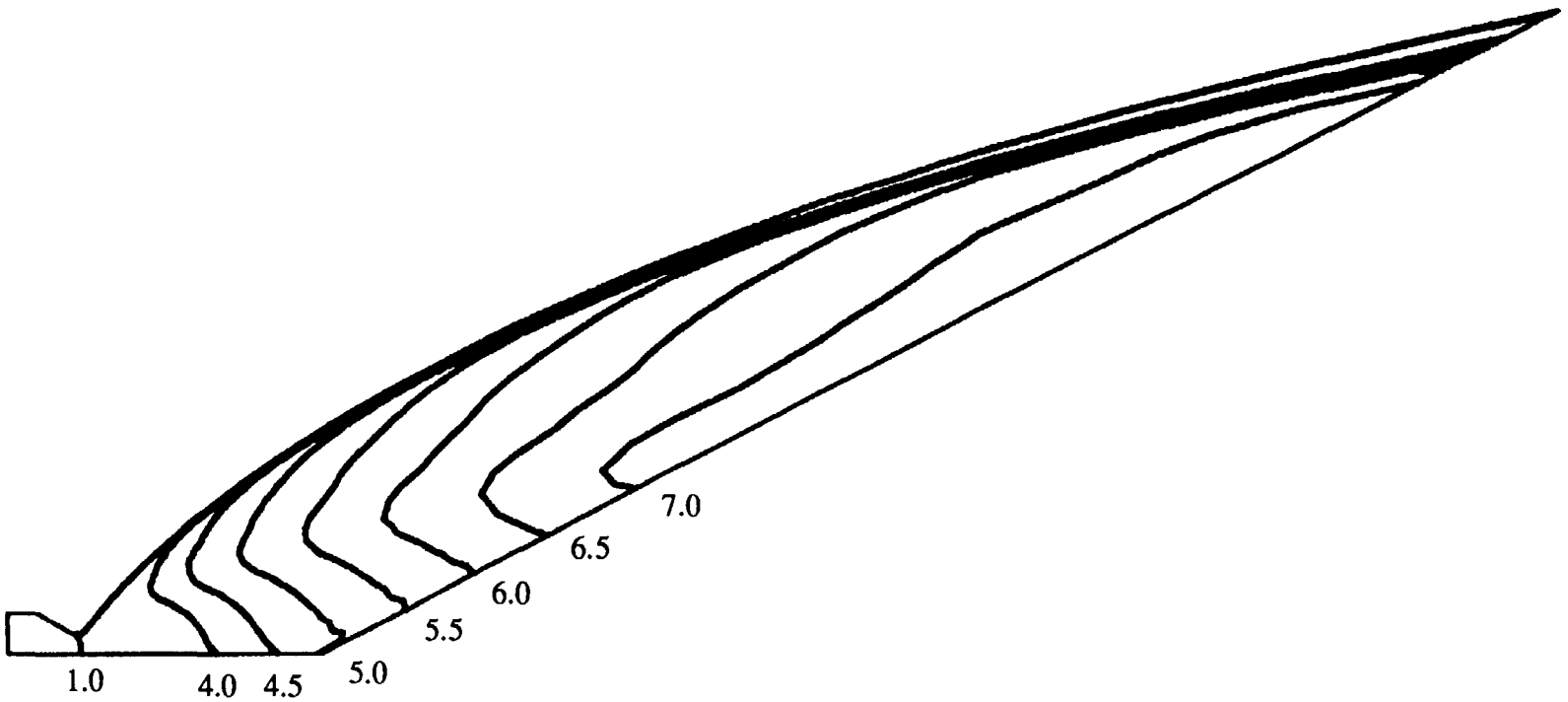

Figure 39. Mach number contour predictions for the LeRC high area ratio nozzle using a viscous, multiple diffusing, chemically reacting analysis (Test case 4).

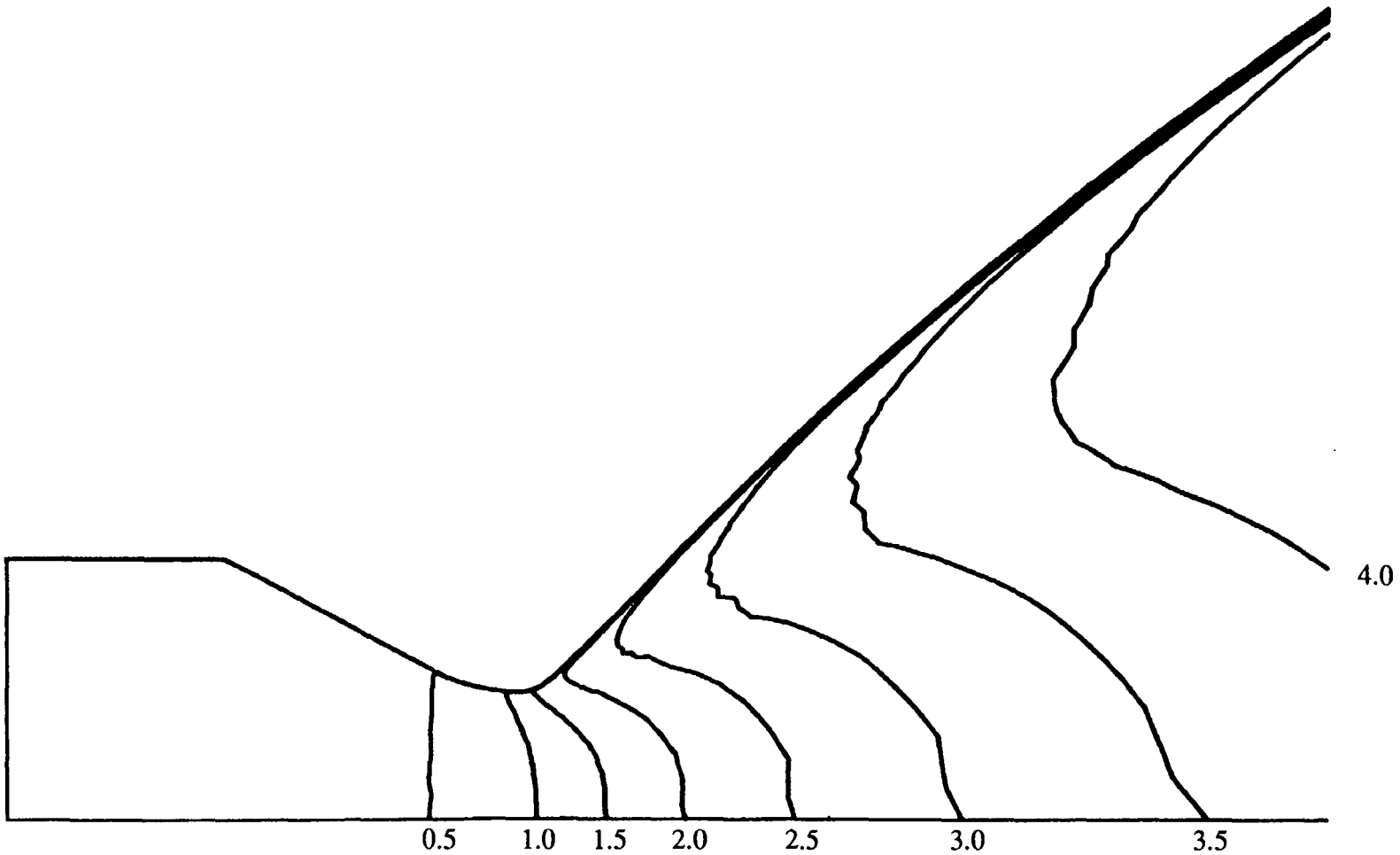

Figure 40. Throat region Mach number contour predictions for the LeRC high area ratio nozzle using a viscous, multiple diffusing, chemically reacting analysis (Test case 4).

7.1.4.2. Comparison of Experimental and Predicted Wall Pressures and Heat Fluxes

In Figures 41 and 42 a comparison of the predicted (Test case 4) and measured static pressure and heat flux distribution in the supersonic region of the nozzle (the only region where measurements were made) is shown. The predictions and measurements are in excellent agreement. The 'kink' in the slope at the last three wall pressure measurements shown in Figure 41 is correctly predicted.

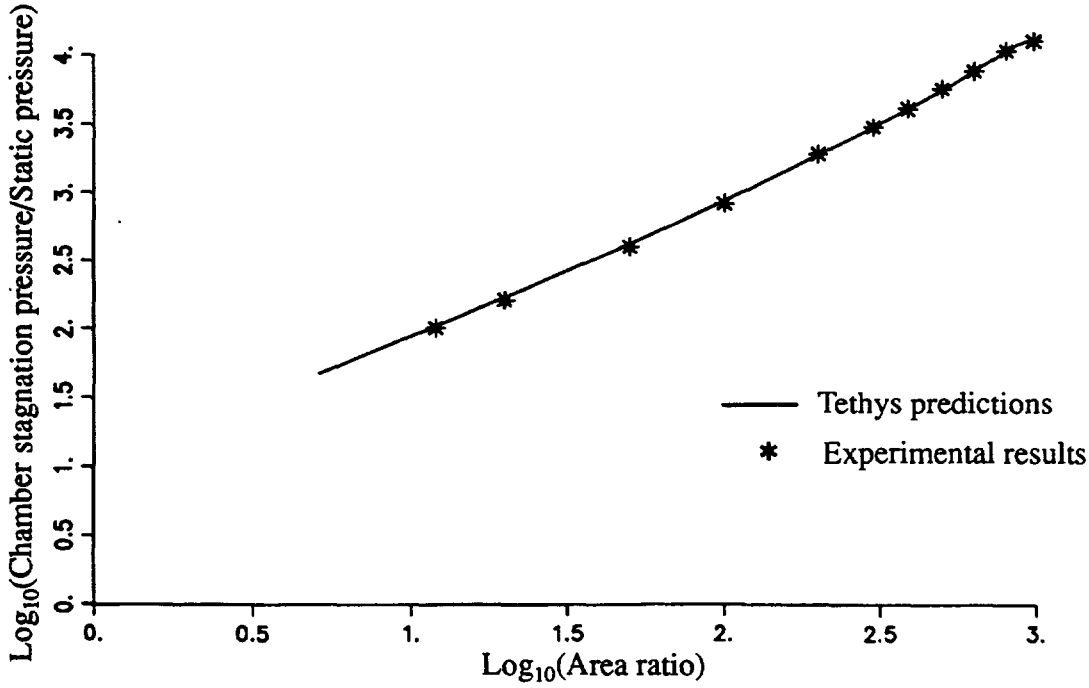

Figure 41. Comparison of experimental wall static pressure measurements and predictions from the Tethys model, Test case 4.

The heat flux profile shown in Figure 42 is observed to be in excellent agreement with experimental measurements, with a slight over prediction in the near throat region, followed by a slight under prediction, and then excellent agreement with experimental measurements as the exit of the nozzle is approached.

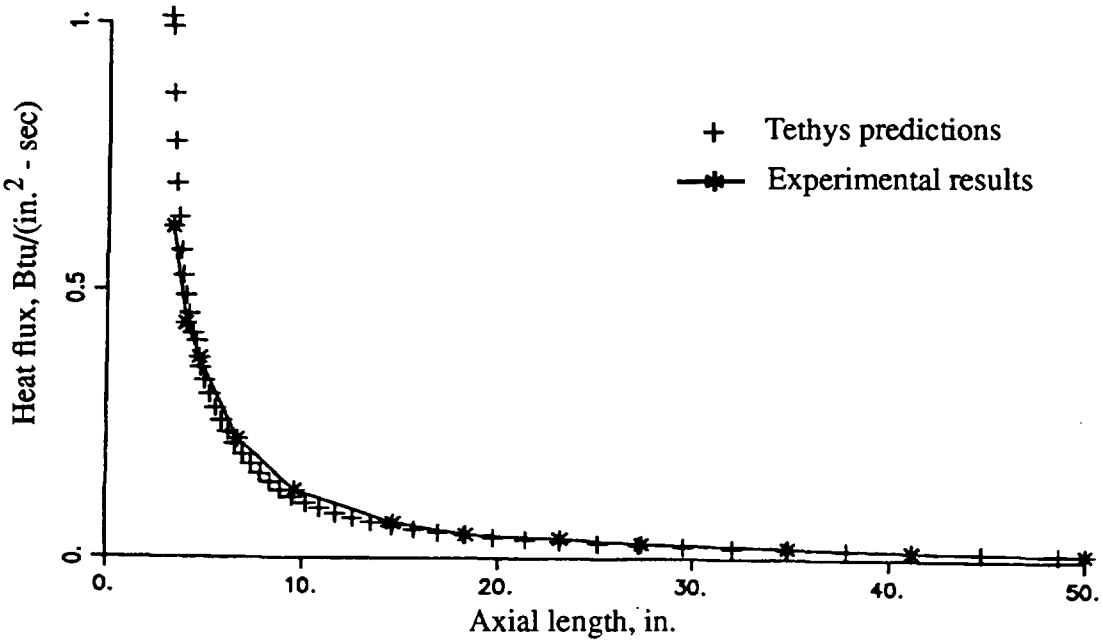

Figure 42. Comparison of experimental heat flux measurements and predictions from Tethys model, Test case 4.

In Figure 43, an examination is made of the differences in wall heat transfer predictions between the three analysis techniques employed, using Test case 4 as the baseline heat flux case. Here it is observed that the difference between all of the analysis cases is rather small, being less than or about a maximum difference of 25 % between Test cases 2 and 3 with Test case 4 tending to be within a 15 % difference of either of the other analysis cases.

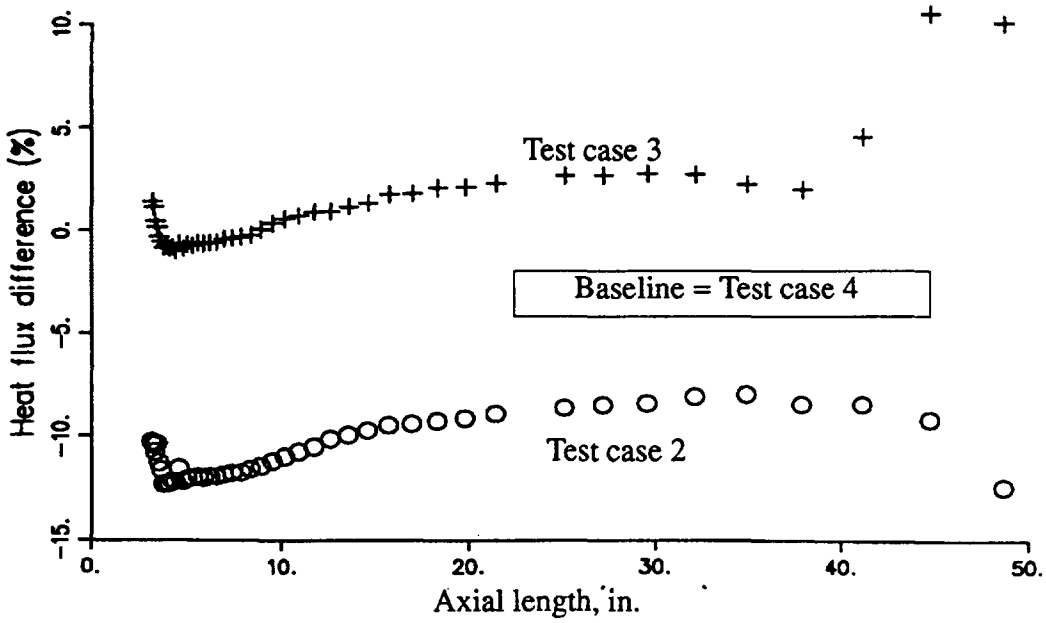

Figure 43. Comparison of the difference in heat transfer predictions between the three different viscous flow analyses.

7.1.4.3. Prediction of Hydrogen Mass Fraction Along the Wall

In Figure 44 the predicted distribution of diatomic hydrogen mass fraction along the wall of the LeRC 1030:1 nozzle is presented for all of the viscous nozzle analysis cases performed. As expected, the concentration of hydrogen along the nozzle wall for the frozen analysis (Test case 2) is constant throughout the length of the nozzle. On the other hand, the mass fraction of hydrogen for the chemically reacting, ordinary diffusion case (Test case 3) increases slightly at the inlet due to the recombination of monatomic hydrogen and then decays back towards the fully mixed, frozen mass fraction as the fluid undergoes a combination of species mixing and freezing of the chemical reaction mechanisms. The most pronounced difference in hydrogen mass fraction predictions is Test case 4, which considered Soret mass transfer. In this case it is seen that the hydrogen mass fraction immediately drops to 60 % of its inlet value, then slowly increases in mass fraction as the boundary layer thickens in the combustion chamber. As the nozzle begins to converge,

the hydrogen mass fraction continues to increase as the ceramic coating applied to the nozzle in this region serves to increase the wall temperature, with a corresponding decrease in the temperature gradient at the wall. The hydrogen mass fraction reaches a local maximum near the throat. Following this maximum, the hydrogen mass fraction rapidly decreases as the Soret mass transfer term strengthens as a result of the rapidly decreasing wall temperature in this region. As the ceramic coated section ends, a discontinuous change in the rate of change of the mass fraction of the hydrogen is observed, followed shortly by a local minimum in hydrogen mass fraction. Although the wall temperatures continue to decrease beyond this region, the hydrogen mass fraction begins to increase as the temperature gradients at the wall begin to decrease and the boundary layer thickens, essentially remixing the fluid. This partial remixing process continues as the nozzle temperature gradient continues to decay throughout the extent of the expansion region of the nozzle.

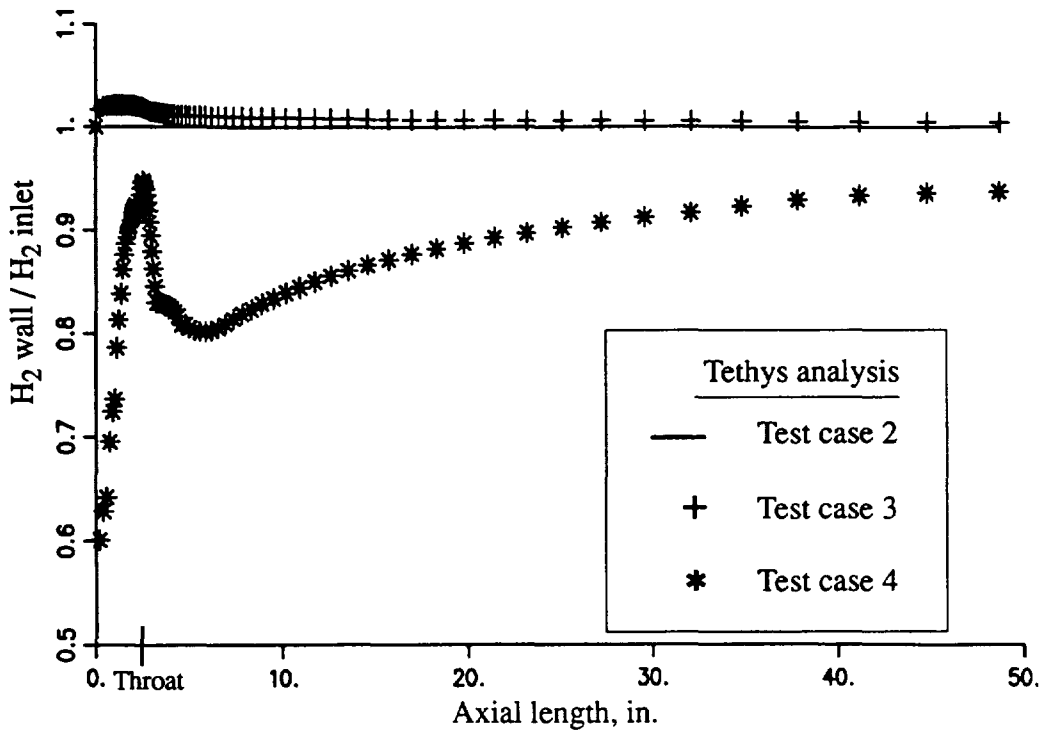

Figure 44. Hydrogen mass fraction predictions along the wall of the LeRC high area ratio nozzle.

7.1.4.4. Performance Predictions

In Table 9, a comparison between the predicted performance parameters for the four test cases is shown. The procedure used to determine nozzle thrust and mass flow rate correspond as nearly as possible to that recommended in the JANNAF nozzle analysis procedure. A complete discussion of the JANNAF procedure can be found in Appendix M. The method involves the numerical integration of the pressure forces and the axial momentum flux across the throat of the nozzle, which in this case was taken to correspond to the first line that extends into the divergent portion of the nozzle, and to sum the pressure and drag forces along the divergent surface of the nozzle.

Table 9. Tethys performance predictions.

	Test case 1 (Frozen, Inviscid)	Test case 2 (Frozen, Viscous)	Test case 3 (Kinetics, Viscous)	Test case 4 (Kinetics, Viscous, with Soret and Dufour effects)
Throat region thrust, lbf	354.04	351.97	349.59	349.51
Throat region mass flow rate, $\dot{m}$, lbm/sec	1.1343	1.1298	1.1115	1.1112
Nozzle divergent region wall pressure thrust, lbf	199.75	203.86	212.05	212.20
Nozzle divergent region shear forces, lbf	0.00	11.72	12.96	12.68
Total vacuum thrust, F_v, lbf	553.79	544.11	548.68	549.03
Specific impulse, $F_v/\dot{m}$, lbf-sec/lbm	488.22	481.60	493.6	494.1
Thrust coefficient, $F_v/(P_cA_T)$	1.959	1.924	1.941	1.942

Focussing primarily on the final performance parameters of specific impulse and thrust coefficient, several conclusions can be drawn. The first is that finite rate kinetic effects seem to have the largest single effect on nozzle performance, with the performance difference between the frozen and kinetic analyses (Test cases 2 and 3, respectively) being about 2.5 %, with the frozen case being lower. Examination of Test cases 1 and 2 reveals that the viscous effects account for a 1.4 % decrease in nozzle performance. The effects of multidiffusion mass and heat transfer account for a predicted increase in nozzle performance of 0.1 %, as evidenced by comparison to Test cases 3 and 4.

The mass flow rate predictions presented in Table 9 are also noteworthy. Examination of the predicted mass flow rates for Test cases 1 and 2 indicates that viscous effects result in a modest decrease in the mass flow rate through the nozzle. This is a boundary layer displacement effect. The primary difference in the predicted mass flow rates between Test cases 2 and 3 is that Test case 3 considered chemical kinetics in the analysis. Here it is seen that because of the release of sensible energy in the subsonic region of the nozzle in the chemically reacting analysis, the critical mass flow rate through the nozzle is about 2 % less than in the chemically frozen analysis. As would be anticipated, the mass flow rate predictions for Test case 3 and 4 are essentially identical.

7.1.4.5. Comparison of Experimental and Predicted Performance

In Table 10, a comparison between the predictions of the Tethys fluid flow model, Test case 4, and experimental measurements is shown along with previous performance predictions that have been made with other models. The TDK prediction method (Reference 1) involves an inviscid (one-dimensional/transonic/method of characteristics)-boundary layer type of analysis with chemical kinetics in the inviscid region while RPLUS (Reference 37) is a chemically reacting Navier-Stokes model which was executed using a 270X60 computational grid.

A comparison of the predictions to the experimental measurements indicates that the Tethys flow model is in far better agreement with experimental measurements than the other computational models. The difference between the predicted and the experimentally measured thrust coefficient and specific impulse are approximately an order of magnitude

smaller in the Tethys model than the TDK or RPLUS nozzle prediction methods.

Table 10. Experimental performance comparison of LeRC 1030:1 nozzle.

Performance criteria	Experimental measurements	Tethys difference, %	TDK difference, %	RPLUS difference, %
Thrust coefficient, $F_v/(P_cA_T)$	1.946	−0.21	−2.5	−1.4
Specific impulse, $F_v/\dot{m}$, lbf-sec/lbm	495.7	−0.33	−2.8	−3.7

Furthermore, since the experimental specific impulse reflects an inviscid, one-dimensional chemical equilibrium correction to account for incomplete combustion, the differences between measured and predicted values of thrust coefficient and specific impulse should be nearly the same, with the only difference being the discharge coefficient of the nozzle, which will be near unity. As seen in Table 10, the proximity to which both the thrust coefficient and specific impulse are in agreement with experimental measurements lends additional credence to the accuracy of the Tethys model.

7.2. 25 lbf Film Cooled Rocket Engine

A low thrust hydrogen/oxygen rocket engine was tested at the NASA LeRC as part of a nozzle contour evaluation program (References 38 and 39). The details of the nozzle geometry that will be used for comparative purposes is shown in Figures 45 to 48. In Figure 45, a schematic of the nozzle geometry and test apparatus is shown, while in Figure 46 a close-up view of the film cooling and injector apparatus is presented. In Figure 46 it is seen that a hydrogen film acts as a wall jet, the hydrogen being injected along the surface of the nozzle, and initially separated from the core by a solid walled sleeve. The sleeve from which the hydrogen film is injected consists of a channelled configuration with the channels merging into an axisymmetric configuration just prior to the end of the sleeve, as shown in Figure 47. A detail drawing of the throat region of the nozzle in shown in Figure 48.

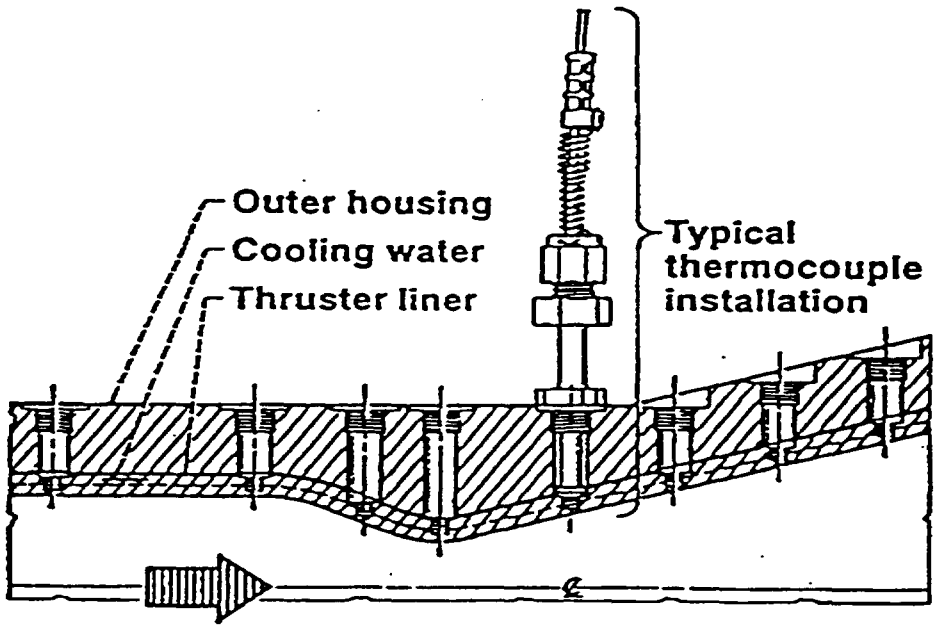

Figure 45. 25 lbf film cooled rocket hardware and instrumentation schematic.

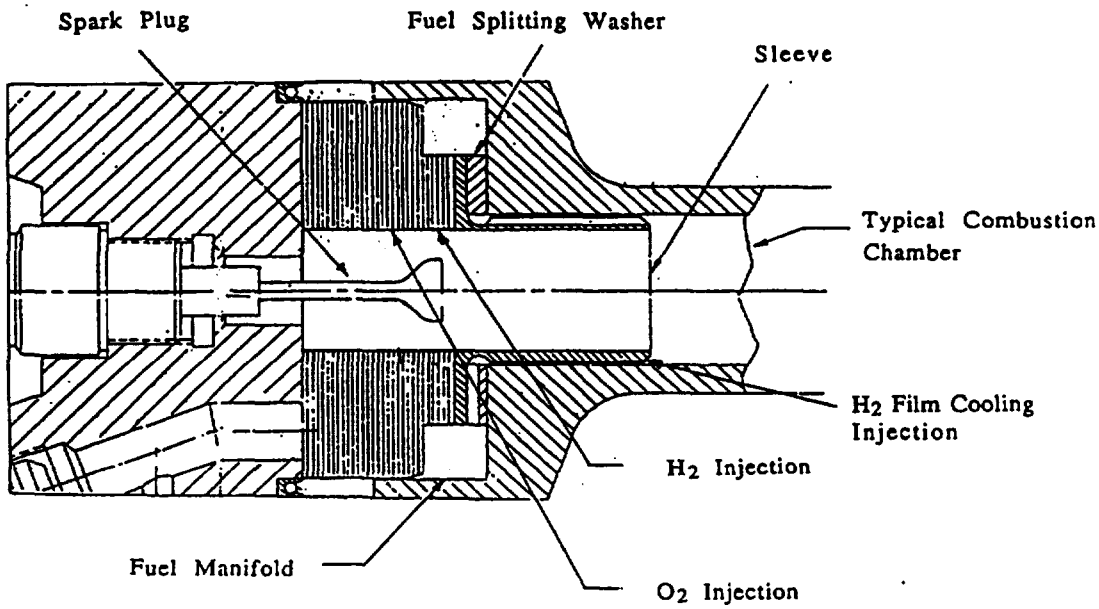

Figure 46. Injector and film cooled sleeve assembly.

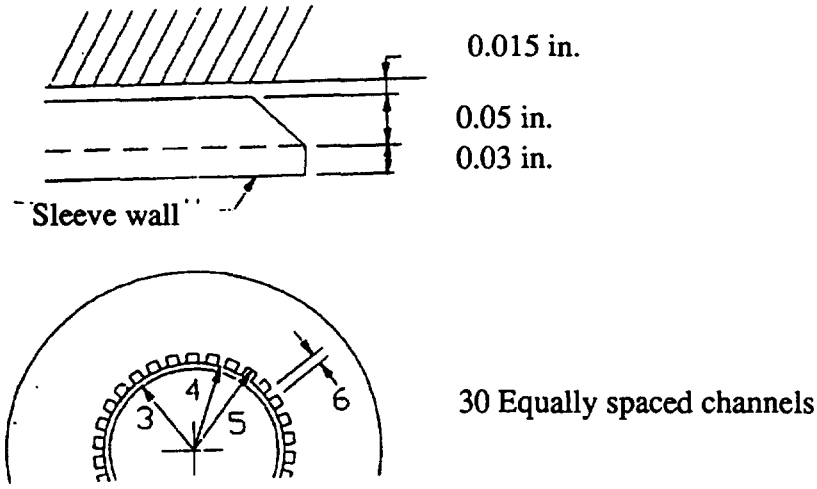

3 - Sleeve inside diameter = 0.811 in.

4 - Sleeve outside diameter = 0.870 in.

5 - Channel outside diameter = 0.969 in.

6 - Channel width = 0.055 in.

Figure 47. Film cooled sleeve geometry.

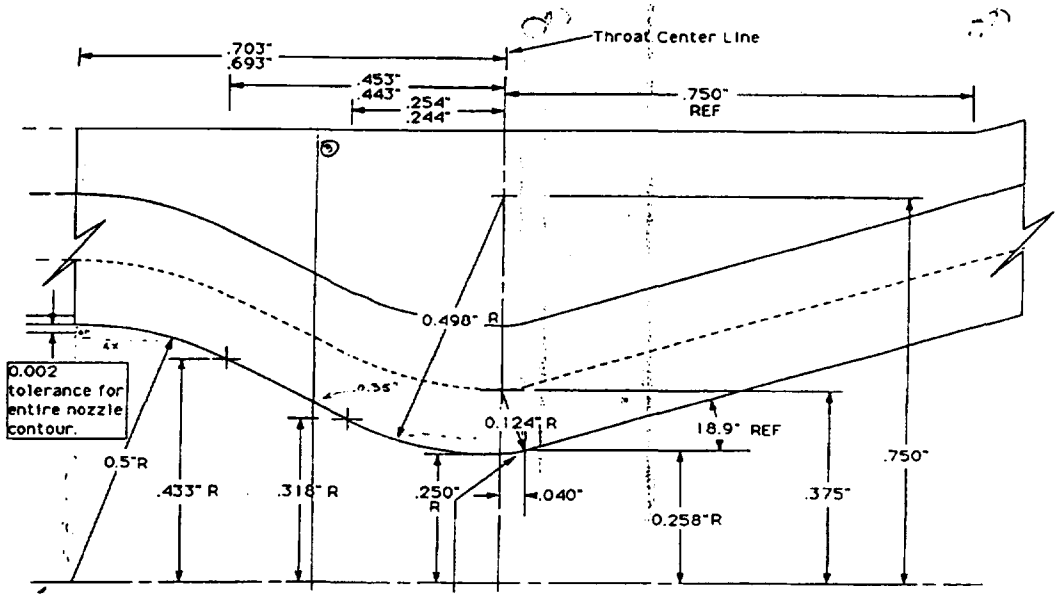

Figure 48. Detail drawing of the 25 lbf film cooled nozzle.

Similar to the LeRC 1030:1 nozzle, this nozzle was tested in a near vacuum environment. The rocket engine exhaust gasses flowed from the nozzle into a diffuser where the pressure was partially recovered. The final step in the removal of the exhaust gasses was accomplished by a combination of entrainment with ejectors and spray cooler condensation (Figure 49).

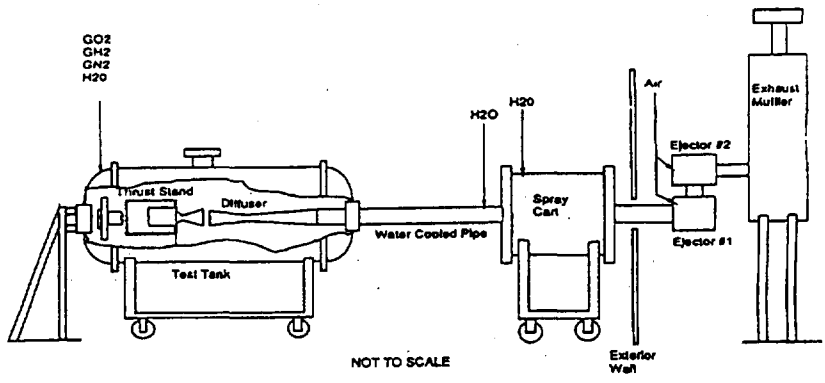

Figure 49. Experimental facility used for the 25 lbf film cooled nozzle tests.

The nominal operating conditions for the 25 lbf film cooled nozzle are given in Table 11.

.

Table 11. Nominal operating conditions for the 25 lbf film cooled nozzle.

Design parameter	Nominal value
Chamber pressure, lbf/in.^{2}	75.0
Thrust, lbf	25.0
Overall mixture ratio	8.0
Core mixture ratio	20.0
Propellant mass flow rate, lbm/sec	0.08

Experimental measurements of the following parameters were made:

- Nozzle thrust
- Fluid mass flow rate
- Combustion chamber pressure
- Nozzle wall static pressure
- Nozzle wall temperature
- Global heat transfer rate

7.2.1. Analytical Assumptions for the 25 lbf Film Cooled Nozzle

Three critical assumptions regarding the performance of the 25 lbf film cooled rocket were made so that analytical results could be generated in an expedient manner. The critical assumptions made were that the flow was turbulent and could be reasonably modelled by an algebraic turbulence model, that the composition of the core inlet fluid flow of the nozzle was known, and that the radial and tangential velocity distribution at the nozzle inlet was zero for both the film and the core flow.

The assumption of turbulent flow was based on the reasoning that the most crucial aspect of the analysis was the modelling of the film/core interaction in the combustion

chamber where the flow is almost certainly turbulent. On the other hand, the flow is also likely to experience a significant amount of laminarization, both along the wall and in the mixing layer, as it accelerates through the converging/diverging portion of the nozzle which would not likely be adequately modelled by an algebraic turbulence model. However, since the nozzle is short, the overall shear stresses acting on the nozzle will be relatively minor and contribute only a small degradation of the total nozzle thrust.

The assumption of a known chemical, thermal, and velocity distribution in the core inlet flow region was required. Because this was deemed to be a critical assumption in the analysis, two variations of the core flow inlet conditions were examined, one which assumed a fully mixed core and the other which was based on recent temperature and species measurements of a similar injector/combustor (Reference 40).

Because the hydrogen film traversed through a three-dimensional channel configuration prior to injection/mixing with the core flow, it is certain that some distribution of radial and tangential velocity will exist at the inlet region of the hydrogen film cooled section. However, these components were assumed to be of relatively minor importance compared to the axial component of the velocity. Similarly, the oxygen and hydrogen propellants in the core region of the combustion chamber are injected radially and are also subjected to the effects of a blunt spark plug ignitor. Under these boundary conditions, the core flow will undoubtedly have some distribution of radial and tangential velocity for a distance downstream of the region where the propellants are injected. Unfortunately, adequate modelling of these conditions would require a three-dimensional analysis which is beyond the capabilities of the Tethys model. Instead, the sensitivity of the nozzle performance to the extent of core mixing was examined.

7.2.2. Boundary Conditions for the 25 lbf Film Cooled Nozzle

The boundary conditions applied to the flowfield simulation are presented in Table 12. Several important and unique aspects of the boundary conditions employed are that the viscous, chemically reacting, reference plane characteristics method was employed at the inlet and exit boundaries with the exception of the solid wall region at the nozzle inlet. In this solid wall region, reference plane characteristics could not be used because the

turbulence model employed assumed that the distance from the wake producing body was relatively large. The characteristics technique employed along the nozzle centerline employed a chemically frozen, inviscid, waveline equation. It is also worthy of note that instead of the standard procedure of specifying the stagnation pressure at the nozzle inlet, the mass flux was specified, with the combustion chamber stagnation pressure that the nozzle was operating at being determined by the choking of the flow at the nozzle throat. Using this procedure of specifying the mass flow rates at the nozzle entrance, the flow split between the core and the film can be maintained exactly.

Table 12. Boundary conditions applied to the 25 lbf film cooled nozzle.

Inlet			Exit	Wall	Centerline**
Core	Sleeve wall	Film	-	-	-
MOC*	$\frac{\partial P}{\partial \xi} = 0$	MOC*	MOC*	$\frac{\partial P}{\partial n} = 0$	MOC
$\rho u = 20.42$	$u = 0$	$\rho u = 4.0193$	MOC	$u = 0$	$\frac{\partial s}{\partial \eta} = 0$
$v = 0$	$v = 0$	$v = 0$	MOC	$v = 0$	$v = 0$
$h_0 = -9.98 \frac{Btu}{lbm}$	$T = 1400$ R	$h_0 = 582 \frac{Btu}{lbm}$	MOC	$T = T(x)$	$\frac{\partial h_0}{\partial \eta} = 0$
Chemical equilibrium	$j_i = 0$	$\omega_{H_2} = 1.0$	MOC	$j_i = 0$	$\frac{\partial \omega_i}{\partial \eta} = 0$
*At the points nearest the sleeve wall, the pressure gradient was assumed to be zero			* At subsonic contravarient velocities, $P_{exit} = 0.15$ psia. **Near the nozzle exit, reflective boundary conditions were applied.		

The temperature distribution imposed on the nozzle wall was derived from interpolation of experimental data, where available, and is shown in Figure 50. The wall temperature at the exhaust of the nozzle was not measured and was estimated by assuming that the temperature at the nozzle exit was equal to the water temperature that was used for cooling the nozzle walls.

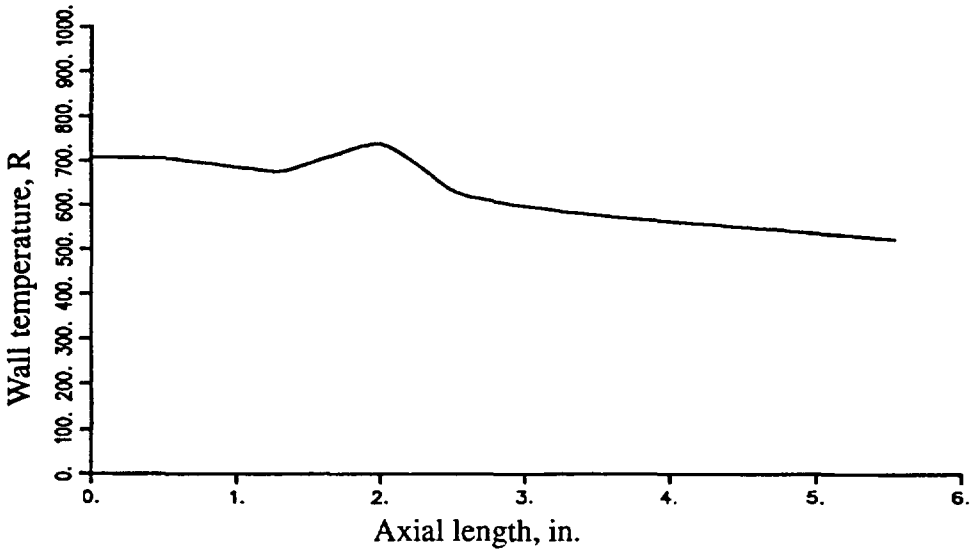

Figure 50. Temperature distribution used for the wall boundary condition of the Tethys simulation for the 25 lbf film cooled nozzle.

7.2.3. Computational Grid Used for the 25 lbf Film Cooled Nozzle Study

In Figure 51, the 91X51 computational grid used for the analysis of the 25 lbf nozzle is presented. Since one of the fundamental aspects of the performance of this nozzle was the effectiveness of the hydrogen film coolant to mix and react with the oxygen rich core, a relatively large percentage of the computational grid points is contained within the subsonic portion of the nozzle.

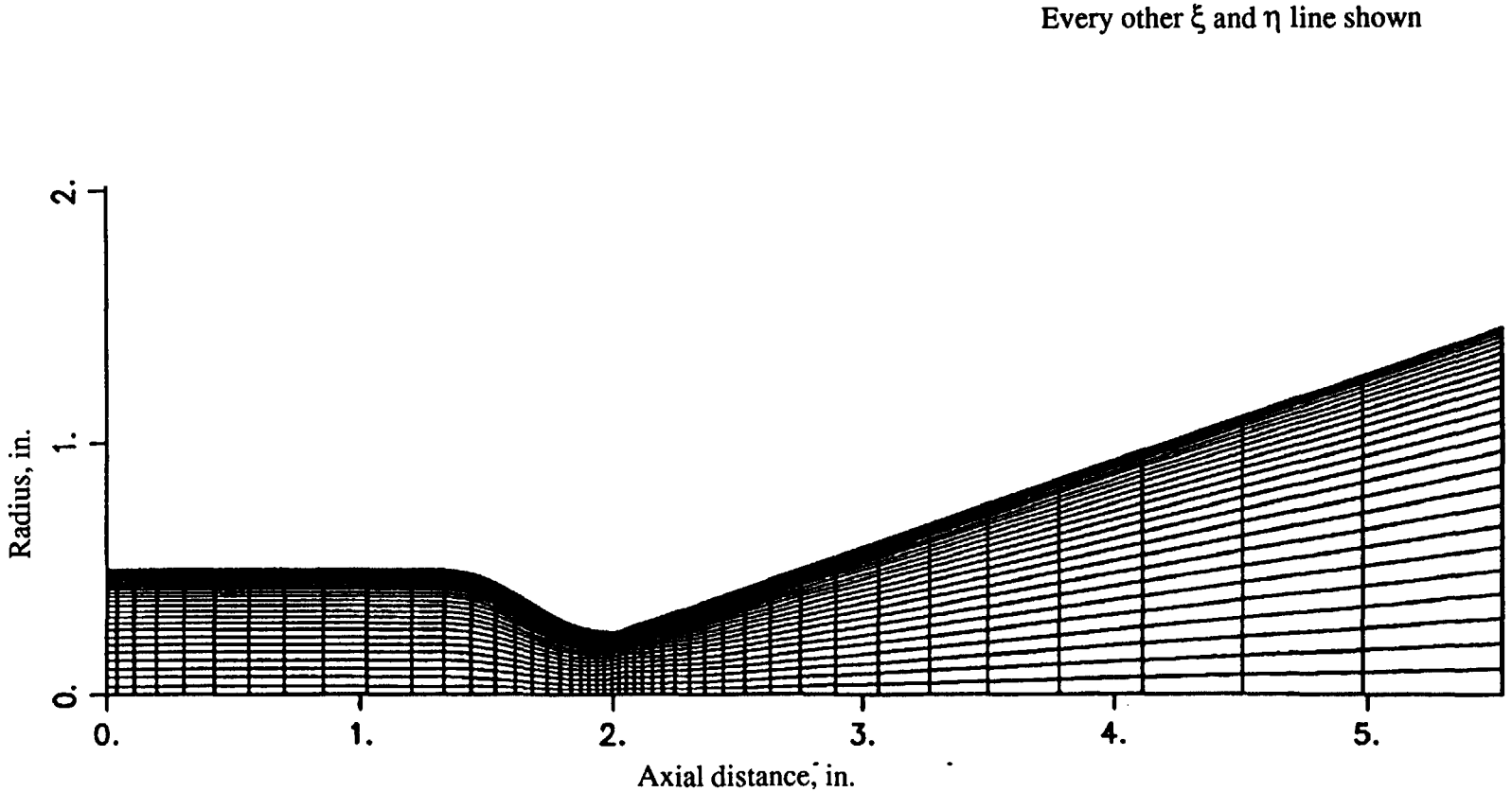

Figure 51. Computational grid employed for the 25 lbf film cooled nozzle analysis.

The grid was generated by using the techniques described below. For $1.2 \leq x \leq x_{Exit}$, 71 nozzle axial points were established using the following relation:

$$x = x_{Throat}\left[1 + \frac{\sinh\left[\tau(\xi - B)\right]}{\sinh(\tau B)}\right] \tag{7.2.1}$$

where B and τ are as defined in Section 6.1, with the packing factor, τ, used in the film cooled nozzle analysis being equal to 6.0. The total nozzle length and the distance to the throat are offset by 1.2 inches to accommodate packing in the combustion chamber section of the nozzle. For $0 \leq x \leq 1.2$, the first 20 grid points were determined through the following expression:

$$x = 1.2\left[\frac{N-1}{20}\right]^{1.5} \tag{7.2.2}$$

where N is the grid point number. The locations of the interior points were determined by extending a straight line from the centerline to the corresponding points established along the nozzle contour. The points along this line were packed near the nozzle wall using the following relation:

$$\phi \equiv \frac{r}{r_{nozzle}} = \frac{a - b\left[\frac{a}{b}\right]^{1-\eta}}{\left[\frac{a}{b}\right]^{1-\eta} + 1} \tag{7.2.3}$$

where $a = \beta + 1$, $b = \beta - 1$, and $\beta = 1.08$, except near the throat region (from node number 30 to node number 65), where the packing factor, β, was linearly (in computational space) reduced to a value of 1.02 at the throat.

7.2.4. Analytical Study of the 25 lbf Film Cooled Nozzle

Two different simulations were employed to examine the importance of stratified flow. One case assumed that the core of the flow was fully mixed and had an overall mixture ratio of 20. The other case assumed that the flow was highly stratified, as shown in Figure 52. The extent and profile of the core stratification was estimated by piecing together measurements on a similar injector (i.e., a square injector that operated at a core mixture ratio of 24, as discussed in Reference 40) which indicated that the centerline temperature of the core was about 3200 R and that the presence of hydrogen and oxygen was negligible near the sleeve wall. Applying these two pieces of information and further assuming that the temperature measurements were solely the result of incomplete mixing, a power law profile was generated.

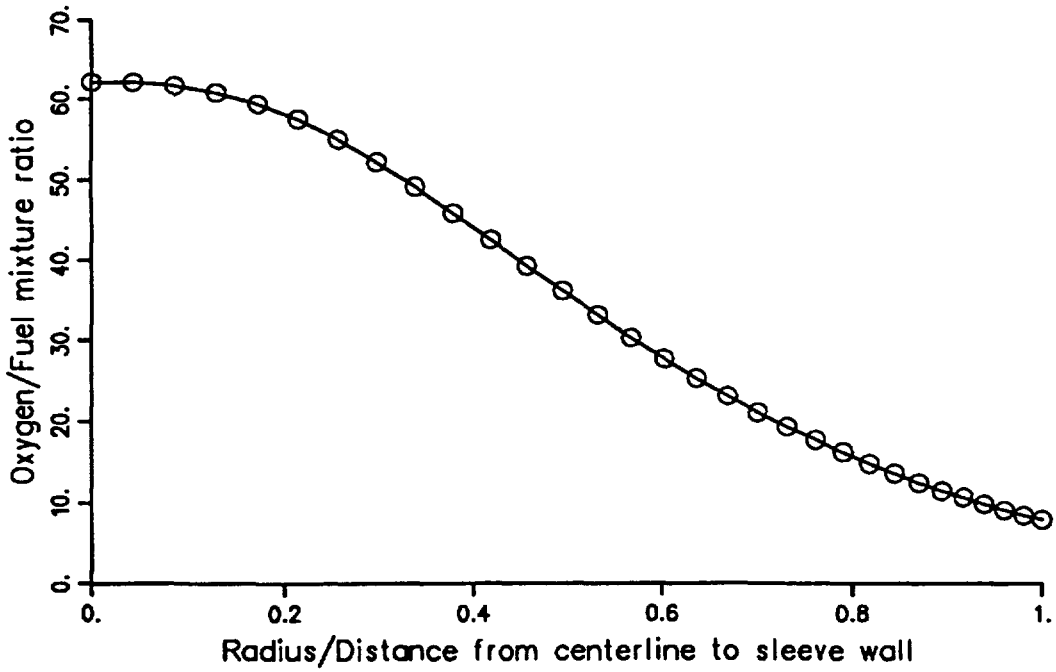

Figure 52. Oxygen to fuel mixture ratio profile assumed for the stratified core analysis.

Two cases are presented in Table 13. Since the modelling of the film/core combustion process was deemed to be an important consideration, chemically reacting fluid flow, with eight chemical reactions, was common to all of the analyses. Turbulent flow was

considered for both of the cases presented herein. Since the flow was taken to be turbulent and the primary intent of this study was to examine the mixing of the fluid core and the film, all mass diffusion terms and heat transfer modes were employed. Likewise, the turbulent Prandtl number used in this analysis corresponds to experimental measurements obtained in a free turbulent shear flow environment (Reference 41).

Table 13. Analysis methods used for the 25 lbf film cooled nozzle.

Tethys analysis	Test case 1 (fully mixed core)	Test case 2 (stratified core)
Number of species considered	6 (H_2O, H_2, O_2, OH, H, O)	6 (H_2O, H_2, O_2, OH, H, O)
Thermal diffusion	Yes	Yes
Interdiffusion heat transfer	Yes	Yes
Dufour heat transfer	Yes	Yes
Kinetics Number of chemical reactions	Yes 8	Yes 8
Turbulence	Yes	Yes
Artificial diffusion	Nonlinear, second order model, 100 % of recommended value.	Nonlinear, second order model, 100 % of recommended value.
Artificial diffusion added to MOC equations	Inlet-Yes Exit-Yes Centerline-Yes	Inlet-No Exit-Yes Centerline-Yes
Turbulent Prandtl number	0.5405	0.5405
Turbulent Lewis number	1.0	1.0

The algebraic turbulence model used in the film cooled nozzle simulation employed the Baldwin-Lomax inner region model and a free jet turbulence model in the outer region. The free jet turbulence model used in this analysis was one applied by Gortler

(Reference 42) for the derivation and verification of the velocity profile of a mixing layer:

$$\mu_t = 0.0014\rho\,(x + \Delta x)\,\Delta u \tag{7.2.1}$$

where the velocity defect, Δu, applied in this analysis corresponded, in an approximate manner, to the average velocity difference between the core and the film coolant at the inlet. For consistency, the velocity defect used for both cases was the same, 500 ft/sec. The distance, x, in the above correlation corresponded to the physical distance of a given point to the inlet, along a constant η line. The critical length calculation is offset by an additional distance, Δx, of 0.144 inches (0.012 feet). The value of this offset distance corresponds to the theoretical distance at which the thickness of the mixing layer would be equal to the thickness of the sleeve wall, as illustrated in Figure 53.

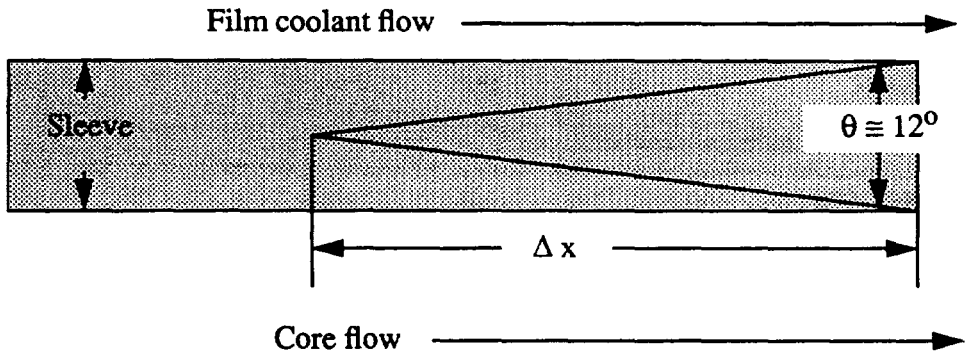

Figure 53. Mixing layer origination point.

While very simple in nature, the above free-stream turbulent mixing layer correlation captures the fundamental features of the mixing process. The 'freezing' of the turbulence, due to flow acceleration in the convergent-divergent portion of the nozzle (see Reference 43) is also reasonably well modelled since the velocity defect is a constant, while the density decreases appreciably (about two orders of magnitude) as the flow accelerates through the nozzle. It is worth noting that the standard free-stream turbulence model employed in the Proteus model yields an identical expression for the turbulent viscosity calculation of a

mixing layer (if the theoretical maximum shear stress value is inserted), the only difference being that the constant is 40 % lower than applied in this analysis and the velocity defect is based on conditions along a constant ξ line.

7.2.5. Analytical Results and Comparison with Experimental Measurements

To examine and compare the analytical predictions with experimental measurements, an examination of the Mach number contours, fluid velocity vectors, species concentrations, pressure distribution, and wall heat flux predictions were made on a local scale. The global heat transfer rate and nozzle performance were compared for the two test cases and measured data.

7.2.5.1. Mach Number Contour Predictions

Due to the conical nature of the nozzle divergence, one would expect that modest shock waves would exist in the supersonic region of the nozzle. In Figures 54 and 55, the predicted Mach number contours for the fully mixed and stratified core flow test cases, respectively, verify what would be intuitively assumed to exist. A rather weak shock wave coalesces at the nozzle centerline and causes the Mach number to decrease from a value of around 3.0 to a value somewhat greater than a Mach number of 2.5. The Mach number contours are essentially insensitive to the nature of the flow stratification, appearing almost identical in both the fully mixed and the stratified core cases. The Mach number contours are highly distorted in the high supersonic region of the nozzle, being much higher (at a given axial location) near the wall than near the centerline. It is evident that the shock waves had a far greater effect near the nozzle centerline region than near the wall region.

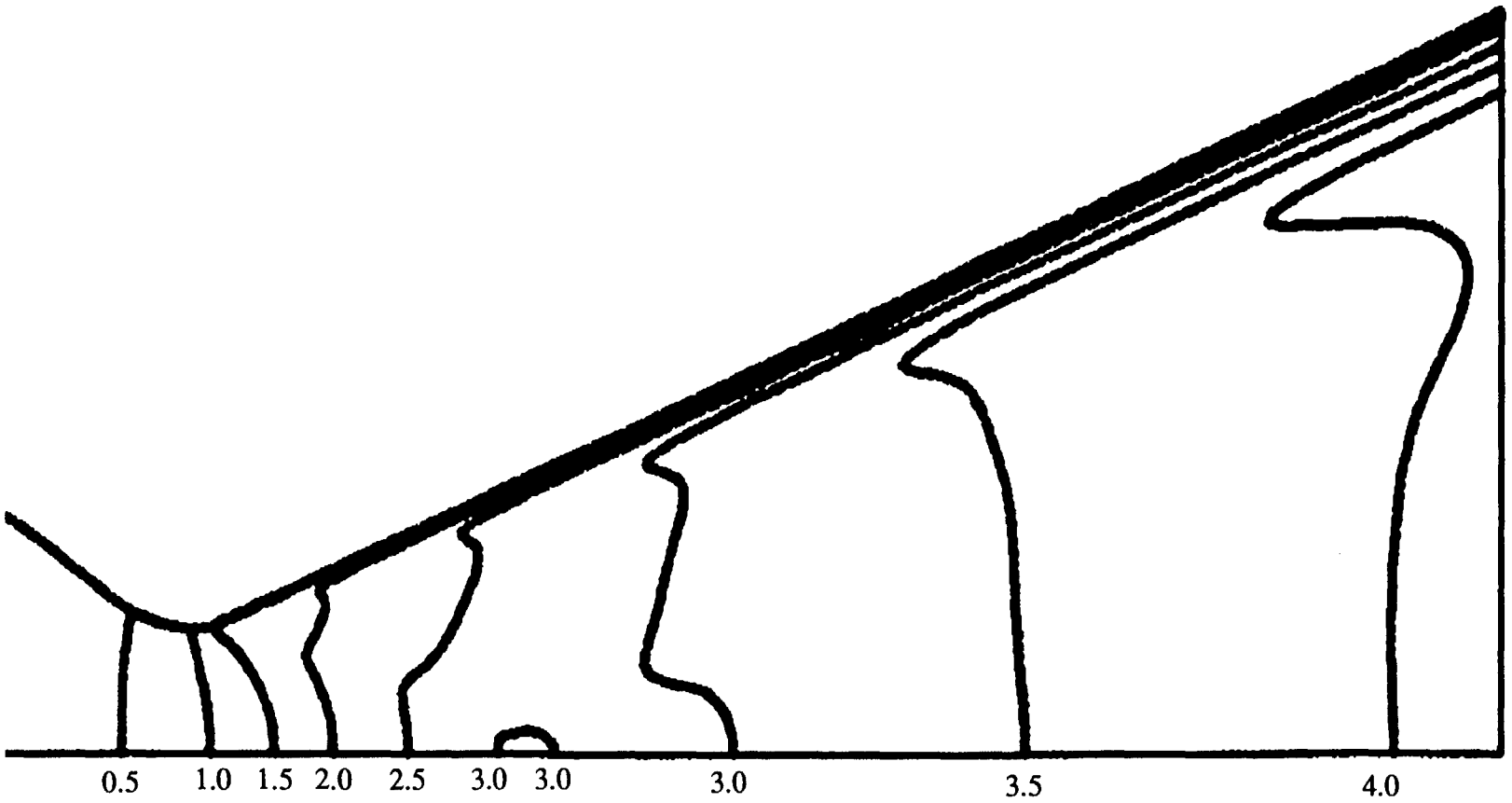

Figure 54. Mach number contour predictions for the 25 lbf film cooled nozzle using the fully mixed core assumption.

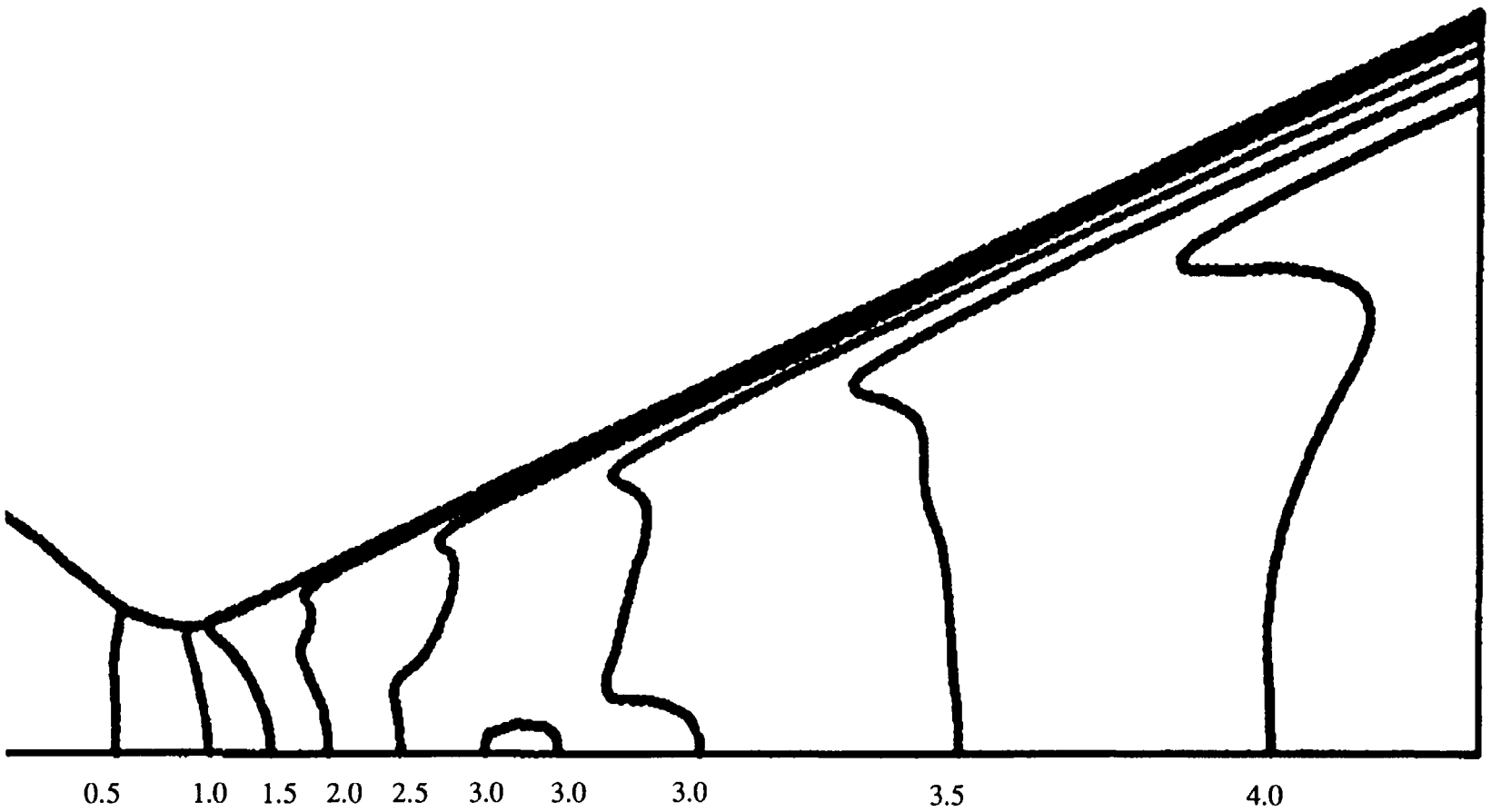

Figure 55. Mach number contour predictions for the 25 lbf film cooled nozzle using the stratified core assumption.

7.2.5.2. Fluid Velocity Vectors

The complicated nature of the film cooled nozzle system and the conical geometry of the supersonic portion of the nozzle might be expected to yield rather complex velocity vectors. However, the predictions from the stratified flow analysis, illustrated in Figures 56 and 57 with every fifth η line and every third ξ line printed, indicate that the flow is very regular in nature, even at the boundaries.

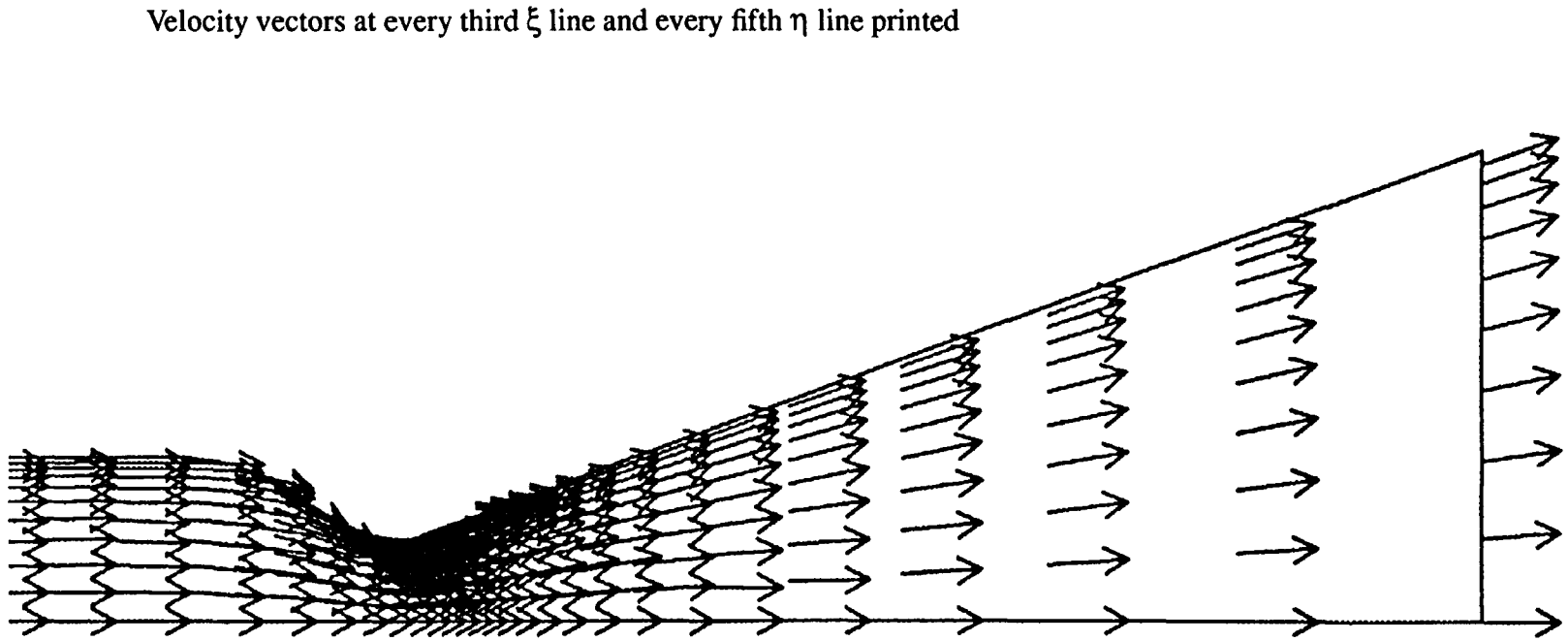

Figure 56. Velocity vector predictions for the 25 lbf film cooled nozzle using the stratified core assumption.

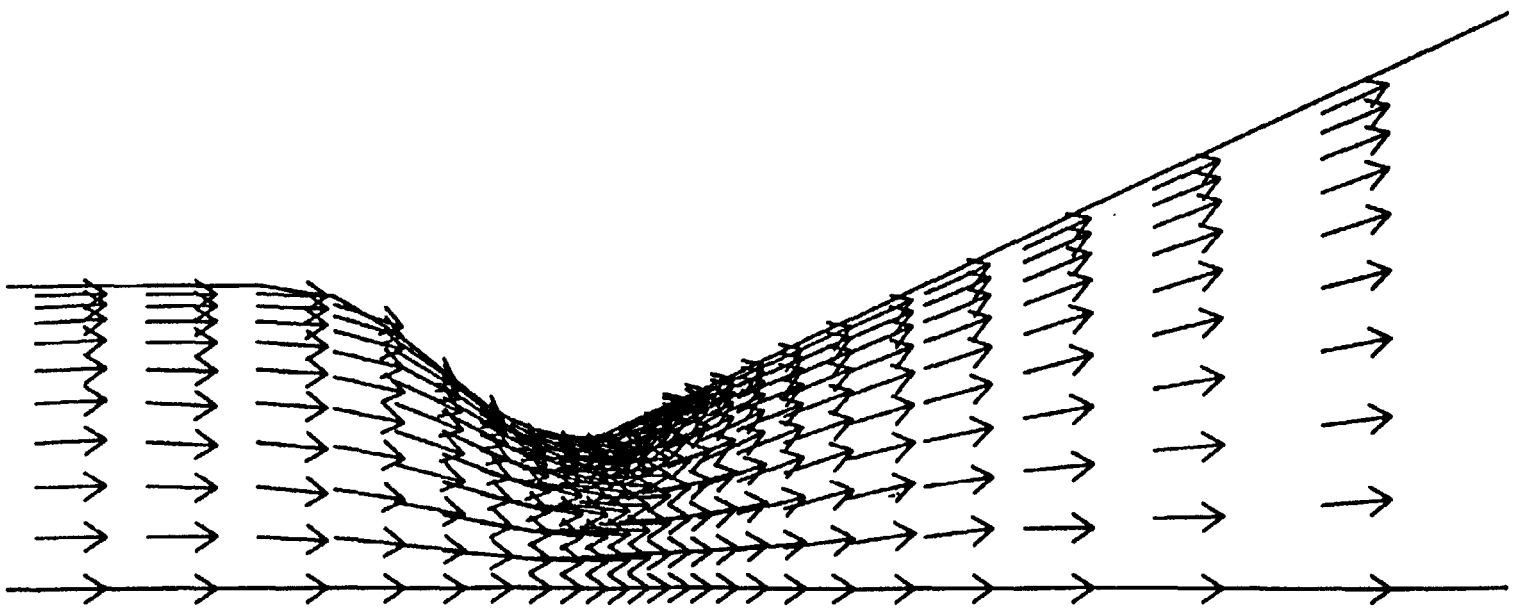

Figure 57. Throat region velocity vector predictions for the 25 lbf film cooled nozzle using the stratified core assumption.

7.2.5.3. Predicted Steam Mass Fraction Contours

In Figures 58 to 61, a contour mapping of the mass fraction of steam (H_2O) is shown for the fully mixed core analysis and the stratified core analysis. In examining these figures, numerous flow features become very evident. The first is that in both the fully mixed and the stratified core cases, fluid mixing is essentially nonexistent in the supersonic region of the nozzle. This is entirely as expected, since the fluid speeds increase rapidly in the transonic portion of the nozzle, while the turbulence quantities tend to 'laminarize'. Another important observation is that the stratified flow case exhibits a much lower mass fraction of steam in the core region of the flow throughout the nozzle. Since the creation of steam is associated with a large increase in thermal energy, one can expect a significantly higher performance from the fully mixed core case. As shown in Section 7.2.5.6, this is exactly the situation.

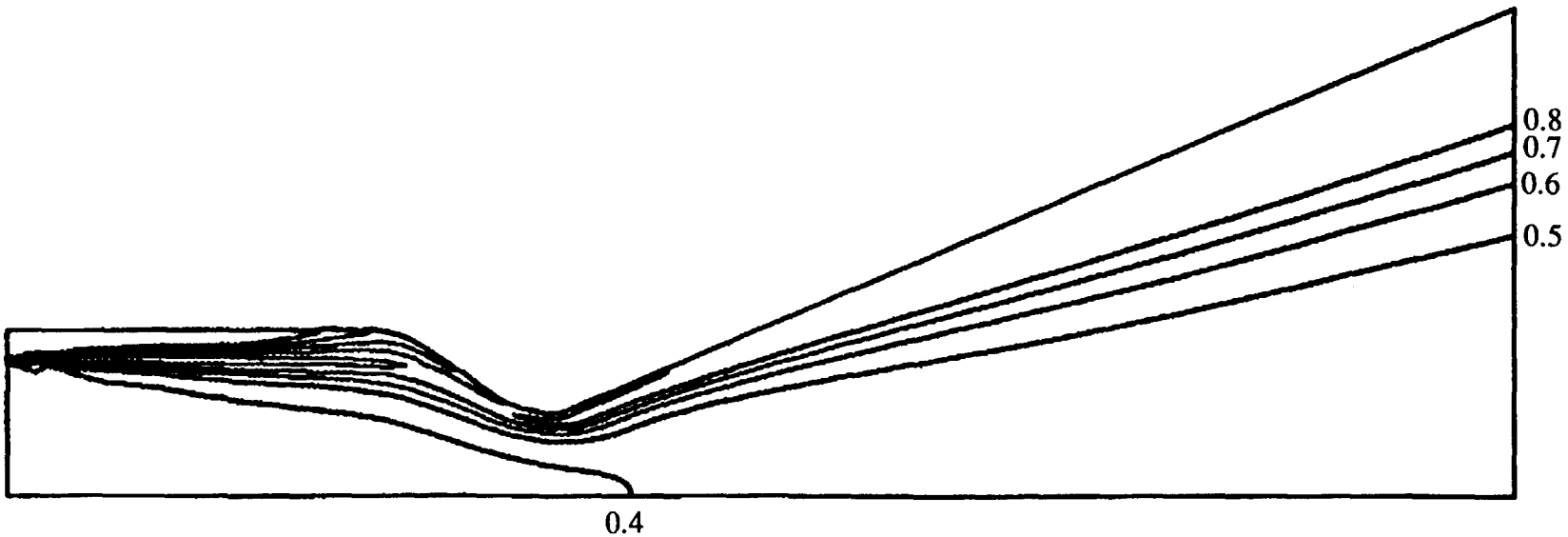

Figure 58. Steam mass fraction contours in the 25 lbf film cooled nozzle using the fully mixed core assumption.

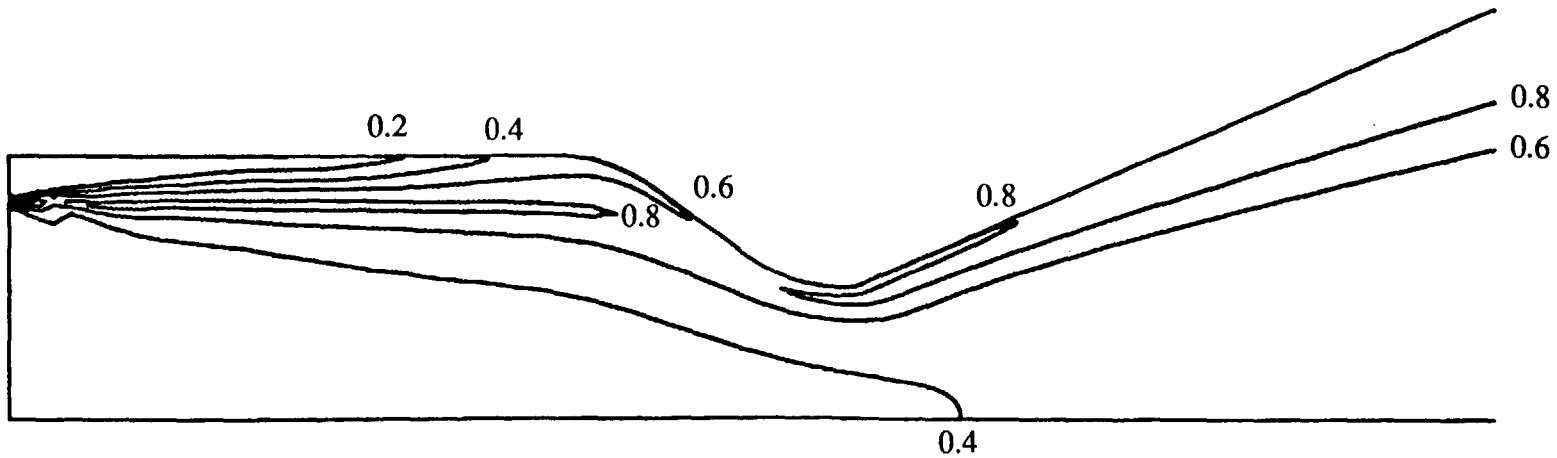

Figure 59. Steam mass fraction contours in the throat region of the 25 lbf film cooled nozzle using the fully mixed core assumption.

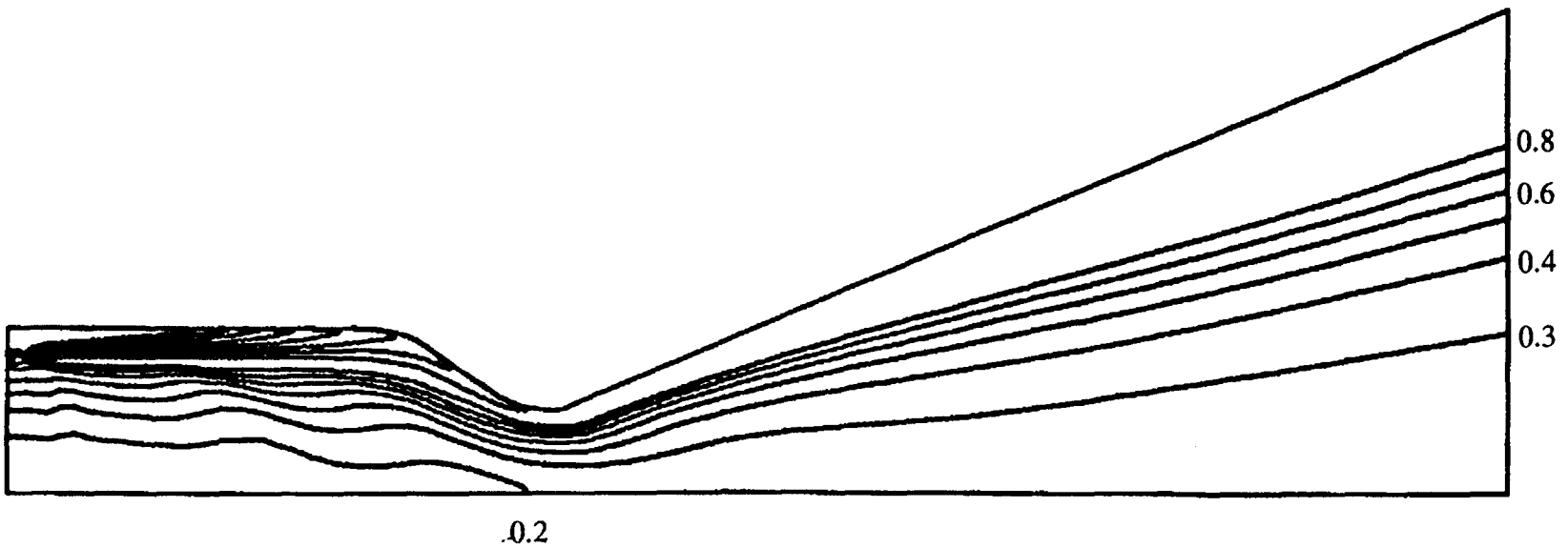

Figure 60. Steam mass fraction contours in the 25 lbf film cooled nozzle using the stratified core assumption.

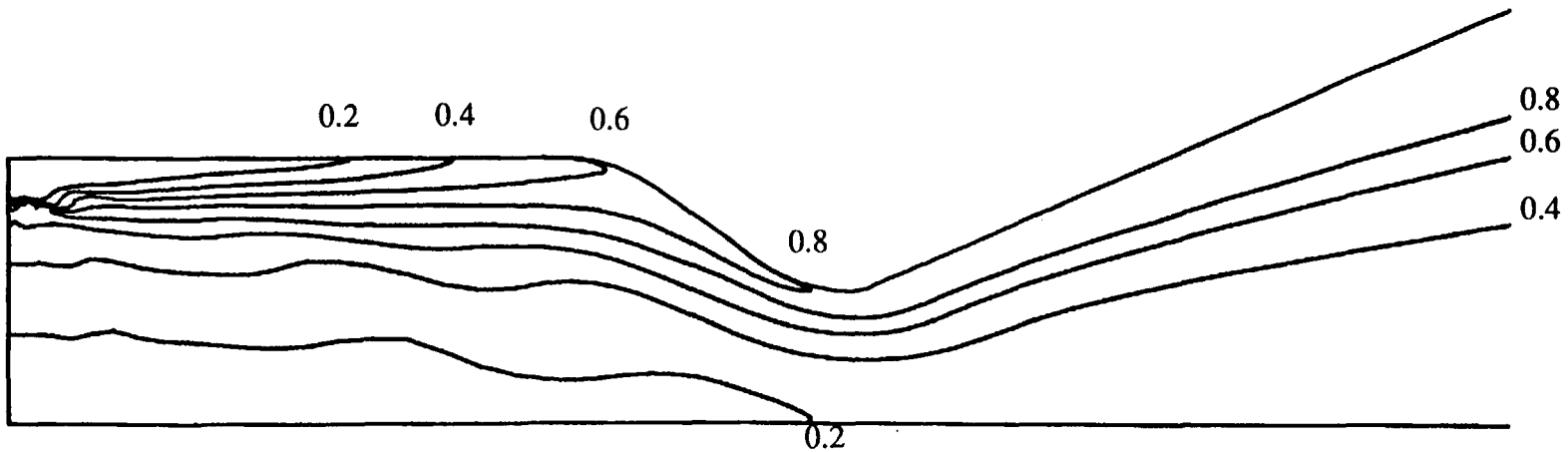

Figure 61. Steam mass fraction contours in the throat region of the 25 lbf film cooled nozzle using the stratified core assumption.

7.2.5.4. Predicted and Measured Pressure Profiles

Analytical predictions of nozzle wall pressure and experimental pressure measurements are presented in Figures 62 and 63 for the fully mixed core analysis and the stratified core analysis cases, respectively. In both of these cases, the wall pressure predictions correlate extremely well with measured data. However, in both cases the predicted pressures are slightly higher than the experimental measurements, with the fully mixed core case being somewhat higher than that predicted in the stratified core case. Most of the discrepancy between predicted and measured wall pressures can be attributed to the fact that the predicted combustion performance was somewhat better (from 6 % to 11 %, as discussed in Section 7.2.5.6) than occurred in the experimental program. As the mass flow rates were used as an input to this analysis, the higher combustion performance is reflected in a higher stagnation pressure at the nozzle inlet.

In both cases, a significant discontinuity in the slope of the pressure distribution is predicted at the location where the diverging nozzle cone attaches to the curved transonic portion of the nozzle. The crispness in the modelling of this effect is noteworthy and would be fully expected to exist in actual test conditions, although the coarseness of the pressure measurements gave no indication of the presence of this effect.

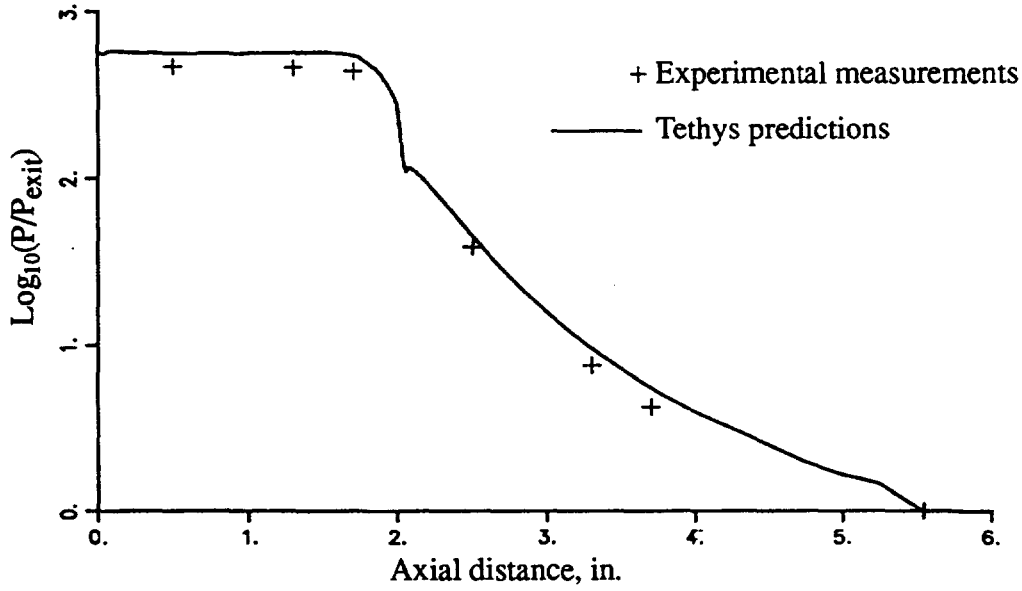

Figure 62. Comparison of experimental and predicted wall pressure distributions in the 25 lbf film cooled nozzle using the fully mixed core assumption.

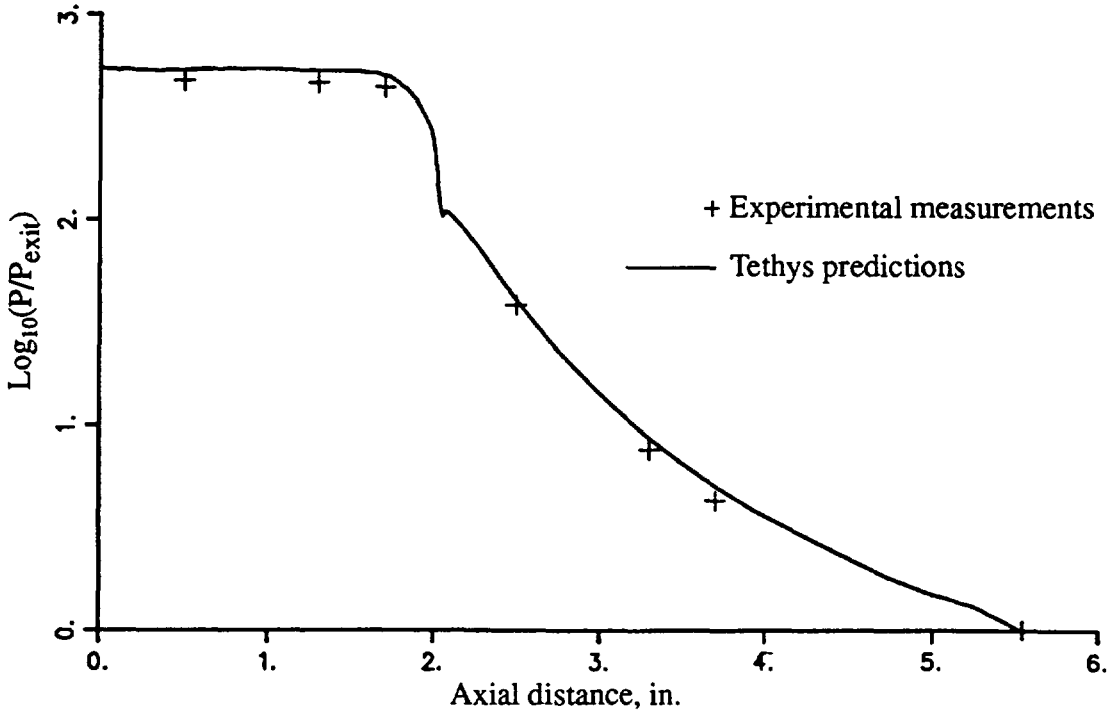

Figure 63. Comparison of experimental and predicted wall pressure distributions in the 25 lbf film cooled nozzle using the stratified core assumption.

7.2.5.5. Predicted and Experimental Heat Transfer Rates

Global measurements of nozzle heat transfer and local measurements of nozzle wall temperature were made. The predicted nozzle wall heat fluxes are shown in Figures 64 and 65 for the fully mixed core and stratified core cases, respectively. While a high level of confidence in the quantitative accuracy of the predictions cannot be expected due to a variety of reasons (which are discussed on page 124), numerous aspects of the heat flux profile predictions are of importance.

An extremely interesting observation is that the peak in the nozzle heat fluxes is appreciably upstream of the nozzle throat, with the peak heat flux location being about 0.2 inches upstream of the nozzle throat. This location is well upstream of the small amount that is normally experienced due to nozzle curvature which causes the sonic line to curve upstream of the throat. This maximum heat flux point would be expected to occur at about 0.04 inches upstream of the nozzle throat (Reference 23, page 100). Instead, the peaking

of the heat flux profile represents the prediction of injector streaking. The streaking occurs because the momentum of the hot film core is significantly larger than that of the hydrogen film coolant, being about 20 times greater, and the core flow has the tendency towards direct impingement onto the wall since the low momentum of the coolant has little ability to force the core flow to turn with the geometry. Instead, the fluid streamlines become concentrated very near the wall of the nozzle.

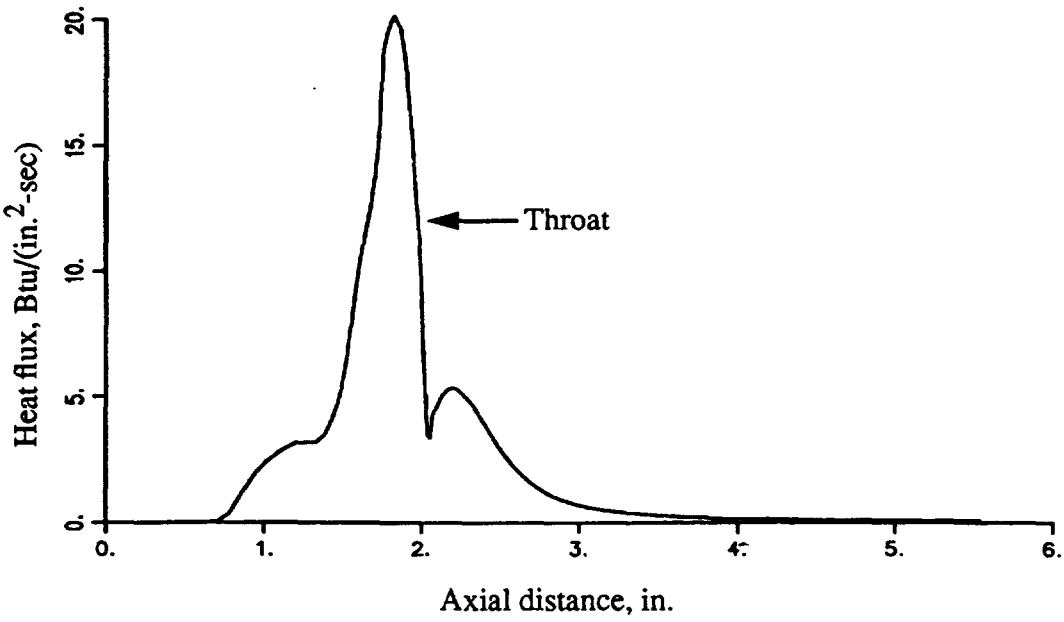

Figure 64. Wall heat flux predictions for the 25 lbf film cooled nozzle using the fully mixed core assumption.

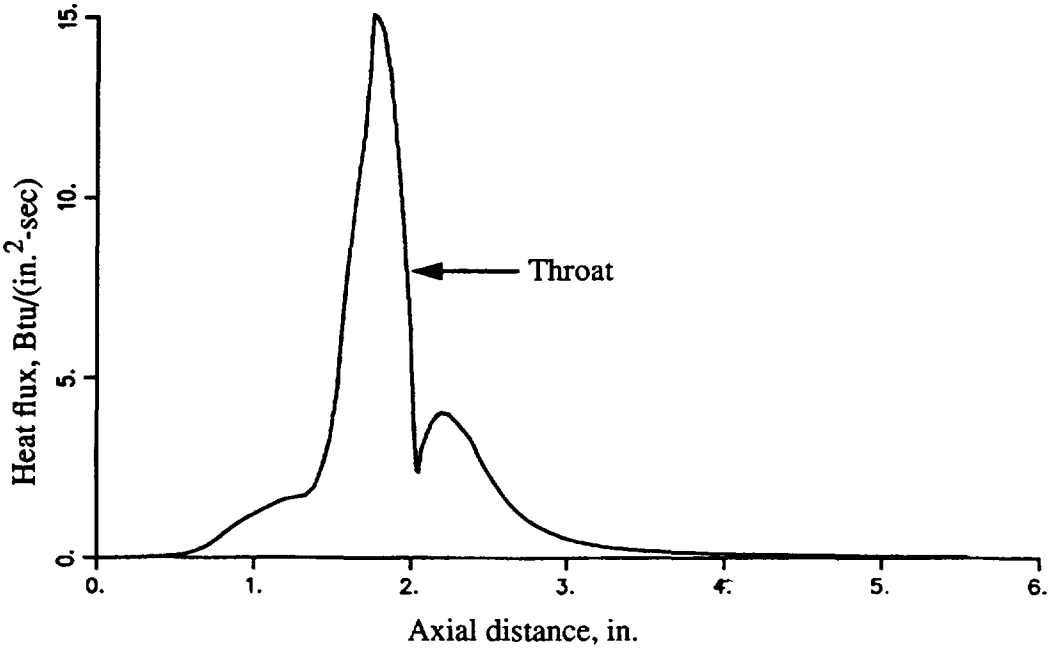

Figure 65. Wall heat flux predictions for the 25 lbf film cooled nozzle using the stratified core assumption.

Another interesting aspect of the heat flux predictions shown in Figures 64 and 65 is the local minimum, followed shortly by a local maximum that occurs just downstream of the throat. In fact, the sharp increase in heat flux corresponds precisely to the region where the geometric transition from the circular arc throat to the conical divergence occurs.

The streaking aspect of the injector is used in Figure 66 to present the wall temperature distribution which would likely exist in the region just upstream of the throat. These predictions (for the stratified core case and the fully mixed core case) are compared to the straight-line-fit temperature distribution as published in a report (Reference 38) detailing the experimental results. Here it is seen that the actual wall temperatures may have been in excess of 100 degrees Rankine hotter than suggested with a straight line fit of the data. Rather surprisingly, the temperature increase is mostly independent of the predictive technique employed. This is the result of scaling the coolant channel resistances to fit the experimentally measured wall temperatures. Hence, the temperature increase is a reflection of the relative increase of the heat flux in this region and is independent of its

actual magnitude.

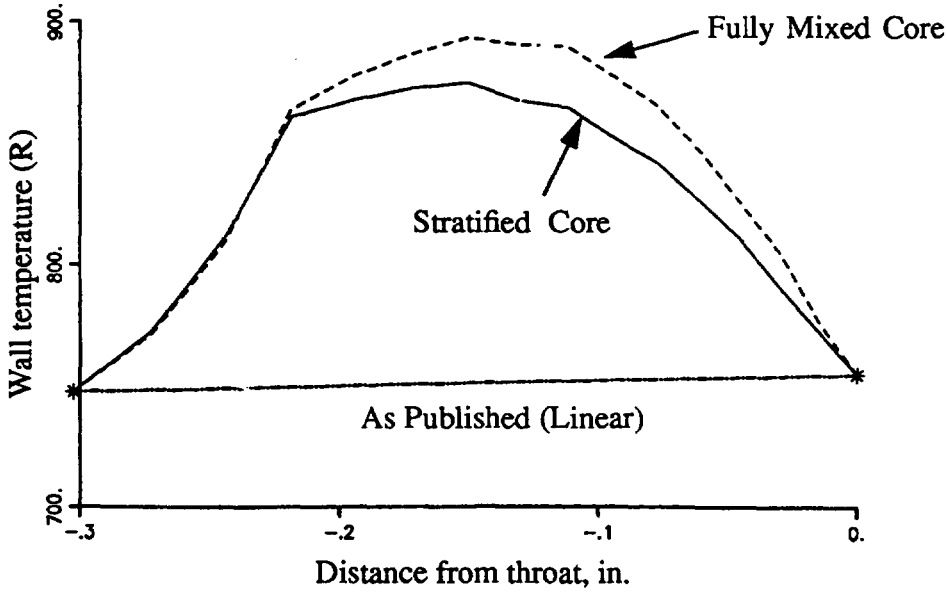

Figure 66. Streaking effects on the wall temperature distribution of the 25 lbf film cooled nozzle.

The global heat transfer rate measurements are presented in Table 14. Surprisingly, the stratified core analysis predicts heat transfer rates that are within 2.6 % of experimental measurements. Because the turbulence model was rather simplistic in nature and the turbulent Prandtl number was tailored to accurately reflect free-stream mixing conditions, in addition to a rather coarse, loosely packed grid and the fact that the constituency of the stratified core itself is only modestly well defined, it is most likely that this high level of agreement between analysis and experiment is a fortuitous result. The predicted heat transfer rates of the fully mixed core nozzle are substantially higher than experimental measurements or that predicted in the stratified core analysis. Undoubtedly, this is the result of the much higher heat flux peak at the region upstream of the throat which in turn is likely due to the existence of unreacted oxygen in close proximity to hydrogen.

Table 14. Comparison of measured and predicted global heat transfer rates.

	Total heat transfer, Btu/sec
Experimental measurements	23.6
Stratified core analysis	23.0
Fully mixed core analysis	31.5

7.2.5.6. Predicted and Measured Performance Parameters

One of the most important requirements of a nozzle analysis is the ability of the model to adequately predict nozzle performance parameters such as specific impulse and thrust coefficient. In the case of this particular film cooled nozzle analysis, this was especially difficult since the chemical composition of the core flow was only modestly well defined. Further, the mixing effects between the film and the fluid core were essential to predict specific impulse and characteristic velocity and would seem to depend heavily on the nature of the turbulence model. In light of these seemingly difficult conditions, the critical performance parameters regarding nozzle performance are compared in Figures 67 and 68 and in Table 15 between the two nozzle analysis cases and experimentally measured results, at a mixture ratio of 8.0.

The measured specific impulse for two slightly different injectors (the difference being a slight difference in the size of the gap between the spark plug base and the combustor walls) used in the test program and the predictions from the Tethys code are shown in Figure 67. Here it is seen that both of the Tethys analysis cases tend to overpredict the performance of the nozzle, but that the performance predictions of the stratified flow case are substantially closer to experimental results than the fully mixed core case. Since the sensitivity of the nozzle to slight changes in the injector geometry caused such a large difference in the experimentally measured performance, being about a 10 lbf-sec/lbm difference at a mixture ratio of 8.00, it is highly probable that the stratified core flowfield assumed at the inlet of the Tethys analysis underestimated the extent of flow stratification.

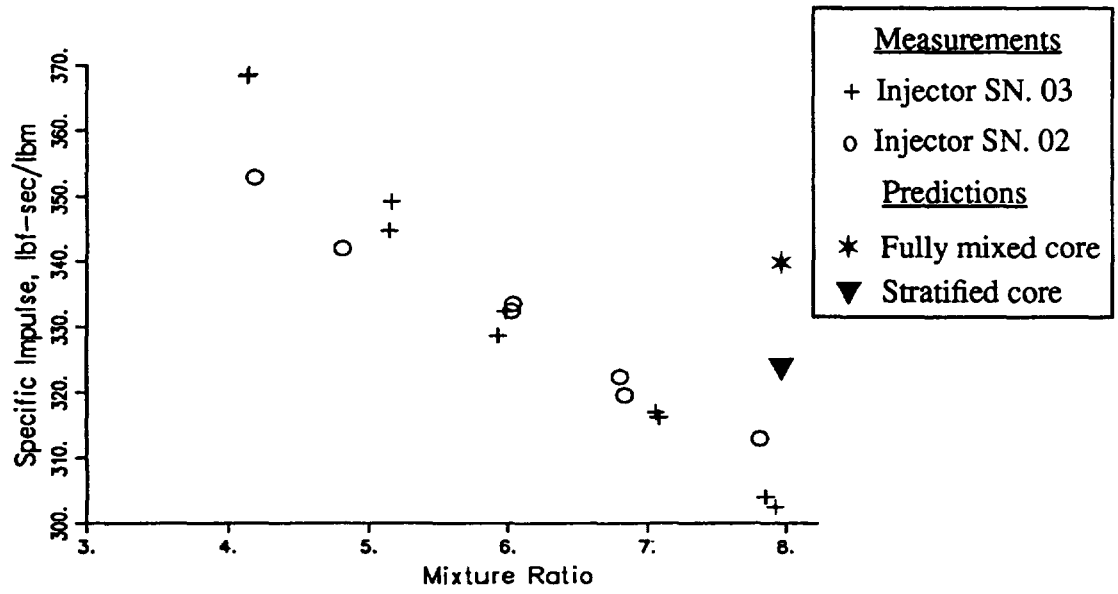

Figure 67. Comparison of experimental and predicted specific impulse for the 25 lbf film cooled nozzle study.

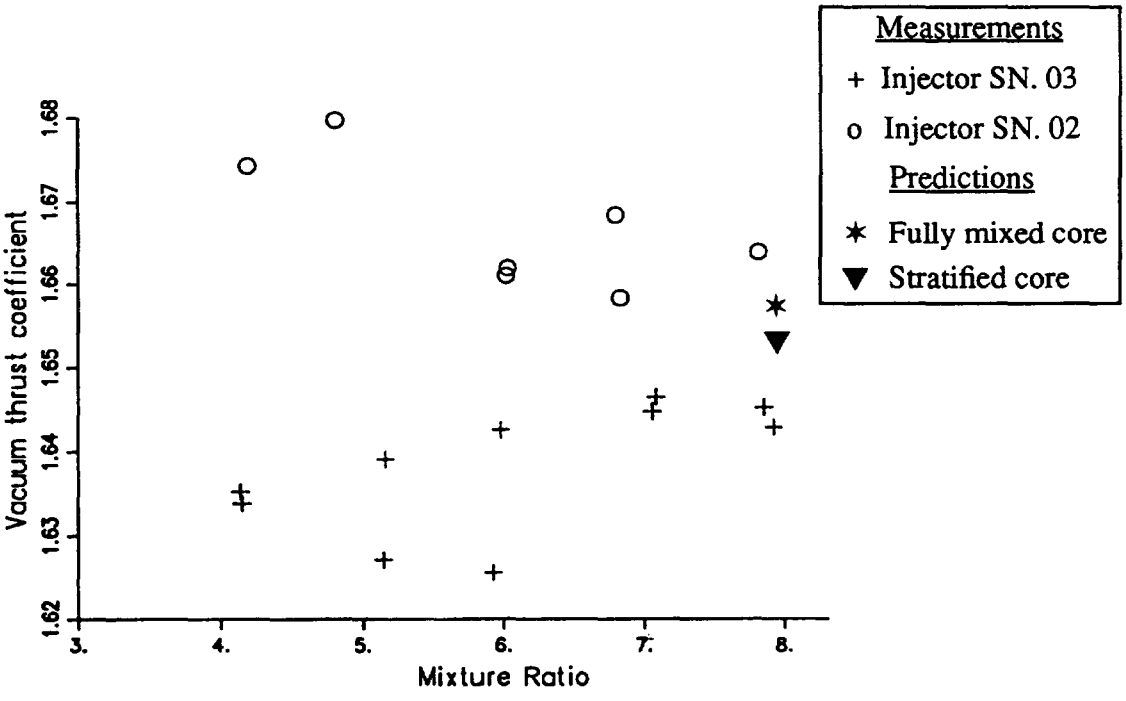

Figure 68. Comparison of experimental and predicted thrust coefficient for the 25 lbf film cooled nozzle study.

A comparison of the measured and predicted thrust coefficients for the film cooled nozzle is shown in Figure 68. Here it is seen that the Tethys predictions for either the stratified core or the fully mixed core are well within the experimental disparity observed between the two injectors that were tested.

A final observation can be drawn by relating the trends of Figure 67 and those of Figure 68, always focussing on the results obtained near the mixture ratio of 8.0. In Figure 67, it is observed that the experimentally measured specific impulse is about 3 % higher for injector SN. 02 as compared to the specific impulse measured for injector SN. 03. In Figure 68, the thrust coefficient observed for injector SN. 02 appears to be about 1 % higher than the thrust coefficient of injector SN. 03. These observations are in contrast to those of the Tethys code results where it is observed that a 5 % difference in specific impulse between the fully mixed core assumption and the stratified core assumption relates to a predicted difference in vacuum thrust coefficient of only 0.2 %. While the experimental and predicted trends of higher specific impulse corresponding to higher thrust coefficients is in agreement, the disparity between the extent to which this occurs suggests that the flow is not only more stratified than used in the Tethys analysis, but that the qualitative nature of the profile is also inaccurate.

In Table 15, a precise comparison between the measurements obtained using the lower performing injector (i.e., injector SN. 02) and the prediction of the Tethys model is made. Here it is seen that the specific impulse and characteristic velocity predictions of the stratified flow case are about 6 % higher than was experimentally measured while the thrust coefficient prediction is within 0.5 % of the experimentally measured value.

In general, the difference between experimental measurements and the stratified core predictions regarding engine performance are about equal to one-half the difference between experimental measurements and the fully mixed core predictions. The exception to this statement is the difference in experimental measurements concerning the nozzle thrust coefficient, where the difference between measured and predicted values in the stratified core analysis is about 50 % closer to experimental measurements than the fully mixed core analysis.

Table 15. Comparison of measured and predicted performance parameters.

Engine performance parameter	Experiment	Fully mixed core analysis	Stratified core analysis	Difference (Analysis / Experiment), %
Specific impulse, $F_v/\dot{m}$, lbf-sec/lbm	304.1	339.9	323.5	Mixed: + 11.5 Stratified: + 6.4
Characteristic velocity, $P_cA_T/\dot{m}$, ft/sec	5947.	6599.	6296.	Mixed: + 11.0 Stratified: + 5.9
Vacuum thrust coefficient, $F_v/(P_cA_T)$	1.645	1.657	1.653	Mixed: + 0.73 Stratified: + 0.49

7.3. Transpiration Cooled Rocket Nozzle

A hydrogen/oxygen transpiration cooled rocket engine was tested at the NASA LeRC in the 1970's (Reference 44). The purpose of the program was to verify the ability of a hydrogen coolant to significantly reduce heat fluxes in the throat region of a rocket nozzle and to demonstrate that a new technique of creating a transpired region by a series of fine platelet stacks produced a reliable, efficient, and economically viable means of transpiration cooling rocket throat sections. Figures of the baseline rocket engine and the transpiration cooled spoolpiece section are shown in Figures 69 and 70. As seen in Figure 69, the demonstration tests for hydrogen transpiration cooling were not performed on a conventional converging-diverging rocket nozzle. Instead tests were performed with a plug and spool engine, with the transpiration coolant being injected into the main stream of the rocket exhaust gasses only along the spoolpiece and limited to a region 0.5 inches in length (see Figure 70), the region ending at the throat. The overall length of the spoolpiece section was 4 inches, and the gap between the spoolpiece and the plug was 0.25 inches at the throat and 0.5 inches in the combustion chamber. The inside diameter of the spoolpiece was 2.6 inches.

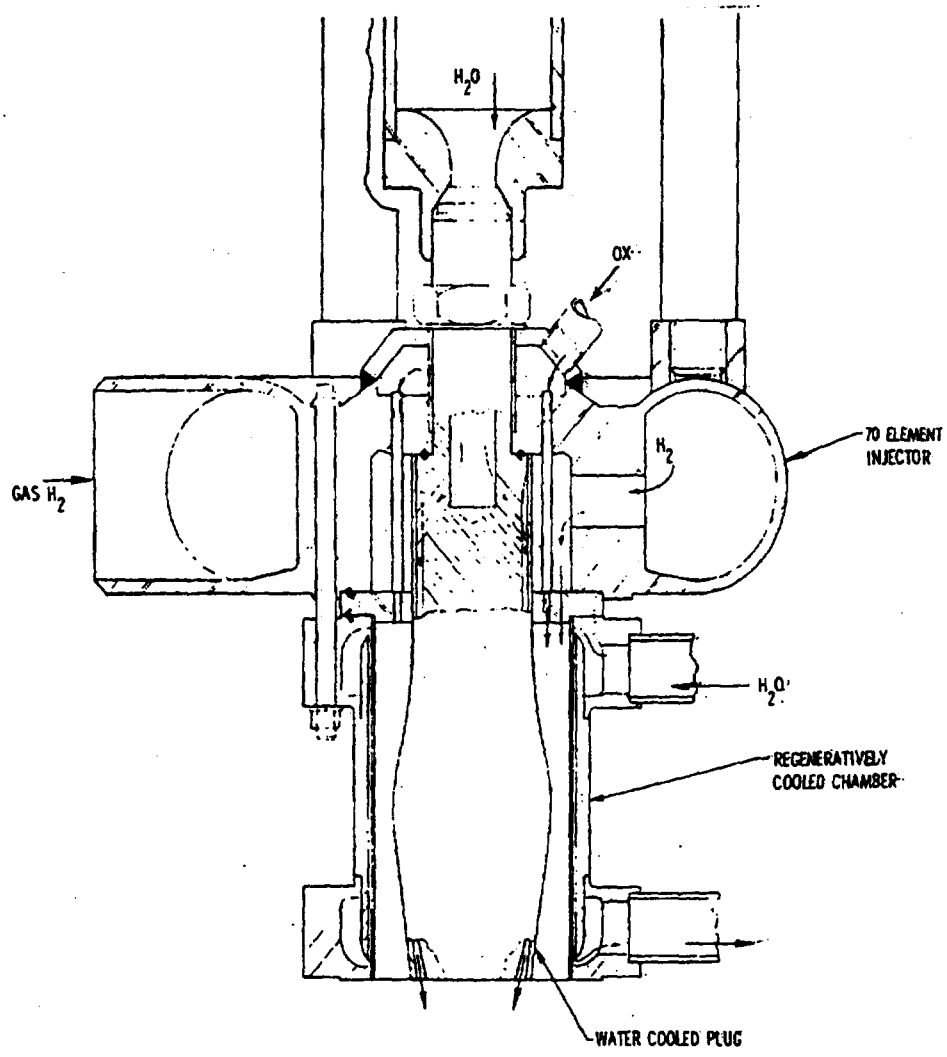

Figure 69. Plug and spool rocket engine tested at NASA LeRC.

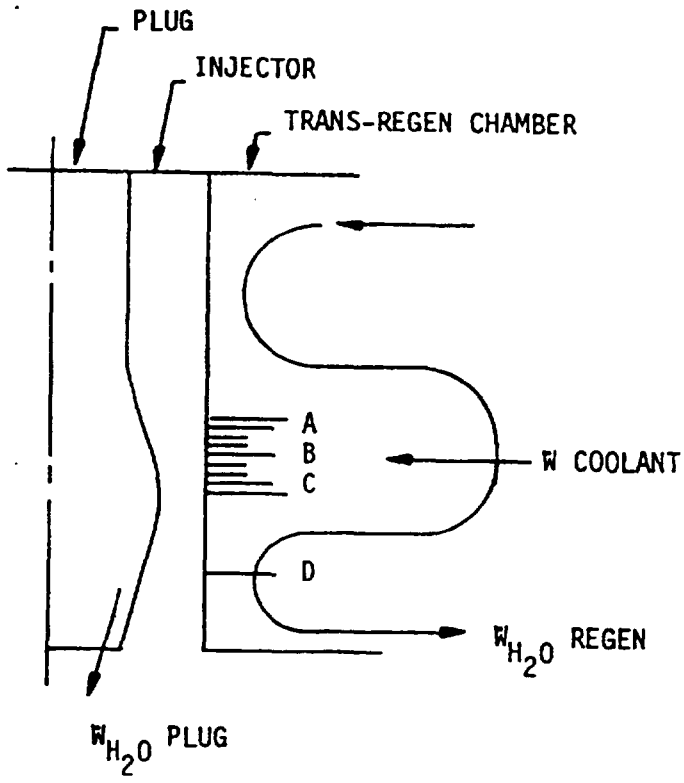

Figure 70. Schematic of the transpiration cooled spoolpiece section.

The nominal operating conditions of the nozzle are given in Table 16. The mixture ratio and chamber pressure were nearly constant throughout the test series, while the hydrogen transpiration mass flow rates were varied from 0.045 lbm/sec to 0.075 lbm/sec.

Table 16. Nominal operating conditions of the transpiration cooled rocket nozzle.

Design Parameter	Nominal Value
Chamber pressure, lbf/in.^{2}	600.0
Oxygen / Fuel mixture ratio	6.0
Transpired hydrogen mass flow rate, lbm/sec	0.045
Transpired section wall temperature, R	900.0

7.3.1. Analytical Modeling of the Transpiration Cooled Rocket Nozzle

Several important assumptions were made concerning the ultimate predictive capabilities of the Tethys model in predicting the flowfield of the transpiration cooled rocket nozzle. Due to the relatively incomplete nature of the experimental data reporting techniques and the significant computational advantages, the hydrogen/oxygen propellant system was assumed to be a frozen mixture of steam and excess hydrogen. Furthermore, the temperature of the transpired coolant was presumed to be equal to the wall temperature of the copper platelet stack through which the fluid flowed. While no direct measurements of the fluid temperature being injected were made, a heat transfer analysis performed during the experimental program indicated that the wall temperatures might be as much as 300 degrees Rankine hotter than the coolant fluid. Instead, the estimated temperature of the coolant fluid was used to represent the wall temperature in the transpired section, reasoning that the enthalpy difference of the coolant is far more critical than the slightly different conduction heat transfer rates that may occur as the result of the wall temperature being suppressed.

7.3.2. Boundary Conditions Employed for the Transpiration Cooled Rocket Nozzle

The boundary conditions applied in the Tethys model simulation are presented in Table 17. As shown in the table, the reference plane characteristic method (MOC) was used at all of the boundaries. In this transpiration cooled analysis, the wall temperature distribution was specified throughout the transpired and solid wall regions. Hence, the mass flow rate requirements needed to yield the prescribed wall temperature was a variable to be determined.

Table 17. Boundary conditions applied to the transpiration cooled rocket nozzle.

Inlet	Exit	Plug Wall	Spool Wall	
			Solid	Transpired
$P_0 = 600$ lbf/in.^{2}	MOC*	MOC	MOC	MOC
MOC	MOC	$\frac{\partial s}{\partial \eta} = 0$	$u = 0$	$u = 0$
$v = 0$	MOC	$V_n = 0$	$v = 0$	$\rho v \Delta h + q'' = 0$
$h_0 = -1.1 \frac{Btu}{lbm}$	MOC	$\frac{\partial h_0}{\partial \eta} = 0$	$T = T(x)$	$T = T(x)$
$\omega_{H_2} = 0.035714$	MOC	$\frac{\partial \omega_{H_2}}{\partial \eta} = 0$	$j_{H_2} = 0$	$j_{H_2} + \rho v \omega_{H_2} = \rho v$
*At subsonic contravarient velocities, the exit pressure was set equal to 61.5 lbf/in.^{2}				

An additional consideration that required investigation was the effect of the transpired surface wall on the flow stream. Due to excessive time in an electropolishing bath, the plates employed for the construction of the transpiration region became rounded, resulting in an extremely rough surface, as illustrated in Figure 71. Consequently, the effect of this roughened surface was examined by conducting a smooth walled coolant section analysis and a rough walled coolant section analysis.

The extent of the rounding caused by the excessive polishing process was measured to be 12 RMS on "Taly-Surf" measurement equipment and corresponded very well with magnified photographs.

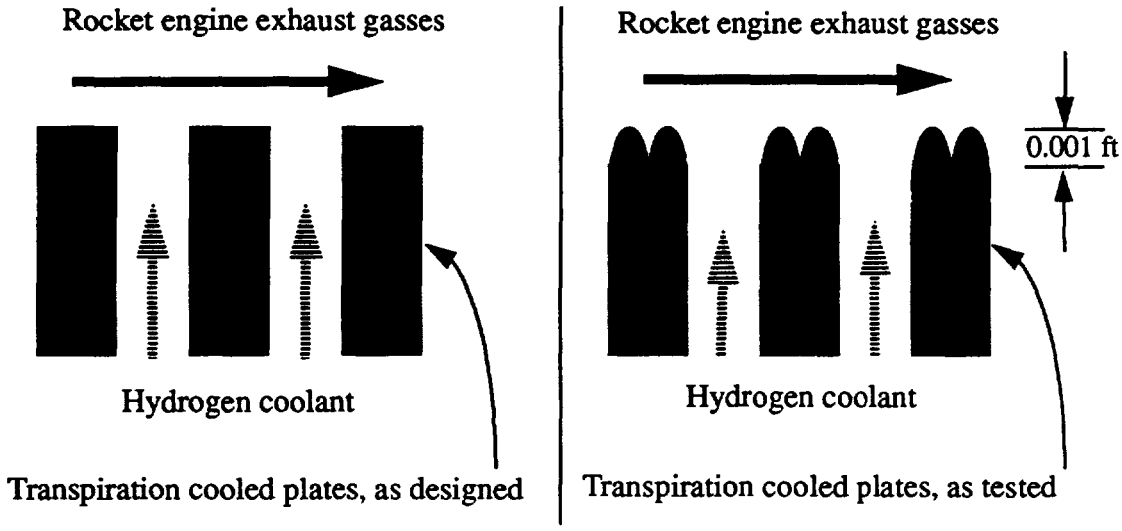

Figure 71. Schematic of surface roughening caused by excessive electropolishing of the transpiration cooled rocket nozzle.

Table 18 summarizes the different assumptions and methodologies employed for the two analyses.

Table 18. Analysis methods used for the transpiration cooled rocket nozzle.

Analysis Parameter	Smooth Wall	Rough Wall
Soret mass transfer	Yes	Yes
Dufour heat transfer	Yes	Yes
Turbulence model	Cebeci-Smith	Cebeci-Smith
Turbulent Prandtl number	0.9	0.9
Turbulent Lewis number	1.0	1.0
Surface roughness, transpired region	None	12 mils (0.001 ft)
Artificial diffusion (main flowfield and MOC equations, except MOC equations applied along the spoolpiece wall)	Second-order non-linear model: 2X recommended level	Second-order non-linear model: 2X recommended level

The spoolpiece temperature distribution used for the transpiration cooled nozzle study is shown in Figure 72. In the solid walled region, the temperature was established from experimental measurements. In the transpiration cooled region, a combination of experimental measurements and temperature correction factors were used to estimate the coolant temperature distribution. The reason for the depression of temperature in the center of the cooled region is possibly due to the nature of the hardware/engine design system which, when heated, preferentially closes those coolant slots that are located nearest the solid wall region. Consequently, the coolant flow will preferentially escape through the center of the transpiration coolant region.

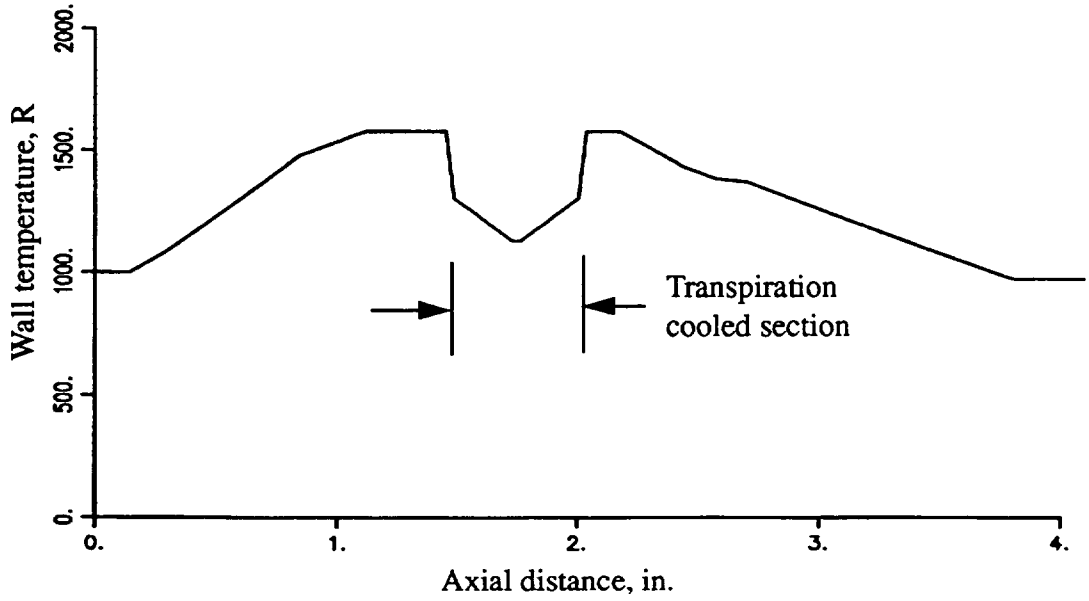

Figure 72. Wall temperature used for analysis of the transpiration cooled rocket nozzle.

7.3.3. Computational Grid Used for Analysis of the Transpiration Cooled Rocket Nozzle

A computational grid with 51 axial and 31 radial grid points was used for the analysis of the transpiration cooled rocket nozzle. The distribution of grid points is presented in Figure 73, where it is observed that a significant amount of axial packing was employed in the region enclosing the transpiration cooled section, and the grid was heavily packed near the no-slip spoolpiece surface.

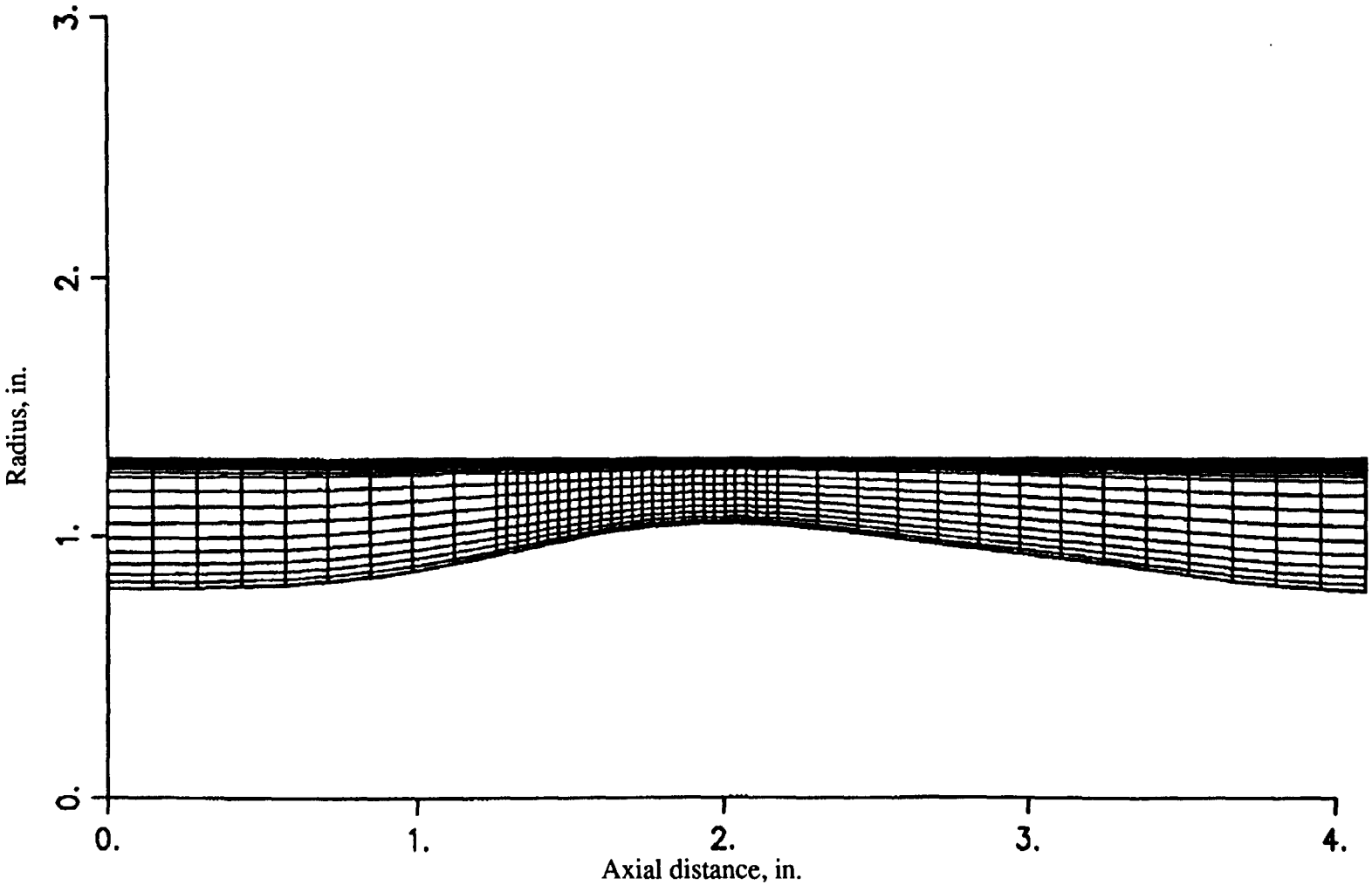

Figure 73. Computational grid employed for the analysis of the transpiration cooled rocket nozzle.

The computational grid was established using algebraic relations. To establish the axial location of the computational lines, the grid was constructed by first assuming that only 31 axial lines were to be constructed, with the following relation:

$$x = x_{Throat}\left[1 + \frac{\sinh\left[\ \tau(\xi - B)\ \right]}{\sinh(\tau B)}\right] \tag{7.3.1}$$

where B and τ are as defined in Section 7.1, with the packing factor, τ, equal to 1.001, which, in essence, resulted in an evenly distributed grid. In the region encompassing the transpiration cooled section, the axial grid point spacing was 20 % of the spacing used in the inlet and exit regions. The extremely tight radial packing employed in this analysis was accomplished using the following relation:

$$\phi = \frac{a - b\left[\frac{a}{b}\right]^{1-\eta}}{1 + \left[\frac{a}{b}\right]^{1-\eta}} \tag{7.3.2}$$

with ϕ being equal to the ratio of the distance from the plug wall divided by the distance from the plug wall to the spoolpiece. The constants a and b given in Equation (7.3.2) are equal to $\beta + 1$ and $\beta - 1$, respectively, with the packing factor, β, being equal to 1.0004 in the smooth surface regions and equal to 1.0008 in the rough surface regions. The relaxation of the packing factor, β, for the rough walled region in the rough walled analysis reflects the fact that significantly less packing is required for a rough walled analysis, since the viscous sublayer does not exist.

Near the wall of the plug surface, enhancement of the radial packing was performed by overwriting the grid points generated in Equation (7.3.2) with the correlation that is presented below. The enhancement was applied to the eight points nearest the surface of the plug wall, which corresponds to the $\eta = 1$ surface.

$$\phi \equiv \frac{r - r_{22}}{r_{wall} - r_{22}} = \left[\frac{N - 22}{31 - 22}\right]^{1.0 - 0.5\left[\frac{N-22}{31-22}\right]} \tag{7.3.3}$$

7.3.4. Analytic Results and Comparison with Experimental Measurements

Since the primary intent of this study was to examine the capabilities of the Tethys model for establishing the mass flow rates required to maintain a rocket engine at a prescribed temperature, the results to be presented will focus primarily on predictions and measurements made in the transpiration cooled region, although some levels of global predictions will be shown to establish the consistency of the Tethys model. Specifically, in the transpired region, the balance in heat flux and mass flow rate will be shown for the two different analyses and will be compared to the overall experimental measurements. Additional results pertaining to predictions involving the flowfield Mach number contours and surface parameters such as heat fluxes and hydrogen mass fractions will also be shown.

7.3.4.1. Mach Number Contour Predictions

The extremely gentle curvature of the subsonic and supersonic regions involved in this geometry would be expected to yield predictions that are nearly one-dimensional in nature. The predicted Mach number contours, as illustrated in Figures 74 and 75, support this reasoning. The Mach number contours have only a modest amount of radial curvature associated with them. As would also be anticipated, the smooth and rough walled analyses yield essentially identical Mach number contours, although extremely close examination of the contours indicates that the subsonic Mach number contours of the rough walled analysis are more tightly packed than those of the smooth walled analysis. This is the result of the increased mass addition experienced with the rough walled analysis. In turn, the increased mass flow rate of the rough wall displaces the boundary layer more than the smooth walled counterpart and consequently, the effective area ratio available for flow acceleration is sightly altered.

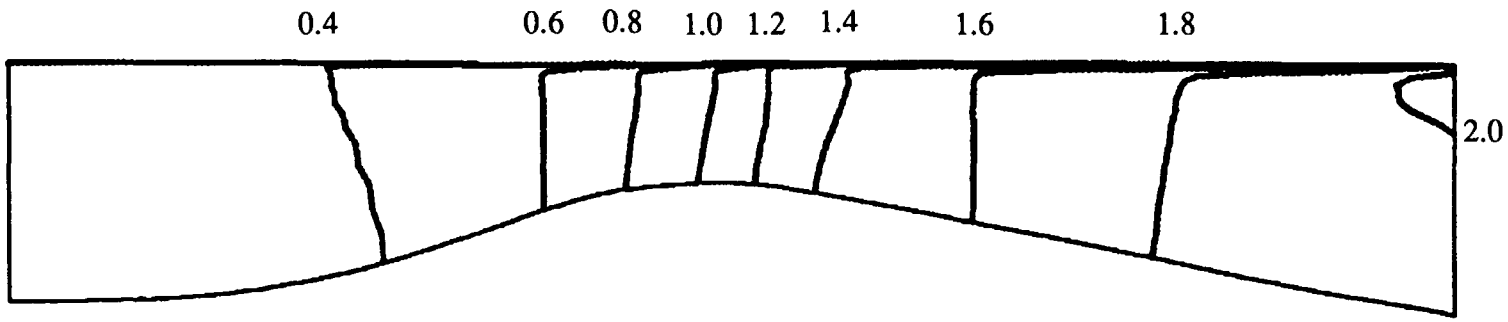

Figure 74. Predicted Mach number contours for the transpiration cooled plug and spool rocket nozzle using a smooth wall analysis.

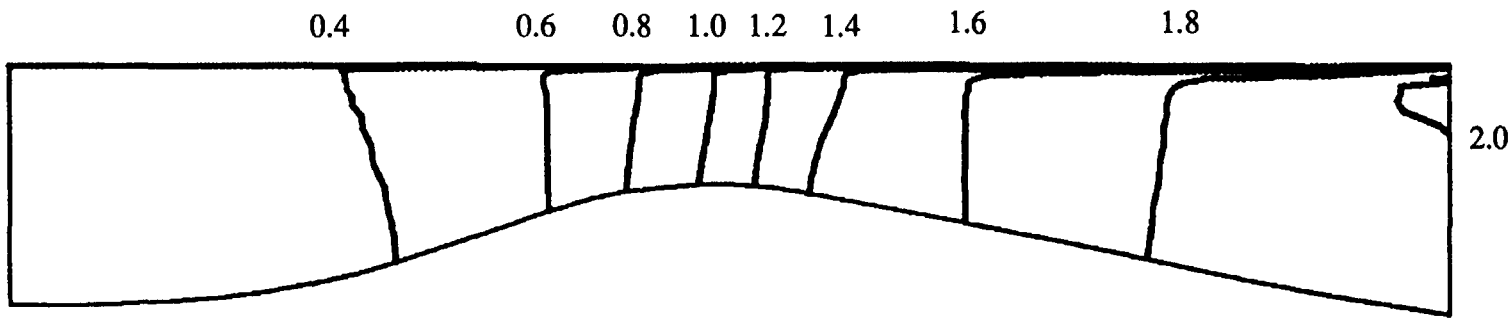

Figure 75. Predicted Mach number contours for the transpiration cooled plug and spool rocket nozzle using a rough wall analysis.

7.3.4.2. Hydrogen Wall Mass Fraction Prediction

The mass fraction of hydrogen along the wall of the spoolpiece is a parameter of interest because of the relation of this term to mass fluxes and the significance of the Soret mass transfer term as compared to other diffusion terms. It is not entirely clear a priori what the effect of turbulence is on the Soret mass diffusion term. On the one hand, the turbulence tends to drive the species towards a fully mixed condition, while on the other hand turbulence creates extremely large temperature gradients very near the wall, thereby making the Soret term also large. In Figures 76 and 77, the predictions for the mass fraction distribution of hydrogen are shown for the smooth and rough transpiration surface cases, respectively. The profiles look very similar in nature, with the exception being that the hydrogen mass fraction in the rough walled analysis is significantly higher than that of the smooth walled case in the region downstream of the transpiration section. Undoubtedly, this is the result of the additional hydrogen required as a coolant in the rough wall analysis.

A final observation is that upstream of the transpiration cooled section, the mass fraction of hydrogen on the wall is actually about one-half that of the core, which is a clear indication of the strength of the Soret mass transfer term even in the presence of turbulent flow.

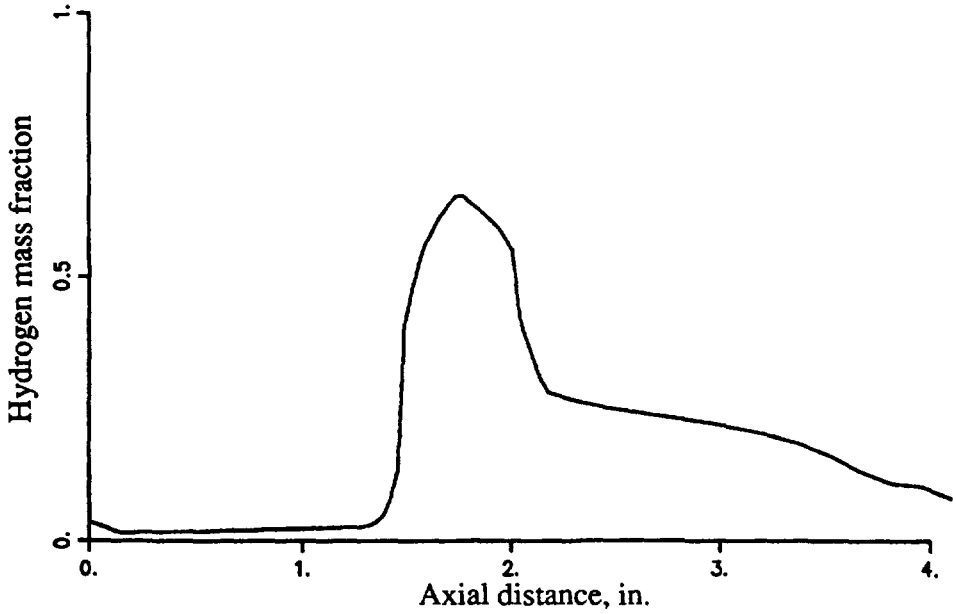

Figure 76. Hydrogen wall mass fraction predictions using a smooth walled analysis.

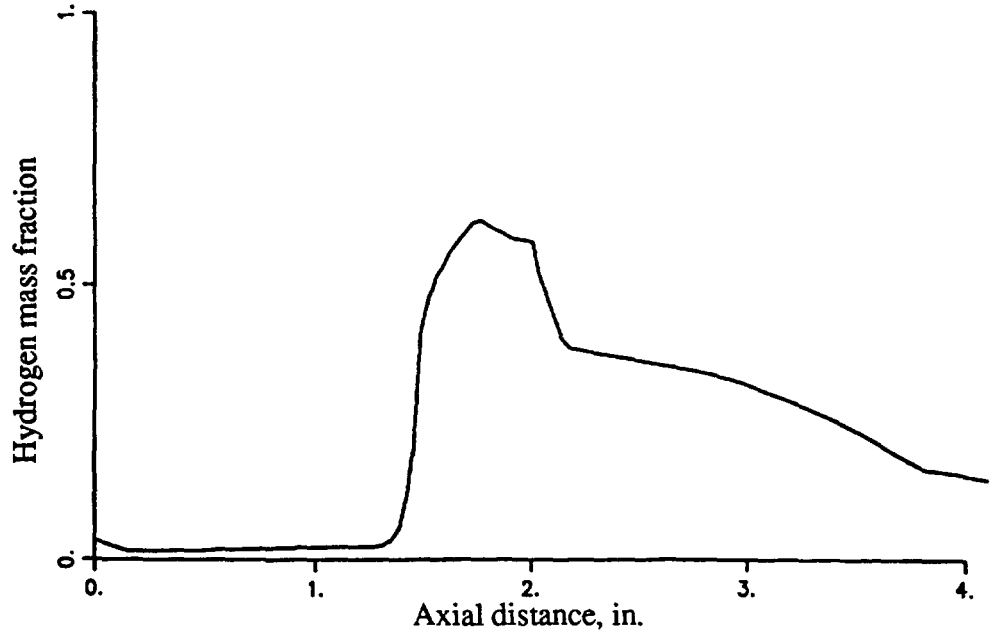

Figure 77. Hydrogen wall mass fraction predictions using a rough walled analysis.

7.3.4.3. Transpiration Coolant Mass Flux Predictions

The critical criteria upon which the success of the transpiration cooled nozzle analysis will be based is the ability to adequately predict the mass flux required to maintain a wall at a prescribed temperature. Because the mass flow that enters a transpired region may exit by diffusion (either ordinary or thermal) and advection, the relative importance of each term is of interest.

In Figure 78, the predictions of mass flux in the transpiration cooled section of the nozzle are presented for the two cases performed along with the averaged mass flux measured in the experimental program. Numerous observations become readily apparent. One of the most obvious is that the mass flux required of a smooth transpiration cooled wall are appreciably lower than was experimentally observed. On the other hand, the rough walled analysis appears to track the experimental mass flux rates rather well until reaching the center of the transpiration section, where the prescribed wall temperature begins to increase. At this point, the mass injected into the fluid stream acts as a film coolant and serves to reduce transpiration requirements until reaching the edge of the transpiration cooled region where the highly accelerating flow of the rocket engine serves to dramatically increase coolant requirements, although the extent to which this occurs may be overexaggerated because of the discontinuous nature of the adjoining boundary conditions. Similar trends are observed in the smooth walled analysis but to a much less extreme. Table 19 summarizes the differences between the observed and predicted transpiration mass flow rates in the plug and spool rocket engine. Here it is observed that the smooth walled prediction is nearly 50 % that of the experimental measurements, while the rough walled prediction is much closer to experimental results, being only 13 % lower than the experimentally measured mass flow rate.

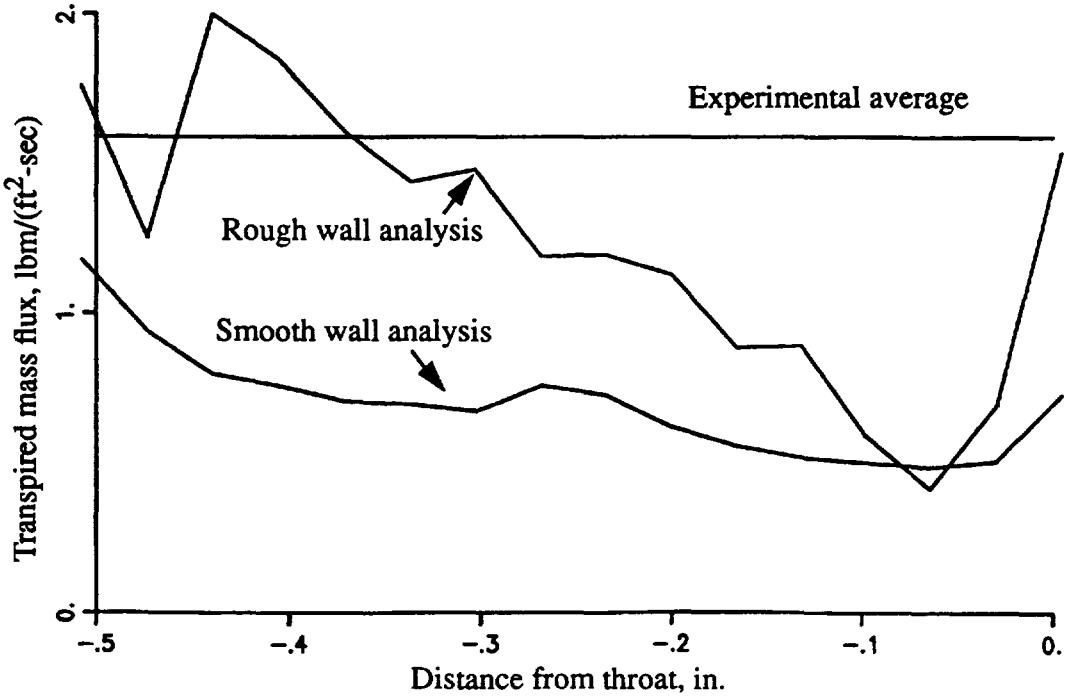

Figure 78. Transpiration coolant mass flux predictions and experimental comparison.

Table 19. Total coolant flow rate requirements.

	Transpiration wall analysis		Experiment	Difference
	Smooth	Rough	----	(Analysis/ Experiment), %
Hydrogen coolant mass flow rate, lbm/sec	0.022	0.039	0.045	Smooth: -51.0 Rough: -13.0

The individual contributions of mass flux into the fluid stream are shown in Figure 79 and Figure 80 for the smooth and rough walled analysis cases, respectively.

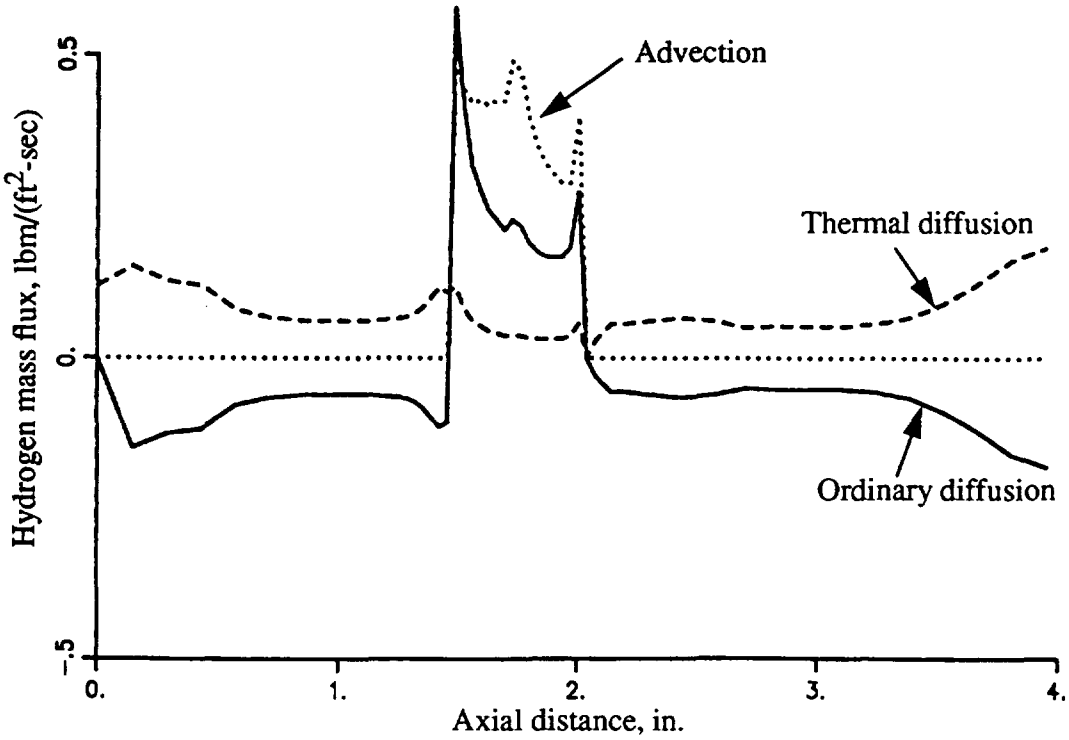

Figure 79. Predicted hydrogen mass fluxes along the wall of the transpiration cooled plug and spool rocket engine using a smooth wall analysis.

Examination of the smooth walled analysis case yields many interesting features. The first is the importance of the Soret mass flux term in both the solid walled and transpiration cooled sections of the nozzle. As the term is always positive, the Soret term drives the lighter fluid (hydrogen) away from the wall and towards the mainstream of the rocket engine exhaust gasses. In the solid walled regions of the flow, the positive Soret hydrogen flux term is balanced by the ordinary diffusion terms to create a no net flux region. On the other hand, in the transpiration cooled section of the engine, the ordinary diffusion flux is directed in the positive direction with the net result being that all hydrogen mass flux terms, advective and diffusive, act to drive the hydrogen into the flow stream.

The rough wall results exhibit most of the same trends as the smooth wall case with the exception that in the transpiration cooled section of the engine the contributions of hydrogen mass flux as the result of ordinary and thermal diffusion are very small compared to the contributions of the advective and turbulent diffusion terms, which would be

expected because of the extremely high level of surface roughness used in the analysis.

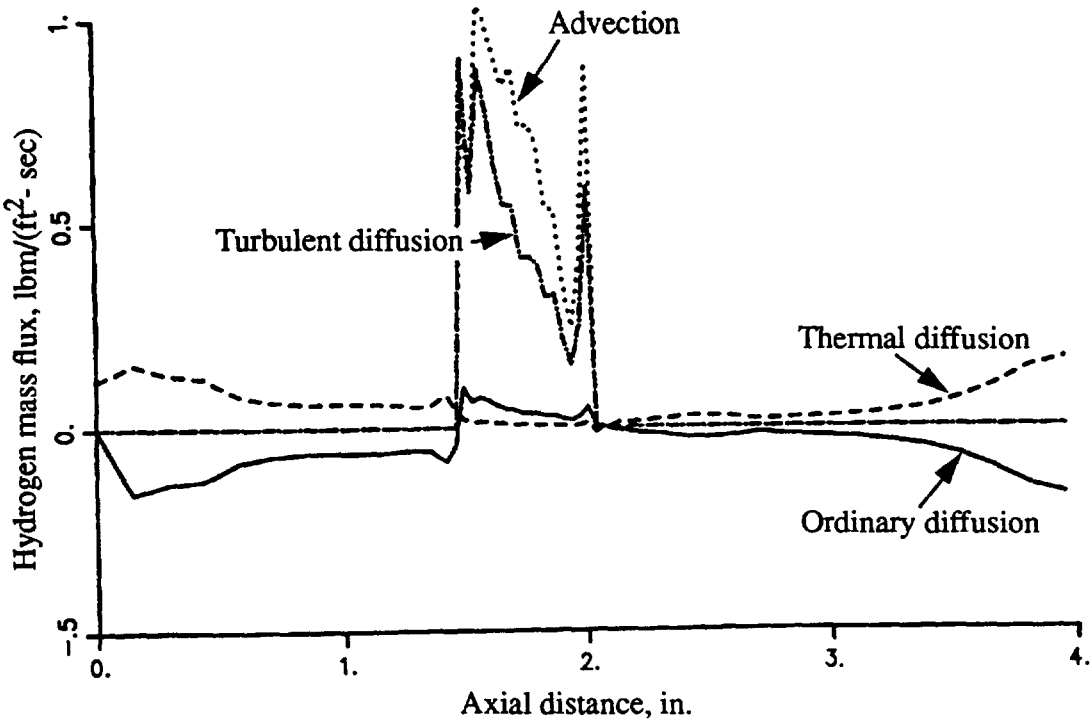

Figure 80. Predicted hydrogen mass fluxes along the wall of the transpiration cooled plug and spool rocket nozzle using a rough wall analysis.

7.3.4.4. Heat flux predictions

The individual contributions of the diffusion heat transfer components are presented in Figures 81 and 82 for the smooth and rough walled cases, respectively. The heat transfer rates due to conduction are seen to vary dramatically throughout the nozzle length. In the smooth wall results, the conduction flux decays significantly in the transpiration cooled section of the nozzle, being about 20 Btu/(in.^{2}-sec) just prior to the transpiration cooled section and decaying to values of less than 10 Btu/(in.^{2}-sec) in the transpiration cooled section. The effect of this film cooling is actually even greater than suggested as the conduction heat flux would normally (i.e., if the wall were solid) be expected to

increase by 50 % in this region as the result of flow acceleration (Reference 45). In the rough walled analysis, the conduction heat flux is seen to oscillate much more significantly with the general tendency of the conduction flux to rise rapidly at the initial section of the roughened/transpired section, proceeded by a sharp decay in temperature gradients in the final half of the transpiration cooled section as the prescribed wall temperature begins to rise.

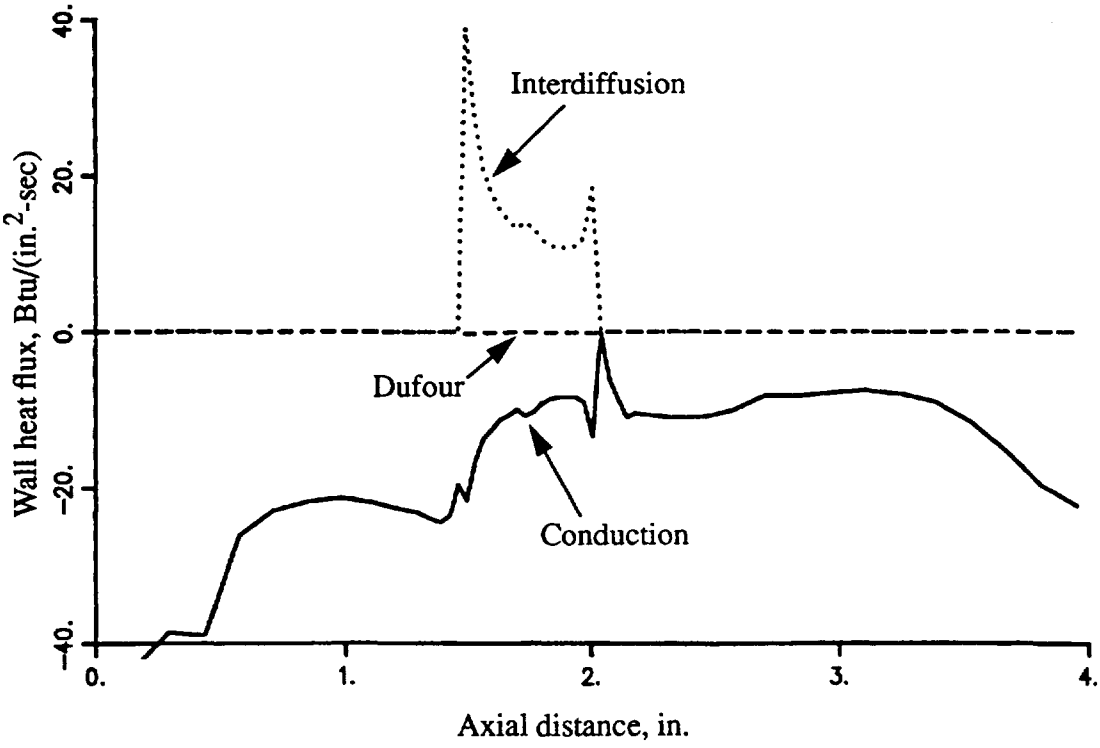

Figure 81. Predicted heat flux into the mainstream of the plug and spool rocket nozzle using a smooth wall analysis.

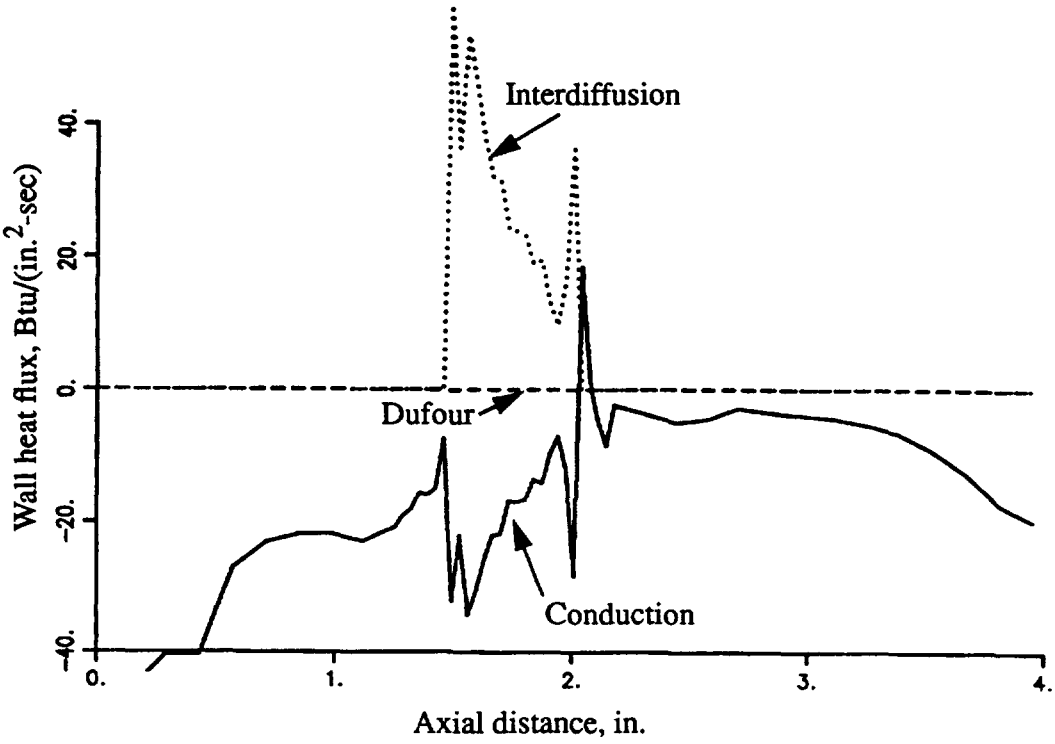

Figure 82. Predicted heat flux into the mainstream of the plug and spool rocket nozzle using a rough wall analysis.

Unlike conduction, the flux of heat as the result of interdiffusional heat transfer is observed to be directed into the main stream of the flow. Since the expression for interdiffusional heat transfer is the product of the mass flux of hydrogen (which is positive in the transpiration cooled section) and the difference between the enthalpy of hydrogen and steam, the diffusion heat flux will be rather large as the enthalpy of hydrogen is near zero at the prescribed spoolpiece wall temperatures but the enthalpy of steam is very large and very negative at the same wall conditions.

A final observation to be made is that the flux of heat as the result of Dufour energy transfer is negligible in both of the analyses performed.

SECTION 8

CONCLUSIONS

A model for the prediction of rocket nozzle performance and heat transfer has been developed and demonstrated for a rather wide spectrum of nozzle geometries and boundary conditions, with the overall conclusion to be drawn that the flowfield model is both extremely versatile and extremely accurate for propulsive nozzle flow simulations. In many aspects, the model is the most comprehensive in the world, as the flow modelling is conservative for both inviscid and viscous flows, and contains a comprehensive capability to model multispecies ordinary diffusion, thermal diffusion, Dufour heat transfer, and chemical kinetics, and is further enhanced by the use of a reference plane method of characteristics at computational boundaries.

The Tethys methodology consistently predicted rocket nozzle thrust coefficient to values within 0.5 % of experimental measurements, and it predicted heat fluxes extremely well under a variety of different nozzle geometries and operating conditions. Furthermore, wall static pressure predictions agreed extremely well with experimental measurements, with the Tethys model predicting kinks and jumps in wall pressure that were either experimentally verified or fully anticipated due to theoretical considerations.

Additional conclusions to be drawn from this modelling effort as regards the modelling of chemical rocket engines in the demonstration studies are contained below.

Soret mass transfer considerations can significantly affect species mass transfer and mass concentrations. In a solid wall region, the thermal mass transfer term resulted in significant changes in species concentrations predictions while yielding only a slight change in heat flux predictions. This is reasoned to be due to the fact that the species flux is zero near a solid wall region. Consequently the potential impact of Soret diffusion on heat transfer is by the change in fluid transport properties, and in the one demonstration case

examined, the change was not appreciable. In a transpiration cooled rocket nozzle, the Soret mass transfer term was a significant diffusion parameter at the wall, provided the surface of the rocket was smooth.

Dufour heat transfer is relatively small. Since the diffusion coefficient in interdiffusional heat transfer contains the difference in enthalpy between two species while that of Dufour heat transfer is the difference in molecular weight, a system comprised primarily of excess fuel and combustion products will likely have a far greater interdiffusional heat transfer rate than Dufour heat transfer.

Chemical kinetics has a significant effect on nozzle performance. In the 1030:1 high area ratio nozzle examined, the performance difference between finite rate chemical kinetics and frozen flow was significantly greater than for other effects.

The viscous, chemically reacting, reference plane method of characteristics is very well suited for chemically reacting rocket nozzle inlets and exhausts. Even in the viscous regions, the reference plane characteristics method performed admirably. The method also proved useful when applied to a stratified flow/film cooled inlet nozzle boundary.

The reference plane method of characteristics can be used on solid surfaces. While similar to the specification of normal pressure gradient under most conditions, the boundary condition appeared superior for the transient stability of the flowfield.

Surface roughness can have an appreciable effect on the coolant requirements of a transpiration cooled nozzle. While the data from the test case examined were rather incomplete, it can be reasonably concluded that the design and fabrication of the transpiration coolant system employed coolant slots and channels that were far too coarse for the extremely thin boundary layers that exist on propulsive nozzles. Consequently, all future transpiration cooling systems need to consider the potential of significantly reduced performance due to surface roughness considerations.

Coring of the centerline region of the nozzle can be used to restrict flowfield computations to regions of physical significance. In the 1030:1 high area ratio nozzle analysis, the centerline region was only 20 % of the length of the wall and allowed significantly greater packing in regions of importance.

SECTION 9

RECOMMENDATIONS

As with the development of almost all good engineering tools, areas requiring further investigation increase with the greater understanding of the real flowfield requirements. Besides the perpetual need for greater documentation and demonstration cases, and the need to extend the modelling to three-dimensional systems, specific improvements of the Tethys model in the following areas are recommended and are discussed in greater detail:

- Enhanced turbulence modelling
- Inclusion of radiation heat transfer
- Extension to other gaseous propulsion systems
- Enhanced characteristic boundary conditions
- Enhanced Neumann boundary conditions
- Enhanced artificial diffusion modelling
- Improved flowfield conservation
- Reduced computational requirements

Other areas of chemical propulsion consideration, such as solid particulate or liquid droplet interactions, are features that may be better suited to other computer models.

Enhanced modelling of the fluid flowfield can be realized by the inclusion of more advanced turbulence models. The k-ε equations for modelling turbulence are currently available in the newest version of Proteus and have been pasted into the Tethys code, awaiting implementation by the inclusion of appropriate calling, reading, and writing commands. Consequently, a more advanced modelling of the turbulent viscosity is readily obtained. However, the real arena in which turbulence modelling of a multispecies

chemical rocket engine needs to be advanced is in the adequate modelling of the turbulent Prandtl and Lewis numbers. Throughout the demonstration studies, both the turbulent Prandtl number and the turbulent Lewis number were set equal to a constant, which was obtained by a 'best guess' type of engineering reasoning based on experimental measurements of a similar situation. More sophisticated models assume that the turbulence is a function of the laminar Prandtl number and the turbulent viscosity. However, in the presence of more complex boundary conditions, such as surface roughness, the turbulent Prandtl number may be several orders of magnitude in error, since the application of the surface roughness model does not decompose drag into the components of skin friction and form drag, thereby invalidating the relations between momentum and heat transfer. Further, the turbulent Prandtl number may be significantly different in the transpiration cooled region of a rocket nozzle because the viscous transport modes of heat transfer are comprised of interdiffusional and Dufour heat transfer terms in addition to traditional heat transfer by conduction. In a similar manner, the turbulent Lewis number is undoubtedly a function of the strength of the Soret thermal diffusion term in addition to the gradients of all of the species present. Since thermal diffusion may result in species gradients even along solid wall boundaries, the need for improved modelling of the turbulent Lewis number is a more encompassing requirement. Consequently, it is the belief of the author that primary effort on turbulence modelling of chemical rocket engines focus on the unique aspects of heat and mass transfer in a chemical rocket engine while making use of the best available turbulent viscosity models.

Inclusion of a radiation heat transfer model would enhance the predictive capabilities of both nozzle performance and more significantly, nozzle heat transfer. While this is primarily true for the combustion chamber region of the nozzle, some amount of radiative heating of the nozzle wall and other cold regions will occur throughout the converging-diverging portion of the nozzle and the fluid dynamics model should include this potentially important heat transfer mode.

Currently, the Tethys model is capable of modelling the flow characteristics of nearly any ideal gas system with the caveat that, unless the fluid is comprised of a hydrogen/oxygen system, the fluid can not be subjected to any chemical reactions or species diffusion

and is limited to a maximum of six chemical species. Since this is a rather serious restriction, the model should be extended to at least eight chemically reacting and diffusing species equations.

Enhanced characteristic boundary condition modelling requirements include improved methods of modelling flow conditions at fluid corners and along the centerline and improving the reasoning involved in the establishment of the boundary conditions needed. Improving the flow solution along the corner points of the flowfield offers the promise of increased numerical stability and accuracy. Enhanced centerline modelling is also critical since geometries that contain strong shock waves near the centerline are incompatible with the constant entropy assumption. The reasoning involving the switch from a characteristic relation to the specification of the static pressure at the outflow region of a nozzle also needs to be improved in order to more accurately assess the performance and heat transfer characteristics of a nozzle near the exhaust region. These aspects of improved boundary condition modelling will all be discussed in greater detail in the paragraphs to follow.

Centerline boundary conditions need to be improved to enhance the ability of the Tethys model to predict shock waves and chemical reactions. Since the centerline of the nozzle represents a fluid pathline, a new set of characteristic relations needs to be developed for application in this region, along with a means of implicitly formulating the species source terms along this pathline.

Currently, the Tethys model employs all characteristic relations when the fluid contravarient velocity (normalized) is greater than the speed of sound, but uses one Dirichlet boundary condition (specification of static pressure) when the contravarient velocity is less than the speed of sound. In reality, this is a distortion from what is actually appropriate since the static pressure should only be specified when the real fluid velocity is less than the speed of sound. In regions where the contravarient velocity is less than the speed of sound but the actual fluid velocity is not, a new boundary condition to replace that currently being applied needs to be investigated. An alternative characteristics method, the bicharacteristic method, does not have this analytical shortcoming and should also be considered.

Neumann boundary conditions, as applied to the solid or transpired surface of a rocket engine, should be extended to be conservative. Due to the complexity of a chemical rocket engine analysis, maximization of solution accuracy with a minimal amount of computational grid points is highly desirable. Changing to a conservative boundary condition formulation offers the promise of improved solution accuracy and reduced computational requirements.

Artificial diffusion modelling in the Tethys code, which was simply extended from the Proteus code, was shown in the validation studies to be nonconservative for a radial flow system. Since these relations were undoubtedly developed for a cartesian coordinate system and then applied to an axisymmetric coordinate system, this finding is not surprising, although it is very bothersome. Since the computational effort necessary for the calculation of the artificial diffusion terms is essentially negligible, far greater emphasis directed towards complete inviscid flow conservation should be pursued.

Further conservation properties of the flowfield should also be pursued. The current formulation of the flow variables is designed such that all of the gradient terms are conservative when the flow variables of concern are constant. In the authors terminology, this is only a first-order conservative system, whereas a second-order conservative system exists when the flowfield is completely satisfied for a linear property gradient existing in the flowfield. If this condition were satisfied, Couette flow modelling would be exact. That is, in the same exacting manner that the author insured that some shear stress terms were equal to zero in a Couette flow condition, the same exactness needs to be applied to the inviscid terms to insure that they are also equal to zero in a Couette flow simulation.

The computational resources required of a complete Tethys flowfield simulation were extensive. Advanced computational techniques, such as multigrid acceleration techniques, and Runge-Kutta time step marching methods, should be considered as a means of improving the flowfield convergence rate. Likewise, reformulation of the implicit operators, such as a linearized flux splitting method and/or decoupling of the species transfer equations from the continuity, momentum, and energy equations, may significantly reduce the computational requirements of a chemically reacting nozzle flowfield problem.

LIST OF REFERENCES

LIST OF REFERENCES

1. Nickerson, G. R., Coats, D. E., and Dang, L. D., Engineering and Programming Manual: Two-Dimensional Kinetics Reference Computer Program (TDK). (SN-63, Software and Engineering Associates, NASA Contract NAS8-35931.) NASA CR-178628, 1985.

2. Kim, S. C., and Overbeke, T. J., Calculations of Gaseous Hydrogen/Oxygen Thruster, AIAA Paper 90-2490, 1990.

3. Reed, B. D., Penko, P. F., Schneider, S. J., and Kim, S. C., Experimental and Analytical Comparison of Flowfields in a 110 N (25 Lbf) H_2/O_2 Rocket, AIAA-91-2283, 1991.

4. Zupanc, Frank J., and Weiss, Jonathan M., Rocket Plume Flowfield Characterization Using Laser Rayleigh Scattering, AIAA Paper 92-3351, 1992.

5. Towne, Charles E., Schwab, John R., and Bui, Trong T., Proteus Two-Dimensional Navier-Stokes Computer Code-Version 2.0 Volume 1-Analysis Description, NASA TM-106336, 1993.

6. Towne, Charles E., Schwab, John R., and Bui, Trong T., Proteus Two-Dimensional Navier-Stokes Computer Code-Version 2.0 Volume 2-User's Guide, NASA TM-106338, 1993.

7. Towne, Charles E., Schwab, John R., and Bui, Trong T., Proteus Two-Dimensional Navier-Stokes Computer Code-Version 2.0 Volume 3-Programmer's Reference, NASA TM-106338, 1993.

8. Bird, R. Byron, Stewart, Warren E., and Lightfoot, Edwin N., Transport Phenomena, John Wiley and Sons, 1960.

9. Baumeister, Theodore, Avallone, Eugene A., and Baumeister, Theodore III, Marks' Handbook for Mechanical Engineers, McGraw-Hill, 1978.

10. Bittker, D. A., and Sculin, V. J., GCKP84 - General Chemical Kinetics Code for Gas-Phase Flow and Batch Processes Including Heat Transfer Effects, NASA TP-2320, 1984.

11. Arrhenius, S. A., Zeitschrift fur Physikalische Chemie, Volume 4, p. 266, 1889.

12. Rubesin, M. W., and Rose, W. C., The Turbulent Mean-Flow, Reynolds-Stress, and Heat-Flux Equations in Mass-Averaged Dependent Variables, NASA TM X-62248, 1973.

13. Incropera, Frank P., Dewitt, David P., Fundamentals of Heat Transfer, John Wiley and Sons, 1981.

14. Kays, W. M., and Crawford, M. E., Convective Heat and Mass Transfer, McGraw-Hill, 1980.

15. Rockwell International, Space Shuttle Main Engine, Publication RI/RD87-142, 1987.

16. Brown, Jim, Expander Cycle Engines for Shuttle Cryogenic Upperstages, AIAA Paper 83-1311, 1983.

17. Robinson, P. J., Space Station Auxiliary Thrust Chamber Technology Final Report, Contract NAS 3-24398, 1990.

18. Reed, Brian D., Testing and Evaluation of Oxide-Coated Iridium/Rhenium Chambers, NASA TM-106442, 1994.

19. Radhakrishnan, Krishnan, and Bittker, David A., LSENS, A General Chemical Kinetics and Sensitivity Analysis Code for Gas-Phase Reactions: User's Guide, NASA TM-105851, 1993.

20. Driscoll, David Infante, Calculation of Nozzle/Aftbody Flowfield Interactions, Ph.D. Thesis, Purdue University, 1991.

21. Hoffman, J. D., The Method of Characteristics applied to Unsteady, One-, Two-, and Three-Dimensional Flows, Thermal Science and Propulsion Center, School of Mechanical Engineering, Purdue University, West Lafayette, Indiana, Report TR-80-07.

22. Marcum, D. L., and Hoffman, J. D., Calculation of Three-Dimensional Flowfields by the Unsteady Method of Characteristics, AIAA Journal, Volume 23, Number 10, pp. 1497-1505, 1985.

23. Zucrow, Maurice J., and Hoffman, Joe D., Gas Dynamics, Volume II, John Wiley and Sons, 1977.

24. Beam, R. M., and Warming, R. F., An Implicit Factored Scheme for the Compressible Navier-Stokes Equations, AIAA Journal, Volume 16, Number 4, pp. 393-402.

25. Cooper, G. K., The PARC Code: Theory and Usage, AEDC TR-87-24, 1987.

26. Shuen, Jian Shun, and Yoon, Seokkwan, Numerical Study of Chemically Reacting Flows Using an LU Scheme, AIAA-88-0436, 1988.

27. Courant, R., Friedrichs, K. O. and Lewy, H., Uber die Partiellen Differenzialgleichungen der Mathematischen Physik, Mathematische Annalen, Volume 100, pp. 32-74.

28. Knight, C. J., and Choi, D., Development of a Viscous Cascade Code Based on Scalar Implicit Factorization, AIAA Journal, Volume 27, Number 5, pp. 581-594.

29. Pulliam, T. H., Artificial Dissipation Models for the Euler Equations, AIAA Journal, Volume 24, Number 12, pp. 1931-1940, 1986.

30. Cuffel, R. F., Back. L. H., and Massier, P. F., Transonic Flowfield in a Supersonic Nozzle with Small Throat Radius of Curvature, AIAA Journal, Volume 7, Number 7, pp 1364-1366, 1969.

31. Pavli, Albert J., Kacynski, Kenneth J., and Smith, Tamara A., Experimental Thrust Performance of a High-Area-Ratio Rocket Nozzle, NASA TP-2720, 1987.

32. Kacynski, Kenneth J., Pavli, Albert J., and Smith, Tamara A., Experimental Evaluation of Heat Transfer on a 1030:1 Area Ratio Rocket Nozzle, NASA TP-2726, 1987.

33. Smith, Tamara A., Pavli, Albert J., and Kacynski, Kenneth J., Comparison of Theoretical and Experimental Thrust Performance of a 1030:1 Area Ratio Rocket Nozzle at a Chamber Pressure of 2413 kN/m^2 (350 psia), NASA TP-2725, 1987.

34. Davidian, Kenneth J., Dieck, Ronald H., and Chuang, Isaac, A Detailed Description of the Uncertainty Analysis for High Area Ratio Rocket Nozzle Tests at the NASA Lewis Research Center, NASA TM-100203, 1987.

35. Pauley, L .L., and Dagher, S. N., A Numerical Investigation of Supersonic Nozzle Boundary Layer Transition, AIAA 91-3559, 1991.

36. Anderson, Dale A., Tannehill, John C., and Pletcher, Richard H., Computational Fluid Mechanics and Heat Transfer, Hemisphere Publishing Company, 1984.

37. Kim, S., Numerical Study of High-Area Ratio H2/O2 Rocket Nozzles, AIAA-91-2434, 1991.

38. Morren, Sybil Huang, Myers, Roger M., Benko, Stephen E., Arrington, Lynn A., and Reed, Brian D., A Laboratory Model of a Hydrogen/Oxygen Engine for Combustion and Nozzle Studies, AIAA-93-1825, 1993.

39. Arrington, Lynn A., and Reed, Brian D., Performance Comparison of Axisymmetric and Three-Dimensional Hydrogen Film Coolant Injection in a 110N Hydrogen/Oxygen Rocket, AIAA-92-3390, 1992.

40. de Groot, W. A., and Tsuei, H. H., Gaseous Hydrogen/Oxygen Performance Characterization, NASA CR-194464, 1994.

41. Gortler, H., Z. Angew. Math. Mech., vol. 22, pp. 244-254, 1939.

42. Van der Hegge Zijnen, B. G., Appl. Sci. Res., Volume 7A, page 277, 1958.

43. Blackwelder, Ron F., and Kovasnay, Leslie S. G., Large Scale Motion of a Turbulent Boundary Layer During Relaminarization, J. Fluid Mechanics, Volume 53, pp. 61-83, 1972.

44. Valler, H. W., Performance of a Transpiration Cooled Rocket Thrust Chamber, NASA CR-159742, 1979.

45. Quentmeyer, Richard J., and Roncase, Elizabeth A., Hot-Gas-Side Heat Transfer Characteristics of Subscale, Plug Nozzle Rocket Calorimeter Chamber, NASA TP-3380, 1993.

46. Zucrow, Maurice J., and Hoffman, Joe D., Gas Dynamics, Volume I, John Wiley and Sons, 1977.

47. Hirschfelder, Joseph O., Curtiss, Charles F., and Bird, R. Byron, Molecular Theory of Gases and Liquids, John Wiley and Sons, 1954.

48. Van der Valk, F., Thermal Diffusion in Ternary Mixtures, Physica, Volume 29, pp. 417-426, 1963.

49. Radhakrishnan, Krishnan, and Bittker, David A., LSENS, A General Chemical Kinetics and Sensitivity Analysis Code for Gas-Phase Reactions. Part I, Theory and Numerical Solution Procedures, NASA Reference Publication to be published in 1994.

50. Gordon, Sanford, and McBride, Bonnie J., Computer Program for Calculation of Complex Chemical Equilibrium Compositions, Rocket Performance, Incident and Reflected Shocks, and Chapman-Jouget Detonations, NASA SP-273, 1976.

51. Boussinesq, V. J., Essai Sur La Theorie Des Eaux Courantes, Mem. Presentes Acad. Sci., Paris, Volume 23, pp. 46, 1877.

52. Baldwin, B. S., and Lomax, H., Thin Layer Approximation and Algebraic Model for Separated Turbulent Flows, AIAA Paper 78-257, 1978.

53. Smith, A. M. O., and Cebeci, T., Numerical Solution of the Turbulent Boundary Layer Equations, Douglas Aircraft Company Report Number DAC33735, 1967.

54. Cebeci, Tuncer, and Smith, A. M. O., Analysis of Turbulent Boundary Layers, Academic Press, 1974.

55. Bittker, David A., Detailed Mechanism for Oxidation of Benzene, Combustion Science and Technology, Volume 79, pp. 49-72, 1991.

56. Svehla, Roger A., Thermodynamic and Transport Properties for the Hydrogen-Oxygen System, NASA SP-3011, 1964.

57. Ibbs, T. L., Grew, K. E., Hirst, A. A., Thermal Diffusion at Low Temperatures, Proc. Phys. Soc., Volume 41, pp. 456-475., 1929.

58. Nickerson, Gary R., Comparison and Evaluation of Computer Program Results for Rocket Engine Performance Prediction, NASA Contract NAS 7-443, 1967.

59. White, Frank M., Viscous Fluid Flow, McGraw-Hill, 1974.

60. Chemical Propulsion Information Agency, CPIA 245: JANNAF Rocket Engine Performance Test Data Acquisition and Interpretation Manual, The John Hopkins University, 1975.

61. Walpole, Ronald E., and Myers, Raymond H., Probability and Statistics for Engineers and Scientists, Macmillan Publishing Company, 1993.

APPENDICES

Appendix A

Interior Point Numerical Algorithm of the Proteus Code

The methodology employed for the solution of axisymmetric flow problems in the Proteus code (Reference 5) is presented in this appendix, which is a reproduction of Appendix B in Reference 5. Although nomenclature and equation numbering represent those employed in the Proteus report, they are consistent with those used throughout the present work. The references cited within Appendix B of the Proteus manual are cited at the end of this appendix. It should be noted that the Proteus model has the capability of modelling swirling flow in the axisymmetric coordinate system, which is a feature not considered in the present work.

B. AXISYMMETRIC ANALYSIS

The analysis used in *Proteus* for axisymmetric flow is essentially the same as for two-dimensional planar flow, described in the main body of this report. However, there are some additional terms in the axisymmetric equations that complicate things somewhat. For that reason, the axisymmetric analysis is described separately in this appendix.

B.1 GOVERNING EQUATIONS

In cylindrical coordinates, the governing equations for axisymmetric flow, with swirl, can be written using vector notation as

$$\frac{\partial(r\mathbf{Q})}{\partial t}+\frac{\partial(r\mathbf{E})}{\partial x}+\frac{\partial(r\mathbf{F})}{\partial r}+\mathbf{H}=\frac{\partial(r\mathbf{E}_V)}{\partial x}+\frac{\partial(r\mathbf{F}_V)}{\partial r}+\mathbf{H}_V \tag{B.1}$$

where

$$\mathbf{Q}=\begin{bmatrix}\rho & \rho u & \rho v & \rho w & E_T\end{bmatrix}^T \tag{B.2a}$$

$$\mathbf{E}=\begin{bmatrix}\rho u\\ \rho u^2+p\\ \rho uv\\ \rho uw\\ (E_T+p)u\end{bmatrix} \tag{B.2b}$$

$$\mathbf{F}=\begin{bmatrix}\rho v\\ \rho uv\\ \rho v^2+p\\ \rho uw\\ (E_T+p)v\end{bmatrix} \tag{B.2c}$$

$$\mathbf{H}=\begin{bmatrix}0\\ 0\\ -p-\rho w^2\\ \rho vw\\ 0\end{bmatrix} \tag{B.2d}$$

$$\mathbf{E}_V = \frac{1}{Re_r}\begin{bmatrix} 0 \\ \tau_{xx} \\ \tau_{xr} \\ \tau_{x\theta} \\ u\tau_{xx} + v\tau_{xr} + w\tau_{x\theta} - \dfrac{1}{Pr_r} q_x \end{bmatrix} \tag{B.}$$

$$\mathbf{F}_V = \frac{1}{Re_r}\begin{bmatrix} 0 \\ \tau_{xr} \\ \tau_{rr} \\ \tau_{r\theta} \\ u\tau_{xr} + v\tau_{rr} + w\tau_{r\theta} - \dfrac{1}{Pr_r} q_r \end{bmatrix} \tag{B}$$

$$\mathbf{H}_V = \frac{1}{Re_r}\begin{bmatrix} 0 \\ 0 \\ -\tau_{\theta\theta} \\ \tau_{r\theta} \\ 0 \end{bmatrix} \tag{B.}$$

Equation (B.1) thus represents, in order, the continuity, x-momentum, r-momentum, θ-momentum (swirl), energy equations, with dependent variables ρ, ρu, ρv, ρw, and E_T. Note that the additional terms in these axisymmetric equations destroy the strong conservation law form of the two-dimensional planar equations presented in Section 2.1. Unfortunately, the axisymmetric form of the equations cannot be put into strong conservation law form (Vinokur, 1974.)

The shear stresses and heat fluxes are given by

$$\tau_{xx} = 2\mu\frac{\partial u}{\partial x} + \lambda\left[\frac{\partial u}{\partial x} + \frac{1}{r}\left(\frac{\partial (rv)}{\partial r}\right)\right]$$

$$\tau_{rr} = 2\mu\frac{\partial v}{\partial r} + \lambda\left[\frac{\partial u}{\partial x} + \frac{1}{r}\left(\frac{\partial (rv)}{\partial r}\right)\right]$$

$$\tau_{\theta\theta} = 2\mu\frac{v}{r} + \lambda\left[\frac{\partial u}{\partial x} + \frac{1}{r}\left(\frac{\partial (rv)}{\partial r}\right)\right]$$

$$\tau_{xr} = \mu\left(\frac{\partial u}{\partial r} + \frac{\partial v}{\partial x}\right) \tag{I}$$

ORIGINAL PAGE IS
OF POOR QUALITY

$$\tau_{x\theta} = \mu \frac{\partial w}{\partial x}$$

$$\tau_{r\theta} = \mu\left(\frac{\partial w}{\partial r} - \frac{w}{r}\right)$$

$$q_x = -k \frac{\partial T}{\partial x}$$

$$q_r = -k \frac{\partial T}{\partial r}$$

In these equations, x, r, and θ represent the axial, radial, and circumferential directions, respectively; and u, v, and w represent the velocities in those directions. The remaining symbols are the same as those in the two-dimensional equations described in Section 2.1.

For turbulent flow, μ, λ, and k represent effective coefficients. The turbulence model is described in Section 9.0. The only modification to the model for axisymmetric flow is the definition of $|\vec{\Omega}|$, the magnitude of the total vorticity. For axisymmetric flow,

$$|\vec{\Omega}| = \left[\left(\frac{\partial w}{\partial r} + \frac{w}{r}\right)^2 + \left(\frac{\partial w}{\partial x}\right)^2 + \left(\frac{\partial v}{\partial x} - \frac{\partial u}{\partial r}\right)^2\right]^{1/2}$$

When the generalized grid transformation of Section 2.3 (with y replaced by r), is applied to equation (B.1) the result is

$$(r\mathbf{Q})_\tau + (r\mathbf{Q})_\xi \xi_t + (r\mathbf{Q})_\eta \eta_t + (r\mathbf{E})_\xi \xi_x + (r\mathbf{E})_\eta \eta_x + (r\mathbf{F})_\xi \xi_r + (r\mathbf{F})_\eta \eta_r + \mathbf{H}$$
$$-(r\mathbf{E}_V)_\xi \xi_x - (r\mathbf{E}_V)_\eta \eta_x - (r\mathbf{F}_V)_\xi \xi_r - (r\mathbf{F}_V)_\eta \eta_r - \mathbf{H}_V = 0 \qquad \text{(B.4)}$$

Although this axisymmetric equation cannot be put into exact strong conservation law form, the procedure used to do so for the two-dimensional equation, described in Section 2.4, is nonetheless applied to equation (B.4). The result is

$$\frac{\partial(r\hat{\mathbf{Q}})}{\partial \tau} + \frac{\partial(r\hat{\mathbf{E}})}{\partial \xi} + \frac{\partial(r\hat{\mathbf{F}})}{\partial \eta} + \hat{\mathbf{H}} = \frac{\partial(r\hat{\mathbf{E}}_V)}{\partial \xi} + \frac{\partial(r\hat{\mathbf{F}}_V)}{\partial \eta} + \hat{\mathbf{H}}_V \qquad \text{(B.5)}$$

where

$$\hat{\mathbf{Q}} = \frac{\mathbf{Q}}{J}$$

$$\hat{\mathbf{E}} = \frac{1}{J}(\mathbf{E}\xi_x + \mathbf{F}\xi_r + \mathbf{Q}\xi_t)$$

$$\hat{\mathbf{F}} = \frac{1}{J}(\mathbf{E}\eta_x + \mathbf{F}\eta_r + \mathbf{Q}\eta_t)$$

$$\hat{\mathbf{H}} = \frac{\mathbf{H}}{J}$$

$$\hat{\mathbf{E}}_V = \frac{1}{J}(\mathbf{E}_V\xi_x + \mathbf{F}_V\xi_r)$$

$$\hat{\mathbf{F}}_V = \frac{1}{J}(\mathbf{E}_V\eta_x + \mathbf{F}_V\eta_r)$$

$$\hat{\mathbf{H}}_V = \frac{\mathbf{H}_V}{J}$$

Using equations (B.2a) through (B.2g) these can be expanded as

$$\hat{\mathbf{Q}} = \frac{1}{J}\begin{bmatrix}\rho & \rho u & \rho v & \rho w & E_T\end{bmatrix}^T \qquad \text{(B}$$

$$\hat{\mathbf{E}} = \frac{1}{J}\begin{bmatrix} \rho u\xi_x + \rho v\xi_r + \rho\xi_t \\ (\rho u^2 + p)\xi_x + \rho uv\xi_r + \rho u\xi_t \\ \rho uv\xi_x + (\rho v^2 + p)\xi_r + \rho v\xi_t \\ \rho uw\xi_x + \rho vw\xi_r + \rho w\xi_t \\ (E_T + p)u\xi_x + (E_T + p)v\xi_r + E_T\xi_t \end{bmatrix} \qquad \text{(B}$$

$$\hat{\mathbf{F}} = \frac{1}{J}\begin{bmatrix} \rho u\eta_x + \rho v\eta_r + \rho\eta_t \\ (\rho u^2 + p)\eta_x + \rho uv\eta_r + \rho u\eta_t \\ \rho uv\eta_x + (\rho v^2 + p)\eta_r + \rho v\eta_t \\ \rho uw\eta_x + \rho vw\eta_r + \rho w\eta_t \\ (E_T + p)u\eta_x + (E_T + p)v\eta_r + E_T\eta_t \end{bmatrix} \qquad \text{(B}$$

$$\hat{\mathbf{H}} = \frac{1}{J}\begin{bmatrix} 0 \\ 0 \\ -p - \rho w^2 \\ \rho vw \\ 0 \end{bmatrix} \qquad \text{(B}$$

$$\hat{\mathbf{E}}_V = \frac{1}{J}\frac{1}{Re_r}\begin{bmatrix} 0 \\ \tau_{xx}\xi_x + \tau_{xr}\xi_r \\ \tau_{xr}\xi_x + \tau_{rr}\xi_r \\ \tau_{x\theta}\xi_x + \tau_{r\theta}\xi_r \\ \beta_x\xi_x + \beta_r\xi_r \end{bmatrix} \tag{B.6e}$$

$$\hat{\mathbf{F}}_V = \frac{1}{J}\frac{1}{Re_r}\begin{bmatrix} 0 \\ \tau_{xx}\eta_x + \tau_{xr}\eta_r \\ \tau_{xr}\eta_x + \tau_{rr}\eta_r \\ \tau_{x\theta}\eta_x + \tau_{r\theta}\eta_r \\ \beta_x\eta_x + \beta_r\eta_r \end{bmatrix} \tag{B.6f}$$

$$\hat{\mathbf{H}}_V = \frac{1}{J}\frac{1}{Re_r}\begin{bmatrix} 0 \\ 0 \\ -\tau_{\theta\theta} \\ \tau_{r\theta} \\ 0 \end{bmatrix} \tag{B.6g}$$

where

$$\beta_x = u\tau_{xx} + v\tau_{xr} + w\tau_{x\theta} - \frac{1}{Pr_r}q_x \tag{B.7a}$$

$$\beta_r = u\tau_{xr} + v\tau_{rr} + w\tau_{r\theta} - \frac{1}{Pr_r}q_r \tag{B.7b}$$

B.2 LINEARIZATION

Solving equation (B.5) for $\partial\hat{\mathbf{Q}}/\partial\tau$ (assuming r is not a function of time) and substituting the result into the time differencing scheme of Beam and Warming, given by equation (3.1), for $\partial(\Delta\hat{\mathbf{Q}}^n)/\partial\tau$ and $\partial\hat{\mathbf{Q}}^n/\partial\tau$ yields

$$\begin{aligned}\Delta\hat{\mathbf{Q}}^n = &-\frac{\theta_1\Delta\tau}{1+\theta_2}\frac{1}{r}\left(\frac{\partial(r\Delta\hat{\mathbf{E}}^n)}{\partial\xi} + \frac{\partial(r\Delta\hat{\mathbf{F}}^n)}{\partial\eta} + \Delta\hat{\mathbf{H}}^n\right) - \frac{\Delta\tau}{1+\theta_2}\frac{1}{r}\left(\frac{\partial(r\hat{\mathbf{E}}^n)}{\partial\xi} + \frac{\partial(r\hat{\mathbf{F}}^n)}{\partial\eta} + \hat{\mathbf{H}}^n\right) \\ &+ \frac{\theta_1\Delta\tau}{1+\theta_2}\frac{1}{r}\left(\frac{\partial(r\Delta\hat{\mathbf{E}}_V^n)}{\partial\xi} + \frac{\partial(r\Delta\hat{\mathbf{F}}_V^n)}{\partial\eta} + \Delta\hat{\mathbf{H}}_V^n\right) + \frac{\Delta\tau}{1+\theta_2}\frac{1}{r}\left(\frac{\partial(r\hat{\mathbf{E}}_V^n)}{\partial\xi} + \frac{\partial(r\hat{\mathbf{F}}_V^n)}{\partial\eta} + \hat{\mathbf{H}}_V^n\right) \\ &+ \frac{\theta_2}{1+\theta_2}\Delta\hat{\mathbf{Q}}^{n-1} + O\left[\left(\theta_1 - \frac{1}{2} - \theta_2\right)(\Delta\tau)^2, (\Delta\tau)^3\right]\end{aligned} \tag{B.8}$$

This equation must be linearized using the procedure described in Section 4.0.

B.2.1 Inviscid Terms

For the inviscid terms the Jacobian coefficient matrix $\partial\hat{\mathbf{E}}/\partial\hat{\mathbf{Q}}$ is

$$\frac{\partial\hat{\mathbf{E}}}{\partial\hat{\mathbf{Q}}} = \begin{bmatrix} \xi_t & \xi_x & \xi_y & 0 & 0 \\ \frac{\partial p}{\partial\rho}\xi_x - uf_1 & \xi_t + f_1 + u\xi_x + \frac{\partial p}{\partial(\rho u)}\xi_x & u\xi_r + \frac{\partial p}{\partial(\rho v)}\xi_x & \frac{\partial p}{\partial(\rho w)}\xi_x & \frac{\partial p}{\partial E_T}\xi_x \\ \frac{\partial p}{\partial\rho}\xi_r - vf_1 & v\xi_x + \frac{\partial p}{\partial(\rho u)}\xi_r & \xi_t + f_1 + v\xi_r + \frac{\partial p}{\partial(\rho v)}\xi_r & \frac{\partial p}{\partial(\rho w)}\xi_r & \frac{\partial p}{\partial E_T}\xi_r \\ -wf_1 & w\xi_x & w\xi_r & \xi_t + f_1 & 0 \\ -f_1\left(f_2 - \frac{\partial p}{\partial\rho}\right) & f_2\xi_x + f_1\frac{\partial p}{\partial(\rho u)} & f_2\xi_r + f_1\frac{\partial p}{\partial(\rho v)} & f_1\frac{\partial p}{\partial(\rho w)} & \xi_t + f_1\left(1 + \frac{\partial p}{\partial E_T}\right) \end{bmatrix} \quad (\text{I}$$

where $f_1 = u\xi_x + v\xi_r$ and $f_2 = (E_T + p)/\rho$. The Jacobian matrix $\partial\hat{\mathbf{F}}/\partial\hat{\mathbf{Q}}$ has the same form as $\partial\hat{\mathbf{E}}/\partial\hat{\mathbf{Q}}$, but wit replaced by η.

For the additional term $\hat{\mathbf{H}}$, the linearization procedure gives

$$\frac{\partial\hat{\mathbf{H}}}{\partial\hat{\mathbf{Q}}} = \begin{bmatrix} 0 & 0 & 0 & 0 & 0 \\ 0 & 0 & 0 & 0 & 0 \\ -\frac{\partial p}{\partial\rho} + w^2 & -\frac{\partial p}{\partial(\rho u)} & -\frac{\partial p}{\partial(\rho v)} & -\frac{\partial p}{\partial(\rho w)} - 2w & -\frac{\partial p}{\partial E_T} \\ -vw & 0 & w & v & 0 \\ 0 & 0 & 0 & 0 & 0 \end{bmatrix} \quad (\text{B}$$

B.2.2 Viscous Terms

To linearize the viscous terms, $\hat{\mathbf{E}}_{V_1}$, $\hat{\mathbf{E}}_{V_2}$, etc., must first be rewritten in terms of the dependent variables, with derivatives in the cylindrical coordinate directions transformed to derivatives in the computational direct using the chain rule. The shear stress and heat flux terms, given by equations (B.3) and (B.7), become

$$\tau_{xx} = (2\mu + \lambda)(\xi_x u_\xi + \eta_x u_\eta) + \frac{\lambda}{r}\left[\xi_r(rv)_\xi + \eta_r(rv)_\eta\right]$$

$$\tau_{rr} = 2\mu(\xi_r v_\xi + \eta_r v_\eta) + \lambda(\xi_x u_\xi + \eta_x u_\eta) + \frac{\lambda}{r}\left[\xi_r(rv)_\xi + \eta_r(rv)_\eta\right]$$

$$\tau_{\theta\theta} = 2\mu\frac{v}{r} + \lambda(\xi_x u_\xi + \eta_x u_\eta) + \frac{\lambda}{r}\left[\xi_r(rv)_\xi + \eta_r(rv)_\eta\right]$$

$$\tau_{xr} = \mu(\xi_r u_\xi + \eta_r u_\eta + \xi_x v_\xi + \eta_x v_\eta)$$

$$\tau_{x\theta} = \mu(\xi_x w_\xi + \eta_x w_\eta)$$

$$\tau_{r\theta} = \mu(\xi_r w_\xi + \eta_r w_\eta) - \mu \frac{w}{r}$$

$$\beta_x = (2\mu + \lambda)(\xi_x u u_\xi + \eta_x u u_\eta) + \frac{\lambda}{r}\left[\xi_r u(rv)_\xi + \eta_r u(rv)_\eta\right]$$
$$+\mu(\xi_r v u_\xi + \eta_r v u_\eta + \xi_x v v_\xi + \eta_x v v_\eta) + \mu(\xi_x w w_\xi + \eta_x w w_\eta)$$
$$+\frac{k}{Pr_r}(\xi_x T_\xi + \eta_x T_\eta)$$

$$\beta_r = 2\mu(\xi_r v v_\xi + \eta_r v v_\eta) + \frac{\lambda}{r}\left[\xi_r v(rv)_\xi + \eta_r v(rv)_\eta\right]$$
$$+\mu(\xi_r u u_\xi + \eta_r u u_\eta + \xi_x u v_\xi + \eta_x u v_\eta) + \mu(\xi_r w w_\xi + \eta_r w w_\eta)$$
$$+\lambda(\xi_x v u_\xi + \eta_x v u_\eta) - \mu \frac{w^2}{r} + \frac{k}{Pr_r}(\xi_r T_\xi + \eta_r T_\eta)$$

The above expressions for the shear stress and heat flux terms are substituted into equations (B.6e) through (B.6g). As in the two-dimensional planar case, the cross derivative terms are separated from the non-cross derivative terms. In addition, for the axisymmetric case the non-derivative terms are included with the cross derivatives.

The resulting five elements of $\hat{\mathbf{E}}_{V_1}$ (excluding the $1/JRe_r$ coefficient) are

$$(\hat{\mathbf{E}}_{V_1})_1 = 0 \tag{B.11a}$$

$$(\hat{\mathbf{E}}_{V_1})_2 = 2\mu\xi_x^2 u_\xi + \lambda\xi_x\left[\xi_x u_\xi + \frac{1}{r}\xi_r(rv)_\xi\right] + \mu\xi_r(\xi_r u_\xi + \xi_x v_\xi) \tag{B.11b}$$

$$(\hat{\mathbf{E}}_{V_1})_3 = 2\mu\xi_r^2 v_\xi + \lambda\xi_r\left[\xi_x u_\xi + \frac{1}{r}\xi_r(rv)_\xi\right] + \mu\xi_x(\xi_r u_\xi + \xi_x v_\xi) \tag{B.11c}$$

$$(\hat{\mathbf{E}}_{V_1})_4 = \mu\xi_x^2 w_\xi + \mu\xi_r^2 w_\eta \tag{B.11d}$$

$$(\hat{\mathbf{E}}_{V_1})_5 = 2\mu(\xi_x^2 u u_\xi + \xi_r^2 v v_\xi) + \lambda\xi_x\left[\xi_x u u_\xi + \frac{1}{r}\xi_r u(rv)_\xi\right] + \lambda\xi_r\left[\xi_x v u_\xi + \frac{1}{r}\xi_r v(rv)_\xi\right]$$
$$+\mu\xi_x(\xi_r v u_\xi + \xi_x v v_\xi + \xi_x w w_\xi) + \mu\xi_r(\xi_r u u_\xi + \xi_x u v_\xi + \xi_r w w_\xi) + \frac{k}{Pr_r}(\xi_x^2 + \xi_r^2)T_\xi \tag{B.11e}$$

For linearization it is convenient to rewrite the last element as

$$(\hat{\mathbf{E}}_{V_1})_5 = \frac{(2\mu+\lambda)}{2}\left[\xi_x^2(u^2)_\xi + \xi_r^2(v^2)_\xi\right] + (\mu+\lambda)\xi_x\xi_r(uv)_\xi + \lambda\xi_r\frac{r_\xi}{r}(\xi_r v^2 + \xi_x uv)$$
$$+\frac{\mu}{2}\left[\xi_x^2(v^2+w^2)_\xi + \xi_r^2(u^2+w^2)_\xi\right] + \frac{k}{Pr_r}(\xi_x^2+\xi_r^2)T_\xi \qquad \text{(B.1}$$

The elements of $\hat{\mathbf{F}}_{V_1}$ have exactly the same form as those of $\hat{\mathbf{E}}_{V_1}$, but with ξ replaced by η.

The five elements of $\hat{\mathbf{E}}_{V_2}$ (again excluding the $1/JRe_r$ coefficient) are

$$(\hat{\mathbf{E}}_{V_2})_1 = 0 \qquad \text{(B.1}$$

$$(\hat{\mathbf{E}}_{V_2})_2 = 2\mu\xi_x\eta_x u_\eta + \lambda\xi_x\left[\eta_x u_\eta + \frac{1}{r}\eta_r(rv)_\eta\right] + \mu\xi_r(\eta_r u_\eta + \eta_x v_\eta) \qquad \text{(B.1}$$

$$(\hat{\mathbf{E}}_{V_2})_3 = 2\mu\xi_r\eta_r v_\eta + \lambda\xi_r\left[\eta_x u_\eta + \frac{1}{r}\eta_r(rv)_\eta\right] + \mu\xi_x(\eta_r u_\eta + \eta_x v_\eta) \qquad \text{(B.1}$$

$$(\hat{\mathbf{E}}_{V_2})_4 = \mu\xi_x\eta_x w_\eta + \mu\xi_r\eta_r w_\eta - \mu\xi_r\frac{w}{r} \qquad \text{(B.1}$$

$$(\hat{\mathbf{E}}_{V_2})_5 = 2\mu(\xi_x\eta_x uu_\eta + \xi_r\eta_r vv_\eta) + \lambda\xi_x\left[\eta_x uu_\eta + \frac{1}{r}\eta_r u(rv)_\eta\right] + \lambda\xi_r\left[\eta_x vu_\eta + \frac{1}{r}\eta_r v(rv)_\eta\right]$$
$$+\mu\xi_x(\eta_r vu_\eta + \eta_x vv_\eta + \eta_x ww_\eta) + \mu\xi_r(\eta_r uu_\eta + \eta_x uv_\eta + \eta_r ww_\eta) - \mu\xi_r\frac{w^2}{r} + \frac{k}{Pr_r}(\xi_x\eta_x + \xi_r\eta_r)T_\eta \qquad \text{(B.1}$$

The last element can be rewritten as

$$(\hat{\mathbf{E}}_{V_2})_5 = 2\mu(\xi_x\eta_x uu_\eta + \xi_r\eta_r vv_\eta) + \lambda\xi_x(\eta_x uu_\eta + \eta_r uv_\eta) + \lambda\xi_r(\eta_x vu_\eta + \eta_r vv_\eta) + \lambda\eta_r\frac{v}{r}(\xi_x u + \xi_r v)r_\eta$$
$$+\mu\xi_x(\eta_r vu_\eta + \eta_x vv_\eta + \eta_x ww_\eta) + \mu\xi_r(\eta_r uu_\eta + \eta_x uv_\eta + \eta_r ww_\eta) - \mu\xi_r\frac{w^2}{r} + \frac{k}{Pr_r}(\xi_x\eta_x + \xi_r\eta_r)T_\eta \qquad \text{(B.1}$$

The elements of $\hat{\mathbf{F}}_{V_2}$ have exactly the same form as those of $\hat{\mathbf{E}}_{V_2}$, but with ξ replaced by η and η replaced by ξ.

The five elements of $\hat{\mathbf{H}}_V$ are

$$(\hat{\mathbf{H}}_V)_1 = 0 \qquad \text{(B.1}$$

$$(\hat{\mathbf{H}}_V)_2 = 0 \qquad \text{(B.1}$$

$$(\hat{\mathbf{H}}_V)_3 = -2\mu\frac{v}{r} - \lambda(\xi_x u_\xi + \eta_x u_\eta) + \frac{\lambda}{r}\left[\xi_r(rv)_\xi + \eta_r(rv)_\eta\right] \qquad \text{(B.1}$$

$$(\hat{\mathbf{H}}_V)_4 = \mu(\xi_r w_\xi + \eta_r w_\eta) - \mu \frac{w}{r} \tag{B.13d}$$

$$(\hat{\mathbf{H}}_V)_5 = 0 \tag{B.13e}$$

Performing the linearization, the Jacobian coefficient matrix $\partial \hat{\mathbf{E}}_{V_1}/\partial \hat{\mathbf{Q}}$ is

$$\frac{\partial \hat{\mathbf{E}}_{V_1}}{\partial \hat{\mathbf{Q}}} = \frac{1}{Re_r}\begin{bmatrix} 0 & 0 & 0 & 0 & 0 \\ \left(\frac{\partial \hat{\mathbf{E}}_{V_1}}{\partial \hat{\mathbf{Q}}}\right)_{21} & \alpha_{xx}\frac{\partial}{\partial \xi}\left(\frac{1}{\rho}\right) & \alpha_{xr}\frac{\partial}{\partial \xi}\left(\frac{1}{\rho}\right) + \alpha'_{xr}\frac{1}{\rho}r_\xi & 0 & 0 \\ \left(\frac{\partial \hat{\mathbf{E}}_{V_1}}{\partial \hat{\mathbf{Q}}}\right)_{31} & \alpha_{xr}\frac{\partial}{\partial \xi}\left(\frac{1}{\rho}\right) & \alpha_{rr}\frac{\partial}{\partial \xi}\left(\frac{1}{\rho}\right) + \alpha'_{rr}\frac{1}{\rho}r_\xi & 0 & 0 \\ \left(\frac{\partial \hat{\mathbf{E}}_{V_1}}{\partial \hat{\mathbf{Q}}}\right)_{41} & 0 & 0 & \alpha_{zz}\frac{\partial}{\partial \xi}\left(\frac{1}{\rho}\right) & 0 \\ \left(\frac{\partial \hat{\mathbf{E}}_{V_1}}{\partial \hat{\mathbf{Q}}}\right)_{51} & \left(\frac{\partial \hat{\mathbf{E}}_{V_1}}{\partial \hat{\mathbf{Q}}}\right)_{52} & \left(\frac{\partial \hat{\mathbf{E}}_{V_1}}{\partial \hat{\mathbf{Q}}}\right)_{53} & \left(\frac{\partial \hat{\mathbf{E}}_{V_1}}{\partial \hat{\mathbf{Q}}}\right)_{54} & \alpha_0\frac{\partial}{\partial \xi}\left(\frac{\partial T}{\partial E_T}\right) \end{bmatrix} \tag{B.14}$$

where

$$\alpha_{xx} = (2\mu + \lambda)\xi_x^2 + \mu\xi_r^2$$

$$\alpha_{rr} = \mu\xi_x^2 + (2\mu + \lambda)\xi_r^2$$

$$\alpha_{zz} = \mu\xi_x^2 + \mu\xi_r^2$$

$$\alpha_{xr} = (\mu + \lambda)\xi_x\xi_r$$

$$\alpha'_{xr} = \frac{\lambda}{r}\xi_x\xi_r$$

$$\alpha'_{rr} = \frac{\lambda}{r}\xi_r^2$$

$$\alpha_0 = \frac{k}{Pr_r}(\xi_x^2 + \xi_r^2)$$

$$\left(\frac{\partial \hat{\mathbf{E}}_{V_1}}{\partial \hat{\mathbf{Q}}}\right)_{21} = -\alpha_{xx}\frac{\partial}{\partial \xi}\left(\frac{u}{\rho}\right) - \alpha_{xr}\frac{\partial}{\partial \xi}\left(\frac{v}{\rho}\right) - \alpha'_{xr}\frac{v}{\rho}r_\xi$$

$$\left(\frac{\partial \hat{\mathbf{E}}_{V_1}}{\partial \hat{\mathbf{Q}}}\right)_{31} = -\alpha_{xr}\frac{\partial}{\partial \xi}\left(\frac{u}{\rho}\right) - \alpha_{rr}\frac{\partial}{\partial \xi}\left(\frac{v}{\rho}\right) - \alpha'_{rr}\frac{v}{\rho}r_\xi$$

$$\left(\frac{\partial \hat{\mathbf{E}}_{V_1}}{\partial \hat{\mathbf{Q}}}\right)_{41} = -\alpha_{zz}\frac{\partial}{\partial \xi}\left(\frac{w}{\rho}\right)$$

$$\left(\frac{\partial \hat{\mathbf{E}}_{V_1}}{\partial \hat{\mathbf{Q}}}\right)_{51} = -\alpha_{xx}\frac{\partial}{\partial \xi}\left(\frac{u^2}{\rho}\right) - \alpha_{rr}\frac{\partial}{\partial \xi}\left(\frac{v^2}{\rho}\right) - \alpha_{zz}\frac{\partial}{\partial \xi}\left(\frac{w^2}{\rho}\right)$$
$$-2\alpha_{xr}\frac{\partial}{\partial \xi}\left(\frac{uv}{\rho}\right) - 2\alpha'_{rr}\frac{v^2}{\rho}r_\xi - 2\alpha'_{xr}\frac{uv}{\rho}r_\xi + \alpha_0\frac{\partial}{\partial \xi}\left(\frac{\partial T}{\partial \rho}\right)$$

$$\left(\frac{\partial \hat{\mathbf{E}}_{V_1}}{\partial \hat{\mathbf{Q}}}\right)_{52} = -\left(\frac{\partial \hat{\mathbf{E}}_{V_1}}{\partial \hat{\mathbf{Q}}}\right)_{21} + \alpha_0\frac{\partial}{\partial \xi}\left(\frac{\partial T}{\partial(\rho u)}\right)$$

$$\left(\frac{\partial \hat{\mathbf{E}}_{V_1}}{\partial \hat{\mathbf{Q}}}\right)_{53} = -\left(\frac{\partial \hat{\mathbf{E}}_{V_1}}{\partial \hat{\mathbf{Q}}}\right)_{31} + \alpha'_{rr}\frac{v}{\rho}r_\xi + \alpha_0\frac{\partial}{\partial \xi}\left(\frac{\partial T}{\partial(\rho v)}\right)$$

$$\left(\frac{\partial \hat{\mathbf{E}}_{V_1}}{\partial \hat{\mathbf{Q}}}\right)_{54} = -\left(\frac{\partial \hat{\mathbf{E}}_{V_1}}{\partial \hat{\mathbf{Q}}}\right)_{41} + \alpha_0\frac{\partial}{\partial \xi}\left(\frac{\partial T}{\partial(\rho w)}\right)$$

The Jacobian coefficient matrix for the remaining non-cross derivative viscous terms, $\partial \hat{\mathbf{F}}_{V_1}/\partial \hat{\mathbf{Q}}$, has the sa
form as $\partial \hat{\mathbf{E}}_{V_1}/\partial \hat{\mathbf{Q}}$, but with ξ replaced by η.

And finally, linearizing $\hat{\mathbf{H}}_V$, the Jacobian coefficient matrix $\partial \hat{\mathbf{H}}_V/\partial \hat{\mathbf{Q}}$ is

$$\frac{\partial \hat{\mathbf{H}}_V}{\partial \hat{\mathbf{Q}}} = \frac{1}{Re_r}\begin{bmatrix} 0 & 0 & 0 & 0 & 0 \\ 0 & 0 & 0 & 0 & 0 \\ \left(\frac{\partial \hat{\mathbf{H}}_V}{\partial \hat{\mathbf{Q}}}\right)_{31} & \left(\frac{\partial \hat{\mathbf{H}}_V}{\partial \hat{\mathbf{Q}}}\right)_{32} & \left(\frac{\partial \hat{\mathbf{H}}_V}{\partial \hat{\mathbf{Q}}}\right)_{33} & 0 & 0 \\ \left(\frac{\partial \hat{\mathbf{H}}_V}{\partial \hat{\mathbf{Q}}}\right)_{41} & 0 & 0 & \left(\frac{\partial \hat{\mathbf{H}}_V}{\partial \hat{\mathbf{Q}}}\right)_{44} & 0 \\ 0 & 0 & 0 & 0 & 0 \end{bmatrix} \quad \text{(B}$$

where

ORIGINAL PAGE IS
OF POOR QUALITY

$$\left(\frac{\partial \hat{\mathbf{H}}_V}{\partial \hat{\mathbf{Q}}}\right)_{31} = \lambda\xi_x \frac{\partial}{\partial\xi}\left(\frac{u}{\rho}\right) + \lambda\xi_r \frac{\partial}{\partial\xi}\left(\frac{v}{\rho}\right) + \lambda\eta_x \frac{\partial}{\partial\eta}\left(\frac{u}{\rho}\right) + \left[2\mu + \lambda(\xi_r r_\xi + \eta_r r_\eta)\right]\frac{1}{r}\frac{v}{\rho} + \lambda\eta_r \frac{\partial}{\partial\eta}\left(\frac{v}{\rho}\right)$$

$$\left(\frac{\partial \hat{\mathbf{H}}_V}{\partial \hat{\mathbf{Q}}}\right)_{32} = -\lambda\xi_x \frac{\partial}{\partial\xi}\left(\frac{1}{\rho}\right) - \lambda\eta_x \frac{\partial}{\partial\eta}\left(\frac{1}{\rho}\right)$$

$$\left(\frac{\partial \hat{\mathbf{H}}_V}{\partial \hat{\mathbf{Q}}}\right)_{33} = -\lambda\xi_r \frac{\partial}{\partial\xi}\left(\frac{1}{\rho}\right) - \left[2\mu + \lambda(\xi_r r_\xi + \eta_r r_\eta)\right]\frac{1}{r}\frac{1}{\rho} - \lambda\eta_r \frac{\partial}{\partial\eta}\left(\frac{1}{\rho}\right)$$

$$\left(\frac{\partial \hat{\mathbf{H}}_V}{\partial \hat{\mathbf{Q}}}\right)_{41} = -\mu\xi_r \frac{\partial}{\partial\xi}\left(\frac{w}{\rho}\right) + \frac{\mu}{r}\frac{w}{\rho} - \mu\eta_r \frac{\partial}{\partial\eta}\left(\frac{w}{\rho}\right)$$

$$\left(\frac{\partial \hat{\mathbf{H}}_V}{\partial \hat{\mathbf{Q}}}\right)_{44} = \mu\xi_r \frac{\partial}{\partial\xi}\left(\frac{1}{\rho}\right) - \frac{\mu}{r}\frac{1}{\rho} + \mu\eta_r \frac{\partial}{\partial\eta}\left(\frac{1}{\rho}\right)$$

B.2.3 Equation Of State

The equation of state given in Section 4.3 must be modified slightly to add the swirl velocity w. Thus,

$$p = (\gamma - 1)\left[E_T - \frac{1}{2}\rho\left(u^2 + v^2 + w^2\right)\right] \tag{B.16}$$

or, in terms of temperature,

$$T = \frac{1}{c_v}\left[\frac{E_T}{\rho} - \frac{1}{2}\left(u^2 + v^2 + w^2\right)\right] \tag{B.17}$$

The derivatives arising from the linearization are the same as those presented in Section 4.3, except for

$$\frac{\partial p}{\partial \rho} = \frac{\gamma - 1}{2}\left(u^2 + v^2 + w^2\right) \tag{B.18a}$$

$$\frac{\partial p}{\partial(\rho w)} = -(\gamma - 1)w \tag{B.18b}$$

$$\frac{\partial T}{\partial \rho} = -\frac{1}{c_v}\left[\frac{E_T}{\rho^2} - \frac{1}{\rho}\left(u^2 + v^2 + w^2\right)\right] \tag{B.18c}$$

$$\frac{\partial T}{\partial(\rho w)} = -\frac{w}{c_v \rho} \tag{B.1}$$

If constant stagnation enthalpy can be assumed, the appropriate equation of state is

$$p = \frac{\gamma - 1}{\gamma} \rho \left[h_T - \frac{1}{2}(u^2 + v^2 + w^2) \right] \tag{B.}$$

and the temperature becomes

$$T = \frac{1}{c_p} \left[h_T - \frac{1}{2}(u^2 + v^2 + w^2) \right] \tag{B.}$$

Again, the derivatives arising from the linearization are the same as in Section 4.3, except for

$$\frac{\partial p}{\partial \rho} = \frac{\gamma - 1}{\gamma} \left[h_T + \frac{1}{2}(u^2 + v^2 + w^2) \right] \tag{B.2}$$

$$\frac{\partial p}{\partial(\rho w)} = -\frac{\gamma - 1}{\gamma} w \tag{B.2}$$

$$\frac{\partial T}{\partial \rho} = \frac{1}{c_p \rho}(u^2 + v^2 + w^2) \tag{B.2}$$

$$\frac{\partial T}{\partial(\rho w)} = -\frac{w}{c_p \rho} \tag{B.2}$$

B.2.4 Linearized Governing Equation

The linearized form of equation (B.8) can now be written as

ORIGINAL PAGE IS
OF POOR QUALITY

$$\Delta\hat{\mathbf{Q}}^n + \frac{\theta_1\Delta\tau}{1+\theta_2}\frac{1}{r}\left\{\frac{\partial}{\partial\xi}\left[r\left(\frac{\partial\hat{\mathbf{E}}}{\partial\hat{\mathbf{Q}}}\right)^n\Delta\hat{\mathbf{Q}}^n\right]+\frac{\partial}{\partial\eta}\left[r\left(\frac{\partial\hat{\mathbf{F}}}{\partial\hat{\mathbf{Q}}}\right)^n\Delta\hat{\mathbf{Q}}^n\right]+\left(\frac{\partial\hat{\mathbf{H}}}{\partial\hat{\mathbf{Q}}}\right)^n\Delta\hat{\mathbf{Q}}^n\right\}$$

$$-\frac{\theta_1\Delta\tau}{1+\theta_2}\frac{1}{r}\left\{\frac{\partial}{\partial\xi}\left[r\left(\frac{\partial\hat{\mathbf{E}}_{V_1}}{\partial\hat{\mathbf{Q}}}\right)^n\Delta\hat{\mathbf{Q}}^n\right]+\frac{\partial}{\partial\eta}\left[r\left(\frac{\partial\hat{\mathbf{F}}_{V_1}}{\partial\hat{\mathbf{Q}}}\right)^n\Delta\hat{\mathbf{Q}}^n\right]+\left(\frac{\partial\hat{\mathbf{H}}_V}{\partial\hat{\mathbf{Q}}}\right)^n\Delta\hat{\mathbf{Q}}^n\right\}=$$

$$-\frac{\Delta\tau}{1+\theta_2}\frac{1}{r}\left(\frac{\partial(r\hat{\mathbf{E}})}{\partial\xi}+\frac{\partial(r\hat{\mathbf{F}})}{\partial\eta}+\hat{\mathbf{H}}\right)^n+\frac{\Delta\tau}{1+\theta_2}\frac{1}{r}\left(\frac{\partial(r\hat{\mathbf{E}}_{V_1})}{\partial\xi}+\frac{\partial(r\hat{\mathbf{F}}_{V_1})}{\partial\eta}+\hat{\mathbf{H}}_V\right)^n$$

$$+\frac{(1+\theta_3)\Delta\tau}{1+\theta_2}\frac{1}{r}\left(\frac{\partial(r\hat{\mathbf{E}}_{V_2})}{\partial\xi}+\frac{\partial(r\hat{\mathbf{F}}_{V_2})}{\partial\eta}\right)^n-\frac{\theta_3\Delta\tau}{1+\theta_2}\frac{1}{r}\left(\frac{\partial(r\hat{\mathbf{E}}_{V_2})}{\partial\xi}+\frac{\partial(r\hat{\mathbf{F}}_{V_2})}{\partial\eta}\right)^{n-1}$$

$$+\frac{\theta_2}{1+\theta_2}\Delta\hat{\mathbf{Q}}^{n-1}+O\left[\left(\theta_1-\frac{1}{2}-\theta_2\right)(\Delta\tau)^2,(\theta_3-\theta_1)(\Delta\tau)^2,(\Delta\tau)^3\right] \tag{B.22}$$

B.3 SOLUTION PROCEDURE

Letting LHS(B.22) represent the left hand side of equation (B.22), we can write

$$LHS(B.22)=\left\{\mathbf{K}+\frac{\theta_1\Delta\tau}{1+\theta_2}\frac{1}{r}\left[\frac{\partial}{\partial\xi}\left(r\frac{\partial\hat{\mathbf{E}}}{\partial\hat{\mathbf{Q}}}-r\frac{\partial\hat{\mathbf{E}}_{V_1}}{\partial\hat{\mathbf{Q}}}\right)+\frac{\partial}{\partial\eta}\left(r\frac{\partial\hat{\mathbf{F}}}{\partial\hat{\mathbf{Q}}}-r\frac{\partial\hat{\mathbf{F}}_{V_1}}{\partial\hat{\mathbf{Q}}}\right)\right]\right\}^n\Delta\hat{\mathbf{Q}}^n \tag{B.23a}$$

where

$$\mathbf{K}=\mathbf{I}+\frac{\theta_1\Delta\tau}{1+\theta_2}\frac{1}{r}\left(\frac{\partial\hat{\mathbf{H}}}{\partial\hat{\mathbf{Q}}}-\frac{\partial\hat{\mathbf{H}}_V}{\partial\hat{\mathbf{Q}}}\right) \tag{B.23b}$$

and $\mathbf{I}$ represents the identity matrix. The term in braces in equation (B.23a) can be factored to give

$$LHS(B.22)=\left[\mathbf{K}+\frac{\theta_1\Delta\tau}{1+\theta_2}\frac{1}{r}\frac{\partial}{\partial\xi}\left(r\frac{\partial\hat{\mathbf{E}}}{\partial\hat{\mathbf{Q}}}-r\frac{\partial\hat{\mathbf{E}}_{V_1}}{\partial\hat{\mathbf{Q}}}\right)\right]^n\left[\mathbf{I}+\mathbf{K}^{-1}\frac{\theta_1\Delta\tau}{1+\theta_2}\frac{1}{r}\frac{\partial}{\partial\eta}\left(r\frac{\partial\hat{\mathbf{F}}}{\partial\hat{\mathbf{Q}}}-r\frac{\partial\hat{\mathbf{F}}_{V_1}}{\partial\hat{\mathbf{Q}}}\right)\right]^n\Delta\hat{\mathbf{Q}}^n$$

$$-\left(\frac{\theta_1\Delta\tau}{1+\theta_2}\right)^2\frac{1}{r^2}\mathbf{K}^{-1}\left[\frac{\partial}{\partial\xi}\left(r\frac{\partial\hat{\mathbf{E}}}{\partial\hat{\mathbf{Q}}}-r\frac{\partial\hat{\mathbf{E}}_{V_1}}{\partial\hat{\mathbf{Q}}}\right)\frac{\partial}{\partial\eta}\left(r\frac{\partial\hat{\mathbf{F}}}{\partial\hat{\mathbf{Q}}}-r\frac{\partial\hat{\mathbf{F}}_{V_1}}{\partial\hat{\mathbf{Q}}}\right)\right]^n\Delta\hat{\mathbf{Q}}^n \tag{B.24}$$

The last term represents the splitting error.

Equation (B.22) can thus be rewritten in spatially factored form, and, neglecting the temporal truncation and splitting error terms, becomes

$$\left[\mathbf{K}+\frac{\theta_1\Delta\tau}{1+\theta_2}\frac{1}{r}\frac{\partial}{\partial\xi}\left(r\frac{\partial\hat{\mathbf{E}}}{\partial\hat{\mathbf{Q}}}-r\frac{\partial\hat{\mathbf{E}}_{V_1}}{\partial\hat{\mathbf{Q}}}\right)\right]^n\left(\mathbf{K}^{-1}\right)^n\left[\mathbf{K}+\frac{\theta_1\Delta\tau}{1+\theta_2}\frac{1}{r}\frac{\partial}{\partial\eta}\left(r\frac{\partial\hat{\mathbf{F}}}{\partial\hat{\mathbf{Q}}}-r\frac{\partial\hat{\mathbf{F}}_{V_1}}{\partial\hat{\mathbf{Q}}}\right)\right]^n\Delta\hat{\mathbf{Q}}^n=$$

$$-\frac{\Delta\tau}{1+\theta_2}\frac{1}{r}\left(\frac{\partial(r\hat{\mathbf{E}})}{\partial\xi}+\frac{\partial(r\hat{\mathbf{F}})}{\partial\eta}+\hat{\mathbf{H}}\right)^n+\frac{\Delta\tau}{1+\theta_2}\frac{1}{r}\left(\frac{\partial(r\hat{\mathbf{E}}_{V_1})}{\partial\xi}+\frac{\partial(r\hat{\mathbf{F}}_{V_1})}{\partial\eta}+\hat{\mathbf{H}}_V\right)^n$$

$$+\frac{(1+\theta_3)\Delta\tau}{1+\theta_2}\frac{1}{r}\left(\frac{\partial(r\hat{\mathbf{E}}_{V_2})}{\partial\xi}+\frac{\partial(r\hat{\mathbf{F}}_{V_2})}{\partial\eta}\right)^n-\frac{\theta_3\Delta\tau}{1+\theta_2}\frac{1}{r}\left(\frac{\partial(r\hat{\mathbf{E}}_{V_2})}{\partial\xi}+\frac{\partial(r\hat{\mathbf{F}}_{V_2})}{\partial\eta}\right)^{n-1}+\frac{\theta_2}{1+\theta_2}\Delta\hat{\mathbf{Q}}^{n-1}\qquad\text{(B.}$$

Using the procedure of Douglas and Gunn (1964), as written by Briley and McDonald (1977), equation (B.25) be split into the following two-sweep sequence.

Sweep 1 (ξ direction)

$$\left[\mathbf{K}+\frac{\theta_1\Delta\tau}{1+\theta_2}\frac{1}{r}\frac{\partial}{\partial\xi}\left(r\frac{\partial\hat{\mathbf{E}}}{\partial\hat{\mathbf{Q}}}-r\frac{\partial\hat{\mathbf{E}}_{V_1}}{\partial\hat{\mathbf{Q}}}\right)\right]^n\Delta\hat{\mathbf{Q}}^*=-\frac{\Delta\tau}{1+\theta_2}\frac{1}{r}\left(\frac{\partial(r\hat{\mathbf{E}})}{\partial\xi}+\frac{\partial(r\hat{\mathbf{F}})}{\partial\eta}+\hat{\mathbf{H}}\right)^n$$

$$+\frac{\Delta\tau}{1+\theta_2}\frac{1}{r}\left(\frac{\partial(r\hat{\mathbf{E}}_{V_1})}{\partial\xi}+\frac{\partial(r\hat{\mathbf{F}}_{V_1})}{\partial\eta}+\hat{\mathbf{H}}_V\right)^n+\frac{(1+\theta_3)\Delta\tau}{1+\theta_2}\frac{1}{r}\left(\frac{\partial(r\hat{\mathbf{E}}_{V_2})}{\partial\xi}+\frac{\partial(r\hat{\mathbf{F}}_{V_2})}{\partial\eta}\right)^n$$

$$-\frac{\theta_3\Delta\tau}{1+\theta_2}\frac{1}{r}\left(\frac{\partial(r\hat{\mathbf{E}}_{V_2})}{\partial\xi}+\frac{\partial(r\hat{\mathbf{F}}_{V_2})}{\partial\eta}\right)^{n-1}+\frac{\theta_2}{1+\theta_2}\Delta\hat{\mathbf{Q}}^{n-1}\qquad\text{(B.}$$

Sweep 2 (η direction)

$$\left[\mathbf{K}+\frac{\theta_1\Delta\tau}{1+\theta_2}\frac{1}{r}\frac{\partial}{\partial\eta}\left(r\frac{\partial\hat{\mathbf{F}}}{\partial\hat{\mathbf{Q}}}-r\frac{\partial\hat{\mathbf{F}}_{V_1}}{\partial\hat{\mathbf{Q}}}\right)\right]^n\Delta\hat{\mathbf{Q}}^n=\mathbf{K}^n\Delta\hat{\mathbf{Q}}^*\qquad\text{(B.}$$

Or, expanding **K** and rearranging,

Sweep 1 (ξ direction)

$$\Delta\hat{\mathbf{Q}}^{*}+\frac{\theta_1\Delta\tau}{1+\theta_2}\frac{1}{r}\frac{\partial}{\partial\xi}\left[r\left(\frac{\partial\hat{\mathbf{E}}}{\partial\hat{\mathbf{Q}}}\right)^{n}\Delta\hat{\mathbf{Q}}^{*}\right]-\frac{\theta_1\Delta\tau}{1+\theta_2}\frac{1}{r}\frac{\partial}{\partial\xi}\left[r\left(\frac{\partial\hat{\mathbf{E}}_{V_1}}{\partial\hat{\mathbf{Q}}}\right)^{n}\Delta\hat{\mathbf{Q}}^{*}\right]+\frac{\theta_1\Delta\tau}{1+\theta_2}\frac{1}{r}\left(\frac{\partial\hat{\mathbf{H}}}{\partial\hat{\mathbf{Q}}}-\frac{\partial\hat{\mathbf{H}}_V}{\partial\hat{\mathbf{Q}}}\right)^{n}\Delta\hat{\mathbf{Q}}^{*}=$$

$$-\frac{\Delta\tau}{1+\theta_2}\frac{1}{r}\left(\frac{\partial(r\hat{\mathbf{E}})}{\partial\xi}+\frac{\partial(r\hat{\mathbf{F}})}{\partial\eta}+\hat{\mathbf{H}}\right)^{n}+\frac{\Delta\tau}{1+\theta_2}\frac{1}{r}\left(\frac{\partial(r\hat{\mathbf{E}}_{V_1})}{\partial\xi}+\frac{\partial(r\hat{\mathbf{F}}_{V_1})}{\partial\eta}+\hat{\mathbf{H}}_V\right)^{n}$$

$$+\frac{(1+\theta_3)\Delta\tau}{1+\theta_2}\frac{1}{r}\left(\frac{\partial(r\hat{\mathbf{E}}_{V_2})}{\partial\xi}+\frac{\partial(r\hat{\mathbf{F}}_{V_2})}{\partial\eta}\right)^{n}-\frac{\theta_3\Delta\tau}{1+\theta_2}\frac{1}{r}\left(\frac{\partial(r\hat{\mathbf{E}}_{V_2})}{\partial\xi}+\frac{\partial(r\hat{\mathbf{F}}_{V_2})}{\partial\eta}\right)^{n-1}+\frac{\theta_2}{1+\theta_2}\Delta\hat{\mathbf{Q}}^{n-1}\qquad\text{(B.27a)}$$

Sweep 2 (η direction)

$$\Delta\hat{\mathbf{Q}}^{n}+\frac{\theta_1\Delta\tau}{1+\theta_2}\frac{1}{r}\frac{\partial}{\partial\eta}\left[r\left(\frac{\partial\hat{\mathbf{F}}}{\partial\hat{\mathbf{Q}}}\right)^{n}\Delta\hat{\mathbf{Q}}^{n}\right]-\frac{\theta_1\Delta\tau}{1+\theta_2}\frac{1}{r}\frac{\partial}{\partial\eta}\left[r\left(\frac{\partial\hat{\mathbf{F}}_{V_1}}{\partial\hat{\mathbf{Q}}}\right)^{n}\Delta\hat{\mathbf{Q}}^{n}\right]$$

$$+\frac{\theta_1\Delta\tau}{1+\theta_2}\frac{1}{r}\left(\frac{\partial\hat{\mathbf{H}}}{\partial\hat{\mathbf{Q}}}-\frac{\partial\hat{\mathbf{H}}_V}{\partial\hat{\mathbf{Q}}}\right)^{n}\Delta\hat{\mathbf{Q}}^{n}=\Delta\hat{\mathbf{Q}}^{*}+\frac{\theta_1\Delta\tau}{1+\theta_2}\frac{1}{r}\left(\frac{\partial\hat{\mathbf{H}}}{\partial\hat{\mathbf{Q}}}-\frac{\partial\hat{\mathbf{H}}_V}{\partial\hat{\mathbf{Q}}}\right)^{n}\Delta\hat{\mathbf{Q}}^{*}\qquad\text{(B.27b)}$$

Applying the spatial differencing formulas of Section 5.0 results in

Sweep 1 (ξ direction)

$$\Delta\hat{\mathbf{Q}}_i^{*}+\frac{\theta_1\Delta\tau}{(1+\theta_2)2\Delta\xi}\frac{1}{r}\left[\left(r\frac{\partial\hat{\mathbf{E}}}{\partial\hat{\mathbf{Q}}}\right)_{i+1}^{n}\Delta\hat{\mathbf{Q}}_{i+1}^{*}-\left(r\frac{\partial\hat{\mathbf{E}}}{\partial\hat{\mathbf{Q}}}\right)_{i-1}^{n}\Delta\hat{\mathbf{Q}}_{i-1}^{*}\right]-\frac{\theta_1\Delta\tau}{(1+\theta_2)2(\Delta\xi)^2}\frac{1}{r}\left[(r_{i-1}f_{i-1}+r_if_i)^{n}g_{i-1}^{n}\Delta\hat{\mathbf{Q}}_{i-1}^{*}\right.$$

$$\left.-(r_{i-1}f_{i-1}+2r_if_i+r_{i+1}f_{i+1})^{n}g_i^{n}\Delta\hat{\mathbf{Q}}_i^{*}+(r_if_i+r_{i+1}f_{i+1})^{n}g_{i+1}^{n}\Delta\hat{\mathbf{Q}}_{i+1}^{*}\right]+\frac{\theta_1\Delta\tau}{1+\theta_2}\frac{1}{r}\left(\frac{\partial\hat{\mathbf{H}}}{\partial\hat{\mathbf{Q}}}-\frac{\partial\hat{\mathbf{H}}_V}{\partial\hat{\mathbf{Q}}}\right)_i^{n}\Delta\hat{\mathbf{Q}}_i^{*}=$$

$$-\frac{\Delta\tau}{1+\theta_2}\frac{1}{r}\left[\delta_\xi(r\hat{\mathbf{E}})+\delta_\eta(r\hat{\mathbf{F}})+\hat{\mathbf{H}}\right]^{n}+\frac{\Delta\tau}{1+\theta_2}\frac{1}{r}\left[\delta_\xi(r\hat{\mathbf{E}}_{V_1})+\delta_\eta(r\hat{\mathbf{F}}_{V_1})+\hat{\mathbf{H}}_V\right]^{n}$$

$$+\frac{(1+\theta_3)\Delta\tau}{1+\theta_2}\frac{1}{r}\left[\delta_\xi(r\hat{\mathbf{E}}_{V_2})+\delta_\eta(r\hat{\mathbf{F}}_{V_2})\right]^{n}-\frac{\theta_3\Delta\tau}{1+\theta_2}\frac{1}{r}\left[\delta_\xi(r\hat{\mathbf{E}}_{V_2})+\delta_\eta(r\hat{\mathbf{F}}_{V_2})\right]^{n-1}+\frac{\theta_2}{1+\theta_2}\Delta\hat{\mathbf{Q}}^{n-1}\qquad\text{(B.28a)}$$

Sweep 2 (η direction)

$$\Delta\hat{Q}_j^n + \frac{\theta_1\Delta\tau}{(1+\theta_2)2\Delta\eta}\frac{1}{r}\left[\left(r\frac{\partial\hat{F}}{\partial\hat{Q}}\right)_{j+1}^n \Delta\hat{Q}_{j+1}^n - \left(r\frac{\partial\hat{F}}{\partial\hat{Q}}\right)_{j-1}^n \Delta\hat{Q}_{j-1}^n\right] - \frac{\theta_1\Delta\tau}{(1+\theta_2)2(\Delta\eta)^2}\frac{1}{r}\left[(r_{j-1}f_{j-1}+r_jf_j)^n g_{j-1}^n \Delta\hat{Q}_{j-1}^n\right.$$

$$\left. -(r_{j-1}f_{j-1}+2r_jf_j+r_{j+1}f_{j+1})^n g_j^n \Delta\hat{Q}_j^n + (r_jf_j+r_{j+1}f_{j+1})^n g_{j+1}^n \Delta\hat{Q}_{j+1}^n\right] + \frac{\theta_1\Delta\tau}{1+\theta_2}\frac{1}{r}\left(\frac{\partial\hat{H}}{\partial\hat{Q}} - \frac{\partial\hat{H}_v}{\partial\hat{Q}}\right)_j^n \Delta\hat{Q}_j^n =$$

$$\Delta\hat{Q}^* + \frac{\theta_1\Delta\tau}{1+\theta_2}\frac{1}{r}\left(\frac{\partial\hat{H}}{\partial\hat{Q}} - \frac{\partial\hat{H}_v}{\partial\hat{Q}}\right)^n \Delta\hat{Q}^* \qquad \text{(B.2}$$

Briley, W. R., and McDonald, H. (1980) "On the Structure and Use of Linearized Block Implicit Schemes," Journal of Computational Physics, Vol. 34 No. 1, pp. 54-73.

Douglas, J., and Gunn, J. E., (1964) "A General Formulation of Alternating Direction Methods. Part I - Parabolic and Hyperbolic Problems," Numerische Mathematik, Vol. 6, pp. 428-453.

Vinokur, M. (1974) "Conservation Equations of Gasdynamics in Curvilinear Coordinate Systems," Journal of Computational Physics, Vol. 14, pp. 105-125.

Appendix B

Interior Point Numerical Algorithm

A comparison between the solution methodology employed in the Proteus code and that employed in the Tethys code is described in this appendix. For the most part, the similarities between the models are extremely close, with the obvious exception that the chemically reacting and diffusing aspects of the Tethys model result in a significant increase in the fluid flow terms that need modelling. The other primary difference between the two codes is in the manner in which the grid transformation metrics and the radius are handled. A discussion of the Tethys code numerical procedure follows, with significant references to Appendix A (which is essentially Appendix B in the Proteus Analysis Guide). A discussion of the differences between the Proteus code and the Tethys code in the manner in which the mass, momentum, and energy equations are modelled is discussed in Sections B.1 and B.2. The equations of state are discussed in Section B.3, and the manner in which the species density equations are solved is discussed in Section B.4. The procedure used to specify fluid entropy and total enthalpy boundary conditions is discussed in Sections B.5 and B.6, respectively.

B.1. Finite Difference Approximation of Advective and Source Terms

The spatial differencing in both the Proteus and Tethys codes employed central difference approximations for both the implicit and explicit sides of the governing equations. Likewise, the grid transformation metrics were evaluated using central difference approximations in both the Tethys and Proteus codes, except at the boundaries where the Proteus code employed a three-point, second-order accurate approximation to the difference equations normal to the surface while the Tethys code employed a two-point first-order accurate difference approximation.

As discussed in Section 3, the governing equations used in the Tethys model were altered slightly from those used in the Proteus model by rewriting the radial pressure gradient into a weak conservation form, as illustrated in Table 20. Further, since the pressure term was rewritten in a conservative form, the K matrix presented in Equation B.23b of

Appendix A reduces to the identity matrix.

Table 20. Comparison of the formulation of the radial pressure gradient.

Proteus code	Tethys code
$\frac{\partial}{\partial r}(rP) - P$	$r \frac{\partial P}{\partial r}$

Likewise, in the effort to maintain one-dimensional flow conservation, the evaluation of the radius in the two codes differed as presented in Table 21.

Table 21. Comparison of the evaluation of the radius terms.

Derivatives with respect to	Proteus model	Tethys model
Radius	Exact	Exact
Axial distance	Exact	Average

In a similar fashion, the evaluation of the radius in the weak conservation form of the radial pressure gradient (in the Tethys code) was evaluated in an exact manner.

B.2. Finite Difference Approximation of Diffusion Terms

In an analogous effort to maintain one-dimensional flow conservation, the evaluation of the metrics and Jacobians in the viscous terms was modified from the methods used in the Proteus code. Due to the lengthy nature of the reevaluation of these terms, the evaluation of the viscous terms acting in the axial momentum equation will be elaborated on in detail, with the extension to the radial momentum equation, the energy equations, and the mass transfer diffusion equations being a rather straightforward extension of the concepts presented herein.

In the transformed coordinate system, the viscous terms of interest in the axial momentum equation are given in Equation (B.2.1) below (neglecting the reference Reynolds number):

$$\frac{\partial}{\partial\xi}\left[\frac{r}{J}\left(\xi_x\tau_{xx}+\xi_r\tau_{xr}\right)\right]+\frac{\partial}{\partial\eta}\left[\frac{r}{J}\left(\eta_x\tau_{xx}+\eta_r\tau_{xr}\right)\right] \tag{B.2.1}$$

The normal and radial shear stress terms can be evaluated in a transformed coordinate system by applying the chain rule, as shown below.

$$\tau_{xx} = (2\mu+\lambda)\left(\xi_x u_\xi+\eta_x u_\eta\right)+\frac{\lambda}{r}\left[\xi_r (rv)_\xi+\eta_r (rv)_\eta\right] \tag{B.2.2}$$

An alternative formulation used in the Tethys model is shown below:

$$\tau_{xx} = (2\mu+\lambda)\left(\xi_x u_\xi+\eta_x u_\eta\right)+\lambda\left[\xi_r v_\xi+\eta_r v_\eta+\frac{v}{r}\right] \tag{B.2.3}$$

For the purpose of comparing the finite difference procedures of the Proteus and Tethys codes, consider only the viscous terms that act on the axial velocity gradient:

$$(2\mu+\lambda)\left(\xi_x u_\xi+\eta_x u_\eta\right) \tag{B.2.4}$$

If the portion of the τ_{xx} term given by Equation (B.2.4) is substituted into Equation (B.2.1) and if only the ξ difference portion of that equation is considered, the resulting expression is given by Equation (B.2.5):

$$\frac{\partial}{\partial\xi}\left[\frac{r\xi_x^2}{J}(2\mu+\lambda)\frac{\partial u}{\partial\xi}\right]+\frac{\partial}{\partial\xi}\left[\frac{r\xi_x\eta_x}{J}(2\mu+\lambda)\frac{\partial u}{\partial\eta}\right] \tag{B.2.5}$$

In Equation (B.2.5), it is observed that the first term is comprised of ξ-only derivatives acting on the axial velocity while the second term consists of ξ and η derivatives acting on the axial velocity. The numerical approximation of Equation (B.2.5) is compared between the Proteus and Tethys codes on a dicretized finite difference basis with extensive reference to the arbitrary computational grid presented in Figure 83. In the four tables that follow, an examination of the procedures of handling both the noncross derivative shear stress terms and the cross derivative shear stress terms is presented. The comparison of the numerical approximation of other components of the diffusion terms is relatively straightforward, with the fundamental differences between the two codes being in the manner in which the metric coefficients and the inverse Jacobians are calculated.

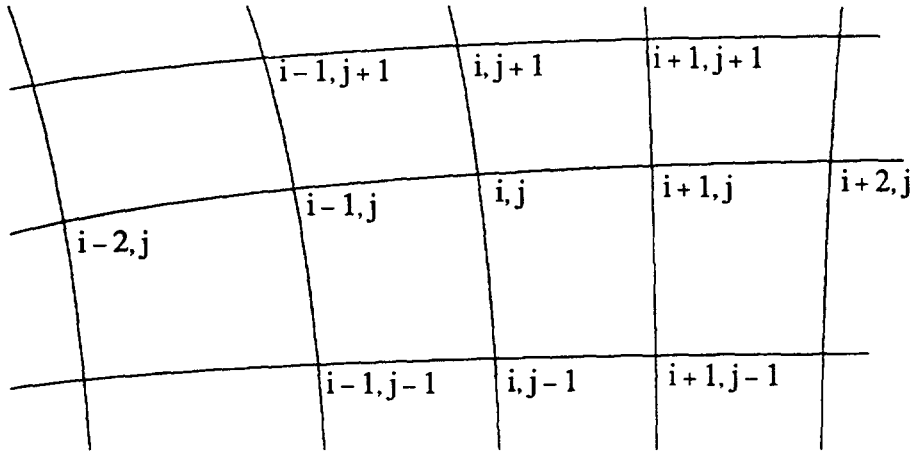

Figure 83. Computational grid for comparison of viscous term finite difference approximations used in Proteus and Tethys codes.

The finite difference approximations of the ξ-only derivatives acting on the axial velocity of the axial shear stress term in the axial momentum equation are given in Table 22 for the Proteus model.

Table 22. Finite difference approximation of a ξ-only derivative component of the axial shear stress term in the axial momentum equation in the Proteus code.

Proteus code approximation for $\frac{\partial}{\partial\xi}\left[\frac{r\xi_x^2}{J}(2\mu+\lambda)\frac{\partial u}{\partial\xi}\right]$
$\approx \left[\frac{(2\mu+\lambda)_{i+1,j}}{2\Delta\xi}\right]\frac{r_{i+1,j}\left[\frac{r_{i+1,j+1}-r_{i+1,j-1}}{2\Delta\eta}\right]^2}{\left[\frac{x_{i+2,j}-x_{i,j}}{2\Delta\xi}\right]\left[\frac{r_{i+1,j+1}-r_{i+1,j-1}}{2\Delta\eta}\right]-\left[\frac{r_{i+2,j}-r_{i,j}}{2\Delta\xi}\right]\left[\frac{x_{i+1,j+1}-x_{i+1,j-1}}{2\Delta\eta}\right]}\left[\frac{u_{i+1,j}-u_{i,j}}{\Delta\xi}\right]$
$+\left[\frac{(2\mu+\lambda)_{i,j}}{2\Delta\xi}\right]\frac{r_{i,j}\left[\frac{r_{i,j+1}-r_{i,j-1}}{2\Delta\eta}\right]^2}{\left[\frac{x_{i+1,j}-x_{i-1,j}}{2\Delta\xi}\right]\left[\frac{r_{i,j+1}-r_{i,j-1}}{2\Delta\eta}\right]-\left[\frac{r_{i+1,j}-r_{i-1,j}}{2\Delta\xi}\right]\left[\frac{x_{i,j+1}-x_{i,j-1}}{2\Delta\eta}\right]}\left[\frac{u_{i+1,j}-u_{i,j}}{\Delta\xi}\right]$
$-\left[\frac{(2\mu+\lambda)_{i,j}}{2\Delta\xi}\right]\frac{r_{i,j}\left[\frac{r_{i,j+1}-r_{i,j-1}}{2\Delta\eta}\right]^2}{\left[\frac{x_{i+1,j}-x_{i-1,j}}{2\Delta\xi}\right]\left[\frac{r_{i,j+1}-r_{i,j-1}}{2\Delta\eta}\right]-\left[\frac{r_{i+1,j}-r_{i-1,j}}{2\Delta\xi}\right]\left[\frac{x_{i,j+1}-x_{i,j-1}}{2\Delta\eta}\right]}\left[\frac{u_{i,j}-u_{i,j-1}}{\Delta\xi}\right]$
$-\left[\frac{(2\mu+\lambda)_{i-1,j}}{2\Delta\xi}\right]\frac{r_{i-1,j}\left[\frac{r_{i-1,j+1}-r_{i-1,j-1}}{2\Delta\eta}\right]^2}{\left[\frac{x_{i,j}-x_{i-1,j}}{2\Delta\xi}\right]\left[\frac{r_{i-1,j+1}-r_{i-1,j-1}}{2\Delta\eta}\right]-\left[\frac{r_{i,j}-r_{i-2,j}}{2\Delta\xi}\right]\left[\frac{x_{i-1,j+1}-x_{i-1,j-1}}{2\Delta\eta}\right]}\left[\frac{u_{i,j}-u_{i,j-1}}{\Delta\xi}\right]$

The analogous approximation of the shear stress term in the Tethys code is presented in Table 23.

Table 23. Finite difference approximation of a ξ-only derivative component of the axial shear stress term in the axial momentum equation in the Tethys code.

Tethys code approximation for $\frac{\partial}{\partial\xi}\left[\frac{r\xi_x^2}{J}(2\mu+\lambda)\frac{\partial u}{\partial\xi}\right]$
$\approx \left[\frac{(2\mu+\lambda)_{i+1,j}}{2\Delta\xi}\right]\frac{\left[\frac{r_{i+1,j}-r_{i,j}}{\ln(r_{i+1,j}/r_{i,j})}\right]\left[\frac{r_{i+1,j+1}-r_{i+1,j-1}}{2\Delta\eta}\right]^2}{\left[\frac{x_{i+1,j}-x_{i,j}}{\Delta\xi}\right]\left[\frac{r_{i+1,j+1}-r_{i+1,j-1}}{2\Delta\eta}\right]-\left[\frac{r_{i+1,j}-r_{i,j}}{\Delta\xi}\right]\left[\frac{x_{i+1,j+1}-x_{i+1,j-1}}{2\Delta\eta}\right]}\left[\frac{u_{i+1,j}-u_{i,j}}{\Delta\xi}\right]$
$+\left[\frac{(2\mu+\lambda)_{i,j}}{2\Delta\xi}\right]\frac{\left[\frac{r_{i+1,j}-r_{i,j}}{\ln(r_{i+1,j}/r_{i,j})}\right]\left[\frac{r_{i,j+1}-r_{i,j-1}}{2\Delta\eta}\right]^2}{\left[\frac{x_{i+1,j}-x_{i,j}}{\Delta\xi}\right]\left[\frac{r_{i,j+1}-r_{i,j-1}}{2\Delta\eta}\right]-\left[\frac{r_{i+1,j}-r_{i,j}}{\Delta\xi}\right]\left[\frac{x_{i,j+1}-x_{i,j-1}}{2\Delta\eta}\right]}\left[\frac{u_{i+1,j}-u_{i,j}}{\Delta\xi}\right]$
$-\left[\frac{(2\mu+\lambda)_{i,j}}{2\Delta\xi}\right]\frac{\left[\frac{r_{i,j}-r_{i-1,j}}{\ln(r_{i,j}/r_{i-1,j})}\right]\left[\frac{r_{i,j+1}-r_{i,j-1}}{2\Delta\eta}\right]^2}{\left[\frac{x_{i,j}-x_{i-1,j}}{\Delta\xi}\right]\left[\frac{r_{i,j+1}-r_{i,j-1}}{2\Delta\eta}\right]-\left[\frac{r_{i,j}-r_{i-1,j}}{\Delta\xi}\right]\left[\frac{x_{i,j+1}-x_{i,j-1}}{2\Delta\eta}\right]}\left[\frac{u_{i,j}-u_{i,j-1}}{\Delta\xi}\right]$
$-\left[\frac{(2\mu+\lambda)_{i-1,j}}{2\Delta\xi}\right]\frac{\left[\frac{r_{i,j}-r_{i-1,j}}{\ln(r_{i,j}/r_{i-1,j})}\right]\left[\frac{r_{i-1,j+1}-r_{i-1,j-1}}{2\Delta\eta}\right]^2}{\left[\frac{x_{i,j}-x_{i-1,j}}{\Delta\xi}\right]\left[\frac{r_{i-1,j+1}-r_{i-1,j-1}}{2\Delta\eta}\right]-\left[\frac{r_{i,j}-r_{i-1,j}}{\Delta\xi}\right]\left[\frac{x_{i-1,j+1}-x_{i-1,j-1}}{2\Delta\eta}\right]}\left[\frac{u_{i,j}-u_{i,j-1}}{\Delta\xi}\right]$

In Tables 24 and 25, the procedure for approximating a representative cross-derivative shear stress term is presented for the two different codes.

Table 24. Finite difference approximation of cross-derivative components of the axial shear stress term in the axial momentum equation in the Proteus code.

Proteus code approximation for $\frac{\partial}{\partial\xi}\left[\frac{r\xi_x\eta_x}{J}(2\mu+\lambda)\frac{\partial u}{\partial\eta}\right]$

$$\approx \left[\frac{(2\mu+\lambda)_{i+1,j}}{2\Delta\xi}\right]\frac{-r_{i+1,j}\left[\frac{r_{i+1,j+1}-r_{i+1,j-1}}{2\Delta\eta}\right]\left[\frac{r_{i+2,j}-r_{i,j}}{2\Delta\xi}\right]}{\left[\frac{x_{i+2,j}-x_{i,j}}{2\Delta\xi}\right]\left[\frac{r_{i+1,j+1}-r_{i+1,j-1}}{2\Delta\eta}\right]-\left[\frac{r_{i+2,j}-r_{i,j}}{2\Delta\xi}\right]\left[\frac{x_{i+1,j+1}-x_{i+1,j-1}}{2\Delta\eta}\right]}\left[\frac{u_{i+1,j+1}-u_{i+1,j-1}}{2\Delta\eta}\right]$$

$$-\left[\frac{(2\mu+\lambda)_{i-1,j}}{2\Delta\xi}\right]\frac{-r_{i-1,j}\left[\frac{r_{i-1,j+1}-r_{i-1,j-1}}{2\Delta\eta}\right]\left[\frac{r_{i,j}-r_{i-2,j}}{2\Delta\xi}\right]}{\left[\frac{x_{i,j}-x_{i-2,j}}{2\Delta\xi}\right]\left[\frac{r_{i-1,j+1}-r_{i-1,j-1}}{2\Delta\eta}\right]-\left[\frac{r_{i,j}-r_{i-2,j}}{2\Delta\xi}\right]\left[\frac{x_{i-1,j+1}-x_{i-1,j-1}}{2\Delta\eta}\right]}\left[\frac{u_{i-1,j+1}-u_{i-1,j-1}}{2\Delta\eta}\right]$$

Table 25. Finite difference approximation of cross-derivative components of the axial shear stres term in the axial momentum equation in the Tethys code.

Tethys code approximation for $\frac{\partial}{\partial\xi}\left[\frac{r\xi_x\eta_x}{J}(2\mu+\lambda)\frac{\partial u}{\partial\eta}\right]$

$$
\begin{aligned}
&\approx \left[\frac{(2\mu+\lambda)_{i+1,j}}{2\Delta\xi}\right]\frac{-\left[\frac{r_{i+1,j+1}-r_{i+1,j-1}}{\ln(r_{i+1,j+1}/r_{i+1,j-1})}\right]\left[\frac{r_{i+1,j+1}-r_{i+1,j-1}}{2\Delta\eta}\right]\left[\frac{r_{i+1,j}-r_{i,j}}{\Delta\xi}\right]}{\left[\frac{x_{i+1,j}-x_{i,j}}{\Delta\xi}\right]\left[\frac{r_{i+1,j+1}-r_{i+1,j-1}}{2\Delta\eta}\right]-\left[\frac{r_{i+1,j}-r_{i,j}}{\Delta\xi}\right]\left[\frac{x_{i+1,j+1}-x_{i+1,j-1}}{2\Delta\eta}\right]}\left[\frac{u_{i+1,j+1}-u_{i+1,j-}}{2\Delta\eta}\right.\\
&+\left[\frac{(2\mu+\lambda)_{i,j}}{2\Delta\xi}\right]\frac{-\left[\frac{r_{i,j+1}-r_{i,j-1}}{\ln(r_{i,j+1}/r_{i,j-1})}\right]\left[\frac{r_{i,j+1}-r_{i,j-1}}{2\Delta\eta}\right]\left[\frac{r_{i+1,j}-r_{i,j}}{\Delta\xi}\right]}{\left[\frac{x_{i+1,j}-x_{i,j}}{\Delta\xi}\right]\left[\frac{r_{i,j+1}-r_{i,j-1}}{2\Delta\eta}\right]-\left[\frac{r_{i+1,j}-r_{i,j}}{\Delta\xi}\right]\left[\frac{x_{i,j+1}-x_{i,j-1}}{2\Delta\eta}\right]}\left[\frac{u_{i,j+1}-u_{i,j-1}}{2\Delta\eta}\right]\\
&-\left[\frac{(2\mu+\lambda)_{i,j}}{2\Delta\xi}\right]\frac{-\left[\frac{r_{i,j+1}-r_{i,j-1}}{\ln(r_{i,j+1}/r_{i,j-1})}\right]\left[\frac{r_{i,j+1}-r_{i,j-1}}{2\Delta\eta}\right]\left[\frac{r_{i,j}-r_{i-1,j}}{\Delta\xi}\right]}{\left[\frac{x_{i,j}-x_{i-1,j}}{\Delta\xi}\right]\left[\frac{r_{i,j+1}-r_{i,j-1}}{2\Delta\eta}\right]-\left[\frac{r_{i,j}-r_{i-1,j}}{\Delta\xi}\right]\left[\frac{x_{i,j+1}-x_{i,j-1}}{2\Delta\eta}\right]}\left[\frac{u_{i,j+1}-u_{i,j-1}}{2\Delta\eta}\right]\\
&-\left[\frac{(2\mu+\lambda)_{i-1,j}}{2\Delta\xi}\right]\frac{-\left[\frac{r_{i-1,j+1}-r_{i-1,j-1}}{\ln(r_{i-1,j+1}/r_{i-1,j-1})}\right]\left[\frac{r_{i-1,j+1}-r_{i-1,j-1}}{2\Delta\eta}\right]\left[\frac{r_{i,j}-r_{i-1,j}}{\Delta\xi}\right]}{\left[\frac{x_{i,j}-x_{i-1,j}}{\Delta\xi}\right]\left[\frac{r_{i-1,j+1}-r_{i-1,j-1}}{2\Delta\eta}\right]-\left[\frac{r_{i,j}-r_{i-1,j}}{\Delta\xi}\right]\left[\frac{x_{i-1,j+1}-x_{i-1,j-1}}{2\Delta\eta}\right]}\left[\frac{u_{i-1,j+1}-u_{i-1,j}}{2\Delta\eta}\right]
\end{aligned}
$$

It should also be noted that, when differenced near a boundary, the Proteus dicretization method described in Tables 22 and 24 replaces, where necessary, central difference methods with three point backward or forward difference methods for the evaluation of grid metrics and inverse Jacobians.

B.3. Equation of State

Due to the multispecies nature of the flow model, coupled with the fact that a rocket engine is subjected to extreme variations in temperature throughout the flow field, the equations of state are significantly more complicated than those for the fully mixed, constant property, fluid considered in the Proteus model. As described in Section 2, the fluid temperature can be related to other fluid flow properties through the following relation:

$$T = \frac{\rho e - \frac{\rho}{2}(u^2+v^2) - \rho \sum_{i=1}^{n} \omega_i (u_{iR} - \bar{C}_{vi}\bar{T}_R)}{\rho \sum_{i=1}^{n} \omega_i \bar{C}_{vi}} \tag{B.3.1}$$

and the pressure is related to the temperature and density through the ideal gas law:

$$P = \rho R T \tag{B.3.2}$$

The relation of the fluid temperature to the dependent properties can be derived in the following manner:

$$\rho e = \sum_{i=1}^{n} \rho_i \left(u_{iR} + \int_{T_R}^{T} C_{vi} dT \right) + \frac{1}{2}\rho (u^2+v^2) \tag{B.3.3}$$

Written in terms of only the fluid temperature and dependent properties, Equation (B.3.3) takes the following form:

$$\rho e = \sum_{i=1}^{n-1} \rho_i (u_{iR} - u_{nR}) + \sum_{i=1}^{n-1} \rho_i \int_{T_R}^{T} (C_{vi} - C_{vn}) dT + \rho u_{nR} + \rho \int_{T_R}^{T} C_{vn} dT + \frac{1}{2}\frac{(\rho u)^2}{\rho} + \frac{1}{2}\frac{(\rho v)^2}{\rho} \tag{B.3.4}$$

Integration of the Equation (B.3.4) and rearrangement yields the following:

$$T = \frac{\rho e - \frac{1}{2}\frac{(\rho u)^2}{\rho} - \frac{1}{2}\frac{(\rho v)^2}{\rho} - \sum_{i=1}^{n-1} \rho_i (u_{iR} - u_{nR}) - \rho u_{nR} + \sum_{i=1}^{n-1} \rho_i (\bar{C}_{vi} - \bar{C}_{vn}) T_R + \rho \bar{C}_{vn} T_R}{\sum_{i=1}^{n-1} \rho_i (\bar{C}_{vi} - \bar{C}_{vn}) + \rho \bar{C}_{vn}} \tag{B.3.5}$$

While Equation (B.3.5) may give the appearance of being an explicit relation for the temperature as a function of the dependent variables, the temperature-averaged specific heats themselves, $\bar{C}_{vi}$ and $\bar{C}_{vn}$, are a function of temperature, thus requiring an iterative solution process in order to insure that the temperature is adequately satisfied by Equation (B.3.5). In the Tethys code, simple updating of the temperature averaged specific heats, following the solution of Equation (B.3.5) was used, and was able to converge to a solution within 0.00001 % of the temperature within twenty iterations or less, usually being much less, and always requiring a negligible amount of computational effort.

The derivatives of the temperature with respect to the other dependent variables can be determined by taking the derivative of Equation (B.3.4), as shown in Equation (B.3.6).

$$\text{(B.3.6)} \quad \partial(\rho e) = \sum_{i=1}^{n-1} (u_{iR} - u_{nR})\,\partial\rho_i + \sum_{i=1}^{n-1} (\bar{C}_{vi} - \bar{C}_{vn})\,(T - T_R)\,\partial\rho_i + \rho C_v \partial T$$

$$+ \bar{C}_{vn}(T - T_R)\,\partial\rho + u_{nR}\partial\rho + u\partial(\rho u) + v\partial(\rho v) - \frac{(u^2 + v^2)}{2}\partial\rho$$

The dependence of the fluid temperature on the dependent properties is given by Equations (B.3.7) through (B.3.11).

$$\text{(B.3.7)} \quad \frac{\partial T}{\partial \rho_i} = \frac{(\bar{C}_{vi} - \bar{C}_{vn})\,(T_R - T) - (u_{iR} - u_{nR})}{\rho C_v}$$

$$\text{(B.3.8)} \quad \frac{\partial T}{\partial \rho} = \frac{(T_R - T)\,\bar{C}_{vn} - u_{nR} + \frac{1}{2}(u^2 + v^2)}{\rho C_v}$$

$$\text{(B.3.9)} \quad \frac{\partial T}{\partial(\rho u)} = -\frac{u}{\rho C_v}$$

$$\text{(B.3.10)} \quad \frac{\partial T}{\partial(\rho v)} = -\frac{v}{\rho C_v}$$

$$\text{(B.3.11)} \quad \frac{\partial T}{\partial(\rho e)} = \frac{1}{\rho C_v}$$

The relationship between the fluid static pressure and the dependent variables can be obtained by employing the relations presented above and realizing that the gas constant is also a variable.

$$P = \rho RT = \bar{R}\sum_{i=1}^{n}\frac{\rho_i}{M_i}T = \bar{R}\left[\sum_{i=1}^{n-1}\rho_i\left(\frac{1}{M_i}-\frac{1}{M_n}\right)+\frac{\rho}{M_n}\right]T \tag{B.3.12}$$

Using Equation (B.3.12), the dependence of the pressure on the dependent variables can be linked through the temperature as given by Equations (B.3.13) though (B.3.17).

$$\frac{\partial P}{\partial \rho_i} = \bar{R}T\left[\frac{1}{M_i}-\frac{1}{M_n}\right]+\rho R\,\frac{\partial T}{\partial \rho_i} \tag{B.3.13}$$

$$\frac{\partial P}{\partial \rho} = \frac{\bar{R}T}{M_n}+\rho R\,\frac{\partial T}{\partial \rho} \tag{B.3.14}$$

$$\frac{\partial P}{\partial (\rho u)} = \rho R\,\frac{\partial T}{\partial (\rho u)} \tag{B.3.15}$$

$$\frac{\partial P}{\partial (\rho v)} = \rho R\,\frac{\partial T}{\partial (\rho v)} \tag{B.3.16}$$

$$\frac{\partial P}{\partial (\rho e)} = \rho R\,\frac{\partial T}{\partial (\rho e)} \tag{B.3.17}$$

B.4. Modelling of the Species Continuity Equations

The requirements to solve a set of species continuity equations in the Tethys model was performed by a straightforward extension of the procedure used to solve the continuity, momentum, and energy equations in the Proteus model, with complete coupling of the species continuity equations to the fluid flow equations, which for a six species system, required the simultaneous solution of a banded, tridiagonal, 9X9 matrix. In general, all of the relational dependences in the species continuity equations to the other dependent variables are a trivial derivation, the exception being the relationship of the species source term to the dependent variables, which is presented in Appendix D.

B.5. Modelling of the Fluid Entropy

At some computational boundaries, the relation between the fluid entropy and the dependent variables was required as the specification of fluid entropy was used in place of the total pressure specification. The equation for the entropy of a mixture of species is derived in Reference 46 and is shown in Equation (B.5.1) below:

$$(B.5.1) \qquad s = R \sum_{i=1}^{n} \omega_i \left(\frac{s}{R}\Big|_i\right) - R \ln(P) - R \sum_{i=1}^{n} x_i \ln(x_i)$$

where the nondimensional entropy (i.e., s/R) of species i is determined from a polynomial curve fit (Reference 47) and is based on conditions at 1 atmosphere. Likewise, in Equation (B.5.1). the units on the pressure are in atmospheres.

In all of the test cases considered, the boundary conditions on the species mass fraction were similar to the those used on the entropy. That is, in cases where the Dirichlet boundary conditions were used on the entropy, Dirichlet boundary conditions were also used on the species boundary conditions. Consequently, the gas constant will follow the variations in the fluid entropy and the following operation can be performed to determine the relation between the entropy and the fluid temperature and pressure. For Dirichlet type boundary conditions on the entropy, the following expression can be written:

$$(B.5.2) \qquad \left(\frac{s}{R}\right)^{n+1} = \left(\frac{s}{R}\right)^{n} + \frac{\partial\left(\frac{s}{R}\right)}{\partial t}\Delta t = \left(\frac{s}{R}\right)^{n} + \left[\left(\frac{C_p}{R}\right)\frac{1}{T}\frac{\partial T}{\partial t} - \frac{1}{P}\frac{\partial P}{\partial t}\right]\Delta t$$

where the relation between the pressure and the temperature to the dependent variables is given in section B.3.

For cases where the computational gradient in entropy and species gradient is equal to zero, the following relations can be used:

$$(B.5.3) \qquad \frac{\partial s}{\partial \eta} = \frac{\partial\left(R\frac{s}{R}\right)}{\partial \eta} = \frac{R\partial\left(\frac{s}{R}\right)}{\partial \eta} + \frac{s}{R}\frac{\partial R}{\partial \eta} = 0$$

where an analogous relation exists if applied along a ξ line. Making use of the fact that the

gas constant is a function only of the mass fractions of each species, Equation (B.5.3) simplifies to the following boundary condition that was modelled in the Tethys code:

$$\frac{\partial\left(\frac{s}{R}\right)}{\partial\eta} = 0 \tag{B.5.4}$$

Equation (B.5.4) can be written in the following implicit manner:

$$\frac{\partial\left(\frac{s}{R}\right)}{\partial\eta} = \frac{\partial\left[\left(\frac{s}{R}\right)^n + \frac{\partial\left(\frac{s}{R}\right)^n}{\partial t}\Delta t\right]}{\partial\eta} = \frac{\partial\left[\left(\frac{s}{R}\right)^n + \left\{\left(\frac{C_p}{R}\right)\frac{1}{T}\frac{\partial T}{\partial t} - \frac{1}{P}\frac{\partial P}{\partial t}\right\}^n \Delta t\right]}{\partial\eta} \tag{B.5.5}$$

where the relation of the temperature and pressure to the dependent variables is given in Section B.3.

B.6. Modelling of the Total Enthalpy

The specification of the fluid total enthalpy, in either Dirichlet of Neumann form, was often employed in the modelling of the boundary conditions along a rocket nozzle, with inlets having a fixed (i.e., Dirichlet) boundary condition while the gradient in total enthalpy (i.e., a Neumann boundary condition) was often employed along a slip wall or a centerline. The equation for the total enthalpy is given in Equation (B.6.1):

$$h_o = \frac{\rho e + P}{\rho} \tag{B.6.1}$$

For Dirichlet type boundary conditions where the total enthalpy desired is specified, the following implicit relations are maintained:

$$h_o^{n+1} = h_o^n + \left(\frac{\partial h_o}{\partial t}\right)^n \Delta t \tag{B.6.2}$$

where the time change of the total enthalpy can be derived from Equation (B.6.1) as

written as shown in Equation (B.6.3):

$$\left(\frac{\partial h_o}{\partial t}\right)^n = \frac{\partial(\rho e) + \partial P}{\rho\ \partial t} - \left[\frac{\rho e + P}{\rho^2}\right]\frac{\partial \rho}{\partial t} \tag{B.6.3}$$

where the relation between the static pressure, P, and the dependent variables is given in Section B.3.

In cases where Neumann boundary conditions are employed, the following relationship is employed:

$$\frac{\partial h_o^{n+1}}{\partial \eta} = \frac{\partial\left[h_o^n + \left(\frac{\partial(\rho e) + \partial P}{\rho\ \partial t} - \left[\frac{\rho e + P}{\rho^2}\right]\frac{\partial \rho}{\partial t}\right)\Delta t\right]}{\partial \eta} \tag{B.6.4}$$

where the computational gradient given by Equation (B.6.4) equals zero. An analogous expression arises if one specifies the gradient in total enthalpy in the ξ direction.

Appendix C

Multicomponent Species Diffusion

The laminar diffusion of a multispecies gas can be contributed to a gradient in species concentration or a gradient in temperature or pressure. The contributions can be written as:

$$j_i = j_i^{(x)} + j_i^{(T)} + j_i^{(p)} \tag{C.0.1}$$

where $j_i^{(x)}$ is the diffusion flux as the result of species concentration gradients, $j_i^{(T)}$ is the diffusion flux due to temperature gradients, and $j_i^{(p)}$ is the diffusion flux due to a pressure gradient. The components of diffusion have the characteristic that the sum of the thermal diffusion species flux is equal to zero. Therefore, since diffusion as the result of a pressure gradient is assumed to be very small in a propulsive nozzle, the following equations for the components of species flux must be true:

$$\sum_{i=1}^{n} j_i^{(x)} = 0 \tag{C.0.2}$$

$$\sum_{i=1}^{n} j_i^{(T)} = 0 \tag{C.0.3}$$

In the sections to follow, the evaluation of the individual components of mass diffusion will be discussed.

C.1. Multispecies Ordinary Diffusion

As described by Bird et al. (Reference 8), the multispecies transfer equations of ordinary diffusion can be written as:

$$j_i^{(x)} = \frac{c^2}{\rho} \sum_{j=1}^{n} M_i M_j D_{ij} \nabla x_i \tag{C.1.1}$$

In general, the multicomponent diffusion equation given in Equation (C.1.1) is rarely used directly due to the complexity of the multicomponent diffusion term, D_{ij}, which is, in general, a function of both temperature and species concentration. Thus, experimental evaluation of such a term would require a large number of variables and is consequently rarely pursued.

Instead, the Stefan-Maxwell equations of multicomponent species transfer, which relate multicomponent species transfer as a function of binary diffusion coefficients, $\wp_{ij}$, are the usual starting point for ordinary, multispecies, mass transfer calculations.

$$\text{(C.1.2)} \qquad \frac{1}{\rho}\sum_{\substack{j=1\\ j\neq i}}^{n}\frac{1}{\wp_{ij}M_j}\left(\omega_i j_j^{(x)} - \omega_j j_i^{(x)}\right) = \sum_{j=1}^{n}\frac{1}{M_j}\left(\omega_j \nabla\omega_i - \omega_i\nabla\omega_j\right)$$

Rigorously, the Stefan-Maxwell equations provide a relation for the multicomponent transfer of species in a first-order sense only. However, extensive experimental tests and analytical predictions have shown that second-order effects, as concerns ordinary diffusion, are quite small (Reference 48).

The significant advantage of the Stefan-Maxwell equations is that they algebraically relate the multicomponent ordinary diffusion fluxes to the binary diffusion coefficients. To a first-order approximation, the binary diffusion coefficients are independent of species concentration and are amenable to experimental determination.

Some simplification in the calculation of the diffusion fluxes can be made by making use of the fact that the sum of the ordinary diffusion fluxes is equal to zero.

$$\text{(C.1.3)} \quad \sum_{\substack{j=1\\ j\neq i}}^{n-1}\left\{\left(\frac{\omega_i}{\rho\wp_{ij}M_j} - \frac{\omega_i}{\rho\wp_{in}M_n}\right)j_j^{(x)} - \frac{\omega_j}{\rho\wp_{ij}M_j}j_i^{(x)}\right\} - \left[\omega_i + \omega_n\right]\frac{j_i^{(x)}}{\rho\wp_{in}M_n}$$

$$= \sum_{j=1}^{n}\frac{1}{M_j}\left(\omega_j\nabla\omega_i - \omega_i\nabla\omega_j\right)$$

Further simplification to the right-hand side of the above equation could be made through the use of the mass conservations relation, $\omega_n = 1 - \sum_{j=1}^{n-1} \omega_j$. However, the determination of the multicomponent thermal diffusion coefficients requires the knowledge of the relation between ordinary species diffusion and all of the species concentration gradient terms. For a four species system, Equation (C.1.3) can be written in the following matrix form:

$$\begin{bmatrix} \phi_{11} & \phi_{12} & \phi_{13} \\ \phi_{21} & \phi_{22} & \phi_{23} \\ \phi_{31} & \phi_{32} & \phi_{33} \end{bmatrix} \begin{bmatrix} j_1^{(x)} \\ j_2^{(x)} \\ j_3^{(x)} \end{bmatrix} = \begin{bmatrix} \beta_{11} \\ \beta_{12} \\ \beta_{13} \end{bmatrix} \nabla \omega_1 + \ldots + \begin{bmatrix} \beta_{41} \\ \beta_{42} \\ \beta_{43} \end{bmatrix} \nabla \omega_4 \tag{C.1.4}$$

The extension to other species systems is apparent. Equation (C.1.4) is solved by factoring the left-hand side into lower-upper triangular matrices and then successively solving for the species dependence vectors, β_i. The resulting solution is in coefficient form:

$$j_i^{(x)} = \sum_{j=1}^{n} C_{ij} \nabla \omega_j \tag{C.1.5}$$

Employing the mass conservation rule, Equation (C.1.5) can be put into a relation involving n – 1 species:

$$j_i^{(x)} = \sum_{j=1}^{n-1} A_{ij} \nabla \omega_j \tag{C.1.6}$$

where $A_{ij} = C_{ij} - C_{in}$.

C.2. Multispecies Thermal Diffusion

The determination of multispecies thermal diffusion is neither a well-developed nor a simple methodology. In contrast to the calculation of multicomponent ordinary diffusion

where the Stefan-Maxwell equations allowed the determination of multicomponent diffusion based on binary diffusion coefficients, the complex nature and relatively poor development of the multicomponent thermal diffusion factor forces reliance on purely theoretical calculations. Given these conditions, an expression developed by Waldman (Reference 49) was adopted for the calculation of the thermal diffusion coefficient. Waldman gives the following expression for the multicomponent thermal diffusion factor:

$$\alpha_{ij} = \frac{8}{3}\left(\frac{M_i M_j}{M_i + M_j}\right)^2 \left[\frac{5}{2} - C_{ij}^*\right]\left(\frac{A_i}{M_i} - \frac{A_j}{M_j}\right) \tag{C.2.1}$$

The coefficient A_i can be determined using the following first-order approximation:

$$\sum_{j=1}^{n} x_j \left(a'_{ij} A_i + a''_{ij} A_j\right) = \frac{15}{4} \tag{C.2.2}$$

The a'_{ij} and a''_{ij} coefficients are a function only of the binary masses and the temperature of the species.

$$a'_{ij} = 5\frac{M_i M_j}{M_i + M_j} F_{ij} \tag{C.2.3}$$

$$a''_{ij} = 5\frac{(M_i M_j)^2}{(M_i + M_j)^3} F_{ij}^* \tag{C.2.4}$$

where the coefficients F_{ij} and F_{ij}^* are defined as follows:

$$F_{ij} = 6\left(\frac{M_i}{M_i + M_j}\right)^2 + \left[5 - \frac{12}{5}B_{ij}^*\right]\left(\frac{M_j}{M_i + M_j}\right)^2 + \frac{16}{5}\frac{M_i M_j}{(M_i + M_j)^2} A_{ij}^* \tag{C.2.5}$$

$$F_{ij}^* = \frac{12}{5}B_{ij}^* + \frac{16}{5}A_{ij}^* - 11 \tag{C.2.6}$$

The nondimensional terms, A_{ij}^*, B_{ij}^*, and C_{ij}^*, are functions of the Ω integrals, which in turn are functions of the properties of the species-pair combination and the fluid temperature (Reference 48).

Using the expressions presented in Equations (C.2.3) to (C.2.6), Equation (C.2.2) can be solved by the simultaneous solution of a set of equations equal in number to the number of species present. Once Equation (C.2.2) has been solved, Equation (C.2.1) can be solved for the multicomponent species thermal diffusion factor, α_{ij}. As defined, the thermal diffusion coefficient, D_i^T, is related to the diffusion factor by the following relation:

$$D_i^T = \sum_{j=1}^{n} D_{ij}^* (k_T)_j = \sum_{j=1}^{n} D_{ij}^* x_j \sum_{k=1}^{n} x_k \alpha_{jk}^T \tag{C.2.7}$$

where D_{ij}^* is defined as the coefficient of ordinary species diffusion when based on species mole fraction:

$$j_i^{(x)} \equiv \sum_{j=1}^{n} D_{ij}^* \nabla x_j \tag{C.2.8}$$

A relation for the multicomponent diffusion coefficient based on mole fraction, D_{ij}^*, and one based on mass fraction, C_{ij}, can be determined by equating the flux relations:

$$j_i^{(x)} \equiv \sum_{j=1}^{n} D_{ij}^* \nabla x_j \equiv \sum_{j=1}^{n} C_{ij} \nabla \omega_j \tag{C.2.9}$$

Substitution of the relation between species mass fraction and species mole fraction can be made in Equation (C.2.9) to obtain the relation between D_{ij}^* and C_{ij}.

$$D_{ij}^* = C_{ij} \frac{M_j}{M} - \frac{M_j}{M^2} \sum_{k=1}^{n} C_{ik} x_k M_k \tag{C.2.10}$$

The final form of the equation for the thermal diffusion factor, D_i^T, shown in Equation (C.2.7), was used for the evaluation of the Soret mass and Dufour heat transfer coefficients. Equation (C.2.10) was used for the evaluation of the ordinary diffusion coefficient required in Equation (C.2.7).

Appendix D

Species Source Function

The species source function, σ_i, is a function of species concentration, reaction mechanism, and reaction rates. In Reference 50, the species source function is derived as presented below:

$$\sigma_i = M_i \sum_{j=1}^{m} \Delta\nu_{ij} \left[K_{fj} \prod_{i=1}^{n} \left(\frac{\rho_i}{M_i} \right)^{\nu'_{ij}} - K_{bj} \prod_{i=1}^{n} \left(\frac{\rho_i}{M_i} \right)^{\nu''_{ij}} \right] \tag{D.0.1}$$

where the terms are defined as follows:

ν''_{ij} = Product stoichiometric coefficient of species i for the jth reaction mechanism

ν'_{ij} = Reaction stoichiometric coefficient of species i for the jth reaction mechanism

$\Delta\nu_{ij} = \nu''_{ij} - \nu'_{ij}$

K_{fj} = Forward reaction rate for the jth reaction

K_{bj} = Backward reaction rate for the jth reaction

The reaction mechanism and the forward reaction rates for the gas system of interest (hydrogen-oxygen) are presented in Appendix I.

The forward and backward reaction rates can be related to the equilibrium constant, K_{Pj}, through the following expression (presented in Reference 23, p. 22):

$$\frac{K_{fj}}{K_{bj}} = K_{Pj} (\bar{R}T)^{-\Delta\nu_j} \tag{D.0.2}$$

where $\Delta\nu_j = \sum_{i=1}^{n} \Delta\nu_{ij}$ is the net mole production of the jth reaction. The equilibrium

constant can be determined as a function of the stoichiometric coefficients and the Gibbs Function, g_i:

$$K_{Pj} = \exp\left(-\sum_{i=1}^{n} g_i \Delta\nu_{ij} / (\bar{R}T)\right) \tag{D.0.3}$$

where the Gibbs function used in Equation (D.0.3) is expressed on a molar basis.

Substitution of Equation (D.0.2) and (D.0.3) into Equation (D.0.1) yields the following relation for the species source function:

$$\sigma_i = M_i \sum_{j=1}^{m} \Delta\nu_{ij} \left[[\bar{R}T]^{-\Delta\nu_j} \exp\left(-\sum_{i=1}^{n} g_i \Delta\nu_{ij} / [\bar{R}T]\right) \prod_{i=1}^{n} \left(\frac{\rho_i}{M_i}\right)^{\nu'_{ij}} - \prod_{i=1}^{n} \left(\frac{\rho_i}{M_i}\right)^{\nu''_{ij}} \right] K \tag{D.0.4}$$

The dependence of the species source function on the dependent variables can be determined by partial differentiation of Equation (D.0.4) with respect to the dependent properties and with the realization that the backward reaction rate, K_{bj}, can be a strong function of temperature (Appendix I), and for catalytic reactions, K_{bj} is also a function of the species concentration.

D.1. Relation of the Species Source Function to the Dependent Variables

To accurately describe the dependence of the species source function on the fluid density and the species densities, it is necessary to recast the species source function of Equation (D.0.4) into a form that is independent of the final species density term, ρ_n, as this term is not a dependent variable since it is related to the other species densities by the relation:

$$\rho_n = \rho - \sum_{i=1}^{n-1} \rho_i \tag{D.1.1}$$

Using Equation (D.1.1), terms contained in Equation (D.0.4) can be recast in terms of the dependent species densities solved in the Tethys model. Thus,

$$\text{(D.1.2)} \quad \prod_{i=1}^{n}\left(\frac{\rho_i}{M_i}\right)^{\nu''_{ij}} = \prod_{i=1}^{n-1}\left(\frac{\rho_i}{M_i}\right)^{\nu''_{ij}} \left\{\left[\frac{\rho}{M_n}\right]-\left[\frac{\sum_{i=1}^{n-1}\rho_i}{M_n}\right]\right\}^{\nu''_{nj}}$$

The derivative of Equation (D.1.2) with respect to the fluid and species densities is as follows:

$$\text{(D.1.3)} \quad \frac{\partial}{\partial\rho}\left[\prod_{i=1}^{n}\left(\frac{\rho_i}{M_i}\right)^{\nu''_{ij}}\right] = \frac{\nu''_{nj}}{M_n}\left\{\left[\frac{\rho}{M_n}\right]-\left[\frac{\sum_{i=1}^{n-1}\rho_i}{M_n}\right]\right\}^{\nu''_{nj}-1} \prod_{i=1}^{n-1}\left(\frac{\rho_i}{M_i}\right)^{\nu''_{ij}} = \frac{\nu''_{nj}}{\rho_n}\prod_{i=1}^{n}\left(\frac{\rho_i}{M_i}\right)^{\nu''_{ij}}$$

In a similar manner, the derivative of Equation (D.1.2) with respect to the species densities is as follows:

$$\text{(D.1.4)} \quad \frac{\partial}{\partial\rho_i}\left[\prod_{i=1}^{n}\left(\frac{\rho_i}{M_i}\right)^{\nu''_{ij}}\right] = -\frac{\nu''_{nj}}{\rho_n}\prod_{i=1}^{n}\left(\frac{\rho_i}{M_i}\right)^{\nu''_{ij}} + \frac{\nu''_{ij}}{\rho_i}\prod_{i=1}^{n}\left(\frac{\rho_i}{M_i}\right)^{\nu''_{ij}}$$

The complete dependence of the species source function with respect to the fluid density is shown in Equation (D.1.5):

$$\text{(D.1.5)} \quad \frac{\partial\sigma_i}{\partial\rho} = \left[\begin{array}{l} M_i\sum_{j=1}^{m}\Delta\nu_{ij}\left[\frac{\nu'_{nj}}{\rho_n}K_{Pj}[\bar{R}T]^{-\Delta\nu_j}\prod_{i=1}^{n}\left(\frac{\rho_i}{M_i}\right)^{\nu'_{ij}}-\frac{\nu''_{nj}}{\rho_n}\prod_{i=1}^{n}\left(\frac{\rho_i}{M_i}\right)^{\nu''_{ij}}\right]K_{bj} \\ + M_i\sum_{j=1}^{m}\Delta\nu_{ij}\left[K_{Pj}[\bar{R}T]^{-\Delta\nu_j}\prod_{i=1}^{n}\left(\frac{\rho_i}{M_i}\right)^{\nu'_{ij}}-\prod_{i=1}^{n}\left(\frac{\rho}{M_i}\right)^{\nu''_{ij}}\right]\frac{\partial K_{bj}}{\partial\rho} \\ + M_i\sum_{j=1}^{m}\Delta\nu_{ij}\left[\left[-\Delta\nu_j K_{Pj}[\bar{R}T]^{(-\Delta\nu_j-1)}+(\bar{R}T)^{-\Delta\nu_j}\frac{\partial K_{Pj}}{\partial T}\right]\prod_{i=1}^{n}\left(\frac{\rho_i}{M_i}\right)^{\nu'_{ij}}\right]K_{bj}\frac{\partial T}{\partial\rho} \end{array}\right]$$

The dependence of the species source function on the species densities has a similar form.

$$(D.1.6)\quad \frac{\partial \sigma_i}{\partial \rho_k} = \left[\begin{array}{l} M_i \sum_{j=1}^{m} \Delta\nu_{ij} \left[\left[\frac{\nu'_{kj}}{\rho_k} - \frac{\nu'_{nj}}{\rho_n} \right] K_{Pj} [\bar{R}T]^{-\Delta\nu_j} \prod_{i=1}^{n} \left(\frac{\rho_i}{M_i} \right)^{\nu'_{ij}} - \left[\frac{\nu''_{kj}}{\rho_k} - \frac{\nu''_{nj}}{\rho_n} \right] \prod_{i=1}^{n} \left(\frac{\rho_i}{M_i} \right)^{\nu''_{ij}} \right] K_{bj} \\ + M_i \sum_{j=1}^{m} \Delta\nu_{ij} \left[K_{Pj} [\bar{R}T]^{-\Delta\nu_j} \prod_{i=1}^{n} \left(\frac{\rho_i}{M_i} \right)^{\nu'_{ij}} - \prod_{i=1}^{n} \left(\frac{\rho}{M_i} \right)^{\nu''_{ij}} \right] \frac{\partial K_{bj}}{\partial \rho_k} \\ + M_i \sum_{j=1}^{m} \Delta\nu_{ij} \left[\left[-\Delta\nu_j K_{Pj} [\bar{R}T]^{(-\Delta\nu_j - 1)} + (\bar{R}T)^{-\Delta\nu_j} \frac{\partial K_{Pj}}{\partial T} \right] \prod_{i=1}^{n} \left(\frac{\rho_i}{M_i} \right)^{\nu'_{ij}} \right] K_{bj} \frac{\partial T}{\partial \rho_k} \end{array} \right]$$

The dependence of the species source function on the other dependent variables is significantly simpler, being a function only of the relation between the particular dependent property and the fluid temperature.

$$(D.1.7)\quad \frac{\partial \sigma_i}{\partial (\rho u)} = \frac{\partial \sigma_i}{\partial T} \frac{\partial T}{\partial (\rho u)} = \left[\begin{array}{l} M_i \sum_{j=1}^{m} \Delta\nu_{ij} \left[K_{Pj} (\bar{R}T)^{-\Delta\nu_j} \prod_{i=1}^{n} \left(\frac{\rho_i}{M_i} \right)^{\nu'_{ij}} - \prod_{i=1}^{n} \left(\frac{\rho_i}{M_i} \right)^{\nu''_{ij}} \right] \frac{\partial K_{bj}}{\partial T} \frac{\partial T}{\partial (\rho u)} \\ + M_i \sum_{j=1}^{m} \Delta\nu_{ij} \left[\left[-\Delta\nu_j K_{Pj} (\bar{R}T)^{-\Delta\nu_j - 1} + (\bar{R}T)^{-\Delta\nu_j} \frac{\partial K_{Pj}}{\partial T} \right] \prod_{i=1}^{n} \left(\frac{\rho_i}{M_i} \right)^{\nu'_{ij}} \right] K_{bj} \frac{\partial T}{\partial (\rho u)} \end{array} \right]$$

$$(D.1.8)\quad \frac{\partial \sigma_i}{\partial (\rho v)} = \frac{\partial \sigma_i}{\partial T} \frac{\partial T}{\partial (\rho v)} = \left[\begin{array}{l} M_i \sum_{j=1}^{m} \Delta\nu_{ij} \left[K_{Pj} (\bar{R}T)^{-\Delta\nu_j} \prod_{i=1}^{n} \left(\frac{\rho_i}{M_i} \right)^{\nu'_{ij}} - \prod_{i=1}^{n} \left(\frac{\rho_i}{M_i} \right)^{\nu''_{ij}} \right] \frac{\partial K_{bj}}{\partial T} \frac{\partial T}{\partial (\rho v)} \\ + M_i \sum_{j=1}^{m} \Delta\nu_{ij} \left[\left[-\Delta\nu_j K_{Pj} (\bar{R}T)^{-\Delta\nu_j - 1} + (\bar{R}T)^{-\Delta\nu_j} \frac{\partial K_{Pj}}{\partial T} \right] \prod_{i=1}^{n} \left(\frac{\rho_i}{M_i} \right)^{\nu'_{ij}} \right] K_{bj} \frac{\partial T}{\partial (\rho v)} \end{array} \right]$$

$$(D.1.9)\quad \frac{\partial \sigma_i}{\partial (\rho e)} = \frac{\partial \sigma_i}{\partial T} \frac{\partial T}{\partial (\rho v)} = \left[\begin{array}{l} M_i \sum_{j=1}^{m} \Delta\nu_{ij} \left[K_{Pj} (\bar{R}T)^{-\Delta\nu_j} \prod_{i=1}^{n} \left(\frac{\rho_i}{M_i} \right)^{\nu'_{ij}} - \prod_{i=1}^{n} \left(\frac{\rho_i}{M_i} \right)^{\nu''_{ij}} \right] \frac{\partial K_{bj}}{\partial T} \frac{\partial T}{\partial (\rho e)} \\ + M_i \sum_{j=1}^{m} \Delta\nu_{ij} \left[\left[-\Delta\nu_j K_{Pj} (\bar{R}T)^{-\Delta\nu_j - 1} + (\bar{R}T)^{-\Delta\nu_j} \frac{\partial K_{Pj}}{\partial T} \right] \prod_{i=1}^{n} \left(\frac{\rho_i}{M_i} \right)^{\nu'_{ij}} \right] K_{bj} \frac{\partial T}{\partial (\rho e)} \end{array} \right]$$

The dependence of the fluid temperature on the dependent properties is described in Appendix B, while the dependence of the backward reaction rate, K_{bj}, and the equilibrium constant, K_{pj}, are described in the following sections.

D.2. Backward Reaction Rate, K_{bj}

The backward reaction rate of the hydrogen-oxygen system of interest is assumed to obey a modified form of the Arrhenius equation (Reference 23):

$$K_{bj} = B_j T^{\alpha_j} \exp\left[-E_j/(\bar{R}T)\right] \tag{D.2.1}$$

where A_j, α_j, and E_j are experimentally estimated coefficients. When third body (i.e., catalytic) chemical reactions are considered, the assumption is made (supported by theoretical and experimental measurements, as discussed in Reference 1) that the reaction rate coefficients a_j and E_j are independent of the third body reaction. Consequently, a mean third body reaction rate, A_j, can be used, which is defined by the following expression:

$$K_{bj} = T^{\alpha_j}\left[\sum_{i=1}^{n} \rho_i B_{ij}/M_i\right] \exp\left[-E_j/(\bar{R}T)\right] \tag{D.2.2}$$

where the mean reaction rate is equal to the density weighted sum of the third body reaction rate coefficients:

$$B_j = \sum_{i=1}^{n} \rho_i B_{ij}/M_i \tag{D.2.3}$$

To facilitate a simple derivation, Equation (D.2.3) can be recast in terms of the fluid density and the dependent species densities:

$$K_{bj} = T^{\alpha_j} \exp\left[-E_j/(\bar{R}T)\right] \left[\rho B_{nj}/M_n + \sum_{i=1}^{n-1} \rho_i \left(B_{ij}/M_i - B_{nj}/M_n\right)\right] \tag{D.2.4}$$

In this form, differentiation with respect to the dependent variables is readily accom-

plished. The results are presented in Equations (D.2.5) to (D.2.11).

For catalytic reactions, the dependence of the backward chemical reaction rate is shown in Equation (D.2.5) and (D.2.6).

$$\frac{\partial K_{bj}}{\partial \rho} = \frac{K_{bj}}{T}\left(\alpha_j + \frac{E_j}{\bar{R}T}\right)\frac{\partial T}{\partial \rho} + T^{\alpha_j}\exp\left[-E_j/(\bar{R}T)\right] B_{nj}/M_n \tag{D.2.5}$$

$$\frac{\partial K_{bj}}{\partial \rho_i} = \frac{K_{bj}}{T}\left(\alpha_j + \frac{E_j}{\bar{R}T}\right)\frac{\partial T}{\partial \rho_i} + T^{\alpha_j}\exp\left[-E_j/(\bar{R}T)\right] \left[B_{ij}/M_i - B_{nj}/M_n\right] \tag{D.2.6}$$

For binary exchange reactions, the backward chemical reaction rate is related to the species densities only in there relation to the fluid temperature, as shown in Equation (D.2.7) and (D.2.8):

$$\frac{\partial K_{bj}}{\partial \rho} = \frac{K_{bj}}{T}\left(\alpha_j + \frac{E_j}{\bar{R}T}\right)\frac{\partial T}{\partial \rho} \tag{D.2.7}$$

$$\frac{\partial K_{bj}}{\partial \rho_i} = \frac{K_{bj}}{T}\left(\alpha_j + \frac{E_j}{\bar{R}T}\right)\frac{\partial T}{\partial \rho_i} \tag{D.2.8}$$

For either catalytic or binary exchange reactions, the backward chemical reaction rate is independent of ρu, ρv, and ρe, except for the dependence of these properties on the fluid temperature:

$$\frac{\partial K_{bj}}{\partial (\rho u)} = \frac{K_{bj}}{T}\left(\alpha_j + \frac{E_j}{\bar{R}T}\right)\frac{\partial T}{\partial (\rho u)} \tag{D.2.9}$$

$$\frac{\partial K_{bj}}{\partial (\rho v)} = \frac{K_{bj}}{T}\left(\alpha_j + \frac{E_j}{\bar{R}T}\right)\frac{\partial T}{\partial (\rho v)} \tag{D.2.10}$$

$$\frac{\partial K_{bj}}{\partial(\rho e)} = \frac{K_{bj}}{T}\left(\alpha_j + \frac{E_j}{\bar{R}T}\right)\frac{\partial T}{\partial(\rho e)} \tag{D.2.11}$$

The dependence of the fluid temperature on the dependent variables is presented in Appendix B.

D.3. Equilibrium Constant, K_{Pj}

The relation for the equilibrium constant, in terms of the Gibbs free energy and the stoichiometric coefficients, is given by Equation (D.0.3), which is repeated here.

$$K_{Pj} = \exp\left(-\sum_{i=1}^{n} g_i \Delta\nu_{ij} / (R_i T)\right) \tag{D.3.1}$$

where the Gibbs Function, g_i, is defined as:

$$g_i = h_i - T s_i^o \tag{D.3.2}$$

Here, the superscript o signifies evaluation at one atmosphere of pressure.

The following form of curve fit to the species enthalpy and entropy is adopted from Reference 47:

$$\frac{h_i}{R_i T} = \left[a_1 + \frac{a_2}{2}T + \frac{a_3}{3}T^2 + \frac{a_4}{4}T^3 + \frac{a_5}{5}T^4 + \frac{a_6}{T}\right]_i \tag{D.3.3}$$

$$\frac{s_i^o}{R_i} = \left[a_1 \ln(T) + a_2 T + \frac{a_3}{2}T^2 + \frac{a_4}{3}T^3 + \frac{a_5}{4}T^4 + a_7\right]_i \tag{D.3.4}$$

Substitution of Equations (D.3.3) and (D.3.4) into Equation (D.3.2) and rearranging terms yields the following expression:

$$K_{Pj} = \exp\left(-\sum_{i=1}^{n}\left[a_1(1 - \ln(T)) - \frac{a_2}{2}T - \frac{a_3}{6}T^2 - \frac{a_4}{12}T^3 - \frac{a_5}{20}T^4 + \frac{a_6}{T} - a_{7i}\right]_i \Delta\nu_{ij}\right) \tag{D.3.5}$$

The dependence of the equilibrium constant on the temperature can be determined by taking the natural logarithm of Equation (D.3.5) and differentiating:

$$\frac{dK_{Pj}}{K_{Pj}} = -\sum_{i=1}^{n}\left[-a_1\frac{1}{T} - \frac{a_2}{2} - \frac{a_3}{3}T - \frac{a_4}{4}T - \frac{a_5}{5}T^3 - \frac{a_6}{T^2}\right]_i (\Delta\nu_{ij})\,dT \tag{D.3.6}$$

Further rearrangement and resubstitution yields the following expression for the relationship between the equilibrium constant and the fluid temperature:

$$\frac{dK_{Pj}}{dT} = \left[\frac{K_{Pj}}{T}\right]\sum_{i=1}^{n}\frac{h_i}{R_i T}(\Delta\nu_{ij}) \tag{D.3.7}$$

The equilibrium constant is seen to be a function only of the fluid temperature. The relationship between the fluid temperature and the dependent variables is given in Appendix B.

Appendix E

Time-Averaged, Density-Weighted, Turbulent Flow Equations

The use of a density-weighted technique has come into favor as the preferred means of time-averaging the Navier-Stokes equations in compressible flow situations. The averaging process is performed by first decomposing the velocity, species densities, temperature, energy, enthalpy, and total enthalpy into mean and fluctuating components:

(E.1) $$v = \tilde{v} + v''$$

(E.2) $$w = \tilde{w} + w''$$

(E.3) $$u = \tilde{u} + u''$$

(E.4) $$T = \tilde{T} + T''$$

(E.5) $$\rho_i = \tilde{\rho}_i + \rho_i''$$

(E.6) $$e = \tilde{e} + e''$$

(E.7) $$h = \tilde{h} + h''$$

(E.8) $$H = \tilde{H} + H''$$

where the tilde (~) above the properties is defined as a time-averaged, density weighted term divided by the time-averaged density. The tilde signifies that the following operation has been performed:

(E.9) $$\tilde{\lambda} \equiv \frac{\overline{\rho\lambda}}{\bar{\rho}}$$

Since $\lambda = \tilde{\lambda} + \lambda''$ and $\rho\lambda = \rho\tilde{\lambda} + \rho\lambda''$, the averaging process yields:

(E.10) $$\overline{\rho\lambda} = \bar{\rho}\tilde{\lambda} + \overline{\rho\lambda''}$$

Division by the time-averaged density yields:

(E.11) $$\frac{\overline{\rho\lambda}}{\bar{\rho}} \equiv \tilde{\lambda} = \tilde{\lambda} + \frac{\overline{\rho\lambda''}}{\bar{\rho}}$$

Since the time-averaged density, $\bar{\rho}$, is a finite number, it must be true that the numerator of the second term on the right hand side of Equation (E.11), $\overline{\rho\lambda''}$, is equal to zero. This correlation is fundamental to the density-weighted technique that follows. It will be further assumed that the time-average of all diffusion terms is equal to the density weighted, time-average of each of the individual terms comprising the constitutive equation. For instance, the time-averaged shear stress, $\bar{\tau}_{xr}$, is assumed to be equal to the following:

(E.12) $$\bar{\tau}_{xr} = -\mu\left[\frac{\partial\tilde{u}}{\partial r} + \frac{\partial\tilde{v}}{\partial x}\right]$$

The fluid viscosity, and all other properties, including chemical reaction rates and equilibrium constants, are evaluated at the time-averaged temperature and species concentration.

Recall the cylindrical coordinate system form of the Navier-Stokes equations:

(E.13) $$\frac{\partial}{\partial t}r\begin{bmatrix}\rho\\ \rho u\\ \rho v\\ \rho e\\ \rho_i\end{bmatrix} + \frac{\partial}{\partial x}r\begin{bmatrix}\rho u\\ \rho u^2+P\\ \rho uv\\ (\rho e+P)u\\ \rho_i u\end{bmatrix} + \frac{\partial}{\partial r}r\begin{bmatrix}\rho v\\ \rho uv\\ \rho v^2+P\\ (\rho e+P)v\\ \rho_i v\end{bmatrix} + \begin{bmatrix}0\\ 0\\ -(P+\rho w^2)\\ 0\\ -r\sigma_i\end{bmatrix} = \begin{bmatrix}\text{Viscous}\\ \text{terms}\end{bmatrix}$$

where the centrifugal force, ρw^2, is retained, even for two-dimensional flow with no average tangential flow. For brevity of approach, the alternative to the description of the radial pressure gradient is shown in Equation (E.13) and, as will be shown in the following discussion, the turbulent aspect of the flow has no effect on the pressure gradient terms other than to change the terms to a time-averaged quantity.

Decomposing the enthalpy($H = E_T + P = \rho [h + (u^2 + v^2)/2]$), velocity, mass density, and energy into fluctuating and time-averaged quantities, Equation (E.13) can be written as shown in the following equation:

$$\frac{\partial}{\partial t} r \begin{bmatrix} \rho \\ \rho(\tilde{u}+u'') \\ \rho(\tilde{v}+v'') \\ \rho(\tilde{e}+e'') \\ \tilde{\rho}_i + \rho_i'' \end{bmatrix} + \frac{\partial}{\partial x} r \begin{bmatrix} \rho(\tilde{u}+u'') \\ \rho(\tilde{u}+u'')^2 + P \\ \rho(\tilde{u}+u'')(\tilde{v}+v'') \\ (\tilde{H}+H'')(\tilde{u}+u'') \\ (\tilde{\rho}_i + \rho_i'')(\tilde{u}+u'') \end{bmatrix}$$

(E.14)

$$+ \frac{\partial}{\partial r} r \begin{bmatrix} \rho(\tilde{v}+v'') \\ \rho(\tilde{u}+u'')(\tilde{v}+v'') \\ \rho(\tilde{v}+v'')^2 + P \\ (\tilde{H}+H'')(\tilde{v}+v'') \\ (\tilde{\rho}_i + \rho_i'')(\tilde{v}+v'') \end{bmatrix} + \begin{bmatrix} 0 \\ 0 \\ -(P + \rho(\tilde{w}+w'')^2) \\ 0 \\ -r\sigma_i \end{bmatrix} = \begin{bmatrix} \text{Viscous} \\ \text{terms} \end{bmatrix}$$

Note that the density has not been decomposed into average and fluctuating components. This is an attribute of the density weighting technique. If the above equations are time-averaged, the density-weighted, time-averaged, Navier-Stokes, equations are:

$$\frac{\partial}{\partial t}r\begin{bmatrix}\bar{\rho}\\ \bar{\rho}\tilde{u}\\ \bar{\rho}\tilde{v}\\ \bar{\rho}\tilde{e}\\ \tilde{\rho}_i\end{bmatrix} + \frac{\partial}{\partial x}r\begin{bmatrix}\bar{\rho}\tilde{u}\\ \bar{\rho}\tilde{u}^2+\overline{\rho u''^2}+\bar{P}\\ \bar{\rho}\tilde{u}\tilde{v}+\overline{\rho u''v''}\\ \tilde{H}\tilde{u}+\overline{H''u''}\\ \tilde{\rho}_i\tilde{u}+\overline{\rho_i''u''}\end{bmatrix}$$

(E.15)

$$+ \frac{\partial}{\partial r}r\begin{bmatrix}\bar{\rho}\tilde{v}\\ \bar{\rho}\tilde{u}\tilde{v}+\overline{\rho u''v''}\\ \bar{\rho}\tilde{v}^2+\overline{\rho v''^2}+\bar{P}\\ \tilde{H}\tilde{v}+\overline{H''v''}\\ \tilde{\rho}_i\tilde{v}+\overline{\rho_i''v''}\end{bmatrix} + \begin{bmatrix}0\\ 0\\ -(\bar{P}+\overline{\rho w''^2})\\ 0\\ -r\overline{\sigma_i}\end{bmatrix} = \begin{bmatrix}\text{Viscous}\\ \text{terms}\end{bmatrix}$$

The time-averaged terms containing the stagnation enthalpy, H'', should be decomposed into a more fundamental form:

$$H = \rho\,[h + (u^2+v^2+w^2)/2] \tag{E.16}$$

Furthermore, the enthalpy, h, is the sum of the mass weighted species enthalpies:

$$\rho h = \sum_{i=1}^{n}\rho_i h_i \tag{E.17}$$

Now, decomposing the stagnation enthalpy into mean and fluctuating components yields:

$$\text{(E.18)} \qquad \tilde{H} + H'' = \sum_{i=1}^{n} (\tilde{\rho}_i + \rho_i'')\,(\tilde{h}_i + h_i'') + \rho\,[\,(\tilde{u} + u'')^2 + (\tilde{v} + v'')^2 + w''^2\,]/2$$

Multiplication of Equation (E.18) by the fluctuating axial velocity, u", and time-averaging results in the following expression:

$$\text{(E.19)} \qquad \overline{H''u''} = \sum_{i=1}^{n} (\tilde{h}_i\overline{\rho_i''u''} + \tilde{\rho}_i\overline{h_i''u''}) + \tilde{v}\overline{\rho u''v''} + \tilde{u}\overline{\rho u''^2} + (\overline{\rho u''^3} + \overline{\rho v''^2 u''} + \overline{\rho u'' w''^2})/2$$

Similarly, multiplying Equation (E.18) by the fluctuating radial velocity, v", and time-averaging yields the following:

$$\text{(E.20)} \qquad \overline{H''v''} = \sum_{i=1}^{n} (\tilde{h}_i\overline{\rho_i''v''} + \tilde{\rho}_i\overline{h_i''v''}) + \tilde{u}\overline{\rho u''v''} + \tilde{v}\overline{\rho v''^2} + (\overline{\rho v''^3} + \overline{\rho v'' u''^2} + \overline{\rho v'' w''^2})/2$$

Assuming that the triple correlation turbulent fluctuations are negligible, the stagnation enthalpy expressions in Equations (E.19) and (E.20) simplify to the following:

$$\text{(E.21)} \qquad \overline{H''u''} = \sum_{i=1}^{n} (\tilde{h}_i\overline{\rho_i''u''} + \tilde{\rho}_i\overline{h_i''u''}) + \tilde{v}\overline{\rho u''v''} + \tilde{u}\overline{\rho u''^2}$$

$$\text{(E.22)} \qquad \overline{H''v''} = \sum_{i=1}^{n} (\tilde{h}_i\overline{\rho_i''v''} + \tilde{\rho}_i\overline{h_i''v''}) + \tilde{u}\overline{\rho u''v''} + \tilde{v}\overline{\rho v''^2}$$

In general, the time-averaged pressure, $\bar{P}$, and species source function, $\bar{\sigma}_i$, will be functions of some time-averaged turbulent terms (e.g., $\bar{P} = \bar{\rho}R\bar{T}$ + Turbulent terms). However, for the flow problems of interest in this study, these terms are small compared to their time-averaged counterparts and consequently were not considered.

Summarizing, the dominant density-weighted, time-averaged, Navier-Stokes equations are:

$$\frac{\partial}{\partial t}\mathbf{r}\begin{bmatrix}\bar{\rho}\\ \bar{\rho}\tilde{u}\\ \bar{\rho}\tilde{v}\\ \bar{\rho}\tilde{e}\\ \tilde{\rho}_i\end{bmatrix}+\frac{\partial}{\partial x}\mathbf{r}\begin{bmatrix}\bar{\rho}\tilde{u}\\ \bar{\rho}\tilde{u}^2+\overline{\rho u''^2}+\bar{P}\\ \bar{\rho}\tilde{u}\tilde{v}+\overline{\rho u''v''}\\ \tilde{H}\tilde{u}+\sum_{i=1}^{n}(\tilde{h}_i\overline{\rho_i''u''}+\tilde{\rho}_i\overline{h_i''u''})+\tilde{v}\overline{\rho u''v''}+\tilde{u}\overline{\rho u''^2}\\ \tilde{\rho}_i\tilde{u}+\overline{\rho_i''u''}\end{bmatrix}$$

(E.23)

$$+\frac{\partial}{\partial r}\mathbf{r}\begin{bmatrix}\bar{\rho}\tilde{v}\\ \bar{\rho}\tilde{u}\tilde{v}+\overline{\rho u''v''}\\ \bar{\rho}\tilde{v}^2+\overline{\rho v''^2}+\bar{P}\\ \tilde{H}\tilde{v}+\sum_{i=1}^{n}(\tilde{h}_i\overline{\rho_i''v''}+\tilde{\rho}_i\overline{h_i''v''})+\tilde{u}\overline{\rho u''v''}+\tilde{v}\overline{\rho v''^2}\\ \tilde{\rho}_i\tilde{v}+\overline{\rho_i''v''}\end{bmatrix}+\begin{bmatrix}0\\ 0\\ -(\bar{P}+\overline{\rho w''^2})\\ 0\\ -\mathbf{r}\bar{\sigma}_i\end{bmatrix}$$

$$=\begin{bmatrix}\text{Viscous}\\ \text{terms}\end{bmatrix}$$

The equations of state are taken to be unchanged by the presence of turbulence:

(E.24) $$\bar{P} = \bar{\rho} R \bar{T}$$

where the gas constant of the mixture, R, is equal to the universal gas constant divided by a mean molecular weight:

(E.24.1) $$R = \frac{\bar{\bar{R}}}{\bar{\bar{M}}}$$

where the mean molecular weight of the mixture is defined as:

(E.24.2) $$\bar{\bar{M}} = \left[\sum_{i=1}^{n} \left(\frac{\tilde{\rho}_i}{\bar{\rho} M_i} \right) \right]^{-1}$$

The relation of the total energy to the internal energy and the velocity is also assumed to be unchanged by the presence of turbulence:

(E.25) $$\bar{\rho}\tilde{e} = \sum_{i=1}^{n} \tilde{\rho}_i \left(\int_{T_R}^{\bar{T}} C_{vi} d\bar{T} + u_{iR} \right) + \bar{\rho} \left(\tilde{u}^2 + \tilde{v}^2 \right) / 2$$

Appendix F

Turbulence Modelling

F.1. The Boussinesq Approximation

The time-averaging of the Navier-Stokes equations results in the creation of numerous turbulence quantities for which no known solution exists. These terms are, however, usually modelled by assuming they have 'viscous-like' behavior, commonly referred to as the Boussinesq approximation (Reference 51). For example, the turbulence term, $\overline{\rho u'' v''}$, is usually modelled as follows:

$$-\overline{\rho u'' v''} = \tau^t_{rx} = \mu^t \left[\frac{\partial \tilde{u}}{\partial r} - \frac{\partial \tilde{v}}{\partial x}\right] \tag{F.1.1}$$

In a similar fashion, turbulent heat transfer and mass fluxes are approximated by the following diffusion equations:

$$-\overline{\rho_i'' v''} = -\, j^t_{ir} = \tilde{\rho}\, \wp^t_{iM} \frac{\partial \tilde{\omega}_i}{\partial r} \tag{F.1.2}$$

$$-\sum_{i=1}^{n} \tilde{\rho}_i \overline{h_i'' v''} = -\, \rho C_p \overline{T'' v''} = k^t \frac{\partial \tilde{T}}{\partial r} \tag{F.1.3}$$

$$-\sum_{i=1}^{n} \tilde{h}_i \overline{\rho_i'' v''} = -\sum_{i=1}^{n} \tilde{h}_i\, j^t_{i,r} = \sum_{i=1}^{n} \tilde{h}_i \tilde{\rho}\, \wp^t_{iM} \frac{\partial \tilde{\omega}_i}{\partial r} \tag{F.1.4}$$

Analogous expressions exist for the turbulent stress terms containing the axial velocity.

Turbulent shear stress terms containing the square of the velocity are also assumed to have viscous-like behavior analogous to the laminar counterpart:

$$-\overline{\rho u'' u''} = \tau^t_{xx} = 2\mu^t \frac{\partial \tilde{u}}{\partial x} + \lambda^t \left[\frac{\partial \tilde{u}}{\partial x} + \frac{1}{r}\frac{\partial}{\partial r}(r\tilde{v})\right] \tag{F.1.5}$$

Similar expressions occur for the modelling of $\overline{\rho v'' v''}$ and $\overline{\rho w'' w''}$.

Further analogies between turbulent stresses and their laminar counterparts can be made by introduction of turbulent Prandtl and Lewis Numbers.

(F.1.6) $$Pr^t = \frac{\mu^t \; C_p}{k^t}$$

(F.1.7) $$Le^t = \frac{\bar{\rho} \; C_p \; \wp^t_{iM}}{k^t}$$

The expressions given by Equations (F.1.1) to (F.1.7) are the typical starting points for turbulence modelling, with the modelling goal being to find suitable correlations for the turbulent coefficients introduced by the Boussinesq approximation (i.e., μ^t, k^t, $\wp^t_{iM}$, and λ^t). Primary focus has been on finding a suitable correlation for the turbulent viscosity and modelling the remaining turbulence terms through either the introduction of a constant or an algebraic expression. In this study, the turbulent viscosity was modelled by the use of an algebraic turbulence model, whereas the turbulent Prandtl and Lewis number models were assumed to be constant. In the sections to follow, a description of the various models applied for this study or available to use in the Tethys flow modelling computer code, is made.

F.2. Algebraic Turbulence Model

The basic algebraic turbulence model adopted for this study is the Baldwin-Lomax model (Reference 52), which is a two-layer algebraic turbulence model. Thus,

(F.2.1) $$\mu^t = \left\{ \begin{array}{ll} \mu^t_{inner} & \text{for } y_n \leq y_b \\ \mu^t_{outer} & \text{for } y_n > y_b \end{array} \right\}$$

where y_n is the normal distance from the wall and y_b is the distance at which the outer and inner viscosity values match.

The inner region turbulent viscosity in the modified Baldwin-Lomax model has the following form:

(F.2.2) $$\mu^t_{inner} = \rho l^2 |\Omega|$$

where l is the mixing length and Ω is the total vorticity. The mixing length is given by the expression:

(F.2.3) $$l = \kappa y_n [1 - \exp(-y^+/A^+)]$$

and the magnitude of the total vorticity is defined as:

(F.2.4) $$|\Omega| = \left|\frac{\partial \tilde{v}}{\partial x} - \frac{\partial \tilde{u}}{\partial y}\right|$$

In Equation (F.2.3) for the mixing length, the variable κ is the von Karman constant (taken to be equal to 0.4), the variable y^+ is the nondimensional distance from the wall, and A^+ is the Van Driest damping factor:

(F.2.5) $$y^+ = \frac{\sqrt{\tau_w \rho_w}}{\mu_w} y_n$$

(F.2.6) $$A^+ = \frac{26}{N^2}$$

Where N^2 is given by the following relations:

(F.2.7) $$N^2 = 1 + 11.8 \frac{\partial P}{\partial \phi} \sqrt{\rho_w \mu_w |\Omega|^3_w}$$

Solid wall regions

$$(F.2.8) \qquad N^2 = -\frac{\partial P}{\partial \phi}\frac{\mu}{(\rho V)_w}\frac{1}{\tau_w}\left[1-\exp\left(\frac{11.8\,(\rho V)_w \mu_w}{\mu\sqrt{\rho_w \tau_w}}\right)\right]+\exp\left(\frac{11.8\,(\rho V)_w \mu_w}{\mu\sqrt{\rho_w \tau_w}}\right)$$

Transpired wall regions

where $\partial P/\partial \phi$ is the pressure gradient tangential to the wall. In the original Proteus code, N^2 was equal to unity. The modified form is attributed to Cebeci (Reference 53).

In the outer region, the turbulent viscosity is computed from the following relation:

$$(F.2.9) \qquad \mu^t_{outer} = \Re C_{cp} F_{Kleb} F_{wake}$$

where $\Re$ is the Clauser constant, taken as 0.0168, and C_{cp} is also a constant, taken to be 1.6. The wake parameter, F_{wake}, is specified by the expression given in Equation (F.2.10):

$$(F.2.10) \qquad F_{wake} = y_{MAX} F_{MAX}$$

where F_{MAX} is the maximum value of the following correlation:

$$(F.2.11) \qquad F_{MAX} = y_n |\Omega| \left[1-\exp\left(-y^+/A^+\right)\right]$$

Wall bounded flows

$$(F.2.12) \qquad F_{MAX} = y_n |\Omega|$$

Free turbulent flows

where y_{MAX} corresponds to the location at which F_{MAX} occurs, as measured from the wall for wall bounded flows and as measured from the location of the maximum or minimum velocity for free turbulent flows. The Klebanoff intermittency factor, F_{Kleb}, accounts for the intermittent turbulent nature of the flow at regions significantly far away from the wall. This factor is given by the following relation:

$$F_{Kleb} = \left[1 + B\left(\frac{C_{Kleb} y_n}{y_{MAX}}\right)^6\right]^{-1} \tag{F.2.13}$$

where B and C_{Kleb} are constants equal to 5.5 and 0.3, respectively.

A special exception to the formulation of the outer region turbulence model was employed for the analysis of a film cooled rocket nozzle, as discussed in Section 7.2. This change was performed so that a reasonable solution for cases having both wall bounded turbulent flow and free stream turbulent flow could be obtained.

F.3. Turbulence Modelling for Roughened Surfaces

The alteration of the turbulence model in consideration of a roughened surface was performed by using a 'displaced distance' model, as described by Cebeci and Smith (Reference 54). In this model, the equations that relate the turbulent viscosity to the distance from the wall is modified by an expression that is a function of the surface roughness, as given below:

$$\Delta y^+ = 0.9\left[\sqrt{k^+} - k^+ \exp\left(-k^+/6.\right)\right] \tag{F.3.1}$$

The nondimensional surface roughness parameter, k^+, is a function of the surface roughness (in equivalent sand grain roughness measures), the shear stress, and the fluid density and viscosity:

$$k^+ \equiv \frac{k\rho\sqrt{\frac{\tau_w}{\rho}}}{\mu} \tag{F.3.2}$$

In the application of Equations (F.3.1) and (F.3.2), since the wall is displaced by a surface roughness parameter, the turbulent viscosity is nonzero even at the wall. Hence, the wall shear stress as used in Equation (F.3.2) is a function of both the laminar and turbulent viscosities at the wall.

The effect of surface roughness on mass and heat transfer is usually not as pronounced as the effect on skin friction, as discussed in Reference 14. However, no correction to the turbulent Prandtl number, Lewis number, or the boundary conditions to account for this phenomena was applied in the turbulence model.

F.4. Turbulence Modelling of Pr^t, Le^t, and λ^t

The turbulent Prandtl Number was assumed to be either a constant, which may vary depending on the specific application, or to have the following relationship with the turbulent viscosity and the laminar Prandtl number:

(F.4.1)
$$Pr^t = \frac{C_{Pr3}}{C_{Pr1}Pr} \frac{1 - \exp\left(-\frac{C_{Pr4}}{\mu^t/\mu}\right)}{1 - \exp\left(-\frac{C_{Pr2}}{(Pr)\,\mu^t/\mu}\right)}$$

where the constants C_{Pr1}, C_{Pr2}, C_{Pr3}, C_{Pr4} , are 0.21, 5.25, 0.20, and 5.0, respectively. Equation (F.4.1) was excerpted from the original Proteus code and was never applied in any Tethys fluid flow simulations.

The turbulent Lewis number, Le^t, was assumed to be constant. Due to the analogy between the transport of species and heat, the Lewis number is likely close to unity. Thus,

(F.4.2)
$$Le^t = 1.0$$

The turbulent second coefficient of viscosity, λ^t, was assumed to be related to the first coefficient of turbulent viscosity, μ^t, in the same manner as their laminar counterparts:

(F.4.3)
$$\frac{\lambda^t}{\mu^t} = \frac{\lambda}{\mu} = -\frac{2}{3}$$

Appendix G

Transformation of the Governing Equations

The axisymmetric version of the Navier-Stokes equations modelled in this study were transformed into a generalized coordinate system. Transformation allows significant ease in modelling the flow equations by the use of central difference approximations, more than offsetting the complexity involved in the transformation. The general equations governing the flow of a multispecies fluid have the following form:

$$\frac{\partial}{\partial t}(rQ) + \frac{\partial}{\partial x}(rE) + \frac{\partial}{\partial r}(rF) + H = \frac{\partial}{\partial x}(rE_v) + \frac{\partial}{\partial r}(rF_v) + H_v \tag{G.1}$$

Consider the generalized transformation of the equations into the following generalized coordinate system:

$$\tau = \tau(t) \tag{G.2}$$

$$\xi = \xi(x,r) \tag{G.3}$$

$$\eta = \eta(x,r) \tag{G.4}$$

Using the above transformations of physical space into computational space and assigning the time derivative to be unaltered by the transformation (i.e. $\tau = t$), the following chain rules can be applied:

$$\frac{\partial \phi}{\partial x} = \frac{\partial \xi}{\partial x}\frac{\partial \phi}{\partial \xi} + \frac{\partial \eta}{\partial x}\frac{\partial \phi}{\partial \eta} \tag{G.5}$$

$$\frac{\partial \phi}{\partial r} = \frac{\partial \xi}{\partial r}\frac{\partial \phi}{\partial \xi} + \frac{\partial \eta}{\partial r}\frac{\partial \phi}{\partial \eta} \tag{G.6}$$

Applying the generalized coordinate transformation from physical to generalized space, the governing flow equations yield the following result:

$$\frac{\partial}{\partial \tau}(rQ) + \frac{\partial \xi}{\partial x}\frac{\partial}{\partial \xi}(rE - rE_v) + \frac{\partial \eta}{\partial x}\frac{\partial}{\partial \eta}(rE - rE_v)$$

(G.7)

$$+ \frac{\partial \xi}{\partial r}\frac{\partial}{\partial \xi}(rF - rF_v) + \frac{\partial \eta}{\partial r}\frac{\partial}{\partial \eta}(rF - rF_v) + H - H_v = 0$$

where the nonconservative pressure gradient term in the radial momentum equation takes the following form:

(G.8)
$$r\frac{\partial P}{\partial r} = r\left[\frac{\partial \xi}{\partial r}\frac{\partial P}{\partial \xi} + \frac{\partial \eta}{\partial r}\frac{\partial P}{\partial \eta}\right]$$

In the present form, the generalized coordinate transformation is in a nonconservative form since the transformation metrics are outside of the partial derivative operators. To the extent possible, the transformation should be put into conservative form, and the transformation metrics should be expressed in terms of physically determined spatial coordinate differences. These operations are performed in the expressions that follow.

Computational distances can be written in terms of the metric derivatives and physical distances, as outlined below:

(G.9)
$$d\xi = \xi_x dx + \xi_r dr$$

(G.10)
$$d\eta = \eta_x dx + \eta_r dr$$

Similarly, physical distances can be written as a function of computational distances:

(G.11)
$$dx = x_\xi d\xi + x_\eta d\eta$$

(G.12)
$$dr = r_\xi d\xi + r_\eta d\eta$$

Solving Equations (G.9) to (G.12) for $d\xi$ and $d\eta$ yields:

(G.13)
$$[x_\xi r_\eta - r_\xi x_\eta]\, d\xi = r_\eta dx - x_\eta dr$$

(G.14) $$[x_\eta r_\xi - r_\eta x_\xi]\, d\eta = r_\xi dx - x_\xi dr$$

Comparing Equations (G.13) and (G.14) with Equations (G.9) and (G.10), shows that the following relations exist between the physical and transformed spatial derivatives:

(G.15) $$\xi_x = r_\eta / (x_\xi r_\eta - r_\xi x_\eta)$$

(G.16) $$\xi_r = -x_\eta / (x_\xi r_\eta - r_\xi x_\eta)$$

(G.17) $$\eta_x = -r_\xi / (x_\xi r_\eta - r_\xi x_\eta)$$

(G.18) $$\eta_r = x_\xi / (x_\xi r_\eta - r_\xi x_\eta)$$

The denominator in Equations (G.15) to (G.18) represents the area of the physical space in relation to the transformed space and is termed the inverse Jacobian, J^{-1},where the direct Jacobian, J, represents the area of transformed space with respect to the physical coordinate system. Therefore, using the Jacobian, J, to represent $(x_\xi r_\eta - r_\xi x_\eta)^{-1}$, Equation (G.7) becomes:

(G.19) $$\frac{\partial}{\partial \tau}(rQ) + r_\eta J \frac{\partial}{\partial \xi}(rE - rE_v) - r_\xi J \frac{\partial}{\partial \eta}(rE - rE_v) - x_\eta J \frac{\partial}{\partial \xi}(rF - rF_v)$$

$$+ x_\xi J \frac{\partial}{\partial \eta}(rF - rF_v) + H - H_v = 0$$

Equation G.19 can be cast in conservation form as follows. First, note that the Jacobian is independent of time, therefore, $(1/J)\,\partial rQ/(\partial \tau) = \partial (rQ/J)$. Next, note that the spatial derivatives have the following characteristics:

(G.20)
$$r_\eta \frac{\partial [rE - rE_v]}{\partial \xi} - r_\xi \frac{\partial [rE - rE_v]}{\partial \eta}$$

$$= \frac{\partial [r_\eta (rE - rE_v)]}{\partial \xi} - \frac{\partial [r_\xi (rE - rE_v)]}{\partial \eta} - [rE - rE_v] \left(\frac{\partial}{\partial \xi} r_\eta - \frac{\partial}{\partial \eta} r_\xi \right)$$

(G.21)
$$- x_\eta \frac{\partial [rF - rF_v]}{\partial \xi} + x_\xi \frac{\partial [rF - rF_v]}{\partial \eta}$$

$$= - \frac{\partial [x_\eta (rF - rF_v)]}{\partial \xi} + \frac{\partial [x_\xi (rF - rF_v)]}{\partial \eta} + [rF - rF_v] \left(\frac{\partial}{\partial \xi} x_\eta - \frac{\partial}{\partial \eta} x_\xi \right)$$

The last terms on the right-hand side of Equations (G.20) and (G.21) cancel out. Therefore, Equation (G.19) can be written as:

(G.22)
$$\frac{\partial \left[\frac{rQ}{J} \right]}{\partial \tau} + \frac{\partial [r_\eta (rE - rE_v)]}{\partial \xi} - \frac{\partial [r_\xi (rE - rE_v)]}{\partial \eta}$$

$$- \frac{\partial [x_\eta (rF - rF_v)]}{\partial \xi} + \frac{\partial [x_\xi (rF - rF_v)]}{\partial \eta} + \frac{H - H_v}{J} = 0$$

In the radial momentum equation, the pressure gradient term can be written in a from similar to the fully conservative counterparts:

(G.23)
$$\frac{r}{J} \left[\xi_r \frac{\partial P}{\partial \xi} + \eta_r \frac{\partial P}{\partial \eta} \right] = r \left[- \frac{\partial (x_\eta P)}{\partial \xi} + \frac{\partial (x_\xi P)}{\partial \eta} \right]$$

Substituting Equations (G.15) to (G.18) into Equation (G.22) yields the transformed

Navier-Stokes equations:

$$\text{(G.24)}\qquad \frac{\partial}{\partial\tau}\left[r\frac{Q}{J}\right] + \frac{\partial}{\partial\xi}\left[\frac{\xi_x(rE - rE_v) + \xi_r(rF - rF_v)}{J}\right] + \frac{\partial}{\partial\eta}\left[\frac{\eta_x(rE - rE_v) + \eta_r(rF - rF_v)}{J}\right] + \frac{H - H_v}{J} = 0$$

Equation (G.24) is the generalized form of the axisymmetric Navier-Stokes equations modelled in this study. Using over-script nomenclature, Equation (G.24) can be written in the following condensed form:

$$\text{(G.25)}\qquad \frac{\partial(r\hat{Q})}{\partial\tau} + \frac{\partial[r(\hat{E} - \hat{E}_v)]}{\partial\xi} + \frac{\partial[r(\hat{F} - \hat{F}_v)]}{\partial\eta} + \hat{H} - \hat{H}_v = 0$$

where the overscripted terms are defined as follows:

$$\text{(G.26)}\qquad \hat{Q} = \frac{Q}{J}$$

$$\text{(G.27)}\qquad \hat{E} = \frac{\xi_x E + \xi_r F}{J}$$

$$\text{(G.28)}\qquad \hat{E}_v = \frac{\xi_x E_v + \xi_r F_v}{J}$$

$$\text{(G.29)}\qquad \hat{F} = \frac{\eta_x E + \eta_r F}{J}$$

$$\text{(G.30)}\qquad \hat{F}_v = \frac{\eta_x E_v + \eta_r F_v}{J}$$

$$\text{(G.31)}\qquad \hat{H} = \frac{H}{J}$$

$$\text{(G.32)}\qquad \hat{H}_v = \frac{H_v}{J}$$

The modelling of the viscous fluxes was performed in nonconservative terms, leaving the conservation aspect of the viscous terms to the proper evaluation of the metrics and flow difference procedures, as outlined in Section 3 and in Appendix B. For instance, the radial heat flux was represented by the following expression:

$$q_r = - k \frac{\partial T}{\partial r} = - k \left[\xi_r \frac{\partial T}{\partial \xi} + \eta_r \frac{\partial T}{\partial \eta} \right] \tag{G.33}$$

Appendix H

Reference Plane Characteristic Method

The method of characteristics has been successfully applied to numerous computational techniques for modelling both the flow in the interior and at the boundaries. In this study, a reference plane characteristic method was applied at computational boundaries. A description of the reference plane method and its derivation from the governing fluid flow equations follows.

In primitive form, the equations of mass, momentum, and energy (for axisymmetric flow) may be written as follows:

(H.1) $$\frac{\partial \rho}{\partial t} + \rho\frac{\partial u}{\partial x} + \rho\frac{\partial v}{\partial r} + u\frac{\partial \rho}{\partial x} + v\frac{\partial \rho}{\partial r} + \frac{\rho v}{r} = 0$$

(H.2) $$\frac{\partial u}{\partial t} + u\frac{\partial u}{\partial x} + v\frac{\partial u}{\partial r} + \frac{1}{\rho}\frac{\partial P}{\partial x} = \frac{\text{Viscous terms}}{\rho}$$

(H.3) $$\frac{\partial v}{\partial t} + u\frac{\partial v}{\partial x} + v\frac{\partial v}{\partial r} + \frac{1}{\rho}\frac{\partial P}{\partial r} = \frac{\text{Viscous terms}}{\rho}$$

(H.4) $$\frac{\partial P}{\partial t} + u\frac{\partial P}{\partial x} + v\frac{\partial P}{\partial r} - a^2\left[\frac{\partial \rho}{\partial t} + u\frac{\partial \rho}{\partial x} + v\frac{\partial \rho}{\partial r}\right] = \text{Viscous and source terms}$$

In generalized coordinates, τ, ξ, and η, Equations (H.1) to (H.4) become:

(H.5) $$\frac{\partial \rho}{\partial \tau} + \rho\left[\xi_x\frac{\partial u}{\partial \xi} + \xi_r\frac{\partial v}{\partial \xi} + \eta_x\frac{\partial u}{\partial \eta} + \eta_r\frac{\partial v}{\partial \eta}\right] + u\left[\xi_x\frac{\partial \rho}{\partial \xi} + \eta_x\frac{\partial \rho}{\partial \eta}\right] + v\left[\xi_r\frac{\partial \rho}{\partial \xi} + \eta_r\frac{\partial \rho}{\partial \eta}\right] + \frac{\rho v}{r} =$$

(H.6) $$\frac{\partial u}{\partial \tau} + u\left[\xi_x\frac{\partial u}{\partial \xi} + \eta_x\frac{\partial u}{\partial \eta}\right] + v\left[\xi_r\frac{\partial u}{\partial \xi} + \eta_r\frac{\partial u}{\partial \eta}\right] + \frac{1}{\rho}\left[\xi_x\frac{\partial P}{\partial \xi} + \eta_x\frac{\partial P}{\partial \eta}\right] = \frac{\text{Viscous terms}}{\rho}$$

(H.7) $$\frac{\partial v}{\partial \tau} + u\left[\xi_x\frac{\partial v}{\partial \xi} + \eta_x\frac{\partial v}{\partial \eta}\right] + v\left[\xi_r\frac{\partial v}{\partial \xi} + \eta_r\frac{\partial v}{\partial \eta}\right] + \frac{1}{\rho}\left[\xi_r\frac{\partial P}{\partial \xi} + \eta_r\frac{\partial P}{\partial \eta}\right] = \frac{\text{Viscous terms}}{\rho}$$

(H.8)
$$\frac{\partial P}{\partial \tau} + u\left[\xi_x \frac{\partial P}{\partial \xi} + \eta_x \frac{\partial P}{\partial \eta}\right] + v\left[\xi_r \frac{\partial P}{\partial \xi} + \eta_r \frac{\partial P}{\partial \eta}\right]$$

$$- a^2\left[\frac{\partial \rho}{\partial \tau} + u\left(\xi_x \frac{\partial \rho}{\partial \xi} + \eta_x \frac{\partial \rho}{\partial \eta}\right) + v\left(\xi_r \frac{\partial \rho}{\partial \xi} + \eta_r \frac{\partial \rho}{\partial \eta}\right)\right] = \text{Viscous and source terms}$$

Substituting the definition of the contravariant velocity in the ξ direction, $U \equiv u\xi_x + v\xi_r$, and rearranging all of the equation such that only ξ derivatives are on the left-hand side yields the following expressions:

(H.9)
$$\frac{\partial \rho}{\partial \tau} + U\frac{\partial \rho}{\partial \xi} + \rho\xi_x \frac{\partial u}{\partial \xi} + \rho\xi_r \frac{\partial v}{\partial \xi} = \Psi_1$$

(H.10)
$$\frac{\partial u}{\partial \tau} + U\frac{\partial u}{\partial \xi} + \frac{\xi_x}{\rho}\frac{\partial P}{\partial \xi} = \Psi_2$$

(H.11)
$$\frac{\partial v}{\partial \tau} + U\frac{\partial v}{\partial \xi} + \frac{\xi_r}{\rho}\frac{\partial P}{\partial \xi} = \Psi_3$$

(H.12)
$$\frac{\partial P}{\partial \tau} + U\frac{\partial P}{\partial \xi} - a^2\left[\frac{\partial \rho}{\partial \tau} + U\frac{\partial \rho}{\partial \xi}\right] = \Psi_4$$

where the terms on the right-hand side of the above expressions are shown in Equations (H.13) to (H.16):

(H.13)
$$\Psi_1 = -\frac{\rho v}{r} - \rho\eta_x \frac{\partial u}{\partial \eta} - \rho\eta_r \frac{\partial v}{\partial \eta} - V\frac{\partial \rho}{\partial \eta}$$

(H.14)
$$\Psi_2 = -\frac{\eta_x}{\rho}\frac{\partial P}{\partial \eta} - V\frac{\partial u}{\partial \eta} + \frac{\text{Viscous terms}}{\rho}$$

(H.15)
$$\Psi_3 = -\frac{\eta_r}{\rho}\frac{\partial P}{\partial \eta} - V\frac{\partial v}{\partial \eta} + \frac{\text{Viscous terms}}{\rho}$$

(H.16)
$$\Psi_4 = -V\frac{\partial P}{\partial \eta} + a^2 V\frac{\partial \rho}{\partial \eta} + \sum_{i=1}^{n}\left[\gamma_i R_i T - (\gamma_i - 1)h_i\right]\sigma_i + \text{Viscous terms}$$

where $V \equiv u\eta_x + v\eta_r$ is the contravariant velocity in the η-direction.

A linear combination of Equations (H.9) to (H.12) can be formed by multiplying by the arbitrary weighting factors, l_i (i = 1, 2, 3, 4), respectively, and then summing. The resulting equation is:

$$(H.17)\quad l_1\left[\frac{\partial\rho}{\partial\tau}+U\frac{\partial\rho}{\partial\xi}+\rho\xi_x\frac{\partial u}{\partial\xi}+\rho\xi_r\frac{\partial v}{\partial r}-\Psi_1\right]+l_2\left[\frac{\partial u}{\partial\tau}+U\frac{\partial u}{\partial\xi}+\frac{\xi_x}{\rho}\frac{\partial P}{\partial\xi}-\Psi_2\right]$$

$$+\ l_3\left[\frac{\partial v}{\partial\tau}+U\frac{\partial v}{\partial\xi}+\frac{\xi_r}{\rho}\frac{\partial P}{\partial\xi}-\Psi_3\right]+l_4\left[\frac{\partial P}{\partial\tau}+U\frac{\partial P}{\partial\xi}-a^2\left(\frac{\partial\rho}{\partial\tau}+U\frac{\partial\rho}{\partial\xi}\right)-\Psi_4\right]=0$$

Equation (H.17) can be rearranged and put into a form that represents coefficients acting on the flow derivatives:

$$(H.18)\quad (l_1-a^2l_4)\frac{\partial\rho}{\partial\tau}+(Ul_1-a^2Ul_4)\frac{\partial\rho}{\partial\xi}+l_2\frac{\partial u}{\partial\tau}+(\rho\xi_x l_1+Ul_2)\frac{\partial u}{\partial\xi}$$

$$+\ l_3\frac{\partial v}{\partial\tau}+(\rho\xi_r l_1+Ul_3)\frac{\partial v}{\partial\xi}+l_4\frac{\partial P}{\partial\tau}+[(\xi_x/\rho)l_2+(\xi_r/\rho)l_3+Ul_4]\frac{\partial P}{\partial\xi}$$

$$=\ l_1\Psi_1+l_2\Psi_2+l_3\Psi_3+l_4\Psi_4$$

The following set of characteristic vectors is defined, which are the coefficients of the partial derivatives in Equation (H.18):

$$(H.19)\quad W_1 = (Ul_1-a^2Ul_4\ ,\ l_1-a^2l_4)$$

$$(H.20)\quad W_2 = (\rho\xi_x l_1+Ul_2\ ,\ l_2)$$

$$(H.21)\quad W_3 = (\rho\xi_r l_1+Ul_3\ ,\ l_3)$$

$$(H.22)\quad W_4 = (\xi_x l_2/\rho+\xi_r l_3/\rho+Ul_4\ ,\ l_4)$$

Then Equation (H.18) can be written in the following form:

(H.23) $$d\rho|_{w_1} + du|_{w_2} + dv|_{w_3} + dP|_{w_4} = l_1\Psi_1 + l_2\Psi_2 + l_3\Psi_3 + l_4\Psi_4$$

The characteristic normal, N, in the $\xi - \tau$ plane is found by selection of the l_i (i = 1, 2, 3, 4) such that the characteristic vector, W_j (j = 1, 2, 3, 4), is normal to N. Mathematically, this condition requires that the dot product of the characteristic normal and characteristic vector be equal to zero.

(H.24) $$N \bullet W_j = 0 \qquad (j = 1, 2, 3, 4)$$

In matrix form, Equation (H.24) is:

(H.25) $$\begin{bmatrix} UN_\xi+N_\tau & 0 & 0 & -a^2(UN_\xi+N_\tau) \\ \rho\xi_x N_\xi & UN_\xi+N_\tau & 0 & 0 \\ \rho\xi_r N_\xi & 0 & UN_\xi+N_\tau & 0 \\ 0 & \xi_x N_x/\rho & \xi_r N_r/\rho & UN_\xi+N_\tau \end{bmatrix} \begin{bmatrix} l_1 \\ l_2 \\ l_3 \\ l_4 \end{bmatrix} = 0$$

For a nontrivial solution, the determinant of the coefficient matrix must be equal to zero, leading to the following requirement:

(H.26) $$(UN_\xi + N_\tau)^2 \left[(UN_\xi + N_\tau)^2 - a^2\xi_x^2 N_\xi^2 - a^2\xi_r^2 N_\xi^2 \right] = 0$$

Equation (H.26) requires that one of the following two expressions must be true:

(H.27) $$UN_\xi + N_\tau = 0$$

(H.28) $$UN_\xi + N_\tau = \pm\, aN_\xi\sqrt{\xi_x^2 + \xi_r^2}$$

Noting that $d\xi/d\tau = -N_\tau/N_\xi$, Equations (H.27) and (H.28) can be written as:

(H.29) $$\frac{d\xi}{d\tau} = U$$

(H.30) $$\frac{d\xi}{d\tau} = U \pm a\sqrt{\xi_x^2 + \xi_r^2}$$

Equation (H.29) represents the projection of the pathline onto the η = constant planes, and Equation (H.30) represents the projection of the Mach cone onto the η = constant plane.

Substitution of Equation (H.29) into Equation (H.25) yields the following expression:

(H.31) $$\begin{bmatrix} 0 & 0 & 0 & 0 \\ \rho\xi_x N_\xi & 0 & 0 & 0 \\ \rho\xi_r N_\xi & 0 & 0 & 0 \\ 0 & \xi_r N_\xi/\rho & \xi_r N_\xi/\rho & 0 \end{bmatrix} \begin{bmatrix} l_1 \\ l_2 \\ l_3 \\ l_4 \end{bmatrix} = 0$$

Solving Equation (H.31) for l_1 to l_4 gives:

(H.32) $$l_1 = 0, \quad \frac{\xi_x N_\xi}{\rho} l_2 + \frac{\xi_r N_\xi}{\rho} l_3 = 0, \quad l_4 \text{ is arbitrary}$$

Two possible solutions are $l_1 = l_4 = 0$ and l_2 arbitrary, or $l_1 = l_2 = l_3 = 0$ and l_4 arbitrary. Substituting $l_1 = l_4 = 0$, l_2 arbitrary, and $l_3 = -\xi_x l_2/\xi_r$, into Equation (H.17) yields one of the two compatibility equations that are valid along the characteristic curve $d\xi/d\tau = U$:

(H.33) $$l_2\frac{du}{d\tau} + Ul_2\frac{du}{d\xi} - \frac{\xi_x}{\xi_r}l_2\frac{dv}{d\tau} - Ul_2\frac{\xi_x}{\xi_r}\frac{dv}{d\xi} + \frac{\xi_x}{\rho}l_2\frac{dP}{d\xi} - \frac{\xi_x}{\rho}l_2\frac{dP}{d\xi} = l_2\Psi_2 - \frac{\xi_x}{\xi_r}l_2\Psi_3$$

Dividing through by the nonzero arbitrary multiplier l_2 and then simplifying Equation (H.34) gives:

(H.34) $$\xi_r du - \xi_x dv = (\xi_r \Psi_2 - \xi_x \Psi_3)\, d\tau$$

where

(H.35) $$du = \frac{\partial u}{\partial \tau}\, d\tau + \frac{\partial u}{\partial \xi}\, \frac{d\xi}{d\tau}\, d\tau$$

(H.36) $$dv = \frac{\partial v}{\partial \tau}\, d\tau + \frac{\partial v}{\partial \xi}\, \frac{d\xi}{d\tau}\, d\tau$$

Substituting $l_1 = l_2 = l_3 = 0$ and l_4 arbitrary into Equation (H.17) yields the other compatibility equation that is valid along the characteristic curve $d\xi/d\tau = U$.

(H.37) $$\left[-a^2 \frac{\partial \rho}{\partial \tau} - a^2 U \frac{\partial \rho}{\partial \xi} + \frac{\partial P}{\partial \tau} + U \frac{\partial P}{\partial \xi} - \Psi_4 \right] l_4 = 0$$

Dividing through by the nonzero arbitrary multiplier l_4 and putting the source term on the right-hand side, Equation (H.37) gives the compatibility equation:

(H.38) $$-a^2 \frac{\partial \rho}{\partial \tau} - a^2 U \frac{\partial \rho}{\partial \xi} + \frac{\partial P}{\partial \tau} + U \frac{\partial P}{\partial \xi} = \Psi_4$$

Along the characteristic line $d\xi/d\tau = U$, Equation (H.38) can be expressed in terms of total derivatives:

(H.39) $$dP - a^2 d\rho = \Psi_4 d\tau$$

Two additional compatibility equations are obtained for the characteristic curves specified by Equation (H.30). Substitution of Equation (H.30) into Equation (H.25) yields:

$$\begin{bmatrix} \pm aN_\xi\sqrt{\xi_x^2+\xi_r^2} & 0 & 0 & \mp a^3N_\xi\sqrt{\xi_x^2+\xi_r^2} \\ \rho\xi_x N_\xi & \pm aN_\xi\sqrt{\xi_x^2+\xi_r^2} & 0 & 0 \\ \rho\xi_r N_\xi & 0 & \pm aN_\xi\sqrt{\xi_x^2+\xi_r^2} & 0 \\ 0 & \xi_x N_\xi/\rho & \xi_r N_\xi/\rho & \pm aN_\xi\sqrt{\xi_x^2+\xi_r^2} \end{bmatrix} \begin{bmatrix} l_1 \\ l_2 \\ l_3 \\ l_4 \end{bmatrix} = 0 \tag{H.40}$$

Solving Equation (H.40) yields:

$$l_1 = a^2 l_4$$

$$l_2 = \mp \frac{\rho\xi_x l_1}{a\sqrt{\xi_x^2+\xi_r^2}} = \mp \frac{\rho a\xi_x l_4}{\sqrt{\xi_x^2+\xi_r^2}} \tag{H.41}$$

$$l_3 = \mp \frac{\rho\xi_r l_1}{a\sqrt{\xi_x^2+\xi_r^2}} = \mp \frac{\rho a\xi_x l_4}{\sqrt{\xi_x^2+\xi_r^2}}$$

l_4 is arbitrary

Substituting Equation (H.41) into Equation (H.17) yields:

$$\mp\frac{\rho a\xi_x l_4}{\sqrt{\xi_x^2+\xi_r^2}}\frac{\partial u}{\partial\tau}+\left(\rho a^2\xi_x l_4\mp\frac{\rho aU\xi_x l_4}{\sqrt{\xi_x^2+\xi_r^2}}\right)\frac{\partial u}{\partial\xi}$$

$$\mp\frac{\rho a\xi_r l_4}{\sqrt{\xi_x^2+\xi_r^2}}\frac{\partial v}{\partial\tau}+\left(\rho a^2\xi_r l_4\mp\frac{\rho aU\xi_r l_4}{\sqrt{\xi_x^2+\xi_r^2}}\right)\frac{\partial v}{\partial\xi}$$

(H.42)

$$+l_4\frac{\partial P}{\partial\tau}+\left(l_4U\mp\frac{a\xi_x^2 l_4}{\sqrt{\xi_x^2+\xi_r^2}}\mp\frac{a\xi_r^2 l_4}{\sqrt{\xi_x^2+\xi_r^2}}\right)\frac{\partial P}{\partial\xi}$$

$$=a^2 l_4\Psi_1\mp\frac{\rho a\xi_x l_4}{\sqrt{\xi_x^2+\xi_r^2}}\Psi_2\mp\frac{\rho a\xi_r l_4}{\sqrt{\xi_x^2+\xi_r^2}}\Psi_3+l_4\Psi_4$$

Substitution for the total derivatives, such as $dP/d\tau = (\partial P/\partial\xi)\,d\xi/d\tau+\partial P/\partial\tau$, where $d\xi/d\tau = U\mp a\sqrt{\xi_x^2+\xi_r^2}$, and likewise for du and dv, Equation (H.42) simplifies to:

$$\text{(H.43)}\quad dP\mp\frac{\rho a\xi_x}{\sqrt{\xi_x^2+\xi_r^2}}du\mp\frac{\rho a\xi_r}{\sqrt{\xi_x^2+\xi_r^2}}dv=a^2\Psi_1\mp\frac{\rho a\xi_x}{\sqrt{\xi_x^2+\xi_r^2}}\Psi_2\mp\frac{\rho a\xi_r}{\sqrt{\xi_x^2+\xi_r^2}}\Psi_3+\Psi_4$$

which is the compatibility equation that applies along the projection of the Mach cone on the constant-η reference plane.

Summarizing, the applicable characteristic and corresponding compatibility equations valid on a constant-η reference plane are given in Table 26.

Table 26. Characteristic and compatibility equations for a constant-η reference plane.

Characteristic equation	Compatibility equation
$\frac{d\xi}{d\tau} = U$	$\xi_r du - \xi_x dv = (\xi_r \Psi_2 - \xi_x \Psi_3)\, d\tau$
$\frac{d\xi}{d\tau} = U$	$dP - a^2 d\rho = \Psi_4 d\tau$
$\frac{d\xi}{d\tau} = U - a\sqrt{\xi_x^2 + \xi_r^2}$	$dP - \frac{\rho a \xi_x}{\sqrt{\xi_x^2 + \xi_r^2}} du - \frac{\rho a \xi_r}{\sqrt{\xi_x^2 + \xi_r^2}} dv$ $= \left(a^2\Psi_1 - \frac{\rho a \xi_x}{\sqrt{\xi_x^2 + \xi_r^2}}\Psi_2 - \frac{\rho a \xi_r}{\sqrt{\xi_x^2 + \xi_r^2}}\Psi_3 + \Psi_4\right) d\tau$
$\frac{d\xi}{d\tau} = U + a\sqrt{\xi_x^2 + \xi_r^2}$	$dP + \frac{\rho a \xi_x}{\sqrt{\xi_x^2 + \xi_r^2}} du + \frac{\rho a \xi_r}{\sqrt{\xi_x^2 + \xi_r^2}} dv$ $= \left(a^2\Psi_1 + \frac{\rho a \xi_x}{\sqrt{\xi_x^2 + \xi_r^2}}\Psi_2 + \frac{\rho a \xi_r}{\sqrt{\xi_x^2 + \xi_r^2}}\Psi_3 + \Psi_4\right) d\tau$

The right-hand side terms, Ψ_1 to Ψ_4, are listed for completeness.

(H.44) $$\Psi_1 = -\frac{\rho v}{r} - \rho\eta_x\frac{\partial u}{\partial\eta} - \rho\eta_r\frac{\partial v}{\partial\eta} - V\frac{\partial\rho}{\partial\eta}$$

(H.45) $$\Psi_2 = -V\frac{\partial u}{\partial\eta} - \frac{\eta_x}{\rho}\frac{\partial P}{\partial\eta} + \frac{\text{Viscous terms}}{\rho}$$

(H.46) $$\Psi_3 = -V\frac{\partial v}{\partial\eta} - \frac{\eta_r}{\rho}\frac{\partial P}{\partial\eta} + \frac{\text{Viscous terms}}{\rho}$$

(H.47) $$\Psi_4 = -V\frac{\partial P}{\partial\eta} + a^2V\frac{\partial\rho}{\partial\eta}$$

$$+ \sum_{i=1}^{n}\left[\gamma_i R_i T - (\gamma_i - 1)\, h_i\right]\sigma_i + \text{Viscous terms}$$

In all cases studied, the right-hand side terms were numerically approximated by a central difference approximation and were averaged between the boundary point and the point adjacent to the boundary. Metric differences were always evaluated within the computational region used by the dependent variables. Since the terms in Equations (H.44) to (H.47) were central differenced, the option of applying artificial diffusion was employed by adding the following expressions to the right-hand sides of the respective equations:

(H.48) $$\nabla_\eta\left[\Gamma\right|_{\eta+1} + \Gamma|_\eta]\,\phi\varepsilon_\eta^{(2)}\Delta_\eta Q$$

where Γ is given by:

(H.49) $$\Gamma = \frac{|V| + a\sqrt{\eta_x^2 + \eta_r^2}}{\Delta\eta} + \frac{|U| + a\sqrt{\xi_x^2 + \xi_r^2}}{\Delta\xi}$$

with |U| and |V| being the absolute values of contravariant velocity in the ξ and η directions, respectively. The parameter $\varepsilon_{\eta}^{(2)}$ is an artificial viscosity coefficient equal to the value applied in the free stream. The specific terms upon which the artificial diffusion expressions act (given by the Q symbol in Equation (H.48)) are listed in Table 27.

Table 27. Artificial diffusion applied to constant–η reference plane characteristic equations.

Right-hand side term	Term upon which artificial diffusion acts	ϕ
Ψ_1	ρ	1
Ψ_2	u	1
Ψ_3	v	1
Ψ_4	$\frac{P}{\rho}$	$\frac{1}{-a^2}$

The viscous terms in the constant-η reference plane characteristic method simplify to the following terms for the axial momentum, radial momentum, and the energy equations.

$$\text{(H.50)}\quad \text{Axial momentum viscous terms} = \frac{\eta_r \partial \tau_{xr}}{\rho \partial \eta} + \frac{\eta_x \partial \tau_{xx}}{\rho \partial \eta} + \frac{\tau_{xr}}{\rho r} + \frac{\xi_r \partial \tau_{xr}}{\rho \partial \xi} + \frac{\xi_x \partial \tau_{xx}}{\rho \partial \xi}$$

$$\text{(H.51)}\quad \text{Radial momentum viscous terms} = \frac{\eta_x \partial \tau_{xr}}{\rho \partial \eta} + \frac{\eta_r \partial \tau_{rr}}{\rho \partial \eta} + \frac{\tau_{rr}}{\rho r} + \frac{\xi_x \partial \tau_{xr}}{\rho \partial \xi} + \frac{\xi_r \partial \tau_{rr}}{\rho \partial \xi} - \frac{\tau_{\theta\theta}}{\rho r}$$

Energy transfer viscous terms

$$= \frac{R}{C_v}\left[\tau_{rr}\eta_r \frac{\partial v}{\partial \eta} + \tau_{xx}\eta_x \frac{\partial u}{\partial \eta} + \tau_{xr}\left(\eta_r \frac{\partial u}{\partial \eta} + \eta_r \frac{\partial v}{\partial \eta}\right)\right]$$

(H.52)

$$+ \frac{R}{C_v}\left[\tau_{rr}\xi_r \frac{\partial v}{\partial \xi} + \tau_{xx}\xi_x \frac{\partial u}{\partial \xi} + \tau_{xr}\left(\xi_r \frac{\partial u}{\partial \xi} + \xi_r \frac{\partial v}{\partial \xi}\right) + \frac{\tau_{\theta\theta}}{r} v_r\right]$$

$$+ \frac{R}{C_v}\left[- \eta_x \frac{\partial q_x}{\partial \eta} + - \eta_r \frac{\partial q_r}{\partial \eta} - \xi_x \frac{\partial q_x}{\partial \xi} - \xi_r \frac{\partial q_r}{\partial \xi} - \frac{q_r}{r}\right]$$

The corresponding equations for the shear stress and heat flux terms are presented in Section 2. The evaluation of terms containing only η derivatives was performed by averaging at the points on the boundary and the ξ point closest to the boundary. The evaluation of the mixed derivatives was performed at the point midway between the boundary point and the next nearest interior ξ point, whereas the evaluation of terms containing only ξ derivatives was performed about the next nearest interior ξ point. No effort was made to make the viscous terms one-dimensionally conservative. However, the fundamental rule of viscous flow conservation, that metric grid points outside of the computational domain not be used, was adhered to in all cases except those terms containing second-order derivatives in the ξ direction.

When applied along a solid wall or a centerline, the viscous terms and the species source function terms were assumed to be negligible.

The characteristic and compatibility equations applicable to the steady state, inviscid, species equations are derived in Reference 23. Simple inspection allowed the extension of those results to transient, diffusive flow. The resultant characteristic and compatibility equations are given in Table 28.

Table 28. Characteristic and compatibility equations for species equations.

Characteristic equation	Compatibility equation
$\frac{d\xi}{d\tau} = U$	$d\omega_i = \psi_{4+i}\, d\tau$

The right-hand side term, ψ_{4+i}, is given below.

$$\text{(H.53)} \quad \psi_{4+i} = \frac{1}{\rho}\left[\sigma_i - \rho V \frac{\partial \omega_i}{\partial \eta} - \xi_x \frac{\partial j_{i,x}}{\partial \xi} - \xi_r \frac{\partial j_{i,r}}{\partial \xi} - \eta_x \frac{\partial j_{i,x}}{\partial \eta} - \eta_r \frac{\partial j_{i,r}}{\partial \eta} - \frac{j_{i,r}}{r} \right]$$

The equations for the diffusive mass flux terms are listed in Section 2.

The handling of the advective and diffusive terms was performed in a manner analogous to the terms arising in the mass, momentum, and energy equations. Likewise, an artificial diffusion option exists for the species transport equations, being identical in form to the equations for mass, momentum, and energy. Table 29 lists the variables to the species equations upon which the artificial diffusion acts.

Table 29. Artificial diffusion applied to the species equations.

Right-hand side term	Term upon which artificial diffusion acts	ϕ
ψ_{4+i}	ω_i	1

The analogous constant-ξ reference plane formulation is readily derived from the constant-η reference plane formulation derived in this appendix, by simply interchanging the ξ and η coordinates wherever they appear in all of the equations.

Appendix I

Chemical Reaction Mechanism and Reaction Rate Constants

Eight possible chemical reactions were considered as potentially significant to the hydrogen-oxygen chemical rocket engine. All of the backward chemical reaction rates were modelled as a modified Arrhenius equation:

$$K_{bj} = B_j T^{\alpha_j} \exp\left[-\frac{E_j}{\bar{R}T}\right] \tag{I.1}$$

where j denotes the specific chemical reaction, and B_j, α_j, and E_j are determined from experimental data. The plausible chemical reactions and reaction rate constants employed in the Tethys code (i.e., the default values) are listed in Table 30. The values of the reaction rate constants were obtained from recommendations made by Bittker (Reference 55) in 1976. The units in the following table are presented in terms of cubic centimeters, degrees Kelvin, calories, moles, and seconds.

Table 30. Chemical reaction rate constants.

Chemical Reaction	B_j	α_j	E_j
$H + H + M \Leftrightarrow H_2 + M$	2.2×10^{14}	0.0	96,000.0
$H + OH + M \Leftrightarrow H_2O + M$	1.3×10^{15}	0.0	105,140.0
$O + O + M \Leftrightarrow O_2 + M$	1.8×10^{18}	− 1.0	118,000.0
$OH + M \Leftrightarrow O + H + M$	7.1×10^{18}	− 1.0	0.0
$O + OH \Leftrightarrow O_2 + H$	1.89×10^{14}	0.0	16,400.0
$H + OH \Leftrightarrow H_2 + O$	4.2×10^{14}	0.0	13,750.0
$H_2O + H \Leftrightarrow H_2 + OH$	4.74×10^{13}	0.0	6098.0
$OH + OH \Leftrightarrow H_2O + O$	6.8×10^{13}	0.0	18,365.0

The default values of the catalytic efficiencies (i.e., $B_{ij}/\bar{B}_j$, as discussed in Section 2.3) used in the Tethys code were obtained from the same reference as the chemical reaction rate constants (Bittker, Reference 55). They are shown in Table 31.

Table 31. Catalytic efficiencies.

Chemical Reaction	H	H_2	H_2O	O	O_2	OH
$H + H + M \Leftrightarrow H_2 + M$	1.0	4.1	15.0	1.0	2.0	1.0
$H + OH + M \Leftrightarrow H_2O + M$	1.0	4.0	20.0	1.0	1.5	1.0
$O + O + M \Leftrightarrow O_2 + M$	1.0	1.0	1.0	1.0	1.0	1.0
$OH + M \Leftrightarrow H + O + M$	1.0	1.0	1.0	1.0	1.0	1.0

Appendix J

Chemical Kinetics Validation

To evaluate the accuracy and methodology employed in modelling the chemical species source term, a comparison was made between a well-established one-dimensional chemical kinetics model, LSENS (Reference 19), and the model employed in Tethys. The geometry and boundary conditions considered in the flow verification study correspond to a supersonic source flow with an area ratio of 100 and a total length of 1 foot, as shown in Figure 84. The inlet boundary conditions employed for the verification roughly correspond to the equilibrium conditions that would exist near the throat of a hydrogen-oxygen rocket engine operating at a H_2/O_2 mixture ratio of 8.0 and a fluid static density near 0.05 lbm/ft^3. The initial velocity was specified such that the initial conditions corresponded to an inlet Mach number of 1.5. Three different inlet fluid densities, encompassing two orders of magnitude in difference, were studied to assure that a rather complete spectrum of chemical recombination rates and mechanisms could be studied. The inlet conditions are presented in Table 32. Reference plane characteristics, with chemical kinetics, were used at the exit plane.

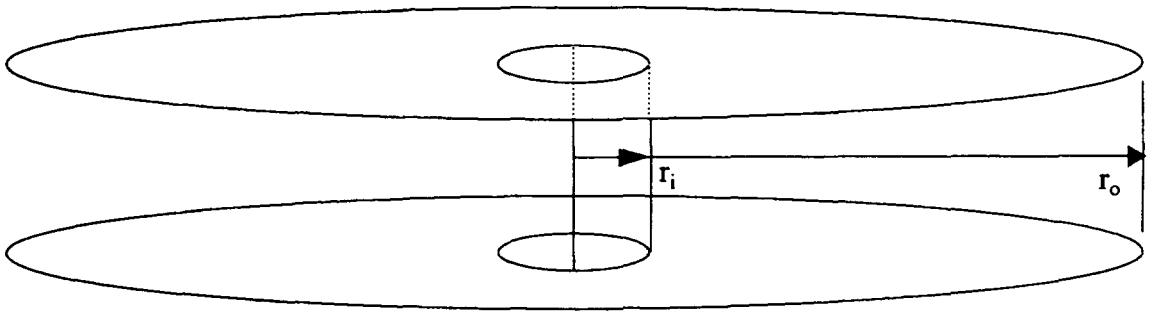

Figure 84. Schematic of source flow geometry used for chemical kinetics validation.

Table 32. Inlet boundary conditions for reacting source flow study.

Property	Inlet value	Units
T	6060.6	R
ρ	0.005, 0.05, 0.5	lbm/ft^3
v	7171.9	ft/sec
ω_{H_2}	0.0156	Dimensionless
ω_{H_2O}	0.7749	Dimensionless
ω_{O_2}	0.0829	Dimensionless
ω_H	0.0025	Dimensionless
ω_{OH}	0.1050	Dimensionless
ω_O	0.0191	Dimensionless

In all of the cases examined, a 21×4 grid point structure was employed in the Tethys analysis, as shown in Figure 85. In general, the one-dimensional flow model, LSENS, used about 500 marching steps. Due to the much larger number of steps taken and the maturity and higher-order accuracy of the LSENS code, it will be assumed to be numerically exact, with the understanding that the coefficients used for the actual chemical reaction rates could be significantly different from those that exist in reality.

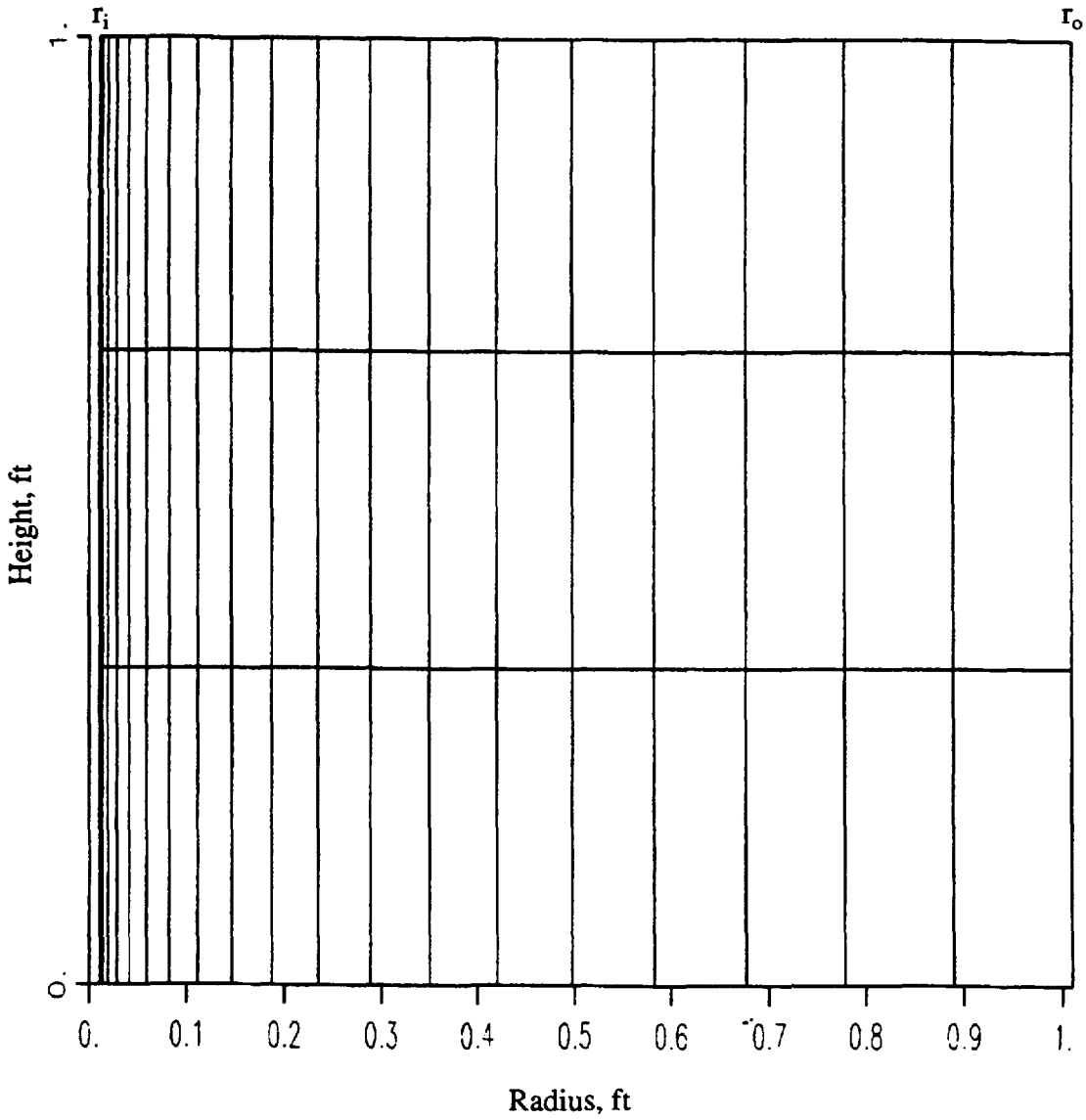

Figure 85. Computational grid used for the chemical kinetics source flow validation.

In Figure 86, the variation of Mach number with the radius ratio (or equivalently, the area ratio), as predicted by the LSENS flow model, is shown for the three different inlet flow cases examined. It is readily observed that the differences in the Mach numbers are fairly large, and solely the result of differences in the chemical reaction mechanisms occurring at the different fluid densities. The tendency for increased chemical recombination to occur at higher densities results in an effective energy release, very similar to a Rayleigh Line effect, with a resultant lowering in fluid Mach number with increasing recombination.

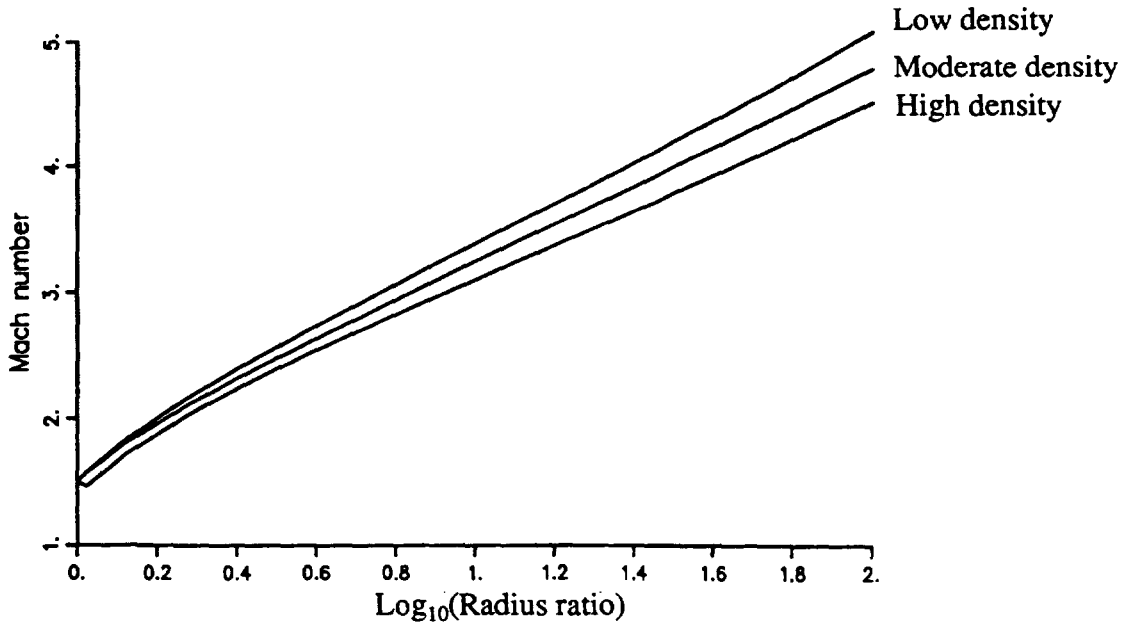

Figure 86. Mach number distribution from LSENS code for chemical kinetics study.

Figure 87 presents the Mach number error associated with using the 21 point grid in the Tethys code. The result are quite good, with the maximum error at any location being less than 3 %. The error is less than 1 % at the nozzle exit.

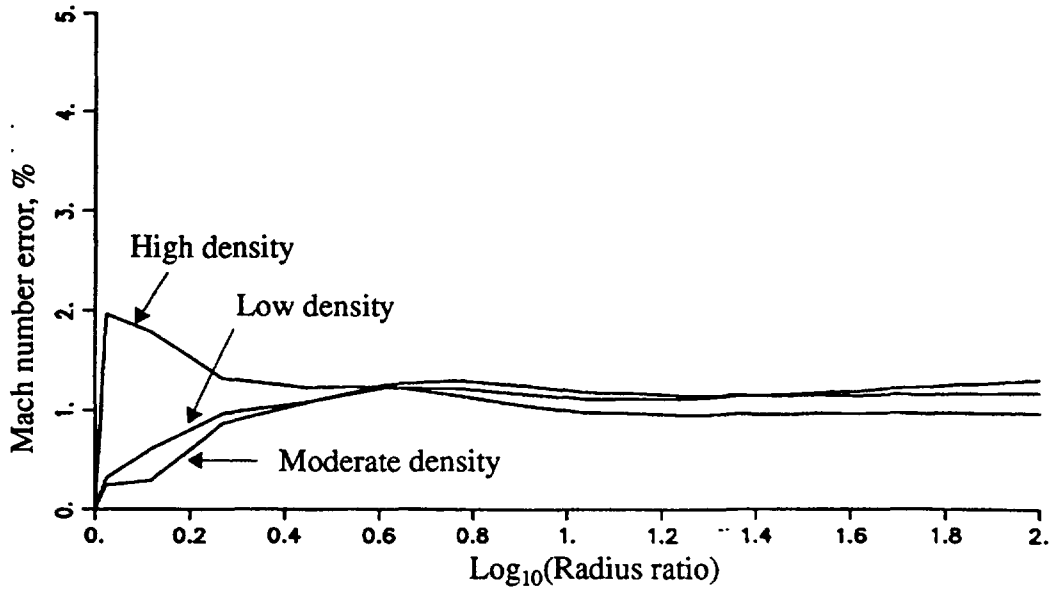

Figure 87. Mach number error associated with Tethys flow model

The results for the high density case suggest that somewhat greater packing of the grid points near the inlet would be beneficial. In fact, approximately twenty percent of the total number of steps taken by the LSENS code were taken between the inlet and the first point used in the Tethys code. It is evident that the species chemical kinetics reaction rates and source term evaluation applied in the Tethys code is very good at predicting the flow Mach number and would correspondingly be expected to accurately predict other fluid properties of interest such as temperature and pressure.

In Tables 33 to 35, the chemical species generation rate at the nozzle inlet is presented for the Tethys and LSENS codes. It is evident that the species generation rates are essentially the same, with the slight differences in generation rates (< 2 %) possibly being due to round-off errors associated with converting the chemical reaction rates and chemical equilibrium constants to consistent units.

Table 33. Species generation rates at the inlet, low density analysis.

Species	σ_i, LSENS code, lbm/(ft^3-sec)	σ_i, Tethys code, lbm/(ft^3-sec)
H_2	-2.6694×10^1	-2.6666×10^1
O_2	3.2694×10^1	3.2643×10^1
OH	1.8899×10^1	1.8369×10^1
H	1.7509×10^1	1.7463×10^1
O	-1.1449×10^2	-1.1433×10^2
H_2O	7.2087×10^1	7.2521×10^1

Table 34. Species generation rates at the inlet, moderate density analysis.

Species	σ_i, LSENS code, lbm/(ft^3-sec)	σ_i, Tethys code, lbm/(ft^3-sec)
H_2	-2.6214×10^3	-2.6190×10^3
O_2	3.2716×10^3	3.2665×10^3
OH	-2.4478×10^3	-2.4588×10^3
H	1.4230×10^3	1.4213×10^3
O	-1.1633×10^4	-1.1617×10^4
H_2O	1.2008×10^4	1.2007×10^4

Table 35. Species generation rates at the inlet, high density analysis.

Species	σ_i, LSENS code, lbm/(ft^3-sec)	σ_i, Tethys code, lbm/(ft^3-sec)
H_2	-2.1414×10^5	-2.1431×10^5
O_2	3.2939×10^5	3.2885×10^5
OH	-4.5825×10^6	-4.5416×10^6
H	-1.8562×10^5	-1.8290×10^5
O	-1.3468×10^6	-1.3451×10^6
H_2O	5.9996×10^6	5.9551×10^6

In Figures 88 to 90, the radial variation (as predicted by the LSENS code) of the radicals OH, H, and O, are shown as the flow expands to an area ratio of 100, for the three different inlet fluid densities studied. From these figures it is readily apparent that the fluid density has a profound effect on the concentration of the radicals, especially monatomic hydrogen and monatomic oxygen.

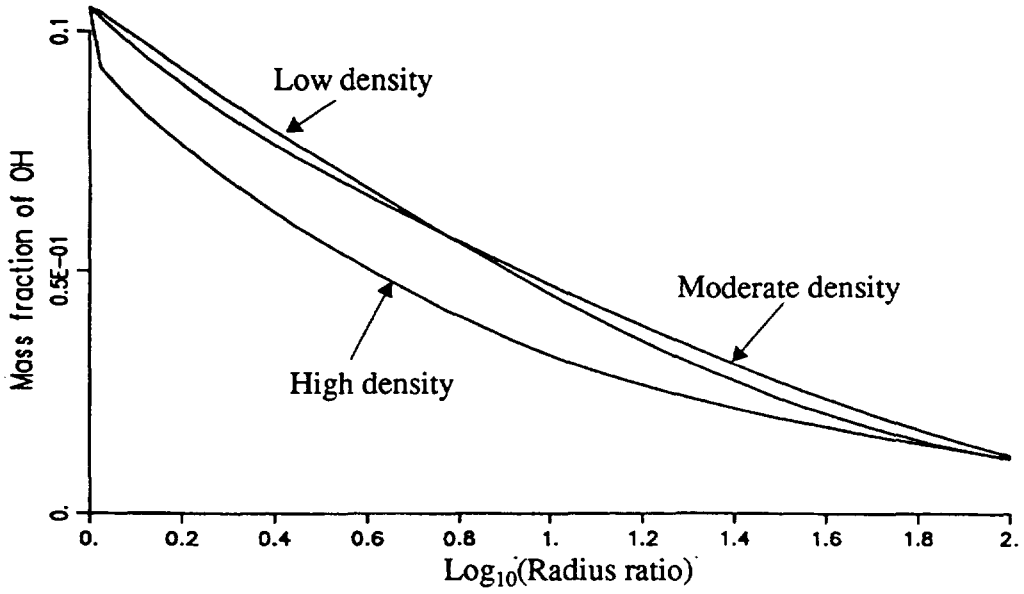

Figure 88. Variation of the OH radical in a chemically reacting source flow study.

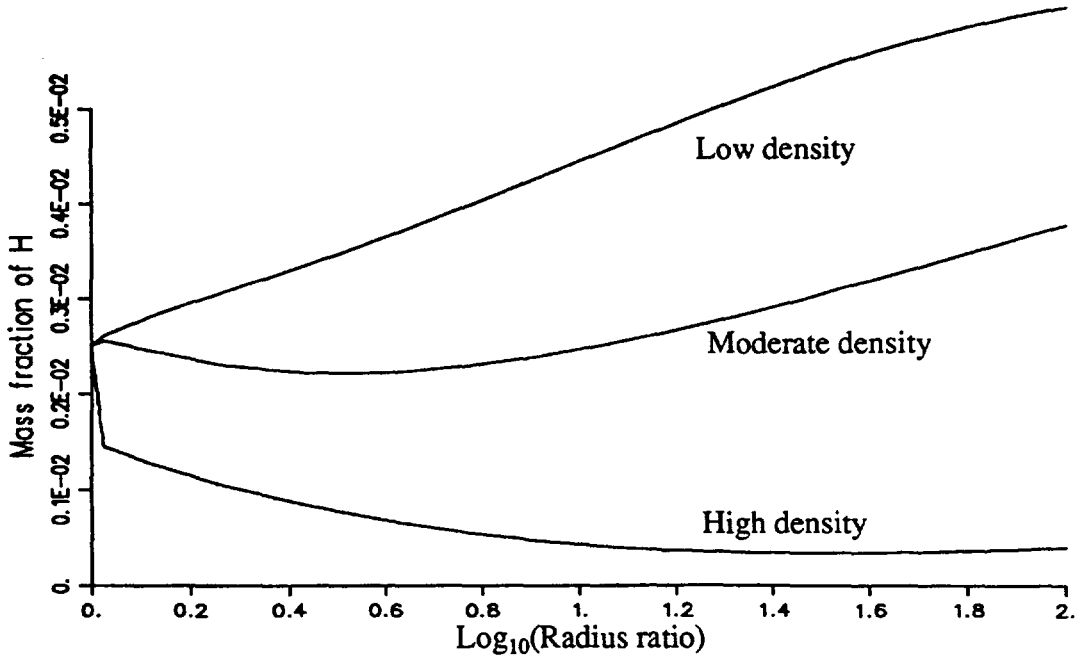

Figure 89. Variation of the monatomic hydrogen radical in a chemically reacting source flow study.

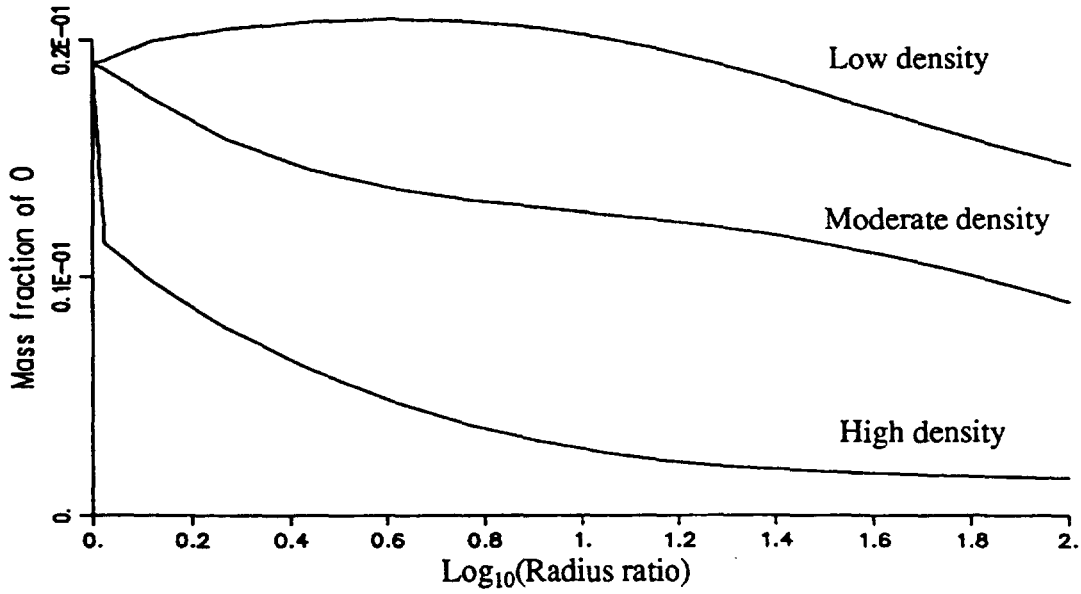

Figure 90. Variation of the monatomic oxygen radical in a chemically reacting source flow study.

In Figures 91 to 93, the error associated with using the Tethys code with the 21 point computational grid is presented. In these figures it is seen that the errors in predicted radical species concentrations is of the same general order of magnitude as the errors in predicting the Mach number presented in Figure 87, with the maximum errors in species mass fraction being less or about 5 % and the maximum error for any given species always occurring with the moderate density test case.

In view of the rather accurate ability of the Tethys model to predict both the fundamental flow properties and radical species concentrations, even with a rather crude computational grid, it is concluded that the species source term is well modelled in the Tethys code.

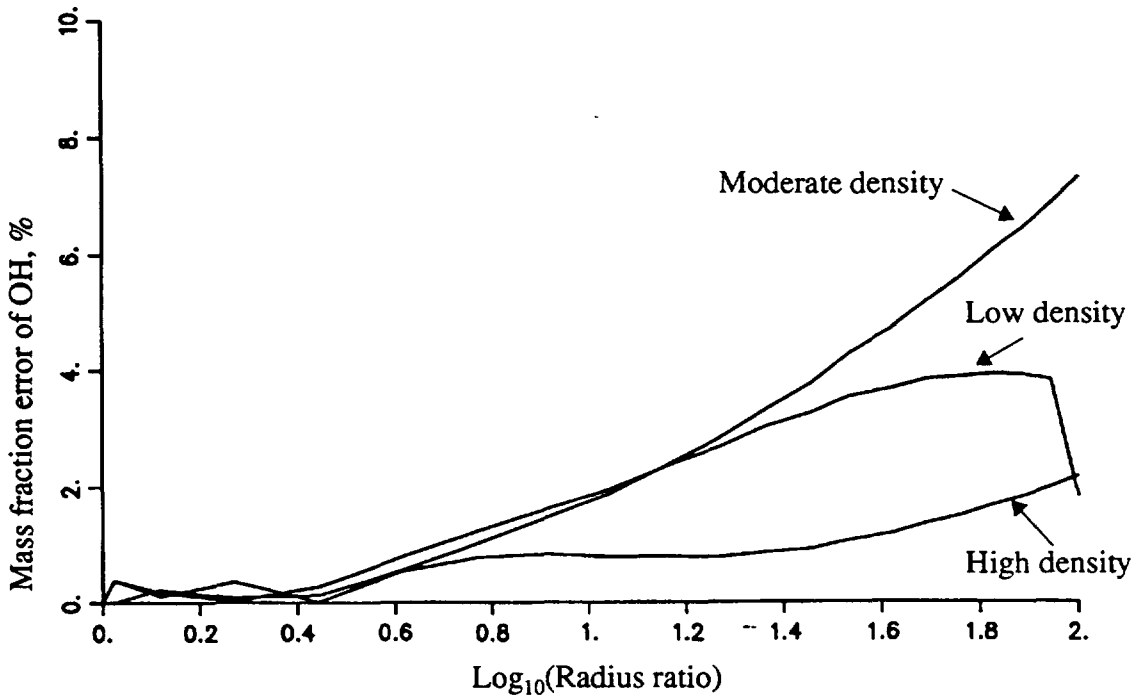

Figure 91. Error in OH mass fraction in a chemically reacting source flow study.

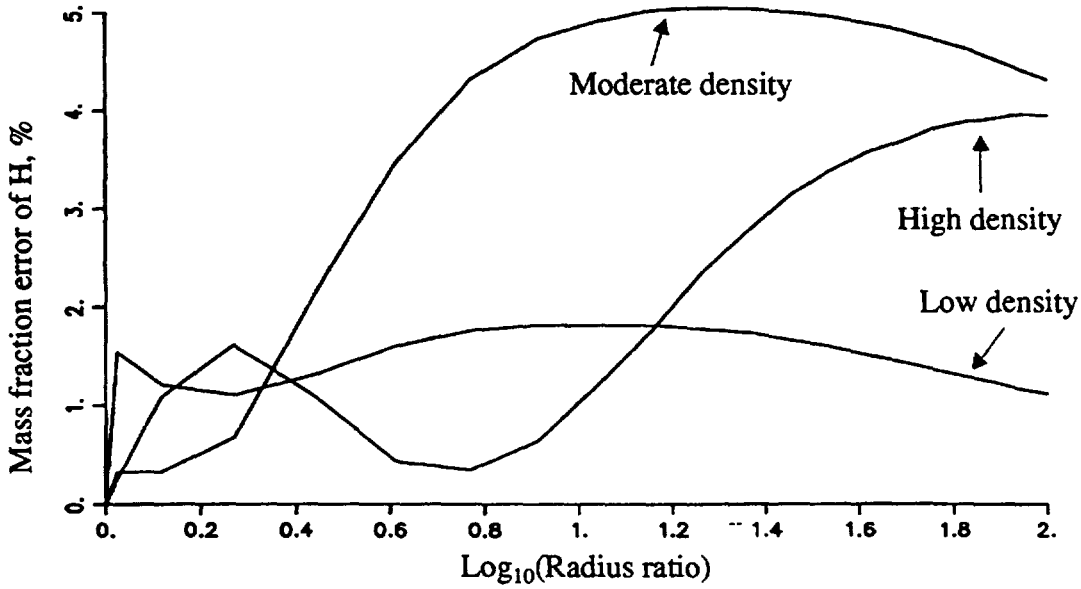

Figure 92. Error in monatomic hydrogen mass fraction in a chemically reacting source flow study.

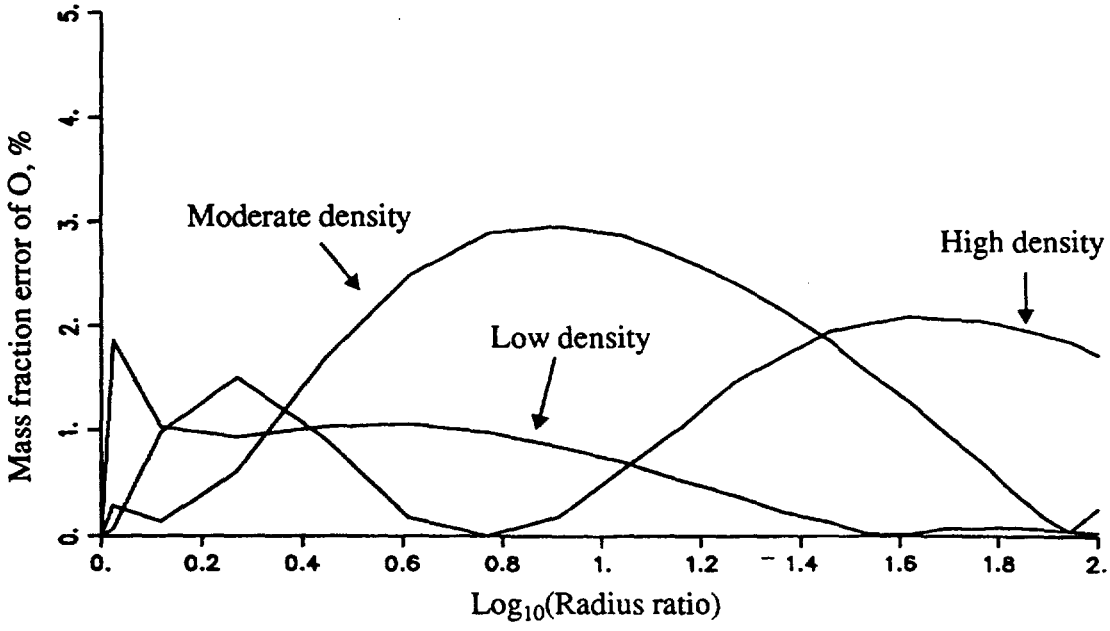

Figure 93. Error in monatomic oxygen species mass fraction in a chemically reacting source flow study.

Appendix K

Fluid Properties Validation

The verification of the fluid properties methodology used in the Tethys model is essential to the accurate prediction of rocket engine performance and heat transfer. Some of the properties, such as specific heat, viscosity, and thermal conductivity, and their corresponding mixture expressions, can be readily verified with existing and mature computer models which employ the same expressions. On the other hand, other coefficients such as the multispecies diffusion coefficient, the thermal diffusion coefficient, and the Dufour coefficient, are much more difficult to verify, requiring one to rely on sparse data or engineering judgement.

K.1. Validation of Specific Heat, Entropy, Thermal Conductivity, and Viscosity

The equations governing the definition of the multispecies specific heat and entropy are based on thermodynamic arguments and are discussed in Section 2 and Appendix B, respectively. The multispecies mixture equation employed for the viscosity and thermal conductivity is of an approximate nature and is given below:

$$\mu = \sum_{i=1}^{n} \frac{x_i \mu_i}{\beta_i} \tag{K.1.1}$$

where the denominator, β_i, for the fluid viscosity is defined as:

$$\beta_i = x_i + \sum_{\substack{j=1 \\ j \neq i}}^{n} x_j \varphi_{ij} \tag{K.1.2}$$

and the empirical expression for the viscosity interaction coefficient, φ_{ij}, is given below:

$$\varphi_{ij} = \frac{1}{4}\left[1 + \left(\frac{\mu_i}{\mu_j}\right)^{1/2} \left(\frac{M_i}{M_j}\right)^{1/4}\right]^2 \sqrt{\frac{2M_j}{M_i + M_j}} \tag{K.1.3}$$

The mixture formula used for the thermal conductivity is given in Equation (K.1.4):

$$k = \sum_{i=1}^{n} \frac{x_i k_i}{\beta_i} \tag{K.1.4}$$

where the denominator, β_i, for the mixture thermal conductivity is defined as:

$$\beta_i = x_i + \sum_{\substack{j=1 \\ j \neq i}}^{n} x_j \Psi_{ij} \tag{K.1.5}$$

and the empirical expression for the thermal conductivity interaction coefficient, Ψ_{ij}, is given by Equation (K.1.6):

$$\Psi_{ij} = \varphi_{ij}\left[1 + \frac{2.41\,(M_i - M_j)\,(M_i - 0.142\,M_j)}{(M_i + M_j)^2}\right] \tag{K.1.6}$$

where φ_{ij} is the viscosity interaction coefficient described in Equation (K.1.3).

To validate that the Tethys model employs proper techniques for predicting the fluid specific heat, entropy, thermal conductivity, and viscosity, two computational cases were studied. In one case, the fluid was near the combustion temperature of a hydrogen-oxygen rocket engine (7000 R). In a second case, the fluid was at 1710.5 R. In both cases, the fluid had an oxygen to fuel ratio of 8.0 and the species concentration was in chemical equilibrium. These two cases represent conditions that are at the high-temperature and the low-temperature portions of the thermodynamic curve fit, with the split occurring at 1800 R. The inlet fluid conditions are given in Table 36. Table 37 compares the fluid properties prediction from CET89 (Reference 47) and the Tethys code. The values are seen to be in excellent agreement, with any slight discrepancies undoubtedly due to the fact that the thermodynamic data file used in the Tethys code was an older version of the data file used by CET89.

Table 36. Fluid conditions for validation of specific heat, thermal conductivity, and viscosity models.

Fluid property	High temperature	Low temperature
Temperature, R	7000.0	1710.5
ω_{H_2}	0.01507	0.02600
ω_{O_2}	0.07910	0.12281
ω_{H_2O}	0.78276	0.58549
ω_{OH}	0.10308	0.19312
ω_{H}	0.00235	0.00815
ω_{O}	0.01764	0.06443

Table 37. Comparison of CET89 and Tethys fluid property predictions.

Fluid property predicted	High temperature		Low temperature	
	CET89	Tethys	CET89	Tethys
Specific heat, C_P, Btu/lbm-R	0.7819	0.7702	0.5570	0.5572
Entropy, s, Btu/lbm-R	4.285	4.274	3.865	3.863
Thermal conductivity, k, Btu/ft-sec $\times 10^5$	9.367	9.349	1.841	1.839
Viscosity, μ, lbm/ft-sec $\times 10^5$	7.521	7.520	2.448	2.448

K.2. Validation of Multiple Species Diffusion Coefficients

Lacking an established computer model upon which to verify the accuracy of the multiple species diffusion coefficient model, the Tethys model was verified by comparing the computational results of a ternary system with the theoretical results. Since the ternary

case represents a multispecies condition that computationally differs from a six species case only in the number of computational loops required in the Tethys code, validation of this case is a reasonable validation of the entire multispecies calculation procedure involved in Tethys.

The exact formulation of the multispecies diffusion coefficients for a ternary system is extremely lengthy, being presented in Reference 9. The ternary system considered comprised hydrogen, oxygen, and steam at a temperature of 1000 R. The values of the binary diffusion coefficients used in the theoretical results and the Tethys model were obtained from curves fits of tabulated values suggested by Svehla (Reference 56), who employed a combination of theory and experimental data. The results of the study are presented in the Table 38 and are shown to be in excellent agreement.

Table 38. Comparison of theoretical and predicted multispecies diffusion coefficients for a ternary system.

Multispecies diffusion coefficient	Theoretical value	Tethys prediction
$A_{H_2-H_2}$	-1.443×10^{-5}	-1.443×10^{-5}
$A_{H_2-O_2}$	-5.350×10^{-5}	-5.351×10^{-5}

K.3. Validation of Thermal Diffusion Coefficient Procedure

Verification of the accuracy of the thermal diffusion model used in the Tethys code, along with the accuracy to which the multiple equations were solved was demonstrated in a rather heuristic manner. First, the case for which binary thermal diffusion data exists, that of the H_2/O_2 species system, was examined and compared with the predictions from the Tethys model. Second, an H_2/O_2 system, complete with reacted and dissociated species present, was examined at numerous temperatures for any irregularities in the shape or magnitude of the diffusion coefficient curves.

In Figure 94, the predicted variation of the thermal diffusion coefficient for an oxygen/hydrogen system from a temperature range of 160 to 530 R is presented, which corresponds to the temperature at which the mean thermal diffusion factor was measured. The integrated average value of the thermal diffusion coefficient predicted by Tethys is 0.206 while the measured value reported in Reference 57 is 0.192. The agreement between predictions and experimental measures is therefore taken to be very good in view of the complexity of the driving forces describing the nature of the thermal diffusion coefficient.

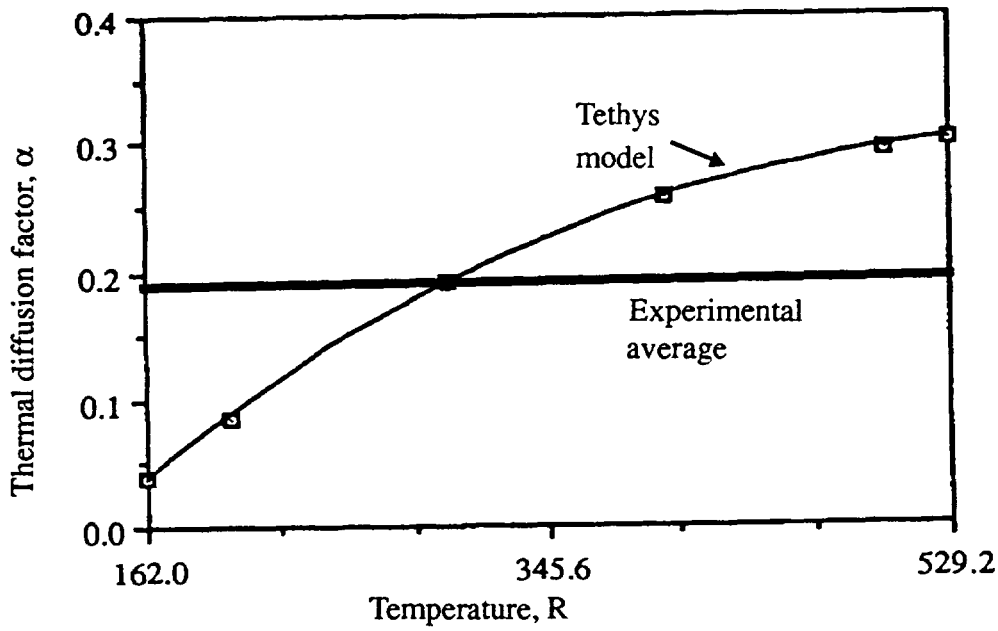

Figure 94. Comparison of experimental and predicted values of the thermal diffusion factor in a hydrogen/oxygen system.

A final heuristic validation of the thermal diffusion modelling is presented in Figure 95, where an oxygen/hydrogen system (at the stoichiometric mixture ratio of 8.0), of the same chemical composition as tested in the chemical kinetics validation studies (Appendix J), is presented. Several conclusions can be drawn from this figure. The first is that the curves appear to be regular in nature and are about an order of magnitude less than that of an unreacted hydrogen/oxygen system. This is as expected since the mass fractions of most of the constituents in the reacted stoichiometric system are rather small. A final observation to be made is that the thermal diffusion coefficient curve for steam is negative

at lower temperatures and becomes positive at temperatures near 1000 R. This is expected since the binary diffusion theory would suggest that the water vapor diffusion coefficient would be a minimum near 700 R, which is in agreement with the predictions shown in Figure 95.

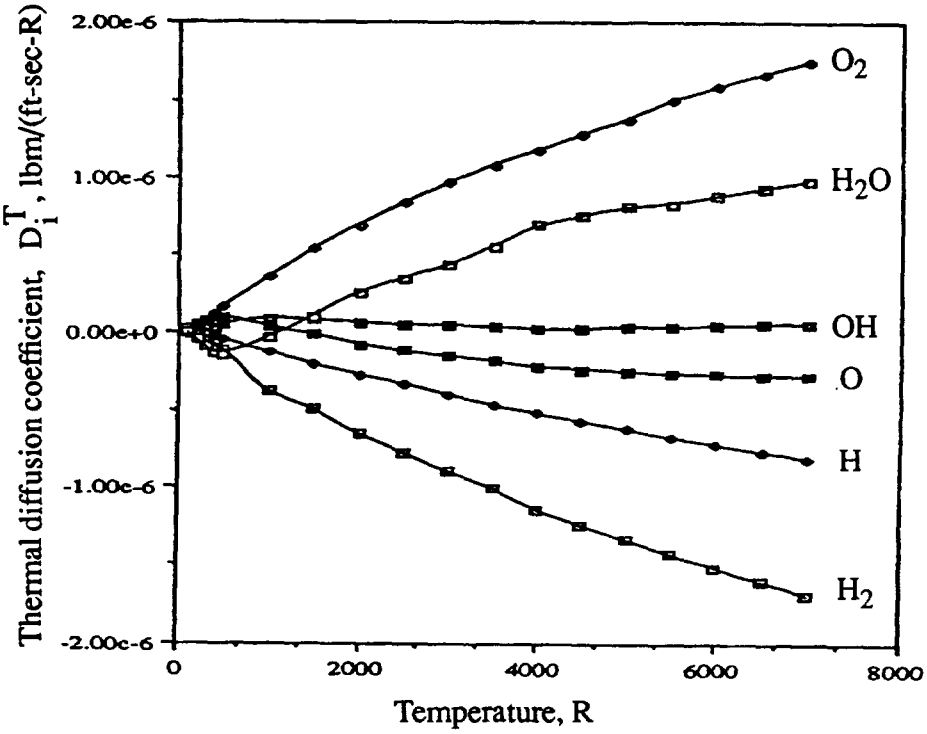

Figure 95. Temperature sensitivity of the thermal diffusion coefficient in a chemically reacted hydrogen/oxygen system.

Appendix L

Flow Modelling Validation of Species Ordinary Diffusion Equations

To validate the accuracy of the Tethys model in describing the transfer of mass as the result of ordinary diffusion, a simple flow model was considered. The viscous flow of a fluid in a pipe, subjected to slip boundary conditions along the wall and a trace concentration of a species at the wall was modelled. This case is entirely analogous to the case of a solid bar at a prescribed temperature that is suddenly subjected to a different temperature at the outer surface. The corresponding computational grid and boundary conditions imposed for this test case are presented in Figure 96 and Table 39.

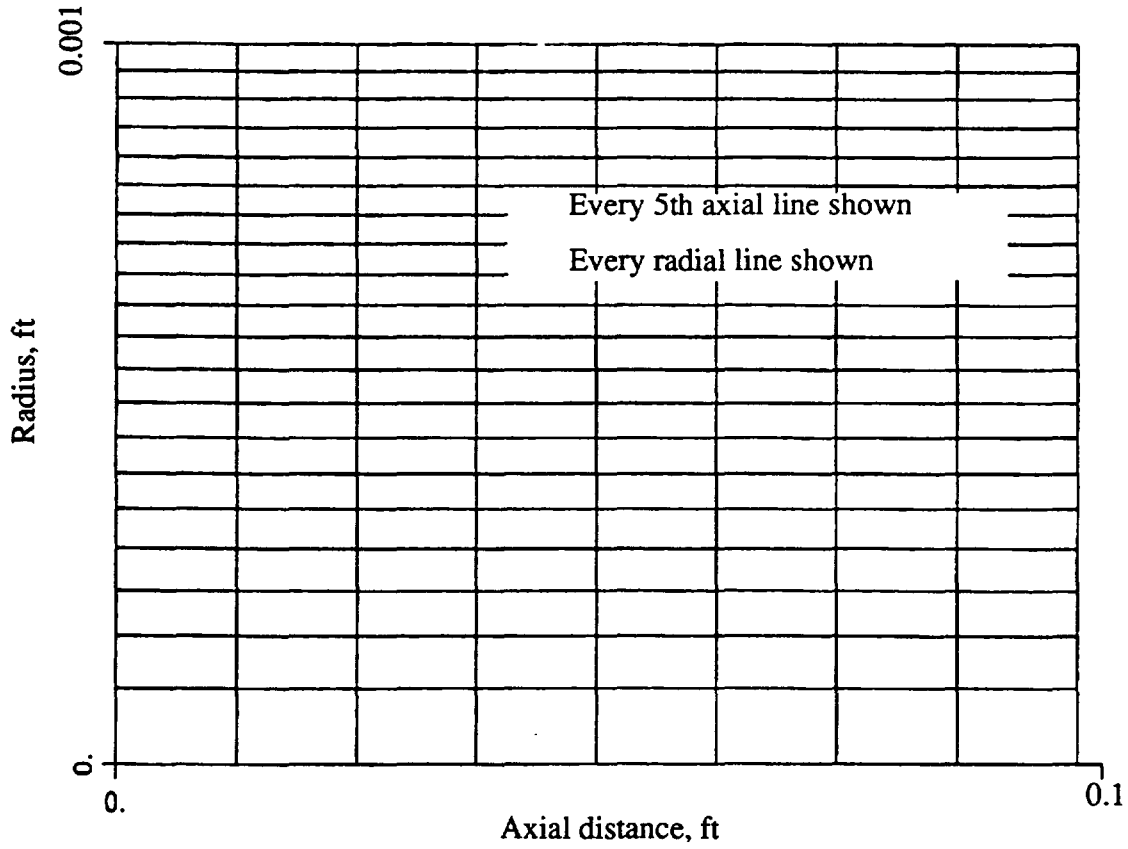

Figure 96. Computational grid and geometry of species diffusion validation study.

Table 39. Boundary conditions for species ordinary diffusion validation study.

Inlet	Exit	Centerline	Wall
$\rho = 0.01 \ \text{lbm/ft}^3$	$\frac{\partial P}{\partial \xi} = 0$	$\frac{\partial P}{\partial \eta} = 0$	$\frac{\partial P}{\partial \eta} = 0$
$u = 1000 \ \text{ft/sec}$	$\frac{\partial u}{\partial \xi} = 0$	$\frac{\partial u}{\partial \eta} = 0$	$\frac{\partial u}{\partial \eta} = 0$
$v = 0$	$\frac{\partial v}{\partial \xi} = 0$	$v = 0$	$v = 0$
$T = 500 \ \text{R}$	$\frac{\partial T}{\partial \xi} = 0$	$\frac{\partial T}{\partial \eta} = 0$	$\frac{\partial T}{\partial \eta} = 0$
$\omega_{H_2} = 1.0e-06$	$\frac{\partial^2 \omega_{H_2}}{\partial \xi^2} = 0$	$\frac{\partial \omega_{H_2}}{\partial \eta} = 0$	$\omega_{H_2} = 1.0e-04$

The results of the Tethys code and theoretical results (extracted from graphical data, Reference 13) are shown in Figure 97. The results at distances greater than 0.025 ft are in excellent agreement with theory, with the most likely reason for the discrepancy at x = 0.025 ft being that the graph from which the theoretical predictions were made was based on the assumption that the Fourier number was rather large.

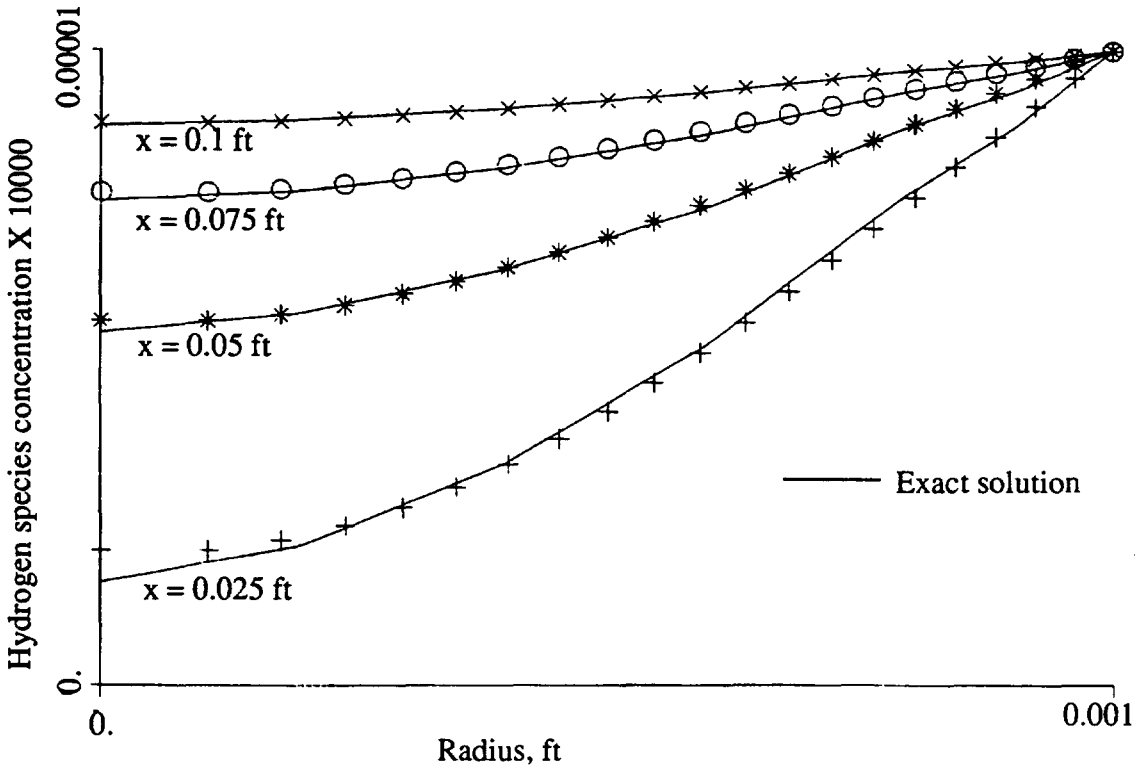

Figure 97. Comparison of theoretical and predicted species concentration for ordinary species diffusion validation studies.

Appendix M

Evaluation of Flowfield Parameters Using the JANNAF Procedure

The prediction of rocket nozzle performance parameters was performed in a manner which conformed with the JANNAF methodology (Reference 58) for nozzle performance prediction as closely as possible. The procedure consists of using a control surface that crosses the throat of the nozzle and envelopes the divergent section of the nozzle and the complete combustor and inlet section, as illustrated in Figure 98.

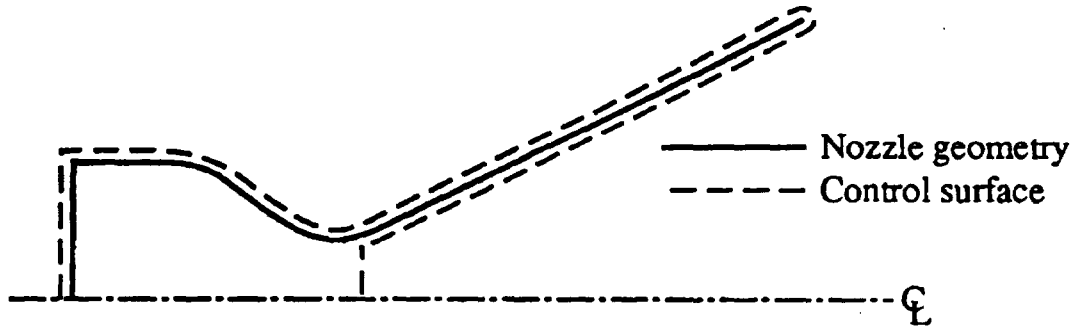

Figure 98. Control surface employed for evaluation of nozzle performance parameters.

Using the control surface shown in Figure 98, the prediction of nozzle performance is obtained by evaluating the pressure forces, momentum flux, and mass flux that cross the throat and the pressure forces and shear forces that act on the divergent section of the nozzle. The procedure for the evaluation of these terms follows.

M.1. Evaluation of Nozzle Throat Region Parameters

Consider a control surface cutting across the throat region of a rocket nozzle, as illustrated in Figure 99, where a constant–ξ line, originating at point o on the centerline, strikes the nozzle wall at the throat, point e.

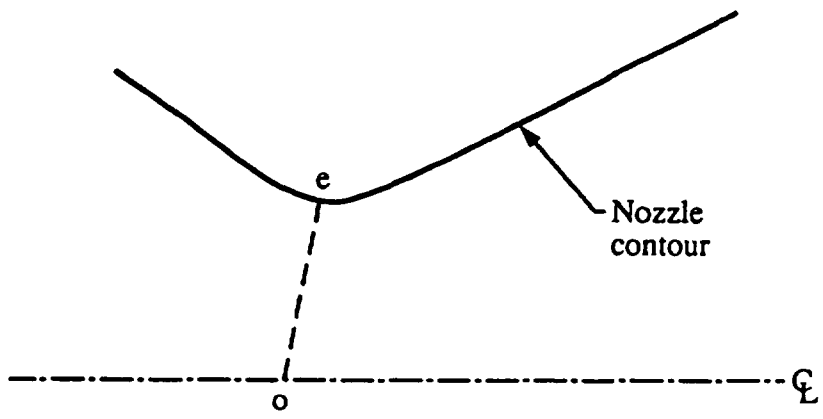

Figure 99. Control surface across the nozzle throat.

The mass flow rate across control surface oe is given by the following equation:

$$\text{(M.1.1)} \qquad \dot{m} = \int_S \rho\,(V \bullet n)\,dA = \int_{r_o}^{r_e} \rho u \pi d(r^2) - \int_{x_o}^{x_e} \rho v 2\pi r dx$$

To maintain consistency with the manner in which the finite difference equations were applied, the numerical evaluation of the mass flux was performed by a centered integration technique, as shown in Equation (M.1.2), where the total number of computational points located on a constant ξ line is denoted by N2, with individual points on that line described by the subscript j.

$$\text{(M.1.2)} \quad \dot{m} \approx \pi \sum_{j=2}^{N2-1} (\rho u)|_j \left[\frac{r^2|_{j+1} - r^2|_{j-1}}{2}\right] - 2\pi \sum_{j=2}^{N2-1} (\rho v r)|_j \left[\frac{x|_{j+1} - x|_{j-1}}{2}\right] + \begin{matrix}\text{Edge}\\ \text{points}\end{matrix}$$

The axial momentum flux crossing the control surface can be estimated in a manner analogous to that in which the mass flow rate is calculated. The resulting expression is given by Equation (M.1.3):

$$\text{(M.1.3)}\qquad \begin{matrix}\text{Axial}\\ \text{momentum}\\ \text{flux}\end{matrix} \approx \pi \sum_{j=2}^{N2-1} \left[(\rho u)\,u\right]\Big|_j \left[\frac{r^2\big|_{j+1} - r^2\big|_{j-1}}{2}\right]$$

$$- 2\pi \sum_{j=2}^{N2-1} \left[(\rho v r)\,u\right]\Big|_j \left[\frac{x\big|_{j+1} - x\big|_{j-1}}{2}\right] + \begin{matrix}\text{Edge}\\ \text{points}\end{matrix}$$

In a similar manner, the contribution of the axial pressure force component acting on the throat control surface can be approximated by Equation (M.1.4):

$$\text{(M.1.4)}\qquad \begin{matrix}\text{Axial}\\ \text{pressure}\\ \text{force}\end{matrix} = \int_{r_o}^{r_e} P\pi dr^2 \approx \pi \sum_{j=2}^{N2-1} P\big|_j \left[\frac{r^2\big|_{j+1} - r^2\big|_{j-1}}{2}\right] + \begin{matrix}\text{Edge}\\ \text{points}\end{matrix}$$

In Equations (M.1.2) to (M.1.4), the edge points are all evaluated using a first-order method.

M.2. Evaluation of Nozzle Divergent Wall Force Components

In order to maintain consistency with the JANNAF nozzle evaluation procedure, it is necessary to evaluate the forces that act upon the nozzle divergent section. The forces are comprised of two component, a thrust contributing component from the fluid static pressure and a degradation component arising from the fluid shear stresses.

The axial component of thrust obtained by the fluid static pressure forces acting on the nozzle surface can be derived in a manner that is entirely analogous to the procedure employed in establishing the pressure forces that act on the control surface crossing the throat. The resulting expression is given by Equation (M.2.1):

$$\text{(M.2.1)}\qquad \begin{matrix}\text{Axial}\\ \text{pressure}\\ \text{force}\end{matrix} = \int_{r_{T1}}^{r_{N1}} P\pi r dr^2 \approx \pi \sum_{i=T1+1}^{N1-1} P\big|_i \left[\frac{r^2\big|_{i+1} - r^2\big|_{i-1}}{2}\right] + \begin{matrix}\text{Edge}\\ \text{points}\end{matrix}$$

where N1 denotes the total number of computational points on the surface of the nozzle wall and T1 corresponds to the computational point that lies at the throat of the nozzle.

The total amount of drag that acts in the divergent region of the nozzle is given by Equation (M.2.2):

$$\text{(M.2.2)}\quad \begin{matrix}\text{Axial}\\ \text{drag}\\ \text{forces}\end{matrix} = \int_{x=T1}^{x=N1} \tau 2\pi r dx \approx \sum_{i=T1+1}^{N1-1} [\tau 2\pi r]_i \left[\frac{x_{i+1}-x_{i-1}}{2}\right] + \begin{matrix}\text{Edge}\\ \text{points}\end{matrix}$$

The evaluation of the drag forces that act on the surface of the nozzle is somewhat more complicated than the expressions given for the pressure force terms since the shear stresses are actually calculated in the Tethys model at the point (see Appendix B) midway between the nozzle surface and the adjoining interior point, as illustrated in Figure 100.

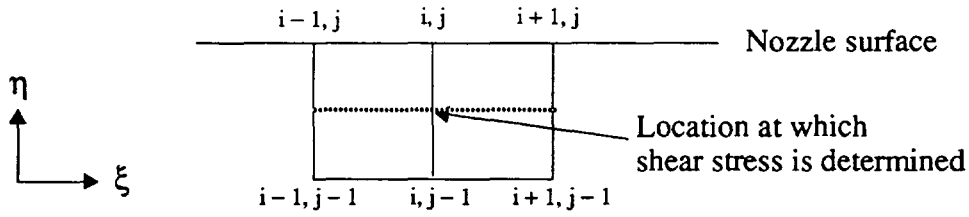

Figure 100. Nozzle surface examination of shear stress calculation procedure.

Consequently, the procedure for determining the shear stresses that act on the nozzle wall is to examine the manner in which the averaged shear stress is calculated and to determine the relation of this term to that which exists along the surface of the nozzle wall. The dependence of the wall shear stress on a nearby point can be determined through consideration of a locally transformed grid. Assuming that the flow is parallel to the nozzle surface and that the difference in radius between the wall point and the nearest interior point is negligible, the transfer of momentum from the fluid to the wall can be determined by solution of the following equation (Reference 59, page 474):

$$\text{(M.2.3)}\quad \frac{\partial \tau_{tn}}{\partial n} = \frac{\partial P}{\partial t}$$

where the t subscript denotes the direction tangent to the wall and the n subscript denotes the direction normal to the wall. Assuming that the tangential pressure gradient at the wall

is constant from the wall surface to the nearest midway interior point (an approximation consistent with the assumption of parallel flow), Equation (M.2.2) can be integrated and rearranged to yield the following:

$$\text{(M.2.4)} \qquad \tau_{tn}\big|_{i,j} = \tau_{tn}\big|_{i,j-1/2} - \frac{\partial P}{\partial t}\Delta n$$

The evaluation of the pressure gradient term in Equation (M.2.4) is a relatively straightforward procedure, with the normal distance corresponding to 1/2 the distance from the wall point at the i, j position to the interior point located at the i, j – 1 location.

The evaluation of the shear stress term located at the i, j – 1/2 point is performed in a manner consistent with the procedure used in Appendix B. Using this procedure, the shear stress terms at the midway point is equal to the following:

$$\begin{aligned}\text{(M.2.5)} \quad \tau_{tn}\big|_{i,j-1/2} \approx & \left[\frac{\mu}{2}\sqrt{\eta_x^2+\eta_r^2}\right]_{i,j}\left[\frac{V_\xi\big|_{i,j} - V_\xi\big|_{i,j-1}}{\Delta\eta}\right] \\ & + \left[\frac{\mu}{2}\frac{\xi_x\eta_x+\xi_r\eta_r}{\sqrt{\eta_x^2+\eta_r^2}}\right]_{i,j}\left[\frac{V_\xi\big|_{i+1,j} - V_\xi\big|_{i-1,j}}{2\Delta\xi}\right] \\ & + \left[\frac{\mu}{2}\sqrt{\eta_x^2+\eta_r^2}\right]_{i,j-1}\left[\frac{V_\xi\big|_{i,j} - V_\xi\big|_{i,j-1}}{\Delta\eta}\right] \\ & + \left[\frac{\mu}{2}\frac{\xi_x\eta_x+\xi_r\eta_r}{\sqrt{\eta_x^2+\eta_r^2}}\right]_{i,j-1}\left[\frac{V_\xi\big|_{i+1,j-1} - V_\xi\big|_{i-1,j-1}}{2\Delta\xi}\right]\end{aligned}$$

where $V_\xi = \dfrac{(u\eta_r + v\eta_x)}{\sqrt{\eta_x^2+\eta_r^2}}$, is the velocity in the tangential direction.

The evaluation of the metric terms contained in Equation (M.2.5) obeys the fundamental philosophy described in Appendix B which, in essence, means that all of the grid points used in the determination of the grid metrics are never outside of the region in which the dependent variables are evaluated.

In cases where Dirichlet boundary conditions were used for the thermal energy equation, a procedure analogous to that used for the evaluation of the shear stress terms was employed for the evaluation of the heat transfer rates.

M.3. Comparison with Experimental Results

In the same manner in which all reasonable attempts to conform with the JANNAF nozzle evaluation procedure were applied to the Tethys code predictions, conformity of the experimental results with the prescribed JANNAF rocket nozzle test evaluation methodology (Reference 60) was also pursued. For the most part, the experimental results that were published were in agreement with the prescribed mannerism of publishing nozzle performance, although the need to maintain consistency between analytical and experimental results required some changes to the experimental performance measurements.

The performance measurement alteration for the 1030:1 high area ratio nozzle tests was that the nozzle experimental evaluation program used an effective total pressure correction concept that was inconsistent with the JANNAF methodology and was not applied in this study.

The 25 lbf film cooled nozzle study, although not stated in the report, used chamber pressure measurements from a location just upstream of the convergent section to report characteristic velocity performance values. In this study, the chamber pressure measurements located at the inlet plane of the combustor were used to compute the nozzle stagnation pressure.

No alteration of the heat flux measurements was made. In the high area ratio nozzle tests, the measurements were included in the report. In the 25 lbf film cooled nozzle study, the measurements were extracted by the author from unpublished coolant water mass flow rate measurements and the measured inlet and outlet temperatures of the water.

Appendix N

Artificial Diffusion Model

The methodology for applying artificial diffusion in the Tethys code is identical to that employed in the Proteus code (Reference 5), which is presented in this appendix and is a reproduction of Section 8 in Reference 5. The references cited within Section 8 of the Proteus manual are cited at the end of this appendix. Although nomenclature represent those employed in the Proteus report, they are consistent with those used throughout the present work, with only one exception. In the Proteus report, the nomenclature used for the spectral radii term is ψ, while in Appendix H the spectral radii is presented using the Greek character Γ.

8.0 ARTIFICIAL VISCOSITY

With the numerical algorithm of Section 7.0, high frequency nonlinear instabilities can appear as the solution develops. For example, in high Reynolds number flows oscillations can result from the odd-even decoupling inherent in the use of second-order central differencing for the inviscid terms. In addition, physical phenomena such as shock waves can cause instabilities when they are captured by the finite difference algorithm. Artificial viscosity, or smoothing, is normally added to the solution algorithm to suppress these high frequency instabilities. Two artificial viscosity models are currently available in the *Proteus* computer code - a constant coefficient model used by Steger (1978), and the nonlinear coefficient model of Jameson, Schmidt, and Turkel (1981). The implementation of these models in generalized nonorthogonal coordinates is described by Pulliam (1986b).

8.1 CONSTANT COEFFICIENT ARTIFICIAL VISCOSITY

The constant coefficient model uses a combination of explicit and implicit artificial viscosity. The standard explicit smoothing uses fourth-order differences, and damps the high frequency nonlinear instabilities. Second-order explicit smoothing, while not used by Steger or Pulliam, is also available in *Proteus*. It provides more smoothing than the fourth-order smoothing but introduces a larger error, and is therefore not used as often. The implicit smoothing is second order and is intended to extend the linear stability bound of the fourth-order explicit smoothing.

The explicit artificial viscosity is implemented in the numerical algorithm by adding the following terms to the right hand side of equation (7.5a) (i.e., the source term for the first ADI sweep.)

$$\frac{\varepsilon_E^{(2)}\Delta\tau}{J}\left(\nabla_\xi\Delta_\xi Q + \nabla_\eta\Delta_\eta Q\right) - \frac{\varepsilon_E^{(4)}\Delta\tau}{J}\left[(\nabla_\xi\Delta_\xi)^2 Q + (\nabla_\eta\Delta_\eta)^2 Q\right] \tag{8.1}$$

where $\varepsilon_E^{(2)}$ and $\varepsilon_E^{(4)}$ are the second- and fourth-order explicit artificial viscosity coefficients. The symbols ∇ and Δ are backward and forward first difference operators. Thus,

$$\nabla_\xi Q_i = Q_i - Q_{i-1}$$

$$\Delta_\xi Q_i = Q_{i+1} - Q_i$$

$$\nabla_\xi\Delta_\xi Q_i = Q_{i+1} - 2Q_i + Q_{i-1}$$

$$(\nabla_\xi\Delta_\xi)^2 Q_i = Q_{i+2} - 4Q_{i+1} + 6Q_i - 4Q_{i-1} + Q_{i-2}$$

Equivalent formulas are used for differences in the η direction.

A few details should be noted at this point. First, the sign in front of the artificial viscosity term be added to equation (7.5a) depends on the sign of the "i" term in the difference formula. For damping, t term must be negative when added to the right hand side of the equations (i.e., explicit artificial viscosi and positive when added to the left hand side (i.e., implicit artificial viscosity.) See Anderson, Tannel and Pletcher (1984) for details. Second, the terms being added are differences only, and not finite differe approximations to derivatives. They are therefore not divided by $\Delta\xi$, etc. Third, the variables being ferenced are Q, not $\hat{Q}$. As noted by Pulliam (1986b), scaling the artificial viscosity terms by $1/J$ makes th consistent with the form of the remaining terms in the equations. Fourth, the terms are also scaled by This makes the steady state solution independent of the time step size (Pulliam, 1986b). And finally, r that the fourth-order difference formula cannot be used at grid points adjacent to boundaries. At th points, therefore, the appropriate fourth-order term in expression (8.1) is replaced by a second-order te Thus, for points adjacent to the $\xi = 0$ and $\xi = 1$ boundaries, $-\varepsilon_E^{(4)}\Delta\tau[(\nabla_\xi\Delta_\xi)^2 Q]/J$ is replaced by

$$+\frac{\varepsilon_E^{(4)}\Delta\tau}{J}\nabla_\xi\Delta_\xi Q \qquad (7.5c)$$

A similar expression is used at points adjacent to the $\eta = 0$ and $\eta = 1$ boundaries.

The implicit artificial viscosity is implemented by adding the following terms to the left hand side of equations specified.

$$-\frac{\varepsilon_I\Delta\tau}{J}\left[\nabla_\xi\Delta_\xi(J\Delta\hat{Q}^n)\right] \quad \text{to equation (7.5a)}$$

$$-\frac{\varepsilon_I\Delta\tau}{J}\left[\nabla_\eta\Delta_\eta(J\Delta\hat{Q}^n)\right] \quad \text{to equation (7.5b)}$$

Note that the addition of the artificial viscosity terms, in effect, changes the original governing pa differential equations. At steady state, the difference equations with the artificial viscosity terms adde tually correspond to the following differential equations.[7]

$$\frac{\partial\hat{E}}{\partial\xi}+\frac{\partial\hat{F}}{\partial\eta}=\frac{\partial\hat{E}_V}{\partial\xi}+\frac{\partial\hat{F}_V}{\partial\eta}+\frac{\varepsilon_E^{(2)}}{J}\left[(\Delta\xi)^2\frac{\partial^2(J\hat{Q})}{\partial\xi^2}+(\Delta\eta)^2\frac{\partial^2(J\hat{Q})}{\partial\eta^2}\right]$$
$$-\frac{\varepsilon_E^{(4)}}{J}\left[(\Delta\xi)^4\frac{\partial^4(J\hat{Q})}{\partial\xi^4}+(\Delta\eta)^4\frac{\partial^4(J\hat{Q})}{\partial\eta^4}\right]$$

[7] These equations represent the use of the constant coefficient artificial viscosity model presented in this section. nonlinear coefficient model to be presented in Section 8.2 is more complicated, but the same principle applie

ORIGINAL PAGE IS
OF POOR QUALITY

The implicit terms do not appear, since they difference $\Delta\hat{Q}$, and in the steady form of the equations $\Delta\hat{Q} = 0$. The artificial viscosity terms do not represent anything physical. The coefficients should therefore be as small as possible, but still large enough to damp any instabilities. Although optimum values will vary from problem to problem, recommended levels are $\varepsilon_\xi^{(4)} = O(1)$ and $\varepsilon_I = 2\varepsilon_\xi^{(4)}$ (Pulliam, 1986b). The recommended level for $\varepsilon_\xi^{(2)}$, when used, is $\varepsilon_\xi^{(2)} = O(1)$.

8.2 NONLINEAR COEFFICIENT ARTIFICIAL VISCOSITY

The nonlinear coefficient artificial viscosity model is strictly explicit. Using the model as described by Pulliam (1986b), but in the current notation, the following terms are added to the right hand side of equation (7.5a).

$$\nabla_\xi\left\{\left[\left(\frac{\psi}{J}\right)_{i+1} + \left(\frac{\psi}{J}\right)_i\right]\left(\varepsilon_\xi^{(2)}\Delta_\xi Q - \varepsilon_\xi^{(4)}\Delta_\xi\nabla_\xi\Delta_\xi Q\right)_i\right\}$$
$$+ \nabla_\eta\left\{\left[\left(\frac{\psi}{J}\right)_{j+1} + \left(\frac{\psi}{J}\right)_j\right]\left(\varepsilon_\eta^{(2)}\Delta_\eta Q - \varepsilon_\eta^{(4)}\Delta_\eta\nabla_\eta\Delta_\eta Q\right)_j\right\} \tag{8.4}$$

The difference operation $\Delta_\zeta\nabla_\zeta\Delta_\zeta Q$ is given by

$$\Delta_\xi\nabla_\xi\Delta_\xi Q_i = Q_{i+2} - 3Q_{i+1} + 3Q_i - Q_{i-1}$$

In the expression (8.4), ψ is defined as

$$\psi = \psi_x + \psi_y \tag{8.5}$$

where ψ_x and ψ_y are spectral radii defined by[8]

$$\psi_x = \frac{|U| + a\sqrt{\xi_x^2 + \xi_y^2}}{\Delta\xi}$$
$$\psi_y = \frac{|V| + a\sqrt{\eta_x^2 + \eta_y^2}}{\Delta\eta} \tag{8.6}$$

Here U and V are the contravariant velocities without metric normalization, defined by

---

[8] It should be noted that the grid increments $\Delta\xi$ and $\Delta\eta$ in these definitions do not appear in the corresponding formulas presented by Pulliam (1986b). This is because the grids used by Pulliam are constructed such that $\Delta\xi = \Delta\eta = 1$, while in *Proteus* $\Delta\xi = 1/(N_1 - 1)$ and $\Delta\eta = 1/(N_2 - 1)$. The definitions used here for ψ_x and ψ_y result in an artificial viscosity level equivalent to that described by Pulliam.

$$U = \xi_t + \xi_x u + \xi_y v$$
$$V = \eta_t + \eta_x u + \eta_y v \qquad (8$$

and $a = \sqrt{\gamma RT}$, the speed of sound.

The parameters $\varepsilon^{(2)}$ and $\varepsilon^{(4)}$ are the second- and fourth-order artificial viscosity coefficients. Instead being specified directly by the user, as they are in the constant coefficient model, in the nonlinear coeffic model they are a function of the pressure field. For the coefficients of the ξ direction differences,

$$(\varepsilon_\xi^{(2)})_i = \kappa_2 \Delta\tau \max(\sigma_{i+1},\ \sigma_i,\ \sigma_{i-1}) \qquad (8$$

$$(\varepsilon_\xi^{(4)})_i = \max[0,\ \kappa_4 \Delta\tau - (\varepsilon_\xi^{(2)})_i] \qquad (8$$

where

$$\sigma_i = \left| \frac{p_{i+1} - 2p_i + p_{i-1}}{p_{i+1} + 2p_i + p_{i-1}} \right| \qquad (8$$

Similar formulas are used for the coefficients of the η direction differences.

The parameter σ is a pressure gradient scaling parameter that increases the amount of second-o smoothing relative to fourth-order smoothing near shock waves. The logic used to compute $\varepsilon^{(4)}$ swit off the fourth-order smoothing when the second-order smoothing term is large.

The parameters κ_2 and κ_4 are user-specified constants. Like the coefficients in the constant coeffic model, the optimum values will be problem-dependent, and are best chosen through experience. Cases been run with values of κ_2 ranging from from 0.01 for flows without shocks to 0.1 for flows with shc and κ_4 ranging from 0.0002 for flows computed with spatially constant second-order time differencin 0.005 for flows computed with spatially varying first-order time differencing. Pulliam (1986b) $\kappa_2 = 0.25$ and $\kappa_4 = 0.01$ as typical values for an Euler analysis.

Like the constant coefficient artificial viscosity model, the nonlinear coefficient model requires sp formulas near boundaries. To apply (8.4) at $i = 2$, $\varepsilon_\xi^{(2)}$ is needed at $i = 1$. It is defined as

$$(\varepsilon_\xi^{(2)})_1 = \kappa_2 \Delta\tau \max(\sigma_2,\ \sigma_1)$$

With the above definition, applying (8.4) at $i = 2$ and $i = N_1 - 1$ requires σ at $i = 1$ and $i = N_1$. The defined as

ORIGINAL PAGE IS
OF POOR QUALITY

$$\sigma_1 = \left| \frac{-p_4 + 4p_3 - 5p_2 + 2p_1}{p_4 + 4p_3 + 5p_2 + 2p_1} \right|$$

$$\sigma_{N_1} = \left| \frac{-p_{N_1-3} + 4p_{N_1-2} - 5p_{N_1-1} + 2p_{N_1}}{p_{N_1-3} + 4p_{N_1-2} + 5p_{N_1-1} + 2p_{N_1}} \right|$$

And, finally, applying (8.4) at $i = 2$ and $i = N_1 - 1$ requires $\Delta_\zeta \nabla_\zeta \Delta_\zeta Q$ at $i = 1$ and $i = N_1 - 1$. There are numerous formulas that could be used. The ones currently in the *Proteus* code are

$$\Delta_\xi \nabla_\xi \Delta_\xi Q_1 = -Q_5 + 5Q_4 - 9Q_3 + 7Q_2 - 2Q_1$$

$$\Delta_\xi \nabla_\xi \Delta_\xi Q_{N_1-1} = Q_{N_1-4} - 5Q_{N_1-3} + 9Q_{N_1-2} - 7Q_{N_1-1} + 2Q_{N_1}$$

Anderson, D. A., Tannehill, J. C., and Pletcher, R. H. (1984) *Computational Fluid Mechanics and Heat Transfer*, Hemisphere Publishing Corporation, McGraw-Hill Book Company, New York.

Jameson, A., Schmidt, W., and Turkel, E. (1981) "Numerical Solutions of the Euler Equations by Finite Volume Methods Using Runge-Kutta Time-Stepping Schemes," AIAA Paper 81-1259.

Pulliam, T. H. (1986b) "Artificial Dissipation Models for the Euler Equations," AIAA Journal, Vol. 24, No. 12, pp. 1931-1940.

Steger, J. L. (1978) "Implicit Finite-Difference Simulations of Flow about Arbitrary Two-Dimensional Geometries," AIAA Journal, Vol. 16, No. 7, pp. 679-686.

Appendix O

Fluid Thermodynamic and Transport Property Equations

The thermodynamic and transport equations used for the individual species and binary species pair combinations comprising a hydrogen- oxygen system is presented in this section. The equation types and specific coefficient values for the individual species thermodynamic and transport properties represent those used in the original input file of the CET89 computer code developed at the NASA Lewis Research Center (Reference 50) and are discussed in Section O.1 and O.2, respectively. The binary species properties were based on recommendations made by Svehla (Reference 56) and are discussed in Section O.3.

O.1. Thermodynamic Properties

The fluid specific heat was represented by a piece-wise polynomial as described in Equation (O.1.1):

$$\frac{C_{pi}}{R_i} = a_1 + a_2\ T + a_3\ T^2 + a_4\ T^3 + a_5\ T^4 \tag{O.1.1}$$

Likewise, the fluid enthalpy is described by the following polynomial:

$$\frac{h_i}{R_i T} = a_1 + \frac{a_2}{2} T + \frac{a_3}{3} T^2 + \frac{a_4}{4} T^3 + \frac{a_5}{5} T^4 + a_6 \tag{O.1.2}$$

and the fluid entropy is described in a similar manner:

$$\frac{s_i}{R_i} = a_1 + a_2\ T + \frac{a_3}{2} T^2 + \frac{a_4}{3} T^3 + \frac{a_5}{4} T^4 + a_7 \tag{O.1.3}$$

where the temperature in Equations (O.1.1) to (O.1.3) is in Kelvin.

Low temperature and high temperature values of the coefficients presented in Equations (O.1.1) to (O.1.3) were used, with the transition from the use of the low temperature to the high temperature coefficients occurring at a temperature of 1000 K. The coefficients used for all the species considered in the hydrogen-oxygen chemical rocket system are given in Tables 40 and 41.

Table 40. Low temperature thermodynamic property coefficients.

	$a_1 \times 10^{-1}$	$a_2 \times 10^{2}$	$a_3 \times 10^{5}$	$a_4 \times 10^{8}$	$a_5 \times 10^{11}$	$a_6 \times 10^{-4}$	$a_7 \times 10^{0}$
H	0.25000000	0.0	0.0	0.0	0.0	2.5474390	−0.45989841
H_2	0.29432327	0.34815509	−0.77713819	0.74997496	−0.25203379	−0.097695413	−1.8186137
H_2O	0.41675564	−0.18106868	0.59450878	−0.48670871	0.15284144	−3.0289546	−0.73087997
O	0.30309401	−0.22525853	0.39824540	−0.32604921	0.10152035	2.9136525	2.6099341
O_2	0.37837136	−0.30233634	0.99492754	−0.98189101	0.33031826	−0.10638107	3.6416345
OH	0.38737299	−0.13393773	0.16348351	−0.052133636	0.0041826975	0.35802349	0.34202406

Table 41. High temperature thermodynamic property coefficients.

	$a_1 \times 10^{-1}$	$a_2 \times 10^{3}$	$a_3 \times 10^{7}$	$a_4 \times 10^{10}$	$a_5 \times 10^{14}$	$a_6 \times 10^{-4}$	$a_7 \times 10^{0}$
H	0.25000000	0.0	0.0	0.0	0.0	2.5474390	−0.45989841
H_2	0.30558123	0.59740400	−0.016747471	−0.21247544	0.25195487	−0.086168476	−1.7207073
H_2O	0.26340654	3.1121899	−9.0278449	1.2673054	−0.69164732	−2.9876258	7.0823873
O	0.25342960	−0.01247817	−0.12562724	0.06902986	−0.063797098	2.9231107	4.9628592
O_2	0.36122139	0.74853166	−1.9820646	0.33749007	−0.23907374	−0.11978151	3.6703308
OH	0.28897814	1.0005879	−2.2048807	0.20191288	−0.03940983	0.38857042	5.5566427

O.2. Transport Properties

The procedure for calculating the viscosity and thermal conductivity of a particular species is given in Equations (O.2.1) and (O.2.2):

$$\mu = E\,T^{A}\exp\left(B/T + C/T^{2} + D\right) \tag{O.2.1}$$

$$k = E\,T^{A}\exp\left(B/T + C/T^{2} + D\right) \tag{O.2.2}$$

where the A, B, C, and D curve fit coefficients are unique for Equations (O.2.1) and (O.2.2) and have two sets of values that are valid in the two temperature intervals from 300 to 1000 K and from 1000 to 5000 K. The values of these coefficients are given in Tables 42 to 45. In the viscosity equation the coefficient E is equal to 6.72×10^{-8}, while in the thermal conductivity equation E is equal to 4.01285×10^{-4}. The units of the viscosity are lbm/(ft-sec), while the units of the thermal conductivity are ft-lbm/(sec^3-R). The temperature to be used in Equations (O.2.1) and (O.2.2) is Kelvin.

Table 42. Low temperature thermal conductivity coefficients.

	A	$B \times 10^{-2}$	$C \times 10^{-4}$	D
H	0.58190587	0.46941424	−0.68759582	4.3477961
H_2	0.93724945	1.9013311	−1.9701961	1.7545108
H_2O	1.5541443	0.66106305	0.55969886	−3.9259598
O	0.73824503	0.11221345	0.31668244	1.78085307
O_2	0.81595343	−0.34366856	0.2278508	1.0050990
OH	1.0657000	0.45300526	−0.37257802	−0.49894757

Table 43. High temperature thermal conductivity coefficients.

	A	$B \times 10^{-3}$	$C \times 10^{-5}$	D
H	0.51631898	−1.4613202	7.1446141	5.5877786
H_2	0.74368397	−0.54941898	2.5676376	3.5553997
H_2O	0.79349503	−1.3340063	3.7864327	2.3591470
O	0.79819261	0.17970493	−0.52900889	1.1797640
O_2	0.80805788	0.11982181	−0.47335931	0.9518913
OH	0.58415552	−0.87533541	2.0830503	3.5371071

Table 44. Low temperature viscosity coefficients.

	A	$B \times 10^{-1}$	$C \times 10^{-3}$	D
H	0.58190587	4.6941424	−6.8759582	0.91591909
H_2	0.68887644	0.48727168	−0.59565053	0.55569577
H_2O	0.7838778	−38.260408	49.040158	0.85222785
O	0.73101989	0.60468346	3.5630372	1.0955772
O_2	0.61936357	−4.4608607	−1.3460714	1.9597562
OH	0.78530133	−16.524903	12.621544	0.69788972

Table 45. High temperature viscosity coefficients.

	A	$B \times 10^{-1}$	$C \times 10^{-4}$	D
H	0.51631898	−146.13202	71.446141	2.1559015
H_2	0.70504381	3.6287686	−0.72255550	0.41921607
H_2O	0.50714993	−68.966913	8.745475	3.0285155
O	0.79832550	18.039626	−5.3243244	0.51131026
O_2	0.63839563	−0.12344438	−2.2885810	1.8056937
OH	0.58936635	−36.223418	2.3355306	2.2363455

O.3. Binary Diffusion Coefficients

The binary diffusion coefficient model used in this study involves a polynomial curve fit of tabular predictions made by Svehla (Reference 61). The form of the curve fit model used in the Tethys model is shown in Equation (O.3.1):

$$\wp_{ij} = \frac{a_1 + a_2 T + a_3 T^2 + a_4 T^3 + a_5 T^4 + a_6 T^5}{C\ P} \qquad \text{(O.3.1)}$$

where the units of the fluid static pressure, P, is atmospheres, the conversion constant C is equal to 1.076365×10^{-3}, and the temperature is expressed in Kelvin. The polynomial curve fit procedure was found to yield a sample coefficient of determination, r^2 (Reference 60, page 405), of 1.000 for all of the tabular data, which indicates that the variation in the tabular data (which contained fourteen points ranging in temperature from 0 to 7000 K) is properly modelled by the polynomial curve to an accuracy of at least 0.05 %.

The values of the coefficients used for every binary species pair considered in the Tethys model are presented in Table 46, with units of ft^2/sec.

Table 46. Binary diffusion coefficients.

$\wp_{ij}$	$a_1 \times 10^2$	$a_2 \times 10^4$	$a_3 \times 10^6$	$a_4 \times 10^{10}$	$a_5 \times 10^{14}$	$a_6 \times 10^{20}$
H-H_2	−6.5538	30.157	14.701	−4.5998	5.7366	−226.23
H-H_2O	−6.6010	−2.5389	9.0676	−6.8087	3.1830	1.2932
H-O	0.72345	16.996	6.9347	−4.3702	4.4986	−183.79
H-O_2	−1.3452	14.659	7.9147	−9.4989	10.668	−480.09
H-OH	−5.3002	10.630	8.9498	−6.0576	2.4253	26.018
H_2-H_2O	−1.5355	13.568	7.0940	−12.650	18.090	−947.24
H_2-O	−3.6271	21.194	5.8545	−2.4850	1.9181	−53.869
H_2-O_2	−2.8965	19.097	5.6091	−7.1199	7.9971	−377.46
H_2-OH	−11.084	28.537	4.6334	−1.9617	1.4647	−63.079
H_2O-O	−74.065	215.35	27.764	−68.597	87.064	−4202.8
H_2O-O_2	−2.0372	5.7462	1.8950	−2.3952	2.6230	−119.82
H_2O-OH	−1.3893	−2.8926	2.8463	−3.9455	4.1437	−177.03
O-O_2	−1.0001	6.0491	1.9629	−1.8505	1.9983	−90.678
O-OH	−1.5942	3.8541	2.7872	−3.0969	3.2659	−142.76
O_2-OH	−2.0099	4.9120	1.9139	−2.5363	2.8288	−129.95

VITA

VITA

Kenneth John Kacynski was born to Albert and Lorraine Kacynski on [redacted], in [redacted]. He received a Bachelor of Science degree from Michigan Technological University in 1983. In July of 1983, Ken began his professional career as an engineer in the Space Propulsion Technology Division at the NASA Lewis Research Center in Cleveland, OH. He married DeLynn Lange on December 17 of the same year. In the spring of 1986, Ken received a Master of Science degree from the University of Toledo. That fall, he began the pursuit of the degree of Doctor of Philosophy at Purdue University, which was completed in 1994. He remains in the Space Propulsion Technology Division where he has been involved with issues related to rocket nozzle performance throughout his career. Ken has two children, Kristopher, born on December 20, 1991, and Nicholas, born on May 27, 1993.

REPORT DOCUMENTATION PAGE

Form Approved
OMB No. 0704-0188

Public reporting burden for this collection of information is estimated to average 1 hour per response, including the time for reviewing instructions, searching existing data sources, gathering and maintaining the data needed, and completing and reviewing the collection of information. Send comments regarding this burden estimate or any other aspect of this collection of information, including suggestions for reducing this burden, to Washington Headquarters Services, Directorate for Information Operations and Reports, 1215 Jefferson Davis Highway, Suite 1204, Arlington, VA 22202-4302, and to the Office of Management and Budget, Paperwork Reduction Project (0704-0188), Washington, DC 20503.

1. AGENCY USE ONLY (*Leave blank*)	2. REPORT DATE	3. REPORT TYPE AND DATES COVERED
	April 1994	Technical Memorandum

4. TITLE AND SUBTITLE
Calculation of Propulsive Nozzle Flowfields in Multidiffusing Chemically Reacting Environments

5. FUNDING NUMBERS
WU-506-42-72

6. AUTHOR(S)
Kenneth John Kacynski

7. PERFORMING ORGANIZATION NAME(S) AND ADDRESS(ES)
National Aeronautics and Space Administration
Lewis Research Center
Cleveland, Ohio 44135-3191

8. PERFORMING ORGANIZATION REPORT NUMBER
E-8665

9. SPONSORING/MONITORING AGENCY NAME(S) AND ADDRESS(ES)
National Aeronautics and Space Administration
Washington, D.C. 20546-0001

10. SPONSORING/MONITORING AGENCY REPORT NUMBER
NASA TM-106532

11. SUPPLEMENTARY NOTES
This report was submitted as a dissertation in partial fulfillment of the requirements for the degree Doctor of Philosophy to Purdue University, West Lafayette, May 1994. Responsible person, Kenneth John Kacynski, organization code 5320, (216) 433-7497.

12a. DISTRIBUTION/AVAILABILITY STATEMENT
Unclassified - Unlimited
Subject Categories 02, 34, and 64

12b. DISTRIBUTION CODE

13. ABSTRACT ***(Maximum 200 words)***

An advanced engineering model has been developed to aid in the analysis and design of hydrogen/oxygen chemical rocket engines. The complete multispecies, chemically reacting and multidiffusing Navier-Stokes equations are modelled, including the Soret thermal diffusion and the Dufour energy transfer terms. In addition to the spectrum of multispecies aspects developed, the model developed in this study is also conservative in axisymmetric flow for both inviscid and viscous flow environments and the boundary conditions employ a viscous, chemically reacting, reference plane characteristics method. Demonstration cases are presented for a 1030:1 area ratio nozzle, a 25 lbf film cooled nozzle, and a transpiration cooled plug and spool rocket engine. The results indicate that the thrust coefficient predictions of the 1030:1 and the 25 lbf film cooled nozzle are within 0.2 to 0.5 %, respectively, of experimental measurements when all of the chemical reaction and diffusion terms are considered. Further, the model's predictions agree very well with the heat transfer measurements made in all of the nozzle test cases. The Soret thermal diffusion term is demonstrated to have a significant effect on the predicted mass fraction of hydrogen along the wall of the nozzle in both the laminar flow 1030:1 nozzle and the turbulent flow plug and spool nozzle analysis cases performed. Further, the Soret term was shown to represent an important fraction of the diffusion fluxes occurring in a transpiration cooled rocket engine.

14. SUBJECT TERMS
Nozzle flowfields; Multidiffusing; Chemically reacting; Film cooling; Transpiration cooling; Thermal diffusion

15. NUMBER OF PAGES
278

16. PRICE CODE
A08

17. SECURITY CLASSIFICATION OF REPORT	18. SECURITY CLASSIFICATION OF THIS PAGE	19. SECURITY CLASSIFICATION OF ABSTRACT	20. LIMITATION OF ABSTRACT
Unclassified	Unclassified	Unclassified	